



**Paleoenvironment and post-depositional changes
recorded in the chemical composition of marine
sediments from the Gulf of Alaska**

presented by

Mark Sebastian Zindorf

A thesis submitted to Newcastle University in partial fulfilment of the requirements for the
degree of Doctor of Philosophy (PhD)

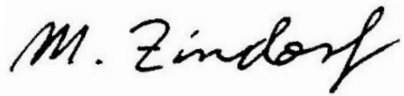
Supervised by

Dr Christian März, Prof Thomas Wagner, Dr Cees van der Land

Newcastle upon Tyne, November 2018

Declaration

I hereby certify that the work presented in this thesis is my own, except where otherwise acknowledged, and has not been submitted previously for a degree at this, or any other University.

A handwritten signature in black ink that reads "M. Zindorf". The signature is written in a cursive style with a large, stylized 'M' and 'Z'.

Mark Zindorf

Abstract

The composition of marine sediments is controlled by an interplay of primary deposition and post-depositional changes, for example organic matter decomposition and authigenic mineral formation. These changes are called early diagenesis and are influenced by external factors, such as sedimentation rates and the supply of organic matter and electron acceptors. IODP Expedition 341 drilled the sites U1417 and U1419 in the Gulf of Alaska. Both sites record a unique feature of diagenetic and primary depositional interplay. At Site U1417 varying sedimentation rates and organic matter input caused cementation and a self-sealing of discrete sediment layers which trapped a methane reservoir in the sediments. Also, a deep pool of sulphate rich waters exists close to the basement. This pool is either invoked by tectonic or volcanic processes or caused by the cut-off of a seawater pool due to varying sedimentation rates. The diagenetic overprint of this site is investigated by inorganic, pore-water and isotope geochemistry and the application of a reaction transport model. At Site U1419 the variability of the oxygen deficient zone in the Gulf of Alaska in response to paleoclimate is recorded by the novel BHT isomer biomarker for marine anammox. Usually oxygen limited conditions also cause trace element accumulations in marine sediments. However, at Site U1419 trace element concentrations do not follow the trends recorded by BHT isomer. Their distribution is affected by other external factors. Copper and nickel are affected by bioproductivity, chromium and vanadium by sedimentary provenance and the accumulation of molybdenum and uranium is prevented by overall high sedimentation rates. This PhD project brings these two features of the interplay between primary deposition and diagenetic overprint in the context of global biogeochemical cycles of organic matter and elements.

To my mum

Acknowledgements

When talking to outsiders about my work, I was sometimes confronted with the opinion that a PhD in Geochemistry must be a rather dull job with lots of desk-work and long hours in the lab. Nothing could be further from the truth (ok, there was lots of desk work and long hours in the lab, but overall it was far away from being dull). Doing my PhD in Newcastle was a unique experience, full of adventures and new impressions and this is not to the least because of the many people I met on my journey.

It was great to work with these people, learn from them and learn about their exciting ways and hear their stories. Therefore, as the first thing in this thesis and before presenting the "hard facts", I want to thank everyone who made the following pages possible, relevant and exciting.

First of all, I thank my three supervisors, Christian, Tom and Cees.

Chris has been and still is an extremely supportive supervisor who always had an open ear to my ideas and questions - even from Leeds. He did everything to support me not only with my project, but also for my development as a scientist. He encouraged me to produce publishable work, go to summer schools and get expedition experience. Chris, I wish you and Sonja and your child all the best for the future. Tom was always very helpful with his experience, big-picture thinking and optimism. Despite being in Edinburgh he was there when I needed advise. Both also really helped me to settle down in Newcastle. After Chris and Tom left Newcastle, Cees took over and supervised me with great enthusiasm, even though he had to care for many other PhD students. I am thankful for the support I received from all three of you.

Then, thanks go to my internal and external examiners. Jon and Sasha, the discussion during my viva was really fruitful and did not only contribute to the improvement of this thesis, but also of the papers coming out of this.

Even though being far from home, it never felt like that. This was due to my family. Thanks to modern communication, I could share all the adventures, everyday stories, but also problems with my sister Janka and my Dad who also was an immeasurable help with my movings. With that he re-discovered Britain as a fabulous holiday destination. I thank you guys for your support and I am glad that you are with me!

To my friends in Newcastle: Sven, Luiza, Stephen, it was always great to go climbing with you, as well as all the other stuff we did together (Halfway hikes, concerts, etc.). Carol and Kirsten, I thank you for all the fun, the scientific discussions and a couple of drinks. Kerry, thanks for talking me into diving. Patri, even though it was sometimes difficult, I enjoyed living with you. I wish you all the best for your way in the future. Rachel, thank you for some nice discussions on anammox, BHT and for helping me with my first postdoc applications.

I sometimes have the feeling that my friends at home didn't get the attention they deserved. All the more, I am thankful that you didn't give up on me, guys! Andreas, Steffi, Felix, Sister and Juju, thanks for the regular skypes and for great holidays we did together (Newcastle, Scotland, USA). Caro, I am very happy that I had you with me for a part of this time. I wish you all the best for your future. Keep on travelling!

Jenny and Maurice, thanks for preparing me for the Geordie experience, before the start of all this.

Thanks go to all the scientists I worked together with on this project: Darci, you were a great help with the biomarker work and doing this was a great chance to get some insight into this completely new field of BHT isomer - something none of my supervisors had any experience with. Sandra, thank you for doing the modelling with me. I fully appreciate that you did this besides of your normal duties and even besides moving to a new institute. All the people from IODP 341: Sean, John, Leah, Jeff, Harald, Laurel and Mo for contributing data and discussing research with me. Mo, Paul and Ty, it was absolutely great, that you invited us to stay at your house on our West Coast road trip!

When I needed advice in the lab, Phil, Paul, Bernie and David were always there. I guess not many students would have graduated at Newcastle without your support. The same is true for Yvonne and Mags who supported us with all the organisational stuff. I am actually quite happy that I left Drummond Building soon after you, so I didn't have to deal with the chaos that emerged after you left (ok, I am exaggerating, but one could feel your absence).

Finally, greetings to everyone I did not mention here. I hope I see you all again soon.

Howay, pet!

Index

Abstract	V
Acknowledgements	VII
Index	IX
List of figures and tables.....	XI
1. Introduction.....	1
1.1 Motivation	1
1.2 Investigated environmental setting	3
1.3 Early diagenetic reactions.....	7
1.4 Geochemical proxies for oxygen deficient zone extent and intensity	11
1.5 Available material and applied methodology	14
1.5.1 Shipboard data and previously available material	14
1.5.2 Analyses conducted for this thesis	19
1.5.3 Further datasets used for comparison	20
1.6 Structure of the study.....	21
Part I Early diagenesis at Site U1417	23
2. Deep Sulphate-Methane-Transition affects sediment diagenesis in the Gulf of Alaska (IODP Site U1417)	25
2.1 Introduction.....	25
2.2 Materials and methods	28
2.3 Results.....	29
2.4 Discussion	31
2.5 Conclusions.....	46
3. The plausibility of a deep buried pore-water sulphate reservoir in marine sediments assessed by reaction transport modelling	49
3.1 Introduction.....	49
3.2 Methods.....	51

3.3 Results.....	58
3.4 Discussion	61
3.5 Further directions of modelling.....	65
3.6 Conclusions	68
Part II Anammox at Site U1419	69
4. Anammox and the oxygen deficient zone in the Gulf of Alaska during Late Glacial Maximum	71
4.1 Introduction	71
4.2 Methods.....	74
4.3 Results.....	76
4.4 Discussion	80
4.5 Conclusions.....	92
5. Synthesis.....	95
Literature	105
Appendices	

List of figures and tables

Figure 1.1 Area of investigation	4
Figure 1.2 Formulas of chemical reactions during early diagenesis	10
Figure 1.3 Chemical structure of BHT and BHT isomer	11
Figure 1.4 Stratigraphic composite record at Site U1417	14
Figure 1.5 Shipboard pore-water and pore-gas data at Site U1417	16
Figure 1.6 Stratigraphic composite record at Site U1419	18
Figure 1.7 Shipboard pore-water and pore-gas data at Site U1419	19
Figure 2.1 Bathymetric map	26
Figure 2.2 Geochemical data at Site U1417	30
Figure 2.3 Fe and S speciation data	31
Figure 2.4 Geochemical data relevant for Ba diagenesis	34
Figure 2.5 Crossplot of Ba vs Sulphate between 200 and 640 mbsf	36
Figure 2.6 Schematic illustration of deep aquifer generating processes	39
Figure 2.7 Seismic profile across Site U1417	41
Figure 2.8 Pyrite-sulphur isotope data	42
Figure 2.9 Pseudo-Van-Krevelen Plot for Site U1417 below 600 m CCSF-B	44
Figure 2.10 Schematic illustration of deep aquifer generation by plate bending faults	45
Figure 3.1 TOC profiles at time of deposition	57
Figure 3.2 Modelled present day scenarios for four different RCM parameters	59
Figure 3.3 Modelled present day scenarios for two refined RCM parameters.....	59
Figure 3.4 Sedimentation rate and position of snapshots	60
Figure 3.5 Transient modelled geochemical profiles of bet fit scenario.....	62
Figure 3.6 Transient modelled geochemical profiles of alternative scenario.....	63
Figure 4.1 Area of investigation	72
Figure 4.2 Components of BHT isomer biomarker	78
Figure 4.3 Inorganic geochemical data at Site U1419.....	79
Figure 4.4 Organic geochemical data at Site U1419	80
Figure 4.5 Crossplot of BHT isomer biomarker vs TOC	82

Figure 4.6 Element/Al ratios for inorganic geochemical data.....	83
Figure 4.7 Crossplot of BHT isomer biomarker vs trace metals.....	84
Figure 4.8 Accumulation rates of inorganic geochemical sediment components.....	87
Figure 4.9 Crossplot of sedimentation rate vs trace metals.....	89
Figure 4.10 Crossplot of TOC vs Cu and Ni.....	90
Figure 4.11 Schematic illustration of processes related to ODZ dynamics.....	91
Table 3.1a Transport parameters.....	53
Table 3.1b Reaction parameters.....	54
Table 3.2 Reaction rates.....	55
Table 3.3 Boundary conditions.....	58
Table 4.1 Average element values for Average Shale and Chugach Terrane.....	77

1. Introduction

1.1 Motivation

Studying marine sediments provides a wealth of information about earth processes including, amongst others, past climates, tectonics and the frontiers of microbial life on planet Earth (Stein et al., 2014). Because marine sediments are accumulated over millions of years and stay relatively undisturbed compared to terrestrial archives over long time periods, they form an ideal archive of depositional and biogeochemical processes, especially for the climate during the time of deposition (e.g. Wefer et al., 1999).

It is of utmost importance for mankind, to understand the workings of the climate system if we want to protect our environment, predict the course of anthropogenic global climate change and assess its impact (IPCC, 2013). A second reason for studying marine sedimentary archives is to reveal periods of time and environments suitable for the formation of raw materials, e.g. oil, natural gas or metal deposits (e.g. Beck and Lehner, 1974; Rona, 2008).

The chemical composition of marine sediments provides information on their formation conditions. The inventory of chemical elements is controlled by primary sediment deposition in several ways. Detrital material, which is deposited at the seafloor, consists of lithogenic components eroded from rocks on land. Different rocks have a distinguishable chemical composition which leaves an imprint in the deposited sediments. Analysing specific elements or minerals can therefore provide information on the provenance (origin) of the sediments. This allows conclusions on factors affecting a certain provenance change, e.g. a change of supply area by advancing ice streams or changing runoff directions (Haughton et al., 1991). The amount and composition of organic material and nutrients deposited at the seafloor holds information about past bioproductivity and the source of the biogenous material (e.g. terrestrial or marine). Biomarkers, molecules that are formed by specific organisms under specific environmental conditions, can be used to refine the distinction of depositional regimes. Changes in redox conditions in the water column caused by high oxygen consumption in combination with insufficient oxygen re-supply by ventilation (e.g. Paulmier and Ruiz-Pino, 2009) facilitate the accumulation of redox sensitive elements (Huerta-Diaz and Morse, 1992; Morford and Emerson, 1999) and influence the preservation of organic matter (Hedges and Keil, 1995; Hartnett et al., 1998).

After primary deposition, decomposition of organic matter sets in, which again can change the composition of marine sediments. This process is called early diagenesis and is driven by microbial life in the sediments. Early diagenesis usually happens as a defined sequence of redox reactions the order of which is controlled by the energy yield provided to the respective microbial communities by the used electron acceptor (Froelich et al., 1979). By this, a defined depth-sequence of redox-zones is installed in marine sediments. Each of these zones has its unique geochemical makeup of dissolved ions in the sedimentary interstitial waters and of diagenetic mineral formations and trace element enrichments (Froelich et al., 1979). These mineral accumulations allow to detect the zones in a sediment succession. The diagenetic decomposition of organic matter alters the concentration of the organic material in the sediments as well as its chemical composition by converting predominantly reactive organic material to CO₂ (e.g. Boudreau and Ruddick, 1991; Hedges and Keil, 1995; Thullner et al., 2009). Thus early diagenesis compromises the use of organic matter as a proxy for paleoproductivity. Also, as diagenesis changes the redox conditions in the sediments, redox sensitive trace elements can be redistributed in the sediment column (Calvert and Pedersen, 2007) and authigenic mineral formation can further change sediment composition by enriching specific elements in delimited horizons (e.g. Hathaway and Degens, 1969; Berner, 1984; Riedinger et al., 2006).

Taking primary deposition, water-column redox conditions and diagenetic reactions together, the chemical makeup of sedimentary sequences is affected by different processes on different time scales. This may cause contradicting signals recorded by different proxies and provides pitfalls for interpretation. For sedimentologists and geochemists, it is essential to distinguish between these processes and their contribution to the finally observed sediment composition.

The study at hand addresses this problem of distinguishing several superimposed proxy signals and investigates the early diagenetic evolution of an open ocean site in relation to changes in primary deposition and tectonics. A second focus lies on the record of water column oxygenation and the factors influencing trace element accumulation on a second site at the continental slope.

1.2 Investigated environmental setting

The Gulf of Alaska (GOA, Figure 1.1 A) is a very well suited environment to study the interplay between deposition and post-depositional overprint. It exhibits an oxygen deficient zone (ODZ; Paulmier and Ruiz-Pino, 2009; Moffitt et al., 2015) which has been found to react to global climate (e.g. McKay et al., 2005; Davies et al., 2011). It intensifies (lower oxygen concentration) and expands in warmer climatic conditions and retreats and weakens (better oxygenation) in colder climatic conditions. This pattern has been confirmed for the past ~15 ka (McKay et al., 2005; Barron et al., 2009; Addison et al., 2012). The Surveyor Fan and Channel (e.g. Reece et al., 2011; see below) with their varying sedimentation rates provide an interesting environment to study non-steady state diagenetic reactions. The diagenetic record has indeed been found to deviate profoundly from the ideal sequence *sensu* Froelich at one site (Jaeger et al., 2014).

The basement in the GOA is formed by the Pacific plate which moves north-westward at an angle of -315.19° at $\sim 53 \text{ mm a}^{-1}$ (DeMets et al., 2010). It is subducted in a low-angle subduction beneath the North American Plate and partly accreted to the continent (Plafker, 1987). The accreted material forms the coastal St. Elias and Chugach Mountain ranges. These mountain ranges are the main source for the sediments which are entering the GOA (Penkrot et al., in press). The sea floor of the GOA is dominated by the Surveyor Fan - one of the largest deep sea fans in the world. In contrast to other fans (e.g. Amazon, Zambesi, Indus), the Surveyor Fan does not have a major river as a sediment source, but is fed by glacially eroded material. It is incised by the Surveyor Channel, an erosional feature of approximately 700 km length and a depth of up to 500 m (Reece et al., 2011).

The GOA is subject to the current systems prevailing in the Pacific Ocean (Figure 1.1 B). The North Pacific Current which crosses the Pacific Ocean at about 40°N reaches the North American coast at the California Margin and is deflected north- and southwards. The northern leg forms the Alaska Current. At the northern end of the GOA the Alaska Current turns south-westwards and from there on is called the Alaska Stream. Part of the Alaska Stream turns south, approximately at the Aleutian Islands, and re-circulates into the Alaska Current, forming the cyclonic Alaska Gyre. Along the coast, relatively fresh melt-water forms the northward running Alaska Coastal Current (Stabeno et al., 2004).

The Alaska Gyre brings nitrate-rich waters to the shelf where they mix with Fe-rich waters of

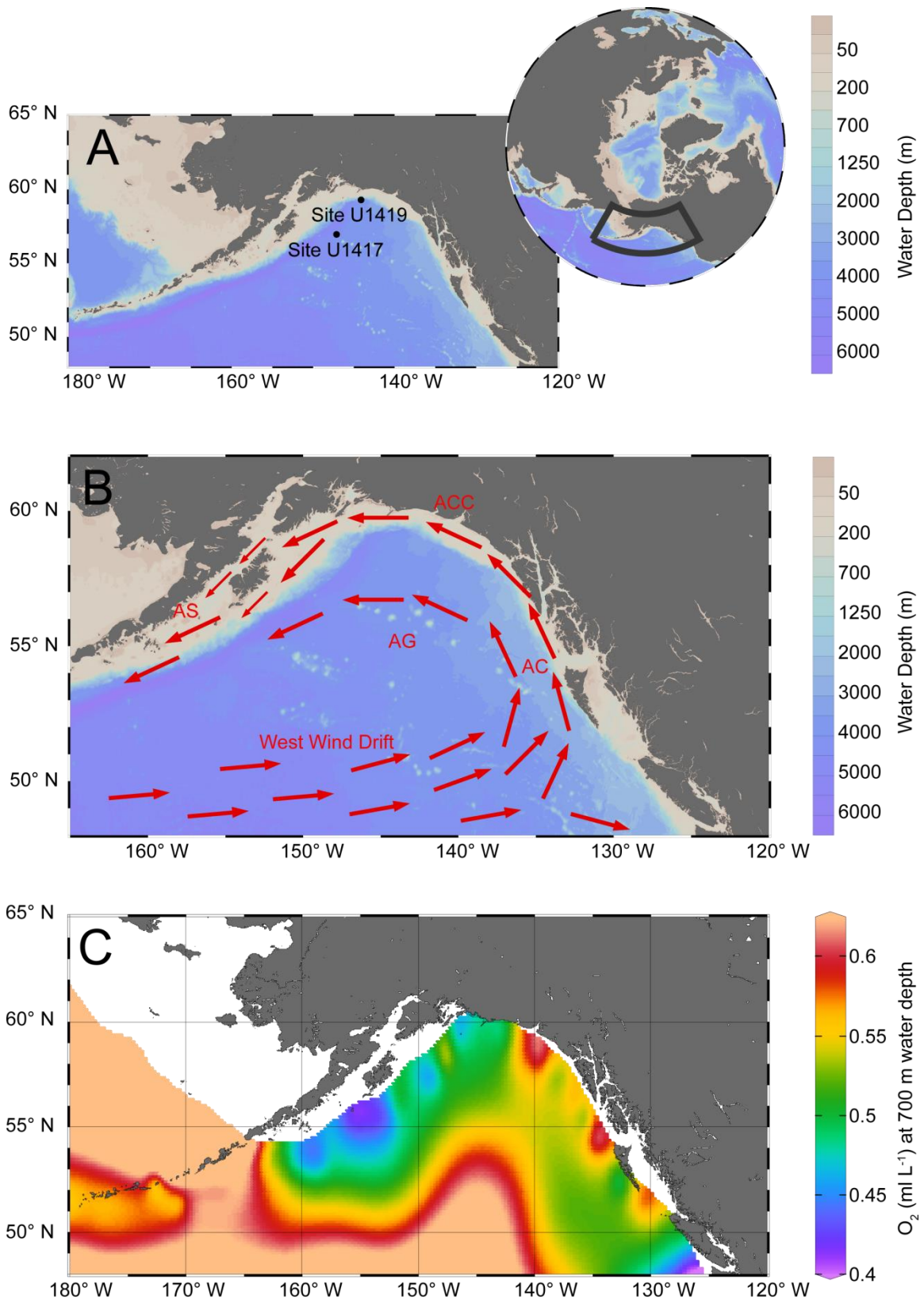


Figure 1.1: Area of investigation A) Bathymetric map of the GOA, positions of sites investigated in this study given by black dots; black polygon in global overview shows position of maps A and C; B) Ocean currents in the GOA; AC: Alaska Current, ACC: Alaska Coastal Current, AG: Alaska Gyre, AS: Alaska Stream; Map redrawn after Barron et al. (2009); C) Oxygen content (ml L^{-1}) at 700 m water depth (O_2 data from World Ocean Atlas 2005; Garcia et al., 2006; all maps created with Ocean Data view; Schlitzer, 2015).

the Alaska Coastal Current. This nutrient-mixing causes phytoplankton blooms in spring. In the centre of the GOA, by contrast, productivity in the Alaska Gyre is iron limited and thus the GOA forms one of the High Nutrient Low Chlorophyll regions of the world (Martin, 1990). The transport of nutrients and especially iron which is mostly derived from fluvial runoff, glacial rock-flour and suboxic dissolution in the shelf is mostly conducted by anticyclonic mesoscale eddies (Whitney and Robert, 2002; Stabeno et al., 2004; Johnson et al., 2005). Generally, the GOA is characterized by a downwelling regime (Weingartner et al., 2005). During the winter months, the atmospheric pressure system of the Aleutian Low lies over the centre of the Alaska Gyre and causes vigorous mixing and upwelling which weakens again during the summer months. This leads to the expression of a seasonal ODZ in 670 to 1060 m water depth (Figure 1.1 C) which is most pronounced during spring and autumn and disappears in summer (Paulmier and Ruiz-Pino, 2009; Moffitt et al., 2015).

Long-term paleoclimate records from the subarctic North Pacific, including Sites from ODP Expedition 145, especially ODP Site 887 on the Patton-Murray Seamount (Rea and Snoeckx, 1995) and drill cores from IODP Expedition 323 to the Bering Sea (Takahashi et al., 2011) show a gradual cooling in climate from mid Pliocene on and a shift to fully glacial conditions with increased ice rafted debris and a sea-surface temperature drop at 2.75 Ma BP at the onset of Northern Hemispheric Glaciation (Maslin et al., 1996). The onset of northern-hemispheric glaciation is marked by the onset of stratification in the North Pacific (Haug et al., 1999). Since the Mid Pleistocene Transition (~1 Ma BP; e.g. Clark et al., 2006) glacial erosion in the coastal ranges increased and outpaced mountain uplift and led to an increased sediment supply to the GOA (Gulick et al., 2015). The reaction of the GOA ODZ to paleoclimate is to date only resolved for the last 17 ka (Addison et al., 2012). It has been found to intensify (less oxygen in the water column) during warmer times and to weaken (more oxygen) during cooler periods (McKay et al., 2005; Barron et al., 2009; Addison et al., 2012). Higher bioproductivity (Addison et al., 2012) and decreased oxygen solubility in warmer waters (Praetorius et al., 2015) in combination with fertilization by suboxic Fe release from the shelf (Addison et al., 2012; Praetorius et al., 2015) are discussed as causes for this climate-oxygenation coupling for the GOA records. Other authors (Van Geen et al., 2006; Cartapanis et al., 2011, 2012) propose changes in ventilation as a reason for ODZ expansion in the North Pacific, potentially triggered by higher influx of oxygen rich subarctic

waters or better oxygenation of equatorial water masses in cold periods. Records for the North Pacific ODZ off California reach as far back as 70 ka (e.g. Cartapanis et al., 2011, 2012), whereas records in the GOA only cover the last 17 ka (McKay et al., 2005; Barron et al., 2009; Addison et al., 2012).

The GOA plays an important role in the modern climate system. Two factors make the GOA susceptible to subtle environmental changes which can then lead to feedback reactions with an effect on global climate. The first factor is the High Nutrient Low Chlorophyll behaviour of the GOA. The limiting factor for bioproductivity in the GOA is iron (Fe) in a bioavailable form (Martin et al., 1989). Changes in Fe input can be caused by variations in glacier runoff along the mountain cordilleras surrounding the Gulf of Alaska (Poulton and Raiswell, 2002; 2005; Raiswell et al., 2006; Statham et al., 2008). This can cause algal blooms and potentially lead to the sequestration of organic carbon (C) at the seafloor and by that to a drawdown of CO₂ from the atmosphere (Martin, 1990; Raiswell et al., 2006). By the climate sensitivity of the Fe input, a feedback mechanism exists between global climate and bioproductivity in the GOA. Another important component of the climate system in the GOA is the ODZ. As described above, it is sensitive to northern hemispheric climate, but it also provides a climatologically important feedback mechanism. The seawater oxygenation influences the efficiency of organic matter remineralization (Hartnett et al., 1998; Burdige, 2007). Under suboxic conditions more organic matter is sequestered and effectively removed from the atmospheric and oceanic carbon cycle. A spatial expansion or intensification of oxygen limited conditions under warmer climatic conditions, e.g. due to an algal bloom caused by higher nutrient input would cause less organic matter being oxidized in the water column and more organic carbon being exported to the seafloor. Additionally, expanding ODZs, especially the shoaling of the upper ODZ boundary, cause habitat loss for macrofauna (Stramma et al., 2008; 2012, Gilly et al., 2013). This affects food webs as well as the security of human nutrition. Here, climate impacts on the GOA can directly impact human economy. IODP Expedition 341 drilled a transect of five sites in the Gulf of Alaska (Jaeger et al., 2014). Two of these sites, U1417 and U1419, are investigated in this thesis (Figure 1.1 A). Site U1417 lies in 4200 m water depth. This site is excellently positioned to study non-steady state diagenesis on a 700 m/16 Ma spanning sediment succession. The site is influenced by the sedimentary environment of the Surveyor Fan. This deep sea fan is predominantly

glacially fed and has no major river as sediment source (Reece et al., 2011). Hence, climatic changes which cause glacier advances or retreats will also affect the erosion on land and sediment input into the Gulf of Alaska. Therefore, sedimentation rates at Site U1417 can be expected to react very sensitive to northern hemispheric climate (e.g. Gulick et al., 2015). Furthermore, the supplied organic matter can be profoundly different from the material deposited on other deep sea fans which were investigated for early diagenesis, such as the Amazon or Zambesi Fans (e.g. Kasten et al., 1998; März et al., 2008a). These river-fed fans provide organic rich detritus from large tropical terrestrial source areas, whereas the Surveyor Fan in the Gulf of Alaska is mainly fed by glacial rock flour (Reece et al., 2011). Tectonic processes related to adjacent Giacomini and Kodiak Sea Mounts (Turner et al., 1973; Silver et al., 1974) and to subduction related plate bending (e.g. Naif et al., 2015) can further influence the diagenetic evolution.

Site U1419 is positioned on the continental slope in 721 m water depth. Therefore it lies within the centre of the present Oxygen Deficient Zone (ODZ) and is perfectly placed to study the interplay between water column oxygenation and sedimentary or diagenetic processes of elementary composition of the sediments. The site has been drilled to a depth of 170 m and a detailed age model reaches until 80 mbsf and spans 54 ka (Walczak and Mix, pers. comm.). This segment will be investigated in this study.

Exploring early diagenesis and the behaviour of the ODZ in the GOA works in partial fulfilment of one of the expeditions aims, to: "Understand the dynamics of productivity, nutrients, freshwater input to the ocean, and surface and subsurface circulation in the northeast Pacific and their role in the global carbon cycle" (Jaeger et al., 2014), linking this study into a broader international research collaboration.

1.3 Early diagenetic reactions

The term early diagenesis describes post-depositional changes of sediment composition and structure related to the degradation of organic matter (OM). Microbes at the seafloor decompose OM by using oxygen, which yields by far the most energy during metabolism, as an electron acceptor (EA). After oxygen is depleted other, less favourable EAs are used to decompose the remaining organic material (Froelich et al., 1979; see Figure 1.2 for reaction

formulas). Again, the organisms using the EA which yields most energy are the most competitive and this EA is used up first. Based on the succession of used EAs, a diagenetic zonation is installed. Electron acceptors are in the order of energy yield: oxygen, nitrate, Mn(oxyhydr)oxides, Fe(oxyhydr)oxides and sulphate (Froelich et al., 1979; Jorgensen, 2006). According to Thullner et al. (2009), bacterial sulphate reduction accounts for 76% of OM remineralization in marine sediments on a global scale. However, in deep sea sediments the relative contribution of oxic respiration to OM remineralization increases. After the bacterial reduction of all EAs, the remaining OM can be converted to methane by methanogenic archaea. The border between the sulphatic and methanogenic zone is called Sulphate-Methane Transition Zone (SMTZ). It usually is established as a clearly defined zone because methane diffuses back into the sulphatic zone, where it reacts with sulphate in a bacterially mediated reaction called anaerobic oxidation of methane (AOM; Reeburgh, 1980; Niewöhner et al., 1998; Boetius et al., 2000; Knittel and Boetius, 2009). This leads to a depletion of both molecules and a peak of hydrogen sulphide in the SMTZ. The SMTZ is a very important environment for microbial life in marine sediments, because it hosts three microbial processes, bacterial sulphate reduction, methanogenesis and AOM (Parkes et al., 2005; Harrison et al., 2009) and further due to the relative importance of sulphate reduction in comparison with other redox processes in marine sediments.

Another process, by which hydrogen sulphide, but also sulphate is produced, is disproportionation (Thamdrup et al., 1993). In this process, elemental sulphur (S) or other intermediate redox states of S are converted in a more reduced and a more oxidized species at the same time. Bacteria mediating this reaction path require iron oxides or manganese oxides to grow (Thamdrup et al., 1993). By S-disproportionation, low sulphate concentrations can be maintained even below the zone of sulphate reduction.

Hydrogen sulphide, the product of sulphate reduction and disproportionation, can react with reduced Fe species from preceding Fe reduction and form Fe monosulphides and pyrite (Berner, 1984; Raiswell and Berner, 1986; Canfield et al., 1992). Methanogenesis produces alkalinity which leads to carbonate mineral precipitation (Hathaway and Degens, 1969; Sun and Turchyn, 2014; Pierre et al., 2016; Wehrmann et al., 2016) and authigenic barites (barium-sulphate) form when sulphate gets depleted and biogenic barite dissolves. Barium ions diffuse upwards, back into the sulphatic zone, where they react with sulphate and form diagenetic barites (Torres et al., 1996; Riedinger et al., 2006; Peketi et al., 2012). Authigenic

pyrites, barites and carbonates precipitate in the vicinity of the SMTZ and can be used to spot recent and ancient SMTZs in sediment records (e.g. Riedinger et al., 2006; Lin et al., 2016; Wehrmann et al., 2016).

During sulphate reduction, sulphur undergoes an isotope fractionation (Canfield, 2001). Bacterial metabolisms process lighter isotopes somewhat faster which causes an enrichment of the lighter isotope in the reaction product. In the case of sulphate, hydrogen sulphide becomes isotopically lighter than the original sulphate, while the remaining sulphate becomes isotopically heavier (Harrison and Thode, 1958; Kaplan and Rittenberg, 1964). By analysing the two most abundant sulphur isotopes, ^{32}S and ^{34}S , on pore-water sulphate or precipitated pyrite, or also on barite, the intensity of sulphate reduction can be estimated (e.g. Strauss, 1997; Ono, 2008; Sim et al., 2011; Strauss et al., 2012). If the sulphate source is limited (closed system conditions), also heavier isotopes become enriched in sulphides (Canfield, 2001). Hence, S isotopes can provide some information on the source of the sulphate during geologic history as well (e.g. Strauss and Schieber, 1990).

The above-described early diagenetic concepts are somewhat idealized and the redox-sequence described by Froelich et al. (1979) is often modified in nature. Non-steady state diagenesis occurs if EAs or electron donors (organic matter) are not supplied in a constant concentration over time or if sedimentation rates fluctuate and modify the diffusion of EAs in the sediment (Kasten et al., 2001, 2003; Contreras et al., 2013). A possible consequence of varying sedimentation rates is that diagenetic fronts, such as the SMTZ, can be locked in a specific depth horizon for a longer period and cause intense authigenic mineral precipitation (Wehrmann et al., 2013; 2016), or that zones migrate up and down in the sediment succession (Contreras et al., 2013). These fluctuations in sedimentation rates or OM supply can, for example, be caused by changes in climate (Meister, 2015). A special case of non-steady state diagenesis is a second EA supply at the base of the sediment succession. This feature has been found in relation to tectonic processes enabling water circulation in deeper sediment layers, such as aquifer generation along seamount flanks (Fisher et al., 2003a; Engelen et al., 2008), or water circulation in faults in accretionary wedges (Torres et al., 2015). Often a second, reversed SMTZ (sulphate diffusing from below, methane diffusing from above) is installed closer to the sediment basement interface (e.g. DeLong, 2004).

Metabolic reactions of organic matter oxidation during early diagenesis

Aerobic respiration	$(CH_2O)_x(NH_3)_y(H_3PO_4)_z + (x + 2y)O_2 \rightarrow xCO_2 + (x + y)H_2O + yHNO_3 + zH_3PO_4$
Nitrate reduction	$5(CH_2O)_x(NH_3)_y(H_3PO_4)_z + 4xNO_3^- \rightarrow xCO_2 + 3xH_2O + 4xHCO_3^- + 2xN_2 + 5yNH_3 + 5zH_3PO_4$
Manganese oxide reduction	$(CH_2O)_x(NH_3)_y(H_3PO_4)_z + 2xMnO_2 + 3xCO_2 + xH_2O \rightarrow 2xMn^{2+} + 4xHCO_3^- + yNH_3 + zH_3PO_4$
Iron oxide reduction	$(CH_2O)_x(NH_3)_y(H_3PO_4)_z + 4xFe(OH)_3 + 7xCO_2 \rightarrow 4xFe^{2+} + 8xHCO_3^- + 3xH_2O + yNH_3 + zH_3PO_4$
Organoclastic sulphate reduction	$2(CH_2O)_x(NH_3)_y(H_3PO_4)_z + xSO_4^{2-} \rightarrow xH_2S + 2xHCO_3^- + 2yNH_3 + 2zH_3PO_4$
Sulphur disproportionation	$4S^0 + 4H_2O \rightarrow 3H_2S + SO_4^{2-} + 2H^+$ $S_2O_3^{2-} + H_2O \rightarrow H_2S + SO_4^{2-}$
Hydrogenotrophic methanogenesis	$CO_2 + 4H_2 \rightarrow CH_4 + 2H_2O$
Acetoclastic methanogenesis	$CH_3COOH \rightarrow CO_2 + CH_4$
Anaerobic oxydation of methane coupled to sulphate reduction	$CH_4 + SO_4^{2-} \rightarrow HS^- + HCO_3^- + H_2O$
Iron monosulphide and pyrite formation	$Fe^{2+} + H_2S \rightarrow FeS + 2H^+$ $FeS + S_x^{2-} \rightarrow FeS_2 + (x - 1)S_x^{2-}$ $FeS + H_2S \rightarrow FeS_2 + H_2$
Alkalinity generation via sulphate reduction	$3SO_4^{2-} + 6H_2O + 2FeOOH \rightarrow 6HCO_3^- + FeS_2 + FeS + 4H_2O$ $3SO_4^{2-} + 3CH_4 + 2FeOOH \rightarrow 3CO_3^{2-} + FeS_2 + FeS + 4H_2O$

Figure 1.2: Formulas of chemical reactions during early diagenesis. Organic matter in typical Redfield Stoichiometry (C/N/P) is assumed, with $x = 106$, $y = 16$ and $z = 1$ (Redfield, 1958). Redrawn after Wehrmann and Ferdelman (2014).

The GOA has never been investigated with respect to early diagenesis before. Initial results from IODP Expedition 341 (Jaeger et al., 2014) show that Site U1417, indeed, shows an uncommon diagenetic profile with exceptionally deep sulphate penetration, no clearly expressed SMTZ below the sulphate reduction zone and a reversed SMTZ at the bottom of the sediment column. The shipboard age model suggests that sedimentation rates were variable over the depositional period, providing potential for non-steady state diagenesis.

1.4 Geochemical proxies for oxygen deficient zone extent and intensity

Some areas of the global ocean exhibit low oxygen contents in intermediate water depths between ~500 and 1500 m. These areas are called Oxygen Minimum Zones or Oxygen Deficient Zones (OMZs or ODZs; Paulmier and Ruiz-Pino, 2009; the more modern term Oxygen Deficient Zone will be used in this thesis; Rush, pers. comm.). The process generating such environments is a combination of a) higher oxygen demand, for example by higher bioproductivity or fertilization and b) limited oxygen re-supply by low ventilation which occurs for example in confined basins and highly stratified waters (e.g. Paulmier and Ruiz-Pino, 2009; Moffitt et al., 2015). ODZs have therefore been detected in confined basins such as the Black Sea and the Arabian Sea or fjords, such as the Saanich Inlet, but also along continental margins with upwelling currents, which promote high bioproductivity, such as off Namibia, Peru/Chile and California/North-West USA and the GOA (Paulmier and Ruiz-Pino, 2009; Moffitt et al., 2015). Hofmann et al. (2011) defined three categories of hypoxia: mild hypoxia with oxygen concentrations < 2.45 ml O₂/L, intermediate hypoxia with < 1.4 ml/L and severe hypoxia with < 0.5 ml/L.

As during early diagenesis (see above), in the water column in the absence of oxygen other, less favourable EAs can be used. In this case the first EA available to microbial respiration is nitrate, which is reduced to ammonium. Therefore, nitrogen (N) cycling plays a significant role in ODZs (Lam and Kuypers, 2011). Some bacteria can re-oxidize ammonium with nitrite or nitrate to N₂ and water in the absence of oxygen (anaerobically). This process is called ANaerobic AMMonium OXidation (anammox; Mulder et al., 1995; Van de Graaf et al., 1995). Anammox can only take place under oxygen-free conditions (Dalsgaard et al., 2014) where ammonium is available and thus occurs in ODZs in the ocean (Kuypers et al., 2003; Hamersley et al., 2007; Lam and Kuypers, 2011; Pitcher et al., 2011). The responsible bacteria (i.e. anammox bacteria) are the only known marine source for the bacteriohopanetetrol stereo-isomer (BHT isomer; Figure 1.3; Rush et al., 2014). This molecule can therefore be used as a biomarker for the anammox process (Rush et al., 2014)

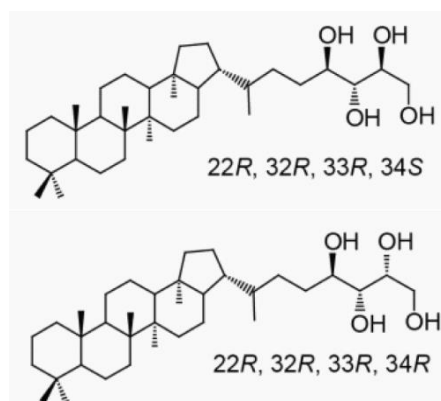


Figure 1.3: Chemical structure of Bacteriohopanetetrol (BHT; above) and BHT-isomer (below). Structures after Rush et al. (2014).

and thus for the intensity or extent of an ODZ (Matys et al., 2017). A disadvantage of this proxy is that there are non-marine sources of BHT isomer and other biomarkers have to be used to confirm that no terrestrial contamination is present (Zhu et al., 2011). Furthermore it is currently disputed if the occurrence of hydrogen sulphide in the water inhibits the anammox bacteria (Dalsgaard et al., 2014; Lipsowers et al., 2016). It is therefore not clear if anammox only takes place in suboxic, non-sulphidic conditions or in the full sub- to anoxic spectrum of the redox cascade. The BHT-isomer biomarker or any other anammox biomarker (e.g. ladderanes; Jaeschke et al., 2009a) has never been applied in the GOA before. Studies, in which bacteriohopanepolyols (BHPs) in the water column have been related to ODZ conditions, exist from various environments, such as the Baltic Sea (Berndmeyer et al., 2013), the Pacific Ocean off California (Kharbush et al., 2013, 2016), the Arabian Sea (Sáenz et al., 2011) and the Cariaco Basin (Wakeham et al., 2012). However, studies where BHT isomer extracted from marine sediments explicitly has been used as proxies for ODZ extent and intensity are rare and only exist from Golfo Dulce (Rush et al., 2014) and the Pacific Ocean off Peru (Matys et al., 2017).

Oxygen deficient conditions also lead to the enrichment or depletion of several redox-sensitive trace metals (TM) in the sediments (e.g. Sirocko et al., 2000; Nameroff et al., 2002; Calvert and Pedersen, 2007; McKay et al., 2007). Trace metals can react to changing redox conditions in two different ways (Calvert and Pedersen, 2007). Some elements change their valency state at some point in the redox cascade and form species which are less or more soluble than the species which predominate under oxic conditions. Elements which fall in this category are chromium (Cr), uranium (U) and vanadium (V; all less soluble under reducing conditions) and manganese (Mn; more soluble under reducing conditions; Calvert and Pedersen, 2007). Other elements, which have only one valency state, can react with products from other redox reactions and form insoluble minerals which precipitate in the sediments. Here, reactions with hydrogen sulphide predominate and the precipitated minerals are usually sulphides (Huerta-Diaz and Morse, 1992; Morse and Luther, 1999). Thus, their enrichment indicates strictly anoxic, sulphidic conditions in marine sediments or the overlying bottom-water. Elements of this type are copper (Cu), molybdenum (Mo) and nickel (Ni; Calvert and Pedersen, 2007). Enrichments or depletion of the respective elements can be used as a proxy for past bottom-water oxygenation conditions (Calvert and Pedersen,

2007). Shortcoming of these proxies is that the TM are also susceptible to other factors controlling the sediment composition. External factors, such as the initial composition of the source material, will affect the background concentration of some elements. In addition, Cu and Ni act as micronutrients and are enriched and exported to the seafloor in OM. Their input can hence also be controlled by bioproductivity (Böning et al., 2015; Steiner et al., 2017). The redox reactions which affect TM distribution in oxic to anoxic water columns also happen in the sediments during early diagenesis (see above) and affect the element distribution between sedimentary pore-waters and the mineral phase in a similar way (Shaw et al., 1990; Morford and Emerson, 1999). Diagenetic pyritization also incorporates sulphide-forming trace elements such as Mo, Cu and Ni (Huerta-Diaz and Morse, 1992) and valency-changing elements such as U and V will diffuse across the sediment water interface and precipitate in suboxic to anoxic sediments (Klinkhammer and Palmer, 1991; Morford et al., 2009). Generally, redox sensitive elements only record oxygenation at or below the seafloor. If the ODZ does not extend into the bottom-waters, reduced TM species would be re-oxidized before reaching the seafloor.

In contrast to the BHT-isomer, which is a relatively new proxy, TM are an established method to trace past ocean oxygenation development and have been used along the Eastern North Pacific margin and in the GOA to reconstruct the extent and intensity of the ODZ. Ortiz et al. (2004) and Dean (2007) conducted studies of bottom-water oxygenation along the California Margin, using TM as a redox-proxy. McKay et al. (2007) studied redox sensitive TM accumulation under ODZ conditions further north, off western Canada. In the GOA, McKay et al. (2005), Barron et al. (2009) and Addison et al. (2012) use TM to study ODZ behaviour and link it to Northern Hemispheric climatic patterns. Due to the disadvantages of all of the here discussed proxies, a serious study of past ODZ behaviour needs to apply a multi-proxy approach. It is for example possible to combine TM with biomarkers and to take the occurrence of laminated intervals, which only occur under strictly anoxic conditions without bioturbation, into account. For a realistic assessment of the conditions, other factors, such as sedimentation rate which influences absolute concentrations of enriched materials (Klinkhammer and Palmer, 1991; McKay and Pedersen, 2014), provenance changes (Penkrot et al. in press) and OM input (Böning et al., 2012, 2015) need to be considered as well.

1.5 Available material and applied methodology

This section will provide an overview about the datasets available from the beginning of the work and the methods applied during the making of this thesis and the rationale behind their application. No details about the precise protocols are given, as these will be described in the chapters where the respective data were used.

1.5.1 Shipboard data and previously available material

Shipboard data Site U1417

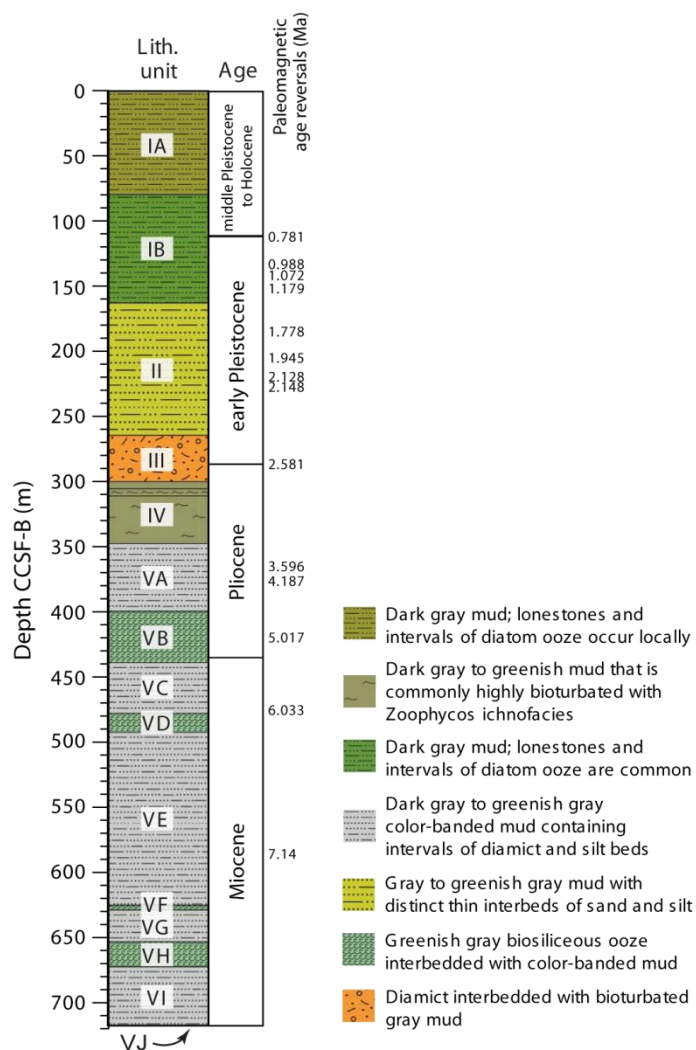


Figure 1.4: Stratigraphic composite record at Site U1417.
Changed after Jaeger et al., 2014.

In 2013, IODP Expedition 341 drilled Site U1417 to ~700 m sediment depth (recovery 70.1%) in the GOA at 56.96° N and 147.11° E (Figure 1.1, Jaeger et al., 2014). The site is located in 4200 m water depth on the Surveyor Fan. It is situated approximately 60 km from the Surveyor Channel, which is the main sediment provider, ~70 km from the Kodiak-Bowie Seamount Chain to the southeast, and ~75 km from the Aleutian Trench to the northwest.

Holes A to E were cored at Site U1417 resulting in a continuous composite record of ~700 m length (core composite depth below seafloor, scale B; CCSF-B; Figure 1.4).

Information from earlier Deep Sea Drilling Project (DSDP) Leg 18 Site 178

(Kulm and Von Huene, 1973), of which Site U1417 is a re-drill, and seismic reflection data (Reece et al., 2011) revealed that the sediment-basement boundary lies at 794 ± 74 m depth,

and coring at Site U1417 was terminated ~50-100 m above basement. The age model for Site U1417 (Jaeger et al., 2014) is based on paleomagnetism (14 datums), biostratigraphy (18 datums), and extrapolated to the basement. For basement age, three basalt basal core samples from DSDP Site 178 were dated using the whole rock $^{40}\text{Ar}/^{39}\text{Ar}$ methods outlined in Benowitz et al. (2014), to more robustly determine the age of the basal sediment at Site U1417. This improved age model will be published as a scientific paper, together with the results of Chapter 2 of this thesis. See Appendix for supplementary text, figures and tables for more details on the $^{40}\text{Ar}/^{39}\text{Ar}$ methods and results. All dating points were included to construct minimum and maximum age models. Sediment ages extend back to 16.5 Ma (early Miocene) at the deepest drilled point of Site U1417 (Jaeger et al., 2014). The new $^{40}\text{Ar}/^{39}\text{Ar}$ dating of the basal basalt lava flow samples from DSDP Site 178 provides an age of 25.80 ± 0.36 Ma. This disagrees with previous assumptions. Originally the basement age at Site U1417 was assumed to be crustal age at 37 – 41.2 Ma (Jaeger et al., 2014). The sediment at Site U1417 consists mainly of hemi-pelagic mud, distal turbidites, and interbedded layers of biosiliceous ooze (Figure 1.4; Jaeger et al., 2014).

On board pore-water and pore-gas was analysed for diagenetically active species. The research in this study partly builds on the diagenetic pore-water profiles analysed on board. Therefore, the results which are reported in Jaeger et al., 2014 will be reported here briefly.

Pore-water and gas from 72 whole-round core samples of 5 to 15 cm thickness was analysed in variable depth resolution. In this thesis, datasets of the following species will be used: Methane, Sulphate, Alkalinity, Ammonium, Ca^{2+} , Ba^{2+} , Fe^{2+} , Li^+ , Mg^{2+} and Sr^+ . Pore-water data are presented in micromole (μM) or millimole (mM), pore-gas as parts per million Volume (ppmV; Figure 1.5). All depth information will be given in meters below seafloor (mbsf) on the CCSF-B scale.

The sulphate content of the pore-water decreases gradually from 27.5 mM at the top of the sediment column to values between 0 and 2 mM at ~200 mbsf (Figure 1.5). Sulphate remains low until ~640 m depth where concentrations increase to 7 mM. Methane concentrations up to 5,100 ppmV were measured between ~450 and ~640 mbsf, consistent with the absence of sulphate.

Alkalinity has two major peaks over the whole record. It is at 6 mM at the top of the core, peaks at 16 mM in 30 mbsf, decreases nearly linearly to 3.3 mM in 220 mbsf, increases to a second peak of 12.6 mM in 375 mbsf and from there decreases to 2.2 mM at the bottom of the core. Ammonium sharply increases from 160 μM at the top of the core to 1200 μM in 30 mbsf and then decreases to 500 μM at the bottom of the core.

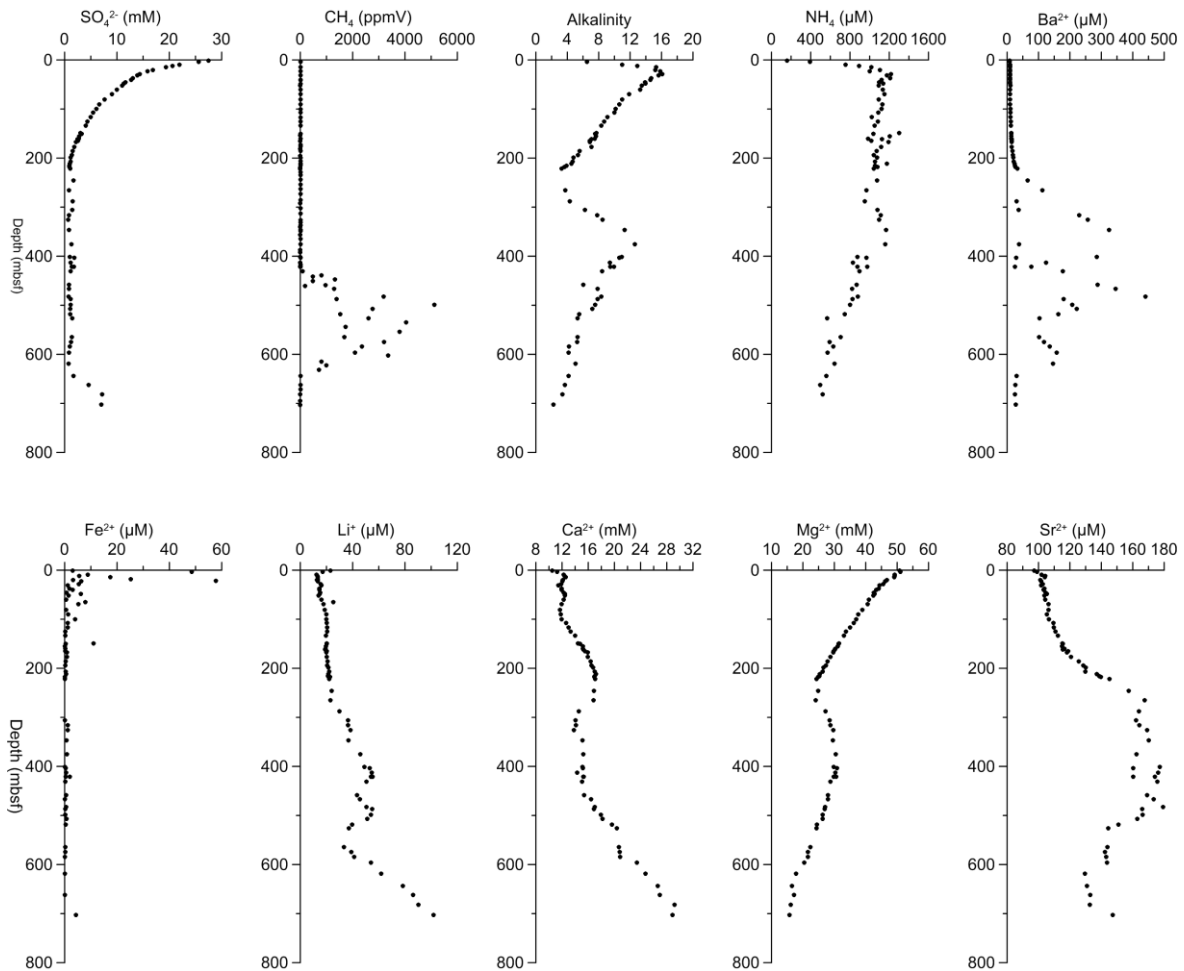


Figure 1.5: Shipboard pore-water and pore-gas data at Site U1417. Sulphate (SO_4^{2-}), Alkalinity, Ca^{2+} , Mg^{2+} (in mM), Methane (CH_4 in ppmV), Ammonium (NH_4), Ba^{2+} , Fe^{2+} , Li^+ , and Sr^{2+} (all in μM)

Pore-water barium (Ba^{2+}) concentrations increase slightly from ~ 8 to ~ 25 μM from 0 to ~ 200 mbsf, followed by much higher values ranging from 25 to 440 μM between ~ 200 mbsf and ~ 640 mbsf. Deeper than ~ 640 mbsf, concentrations remain around 25 μM . Pore-water lithium (Li^+) and calcium (Ca^{2+}) concentrations increase with depth. Both have lowest concentrations at the sediment surface ($\text{Li}^+ \sim 24$ μM , $\text{Ca}^{2+} \sim 10$ mM) where they are approximately at seawater concentration (Li, 2000). Whereas Li^+ shows a broad

concentration maximum of $\sim 55 \mu\text{M}$ between ~ 300 and 550 mbsf , a minimum of $\sim 12 \mu\text{M}$ at $\sim 560 \text{ mbsf}$, and another increase towards the bottom of the core ($\sim 100 \mu\text{M}$), Ca^{2+} increases to $\sim 17 \text{ mM}$ at $\sim 220 \text{ mbsf}$, displays minimum concentrations of $\sim 14 \text{ mM}$ between ~ 300 and 500 mbsf , and increases again to $\sim 30 \text{ mM}$ towards the bottom of the core. Pore-water iron (Fe^{2+}) has a maximum concentration of $\sim 50 \mu\text{M}$ at 3.8 mbsf and a peak of $\sim 57 \mu\text{M}$ at 22 mbsf (Figure 1.5). From there, it decreases to background levels of $< 2 \mu\text{M}$ at 45 mbsf where it stays for the remainder of the section. Some minor peaks up to $10 \mu\text{M}$ only occur between 45 and 150 mbsf . Fe^{2+} increases to $4 \mu\text{M}$ in the deepest sample at $\sim 700 \text{ mbsf}$. Magnesium (Mg^{2+}) linearly decreases from 50 to 20 mM over the top 200 m of the core and the increases back to a broad peak of 30 mM around 400 mbsf and decreases to values $< 20 \text{ mM}$ towards the bottom of the core. Strontium (Sr^{2+}) is at $100 \mu\text{M}$ at the top of the core, increases to values between 150 and $180 \mu\text{M}$ between 250 and 500 mbsf and decreases back to 120 to $140 \mu\text{M}$ at the bottom of the core.

Shipboard data Site U1419

Site U1419 is located in 721 m water depth on the continental slope above the Khitrov basin (See Figure 1.1). Five holes (A-E) were drilled (average recovery 82%) yielding a composite core length of 177 m (Jaeger et al., 2014; Figure 1.6).

The sedimentary material mainly consists of dark grey or greenish grey mud and diamict. Clasts indicate ice rafted debris or gravity mass flows. Over the whole core, 37 samples have been analysed for pore-water and pore-gas (Figure 1.7). Sulphate decreases from 21 mM to 1 mM over the top 18 m of the record. Below this interval, it stays around 1 mM . Methane which was analysed on 22 samples increases sharply to values between 5000 and 28000 ppmV immediately below the depth of sulphate reduction and an SMTZ is well expressed. In the sulphatic interval, low values of methane around $2-5 \text{ ppmV}$ are measured, too. Ammonium increases with depth from $500 \mu\text{M}$ at the top of the core to $4500 \mu\text{M}$ in 70 mbsf and from there decreases to $1900 \mu\text{M}$ in 140 mbsf and slightly increases to $2400 \mu\text{M}$ at the bottom of the record. Dissolved Fe is between 0 and $5 \mu\text{M}$ but shows 3 distinctive peaks: it reaches $13 \mu\text{M}$ in 23 mbsf , $10 \mu\text{M}$ in 60 mbsf and $20 \mu\text{M}$ in 85 mbsf .

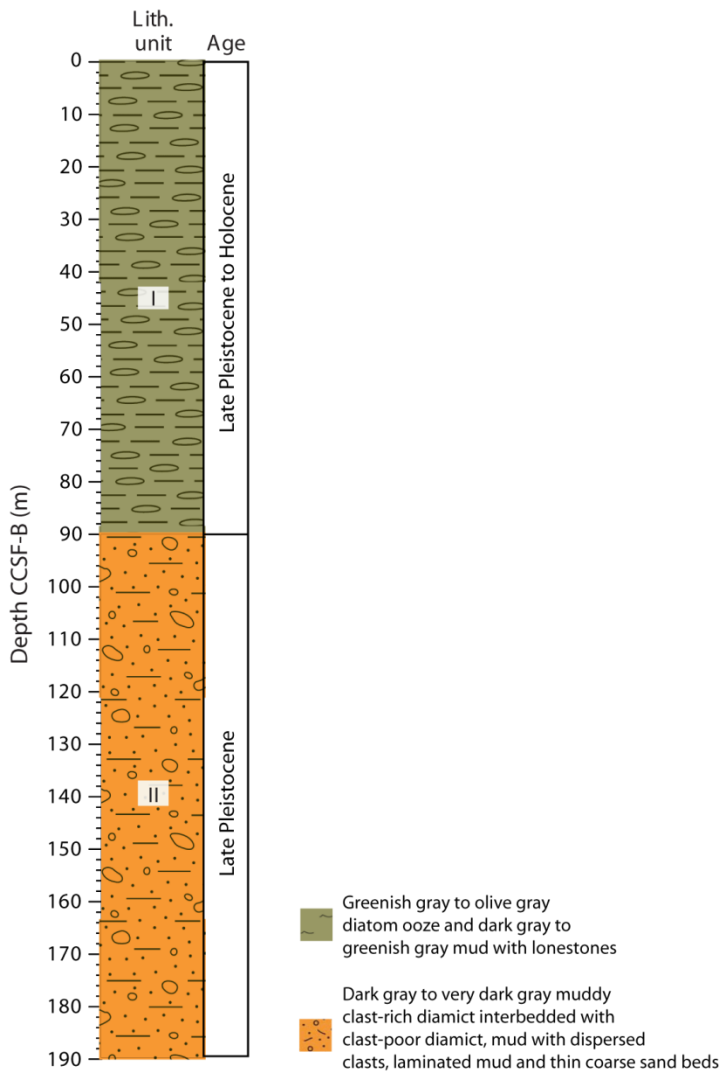


Figure 1.6: Stratigraphic composite record at Site U1419.
 Changed after Jaeger et al., 2014.

The shipboard age model is based on the absence of magnetic reversals and oxygen isotope analysis of benthic foraminifera at the bottom of the core and only suggests that the whole record spans < 60 ka (Jaeger et al., 2014).

A more precise to date unpublished and still preliminary age model based on ¹⁴C analyses goes back to 51 ka BP which are reached in 87 m CCSF-B (Walczak et al., pers. comm.). According to this new age model, sedimentation rates are varying throughout the record, gradually rising from 270 cm ka⁻¹ at 49 ka BP to 360 cm ka⁻¹ at 25 ka⁻¹, peaking at 670 cm ka⁻¹ and falling abruptly to 40 cm ka⁻¹ at 9 ka BP. These are amongst the highest reported sedimentation rates for a depositional setting at the continental slope.

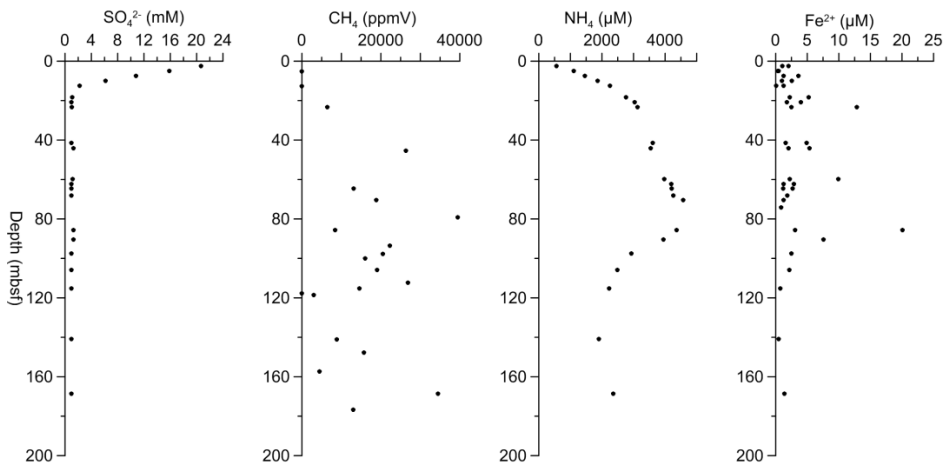


Figure 1.7: Shipboard pore-water and pore-gas data at Site U1419. Sulphate (SO_4^{2-} in mM), Methane (CH_4 in ppmV), Ammonium (NH_4) and Fe^{2+} (in μM).

1.5.2 Analyses conducted for this thesis

To gain an overview about the bulk inorganic geochemical composition of the sediments, wavelength dispersive XRF analysis has been performed on all available sediment samples. This quantitative method provides a fast overview about a wide variety of elements (Si, Ti, Al, Fe, Mn, Mg, Ca, Na, K, P, S, Cl, As, Ba, Ce, Co, Cr, Cu, Ga, Mo, Ni, Nb, Pb, Rb, Sr, Th, Y, V, U, Zn, and Zr) with good detection limits (element dependent). The method has been carried out in collaboration with the workgroup of Dr. Bernhard Schnetger at the University of Oldenburg/ICBM.

Total carbon and sulphur content, as well as total organic carbon are important geochemical quantities to assess a wide range of processes from bioproductivity to diagenesis and carbon burial. They have been analysed with Leco and Carlo Erba elemental combustion analysers.

With XRF and C and S data as first datasets the variability of sediment composition can be assessed and preliminary hypotheses on provenance, paleo-productivity and diagenetic overprint can be postulated. Based on this, further applied methods have been selected.

Iron and sulphur speciation was performed, to assess the diagenetic behaviour of these elements. With the Fe speciation method (Poulton and Canfield, 2005) the total Fe pool in the sediments (FeT) is divided in un- or poorly reactive iron and reactive iron species, (Fe-carbonates, Fe(oxyhydr)oxides, magnetite) which dissolve under ferruginous conditions and are available for sulphide formation under sulphidic conditions. Sulphur speciation (Canfield

et al., 1986) is used to determine how much iron is bound to sulphur as Fe-monosulphides and pyrite (Fe-S). This method was only applied to samples from Site U1417.

Sulphur isotopes of pyrite are a good indicator of bacterial sulphate reduction in marine sediments (see above; Canfield, 2001). Furthermore, they provide information on open or closed system conditions of sulphide formation (i.e. unlimited vs. limited sulphate supply). Because this measure was only important for work conducted at Site U1417, sulphur isotopes (^{32}S and ^{34}S) were analysed on 40 selected samples of Site U1417. These were the samples which yielded a sulphur content sufficient for the analysis. The method was conducted by mass spectrometry on the extracts from the sulphur speciation and carried out in collaboration with the University of Münster and the workgroup of Prof. Harald Strauss.

To further reveal the link between diagenetic zonation and potential paleoclimatic forcing and fluid delivery through the sediments at Site U1417, a reaction transport model was applied (Regnier et al., 2002; Aguilera et al., 2005). The aim was to reconstruct the whole diagenetic evolution over the time of deposition. The reactive transport model was constructed in collaboration with Dr. Sandra Arndt at the University of Bristol.

The stereo-isomer of bacteriohopanetetrol (BHT isomer) has recently been found to be a reliable biomarker for the anammox-process in the marine environment (see above; Rush et al., 2014). It therefore is a good proxy for past ODZ extension or intensity. For this study, the BHT biomarker has been analysed with High-Performance-Liquid-Chromatography-Mass-Spectrometry (HPLC-MS) on samples from Site U1419 to reconstruct the past extent of the GOA ODZ and its link to paleoclimate conditions.

1.5.3 Further datasets used for comparison

In Chapter 2 at Site U1417 a dataset of 7 samples below 600 mbsf was used to assess organic matter reactivity (originally published in Childress, 2016).

Below 640 m (in the lower zone of sulphate enrichment), H- and O-indices are low (H-index ~30-50; O-index ~60-140) indicating the very low reactivity of organic matter in these intervals (Figure 2.9; Childress, 2016).

In Chapter 4 data at Site U1419 are compared to $\delta^{18}\text{O}$ data of the Greenland NGRIP ice core record (Rasmussen et al., 2014) as a proxy for northern hemispheric climate.

Inductively coupled plasma mass spectrometry (ICP-MS) data for the elements Cr, Cu, Ni and V from the workgroup of Prof. John Jaeger at the University of Florida (Kamenov et al., 2009; Penkrot et al., 2018) have been combined with XRF data for these elements at Site U1419 in order to increase data resolution. The XRF and ICP-MS data have been compiled to a single dataset. Comparison of averages, as well as co-plotting have been used to establish comparability of ICP-MS and XRF data.

1.6 Structure of the study

The scientific body of this study is set out in the form of three chapters which will be published as scientific papers in slightly modified form.

The thesis is separated in two parts. In Part 1, Chapters 2 and 3 explore the diagenetic reactions and overprint at IODP Site U1417. The scope of this part is to assess how the interplay between primary sedimentary composition and external factors such as paleoclimate and tectonics influence the diagenetic succession. In this context Chapter 2 focuses on geochemical data of the drilled sediments at Site U1417. The chapter provides an in-depth analysis of the chemical and isotopic composition of the sediments and investigates diagenetic mineral formation in response to primary sediment composition. Chapter 3 follows a modelling approach to test the plausibility of a diagenetic scenario at Site U1417. In this chapter a reaction transport model is used to link the currently observed profiles of diagenetically influenced sediment and pore-water components to initial depositional conditions. It is tested which combination of organic matter reactivity parameters leads to the observed geochemical profiles under the observed sedimentation conditions. At this point no studies of early diagenesis in the GOA exist. Also, this is the first study to investigate early diagenesis on a deep sea fan which is not fed by a river but by glacially eroded material. It can be expected that diagenesis in this environment fundamentally differs from other previously investigated deep sea fans because the sedimentation patterns of glacially derived material will react to Northern Hemispheric climate. Furthermore, the organic matter deposited on the Surveyor Fan will be of a different composition than

fluvially derived material in warmer environments studied on other deep sea fans such as the Amazon or Zambesi Fans. A third aspect of non-steady state diagenesis that can be studied at Site U1417 is the installation of a reverse diagenetic zonation at the bottom of the sediment succession caused by a buried pool or influx of sulphate rich water at the sediment basement interface (Jaeger et al., 2014). Chapter 2 proposes and tests the hypothesis of subduction related plate bending as a previously unexplored process of deep aquifer generation altering the diagenetic evolution of a deep sea site. The combined approaches of the Chapters 2 and 3 also assess the plausibility of the preservation of an old pool of buried seawater sulphate which has never been utilized by bacterial sulphate reduction or AOM over 10 Ma - a second diagenetic process which was previously only proposed (Brumsack et al., 1992), but never conclusively tested.

In Part 2, Chapter 4 assesses the influence of water-column redox conditions on the composition of the sediments at the slope-site U1419. The BHT isomer biomarker is combined with inorganic geochemical trace metal proxies for water column oxidation. Potential reasons, why different proxies show a diverging ability to record past ODZ changes, are discussed and related to the specific environment at Site U1419. This is the first study to combine the BHT isomer with TM proxies and the first study to apply the BHT isomer to the ODZ in the GOA. Furthermore, the study extends the record of past ODZ intensity in the GOA back to 55 ka BP. To date only records as far back as 17 ka BP exist (Addison et al., 2012).

Both parts of the thesis address aspects of processes overprinting the composition of the initially deposited (allochthonous) sedimentary material. Mechanisms of autochthonous element enrichments and mineral formations are discussed and strategies explored to discern different processes on different time scales from one another.

Part I

Early diagenesis at Site U1417

2. Deep Sulphate-Methane-Transition affects sediment diagenesis in the Gulf of Alaska (IODP Site U1417)

2.1 Introduction

Early diagenesis plays an important role in global carbon (C) cycling by controlling the amount of organic C preserved in the sediment or recycled by microbial activity. Remineralisation of organic matter (OM) usually follows a succession of microbially induced redox reactions with organic carbon as the electron donor, and the electron acceptors oxygen, nitrate, manganese (oxyhydr)oxides, iron (oxyhydr)oxides and sulphate, ultimately leading to methanogenesis (Froelich et al., 1979; Jorgensen, 2006). This so-called catabolic sequence is arranged by decreasing energy yields for the microbes involved in the respective redox reactions (Froelich et al., 1979), with sulphate reduction and methanogenesis occurring in the deeper parts of any sedimentary succession. The upper limit of the methanogenic zone is usually equivalent to the maximum depth of sulphate penetration into the sediments: In a Sulphate-Methane Transition Zone (SMTZ), an anaerobic, highly specialised bacteria-archaea consortium uses sulphate as an electron acceptor to anaerobically oxidise methane (Reeburgh, 1980; Niewöhner et al., 1998; Boetius et al., 2000). Despite the low energy yields provided by sulphate reduction and methanogenesis, these reactions account for most of the non-oxic OM decomposition in the global ocean seafloor (Bowles et al., 2014) due to the high abundance of sulphate in seawater and pore-waters compared to other electron acceptors (Bowles et al., 2014). Thus, SMTZs exhibit significantly higher microbial activity than the surrounding sediments, and are biological and geochemical hotspots within the deep marine biosphere (Parkes et al., 2005; Harrison et al., 2009). SMTZs are also important biogeochemical reaction zones where distinct diagenetic signatures are generated. At an SMTZ, sulphate reduction leads to the production of hydrogen sulphide which, in turn, causes the reduction of iron (oxyhydr)oxides and the formation of iron sulphides (most commonly pyrite, FeS_2). Beneath the SMTZ, barite (BaSO_4) dissolves due to its undersaturation in sulphate-free pore-waters, but re-precipitates as authigenic barite from pore-water Ba^{2+} and sulphate slightly above the SMTZ (Von Breyman et al., 1992). Pyrite and barite are therefore common authigenic minerals at SMTZs, and their presence and isotopic compositions can be used to recognise paleo-SMTZs in the geological record (Torres et al., 1996; Riedinger et al., 2006; Peketi et al., 2012).

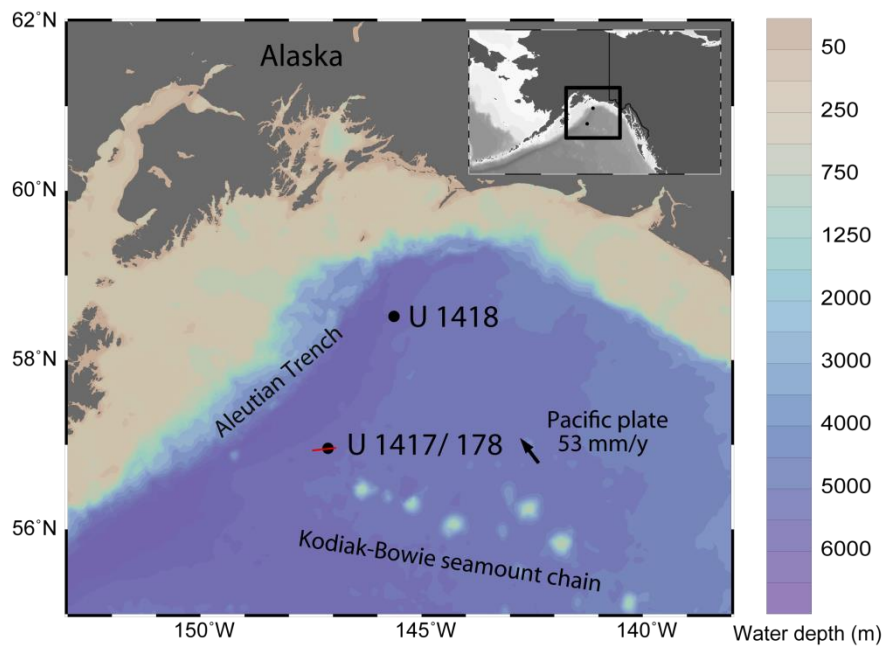


Figure 2.1: Bathymetric map showing position of Sites U1417 and U1418 IODP Expedition 341 and Site 178 DSDP Leg 18; red line across Site U1417 indicates seismic profile of Figure 2.7; arrow indicates direction of Pacific Plate movement (DeMets et al., 2010). Map created with Ocean Data View (Schlitzer, 2015).

Two major aspects of diagenetic processes in marine sediments are of continuing interest: non-steady state diagenesis (Kasten et al., 2003), and deviations from the classic catabolic sequence (Froelich et al., 1979). Non-steady state diagenesis is characteristic of settings where external forcing (including sedimentation rates, OM deposition, methane flux) is highly variable on timescales from days to millennia (Kasten et al., 2003). In such situations, fixation of specific biogeochemical zones can lead to the persistence of certain diagenetic processes in defined sediment intervals (e.g. accumulation of authigenic minerals at the expense of primary minerals). For these diagenetic processes to generate measurable changes in sediment composition, they need to be active (and hence external conditions need to be stable) for tens to thousands of years. On these timescales, changes to external forcing can be induced by a multitude of climatic or oceanographic effects. In deep sea fan sediments, for example, changes can result from drastic episodic decreases in sedimentation rates on glacial-interglacial timescales (e.g. Kasten et al., 1998; Riedinger et al., 2005; März et al., 2008a). In fact, in marine settings affected by cyclic variations in climatic forcing, non-steady state conditions appear to be the rule rather than the exception and often leave geochemical traces in the sediment record (Kasten et al., 2003 and references therein; Riedinger et al., 2005; Contreras et al., 2013).

The observation that the vertical catabolic redox succession as proposed by Froelich et al. (1979) may not always apply in marine sediments is a current research focus. Prominent examples for this exception are reverse SMTZs where sulphate is supplied not from the overlying seawater, but from a sulphate pool located deeper in the sediment (DeLong, 2004). Reverse STMZs above the interface between sediments and the oceanic crust/basement have been reported from various sites, but have so far not been conclusively explained. Most of these sites are located in geodynamically active settings of the ocean, including mid-ocean ridge flanks, proximal to seamounts (e.g. ODP Site 1026 + IODP Site U1301; Engelen et al., 2008) or accretionary prisms (e.g. ODP Site 1229; D'Hondt et al., 2004; IODP Site C0012, Torres et al., 2015). Here, active hydrological circulation provides sulphate-rich water to the deeper sediment layers. Similar to conventional SMTZs, these reverse biogeochemical transitions are hotspots of deep microbial activity (e.g. D'Hondt et al., 2004; DeLong, 2004; Engelen et al., 2008).

One depositional setting where non-steady state diagenesis and a deep source of sulphate co-occur is Site U1417 drilled during Expedition 341 of the Integrated Ocean Drilling Program (IODP) in the Gulf of Alaska (GOA, Figure 2.1). As reported by Jaeger et al. (2014) and Gulick et al. (2015), the site has experienced several order-of-magnitude variations in sedimentation rate since the late Miocene, and the sediments appear to be significantly overprinted by diagenesis. Most remarkably, authigenic carbonates, prevent upward methane diffusion into shallow sediment layers. In addition, there is a significant and unusual occurrence of pore-water sulphate below the methanogenic zone, disconnected from the overlying seawater. Jaeger et al. (2014) postulated the existence of a deep reverse SMTZ at Site U1417. However, both the source of the deep sulphate and its potential impact on diagenetic pathways are unconstrained. Detailed downhole geochemical analyses at Site U1417, coupled with regional geophysical imaging of the sub-seafloor, offer the possibility to explore these two aspects of diagenesis in a deep sea setting.

Here, bulk sediment, pore-water and gas geochemical data from IODP Site U1417 are presented, combined with sequential leaching of Fe and S species and O- and H-index as proxies for organic matter reactivity to estimate their degree of diagenetic overprint, and $\delta^{34}\text{S}$ data from pyrite to reveal the nature of the deep sulphate pool.

2.2 Materials and methods

For shore-based geochemical analyses, 163 sediment samples were taken at ~3 m resolution. This sampling strategy included splits of the pore-water squeeze cakes and additional discrete samples collected from working halves of the split cores. Sediment samples were either directly freeze-dried on board, or initially stored in vacuum-sealed, gas-tight plastic bags with oxygen strippers followed by freeze-drying on shore.

On shore, splits of all sediment samples were homogenised using an agate mortar and pestle, and analysed for Si, Al, Fe and Ba using a wavelength-dispersive XRF (Panalytical Axios max, 4 kW). For this, 700 mg of sample were mixed with 4200 mg di-lithiumtetraborate, pre-oxidized with 1g ammonium nitrate at 500° C and then fused to homogenous glass beads. Calibration of the XRF was done by using 52 SRM and in-house samples resulting in an average absolute error based on all 52 samples of 0.3 wt% Si (0.1), 0.1 wt% Al (0.2), 0.1 wt% Fe (0.2) and 31 ppm Ba (2) (in brackets: precision in rel.% standard deviation for a typical sample). Total carbon (TC), total organic carbon (TOC) and total sulphur (TS) were quantified using Leco and Elemental combustion analysers with a reproducibility better than 5% (TC) and 10% (TOC, TS), checked on duplicates of every tenth sample. Solid phase sediment components are presented as weight % (wt%) or parts per million (ppm) or as ratio to Al.

A sequential Fe and S extraction scheme following the methods of Canfield et al. (1986), Poulton and Canfield (2005) and März et al. (2012) was applied to separate iron carbonates, amorphous/poorly crystalline iron (oxyhydr)oxides, crystalline iron oxides, and magnetite as well as iron monosulphides (e.g. mackinawite, greigite) and pyrite. Iron carbonates were extracted with 1M Na-acetate at pH 4.5 for 24h, amorphous/poorly crystalline iron (oxyhydr)oxides with 1M hydroxylamine HCl and 25% acetic acid for 24h, crystalline iron oxides were extracted with dithionite solution at pH 4.8 for 2h and magnetite was extracted with 1M ammonium oxalate solution for 6h. Ten ml of each solution were applied to the same 0.1 g sample in sequence. For the S extraction, ~0.5 g of sample material were first boiled with 50 ml half-concentrated HCl for 45 min to dissolve all iron monosulphides, then 12 ml fully reduced Cr(II)-chloride were added and boiled for another 45 min to oxidize pyrite. The resulting H₂S of both fractions was trapped as silver sulphide (Ag₂S), weighed and stoichiometrically converted into amounts of Fe bound as FeS and FeS₂, respectively. The iron fractions resulting from the different extraction steps are presented as ratios of highly

reactive Fe (FeHR, sum of Fe in all extraction steps) over total Fe (determined by XRF) (FeHR/FeT), and of sulphide-bound Fe (Fe-S, sum of Fe in monosulphides and pyrite) over highly reactive Fe (Fe-S/FeHR). The latter ratio indicates how much of the available FeHR has been converted into iron sulphides (Poulton et al., 2004). The reproducibility of the Fe extraction was within 5% for all four fractions as checked on triplicate analyses of five samples. The standard error of the S extraction was within 20% as checked by triplicate analysis of three randomly selected samples, mainly due to low total S contents (0.13 – 0.2 wt%) in these samples.

Following the S extraction, the isotopic composition of pyrite-bound S was determined on the precipitated silver sulphide. The two naturally most abundant S isotopes, ^{32}S and ^{34}S , were measured on 200 μg of silver sulphide homogeneously mixed with 300-600 μg vanadium pentoxide using a Carlo Erba Elemental Analyser coupled to a ThermoFinnigan Delta Plus mass spectrometer (EA-IRMS) as described in Strauss et al. (2012). Sulphur isotopes are presented in the standard delta notation ($\delta^{34}\text{S}$) as per mil difference to the international reference material Vienna Canyon Diablo Troilite (V-CDT). Standard deviation on duplicate measurements was 0.3‰ in average and above 1‰ in one sample only. Analytical performance was monitored with international (IAEA S1, S2, S3, NBS 127) and in-house laboratory (Ag_2S) standards.

All pore-water and solid phase constituents are displayed against composite coring depth in meters below seafloor (mbsf) on the CCSF-B scale. In the following, all depth information refers to sediment depth unless stated otherwise.

2.3 Results

The main chemical constituents of the sediments at Site U1417 are Si (av. 26.4 wt%) and Al (av. 8.4 wt%), very similar to average shale (Wedepohl, 1971; 1991). Deeper than ~350 m, Si contents fluctuate significantly and exhibit several peaks that mirror minima in Al. This results in a high Si/Al ratio (Figure 2.2). These peaks do not have equivalents in Zr or Zr/Al, indicating that Si enrichment is probably caused by biogenic diatomaceous productivity and not by enrichment of coarse-clastic material.

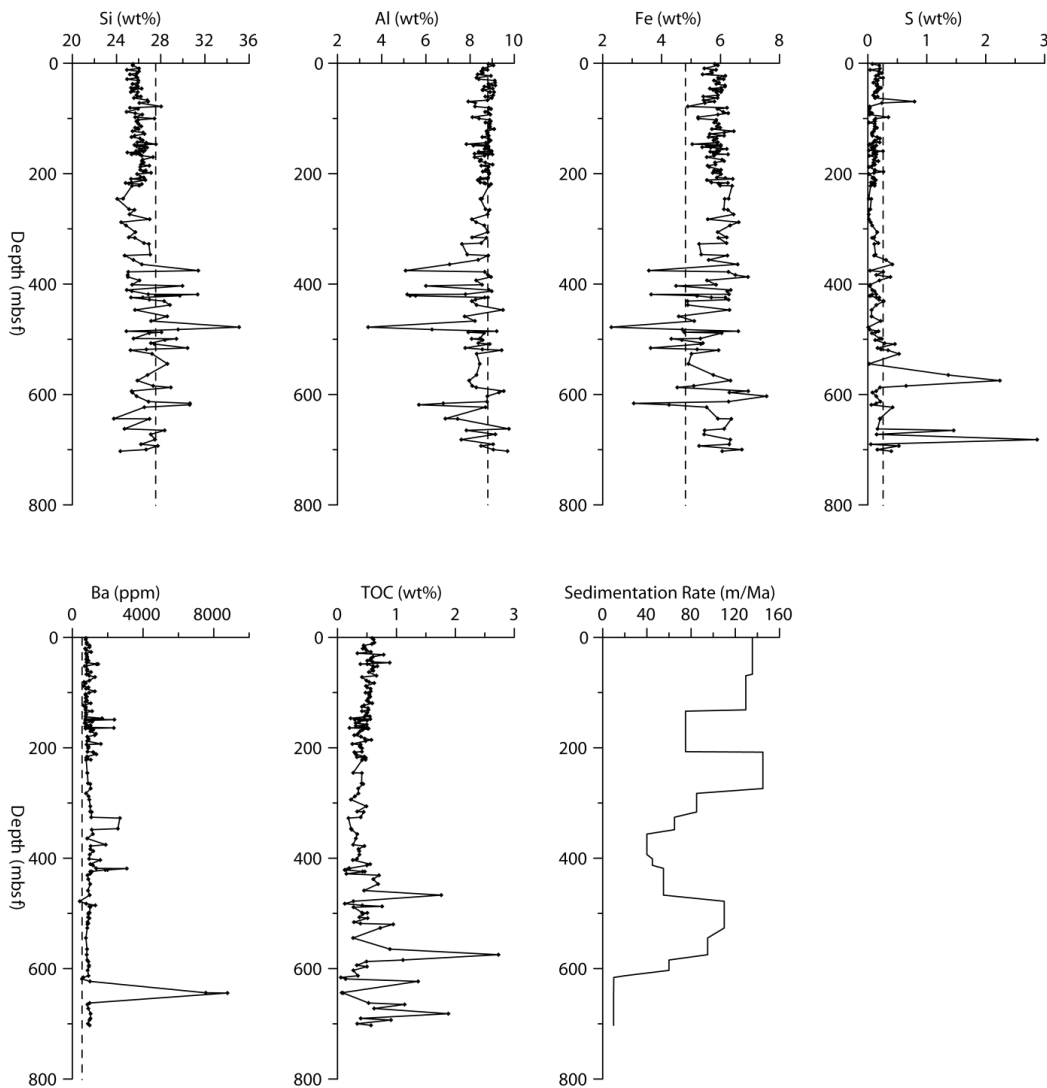


Figure 2.2: Geochemical data at Site U1417. Sedimentary downcore profiles of Si, Al, Fe, S (all as wt%), Ba (ppm), TOC (wt%) and sedimentation rate (cm/ka). Dashed lines indicate average shale contents (Wedepohl, 1971; 1991). Solid black line indicates cemented layer.

Total Fe contents display an average value of 5.7 wt%, but show excursions to much lower values below ~350 m, some of them anti-correlated with peaks in Si. These excursions are not visible in Fe/Al (Figure 2.3), indicating that Fe is not depleted but diluted by diatomaceous Si. On average, 18.4 rel% of Fe_T is in the Fe_{HR} fraction (Figure 2.3). Total S contents are generally low, averaging around 0.2 wt%, but two distinct peaks at ~570 m and ~680 m depth exceed 2 wt%. These maxima occur in depth intervals also exceeding 2 wt% pyrite-bound sulphur, indicating that S enrichments are related to iron sulphide precipitation/accumulation. Iron monosulphides are below detection limit in all samples analysed.

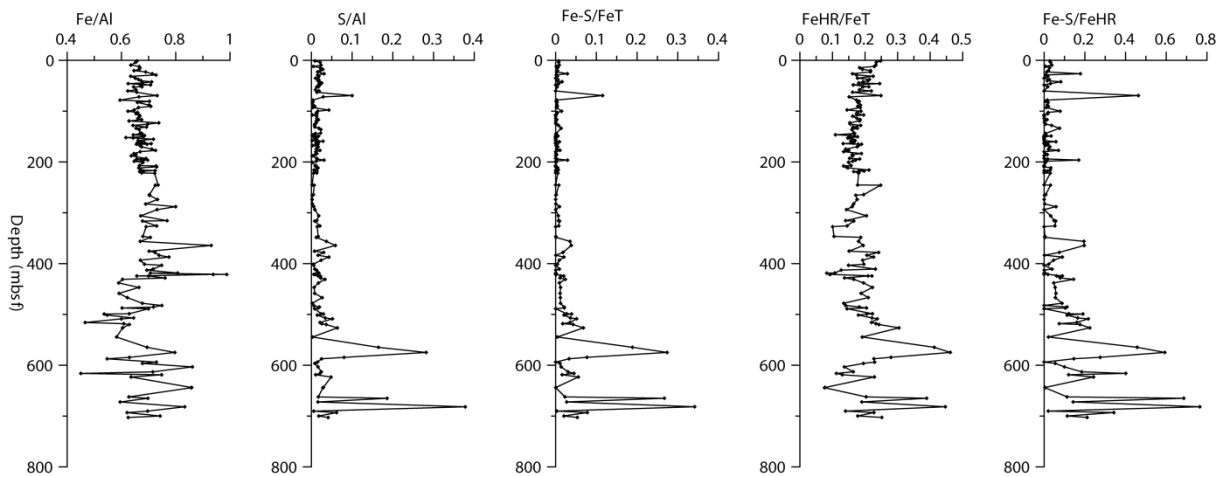


Figure 2.3: Fe and S speciation data. Fe/Al, S/Al, Fe-S/FeT, Fe HR/FeT and Fe-S/Fe HR ratios (all as wt%/wt%)

Total organic carbon (TOC) contents are generally low (av. 0.5 wt%) with a few maxima at ~470 m (1.7 wt%), ~570 m (2.7 wt%) and ~680 m (1.8 wt%) depth (Figure 2.2).

Maximum Ba/Al ratios up to 1200 ppm/wt% are observed at ~160 m, between ~350 and 450 m, and at ~640 m depth, and exceed the background levels of around 80-90 ppm/wt% recorded throughout the entire core (Figure 2.4).

Pyrite $\delta^{34}\text{S}$ values are generally negative (as low as -46‰) but variable throughout the entire cored section. However, at ~300 m and between ~560 and 620 m depth, $\delta^{34}\text{S}$ reaches maximum values of +60‰ (Figure 2.8).

2.4 Discussion

The geochemical data from Site U1417 confirm that the entire sediment record is strongly affected by diagenetic mineral formation. Based on sulphate and methane profiles, the core is divided into two zones where diagenesis appears to be driven by different processes: an upper zone defined by a decline in pore-water sulphate concentrations, reaching down to ~640 m, and a lower section, where sulphate increases with sediment depth below ~640 m. Methane accumulation occurs between ~450 and 640 m and is referred to here as the methanogenic layer. In the upper zone, diagenesis is or has been driven by electron acceptor supply from the overlying seawater. Below the methanogenic layer, a deep SMTZ is formed due to a deep source of sulphate and possibly other electron acceptors.

Diagenesis fuelled by diffusion across the sediment-water interface (0-450 m)

The upper 200 m of the sediment succession at Site U1417 show a “concave-down” pore-water sulphate profile (Figure 1.5; Hensen et al., 2003) and near-total sulphate depletion occurs at ~200 m, which is relatively deep compared to other sites in the GOA (~75 m at Site U1418, Figure 2.1; Jaeger et al., 2014) and worldwide (Bowles et al., 2014 report values <50 m for deep sea settings). A reason for this difference could be the generally low amounts and/or reactivity of OM deposited at the open marine Site U1417 (Meister et al., 2013). Alternatively, or in addition, sulphate penetration depths could be significantly deeper at Site U1417 because no methane is diffusing upwards beyond ~450 mbsf, hence no AOM-driven sulphate reduction occurs. This interpretation is supported by the concave-down shape of the sulphate profile, which argues for a continuous sulphate reduction rate without the influence of AOM (Hensen et al., 2003). Similar profiles have been associated with conditions where organo-clastic sulphate reduction accounts for most of the sulphate depletion (Niewöhner et al., 1998; Kasten et al., 2003). Elevated pyrite contents at Site U1417 only occur at ~70 m depth in a single peak, supporting ongoing sulphate reduction leading to pyrite precipitation in this sediment layer (Figure 2.3). A reason for this localised diagenetic feature cannot be given, as the profiles of other sediment components, e.g. TOC or Si, do not show any correlative anomalies. The current zone of diagenetic Fe reduction lies higher in the sediment succession (at ~4 m depth) as indicated by the Fe^{2+} pore-water profile.

The sediments below the sulphate reduction zone are dominated by a methane-free and low sulphate sediment interval of ~250 m thickness (~200 to 450 mbsf). The base of this interval at ~450 m depth is marked by a strongly cemented carbonate layer that was poorly recovered during drilling due to its high degree of induration within largely soft sediments, and only yielded one angular fragment (~3 cm in diameter) of low-Mg calcite (Jaeger et al., 2014). Such carbonate-cemented layers can form when a SMTZ remains within a specific sediment depth for longer periods of time (e.g. ~2.4 Ma in the Bering Sea according to Pierre et al., 2016; Wehrmann et al., 2016). Due to the higher alkalinity and increased pH in SMTZs produced by anaerobic methane oxidation, authigenic carbonate minerals precipitate, including calcite (CaCO_3) with various amounts of Mg or pure dolomite ($\text{CaMg}(\text{CO}_3)_2$); Hathaway and Degens, 1969; Soetaert et al., 2007; Pierre et al., 2016; Wehrmann et al., 2016). Enhanced carbonate cementation sometimes coincides with higher

porosity/permeability in the original sediments, providing more space for the precipitation of authigenic phases. This cementation has been shown, for example, in sandy turbidite layers in the Bering Sea (Hein et al., 1979; Wehrmann et al., 2011). At Site U1417, shipboard X-ray diffraction (XRD) analysis identified the indurated carbonate layer as quartz-feldspar sand cemented by low-Mg calcite (Jaeger et al., 2014). Pore-water, sedimentological and geophysical data suggest that this authigenic layer acts as a seal at Site U1417, preventing methane from diffusing upwards and inhibiting the development of a shallow SMTZ.

Despite the lack of a shallow SMTZ at U1417, two clusters of Ba/Al maxima are observed at ~160 m and between ~325 and 450 m, most likely resulting from past and/or ongoing authigenic barite precipitation. When pore-water sulphate reaches undersaturation with respect to barite, sedimentary barite dissolves. Barium ions diffuse upwards into the sulphate-rich zone where they re-precipitate as authigenic barite, building diagenetic fronts at the SMTZ. Such authigenic barite fronts can dissolve again when the pore-water becomes depleted in sulphate and undersaturated with respect to barite as the SMTZ moves upwards (Von Breyman et al., 1992; Torres et al., 1996). While the Ba/Al peaks around ~160 m depth indicate ongoing barite formation around the maximum sulphate penetration depth, the peaks between ~325 and 450 m indicate older peaks formed at a paleo-SMTZ which are dissolving at the moment. The recent origin of the upper Ba/Al peaks is indicated by the fact that they are situated above the zone where pore-water is enriched with Ba^{2+} ions. Deeper in the sediment succession, the Ba/Al profile changes its pattern, indicating that the shallow boundary of the barite dissolution zone at U1417 lies at ~220 m depth. The current dissolution of the Ba/Al peaks around 400 m depth is indicated by the coinciding elevated pore-water Ba^{2+} content. The fact that Ba/Al peaks at ~350 m coincide with pyrite peaks supports the hypothesis that this sediment interval represents a paleo-SMTZ. Temporary preservation of barite within sulphate-free sediments has been explained by *in situ* transformation of barite into more stable barium carbonate or barium sulphide, which would not change the observed bulk Ba/Al records (Riedinger et al., 2006). Nevertheless, the pore-water Ba^{2+} profile at Site U1417 shows that this deeper barite accumulation is presently being dissolved due to sulphate depletion (Figure 2.4), and therefore might represent a transient feature.

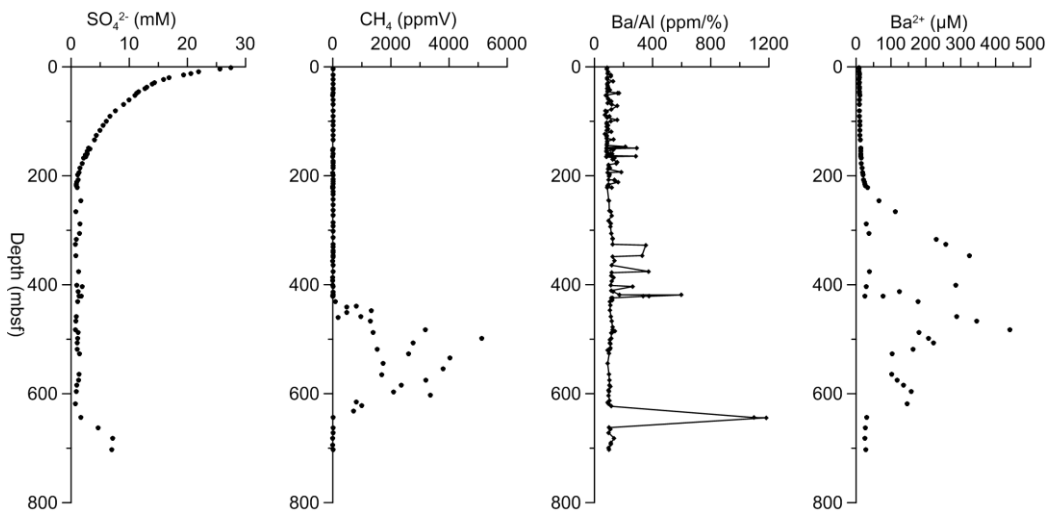


Figure 2.4: Geochemical data relevant for Ba diagenesis. Pore-water SO_4^{2-} (in mM), pore-gas CH_4 (in ppmV), Ba/Al (in ppm/%), Pore-water Ba^{2+} (in μM).

The methanogenic layer (450-640 m)

Below the indurated authigenic carbonate layer at ~450 m, and extending down to ~640 m, pore-waters exhibit methane concentrations up to 5,100 ppmV (Figure 1.5). This zone has markedly higher TOC contents (reaching ~3 wt%) compared to the overlying section (~0.5 wt%), supporting increased methane production related to higher amounts and/or reactivity of OM. The authigenic carbonate layer at ~450 m depth efficiently hinders anaerobic oxidation of methane by sulphate higher up in the sediment column, and might be actively contributing to methane accumulation below. Pore-water sulphate concentrations are very low throughout this entire interval as expected for methane-generating strata.

The Ba/Al ratio in the methanogenic layer is consistently low and reaches detrital background levels (Condie, 1993) whereas dissolved Ba^{2+} is high, indicating long-lasting sulphate-depleted conditions and dissolution of barite. The Fe-S/FeHR ratio is higher here (peaks values of 0.2 - 0.6) than above, reaching a maximum at ~575 m. The elevated Fe-S/FeHR ratio most likely reflects the transformation of iron (oxyhydr)oxides into pyrite within a paleo-SMTZ (Canfield et al., 1992; Raiswell and Canfield, 1998). The dissolved Fe required for Fe-S precipitation could be provided by Fe-oxide reduction coupled to methane oxidation as proposed by Egger et al. (2017). However, the pore-water Fe content in the methanogenic layer is very low, indicating, that this process is not at work anymore.

High values of the FeHR/FeT ratio co-occur with the Fe-S/FeHR enrichments, most likely

related to higher inputs of reactive Fe minerals to Site U1417. This interpretation is in agreement with higher amounts/reactivity of TOC in this interval, as excess terrestrial Fe (mainly as (oxyhydr)oxides that contribute to the FeHR pool) delivered to the GOA should have fertilised primary productivity and enhanced marine OM export to the seafloor (e.g. Martin, 1990). Additionally, diagenetic mobilization of iron (oxyhydr)oxides could have led to the enrichment of FeHR in specific sediment intervals (Kasten et al., 1998).

Low sulphate between 200 and 640 m and a potential cryptic S cycle

Sulphate values below the zone of sulphate reduction (down to 200 mbsf) are above detection limit, but below 2 mM (Figure 1.5). The same pattern is observed in the methane generating strata between 450 and 640 mbsf (Jaeger et al., 2014). Therefore, reasons for these low but non-zero sulphate concentrations are discussed together for both intervals here.

It is possible that either the pore-waters here are indeed sulphate free and the low sulphate measurements are errors, seawater contaminations during drilling or re-oxidized sulphide after core recovery, or low sulphate values below the sulphate reduction front are established by an *in-situ* geochemical process. This could be a cryptic S cycle. In a cryptic S cycle, a reduced S species is re-oxidized to an intermediate S species again below the zone of sulphate reduction by an electron acceptor (Holmkvist et al., 2011). In anoxic sediments, potential electron acceptors can be Mn oxides or Fe oxides (Holmkvist et al., 2011). The resulting intermediate S species then undergoes disproportionation (Thamdrup et al., 1993). In this process simultaneously a more reduced and a more oxidized species is produced. In the case of S disproportionation, sulphate and hydrogen sulphide are the reaction products. By this process, low sulphate concentrations can be maintained in sediments below the sulphate reduction zone. However, in otherwise sulphate-free sediments, the sulphate generated by cryptic cycling will be reduced to hydrogen sulphide by dissimilatory sulphate reduction or AOM again. The cycle is called “cryptic” because the generated sulphate is immediately reduced again and only low sulphate concentrations (close to detection limit) are maintained by this process.

The observation, that sulphate concentrations in methane-free and methane bearing strata at Site U1417 do not differ (in average 1.1 mM sulphate in both sediment sequences) points to re-oxidation or contamination during sampling. If a cryptic S cycle would enrich the sediments below the zone of sulphate reduction between 200 and 640 mbsf with sulphate again, it can be expected that anaerobic oxidation of methane (AOM) would secondarily alter the sulphate profile in the methanogenic layer and sulphate concentrations here would be lower than in the methane-free layer between 200 and 450 mbsf. However, there are still Fe oxides available in the respective sediment intervals (Figure 2.3) which could maintain a cryptic S cycle.

An alternative explanation for the elevated sulphate content could be the dissolution of barites. The whole interval between 200 and 640 mbsf exhibits elevated Ba^{2+} concentrations in the pore-waters. When barite dissolves in pore-waters with low sulphate concentrations, Ba^{2+} ions and sulphate are released to the pore-waters. In the respective interval not enough Ba^{2+} exists to balance the low sulphate concentrations completely, indicating that barite dissolution can only partly explain the elevated sulphate concentrations. Furthermore, pore-water Ba^{2+} and sulphate are anticorrelated in this interval (Figure 2.5) which argues against this hypothesis.

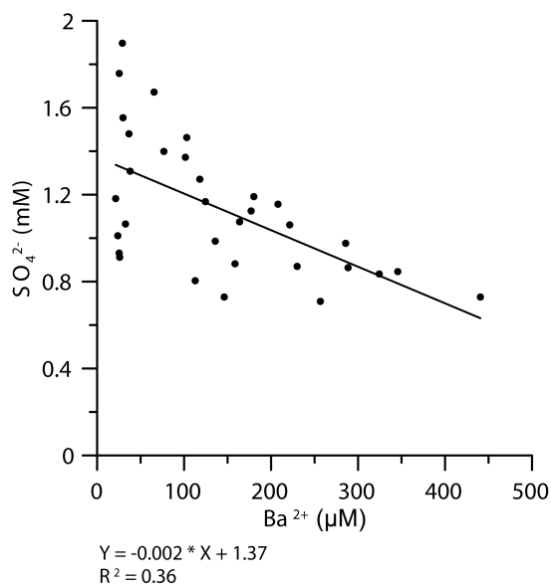


Figure 2.5: Crossplot of Ba^{2+} (μM) vs SO_4^{2-} (mM) between 200 mbsf and 640 mbsf.

Deep sulphate reservoir and reverse SMTZ (below 640 m)

The deepest 60 m at the bottom of the record are characterized by another sulphate-rich zone with sulphate concentrations up to 7 mM below 640 m depth. Between the methanogenic layer and this deep sulphate enrichment lies a deep “reverse” SMTZ which in contrast to a conventional SMTZ *sensu* Froelich, is characterised by methane diffusing down, and sulphate diffusing up.

This reverse SMTZ exhibits the highest Ba/Al peak of the whole U1417 record, likely representing a zone of ongoing diagenetic barite formation. Therefore, an active SMTZ with an electron acceptor supply from below can be assumed. Yet, there is no significant pyrite accumulation in the centre of this zone, and no free hydrogen sulphide was detected during core splitting.

Pore-water Li^+ and Ca^{2+} concentrations increase towards the base of the sediment succession, providing evidence for chemical interaction between sedimentary pore-waters and the oceanic crust (Figure 1.5). The Li^+ and Ca^{2+} ions are leached out of the basaltic basement and diffuse into the pore-waters of the overlying sediments. This indicates that the pool of sulphate-rich water is in contact with, or even circulating through, the oceanic basement (Gieskes et al., 1982). Two other ions, which can also be diagnostic for a deep aquifer leaching ions out of the basement crust, are Mg^{2+} and Sr^{2+} (Gieskes et al., 1982). However, they do not show a similar pattern at Site U1417 (Figure 1.5).

The observation of deep SMTZs with an electron acceptor supply from the bottom of the sediment column is not limited to the GOA, and has been reported previously from other regions in the ocean. Sites where this phenomenon has been described, and more in-depth research has been performed, generally fall into three categories which are depicted in Figure 2.6:

(1) Oceanic spreading centres are common settings for fluid circulation within sediments and the underlying oceanic crust. Here, thermal energy from the hot crust drives fluid motion, and the thin sediment cover supports seawater circulation into and out of the crust (Elderfield et al., 1999; Engelen et al., 2008; Kuhn et al., 2017). Seamount flanks play an even greater role in recharging deep aquifers at the base of the sediment cover, with fluid flow over distances of up to 50 km (Fisher et al., 2003a, 2003b; Hutnak et al., 2006).

(2) At accretionary wedges above subduction zones, compressional dewatering of the accreted and subducting sediments leads to an active regime of subsurface fluid flow (e.g. Expedition 201 Scientific Party, 2002; Torres et al., 2015).

(3) Messinian evaporite layers deposited in the Mediterranean (Messinian Salinity Crisis, Hsü et al., 1973, 1977) represent a special case that does not require active fluid flow but relies on diffusion alone. Sulphate is provided by deeper gypsum-rich layers and can diffuse into the overlying sediment column (Böttcher et al., 1998). This case serves as an example of deep pore-water alteration in a tectonically inactive, but evaporitic depositional setting.

These documented scenarios are not fully applicable or satisfactory for explaining the geochemical observations at Site U1417. The study site lies on a subducting plate, but is presently ~75 km away from the subduction zone. Therefore, it is unlikely that subduction-related dewatering of accreting or subducting sediments accounts for sub-seafloor hydrology at Site U1417. In this area of the open Pacific, no evaporite deposits have been reported and it is highly unlikely that they formed in this open-marine, high-latitude environment in the past. The basement at this site lies below ~800 m of sediment, which is a fairly thick sediment cover compared to seamount or ridge flanks. In addition, not much crustal heat flow can be expected in the GOA, with an oceanic basement age as old as ~43 million years (Gee and Kent, 2007) and overlying pillow basalt ages of ~26 Ma. Seamounts as a source for the deep sulphate-rich water are a more likely explanation. The two seamounts Giacomini Guyot and Kodiak Seamount are in proximity to Site U1417 (Turner et al., 1973) and could provide entry points for seawater. However with 131 km (Kodiak) and 73 km (Giacomini), both are further from the site than the 50 km upper limit of fluid circulation proposed by Fisher et al. (2003a, 2003b) and Hutnak et al. (2006).

Another possibility is that the sulphate pool at U1417 was buried during primary deposition of the deepest sediment layer in the Miocene, and has since then not been consumed completely by bacterial sulphate reduction. A similar scenario was introduced by Brumsack et al. (1992) in the Sea of Japan (ODP Sites 796 and 797). Brumsack et al. state that very low sedimentation rates comparable to the ones at Site U1417 during the Miocene allowed seawater sulphate to penetrate deeply into the sediments. Sulphate diffusion rates from the overlying water column strongly exceeded the rate of sulphate reduction within the

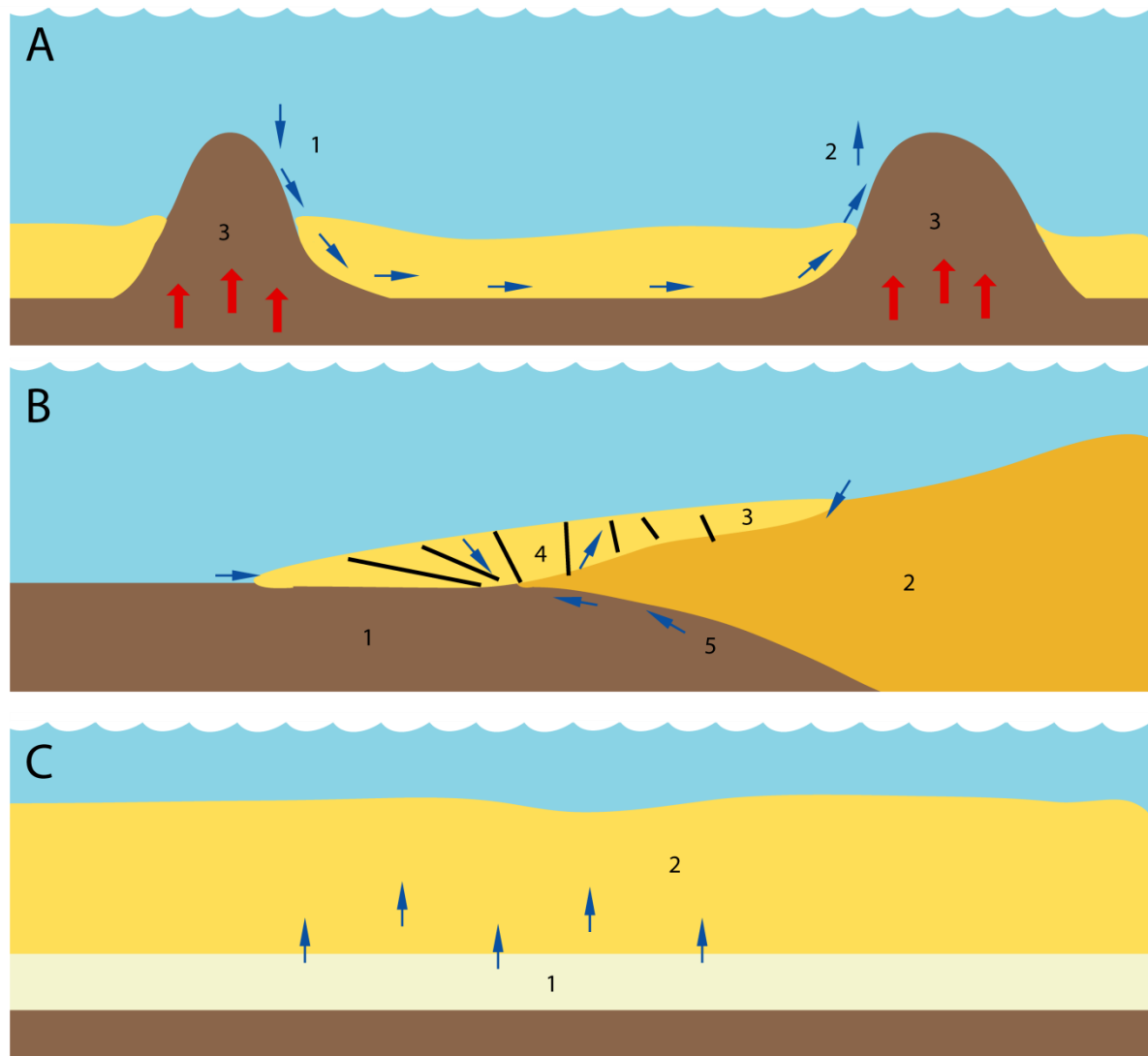


Figure 2.6: Schematic illustration of deep aquifer generating processes (not to scale).

A) Fluid circulation along seamount flanks (e.g. Elderfield et al., 1999). Water enters (1) and exits (2) the sediments at thin sediment coverage at seamount flanks. Heat advection (3) can act as driver for fluid circulation.

B) Water circulation in accretionary wedges (e.g. Torres et al., 2015). Water circulates along the interfaces of incoming oceanic crust (1), continental crust (2) and the accretionary sediment package (3) and through faults in accretionary wedge (4). Further water advects from dewatering subducted plate (5).

C) Fluid diffusion from gypsum-rich evaporitic layers (1) into overlying sediments (2). Special case observed in the Mediterranean Sea (Böttcher et al., 1998).

sediments, preventing significant sulphate depletion in the pore-waters. Thus, when higher sedimentation rates occurred at ~8 Ma BP in the Late Miocene, this deep sulphate reservoir was buried and became isolated from the seawater sulphate pool. Due to low organic matter reactivity in these deep Miocene sediments, sulphate has never been fully reduced until today. Indeed, the lowest ~100 m of the sediment succession at Site U1417 (615+ m) were

deposited over more than 8 Ma under low sedimentation rates ($\sim 1 \text{ cm ka}^{-1}$). A sharp increase in sedimentation rate occurred at 8 Ma (Jaeger et al., 2014), which is represented today by the sediment depth of $\sim 615 \text{ m}$ – right above the current deep SMTZ in $\sim 640 \text{ m}$ depth. A similar process, where, due to low sedimentation rates and organic matter reactivity, electron acceptors diffuse deep into the sediments without being depleted, can currently be seen in the South Pacific Gyre (D'Hondt et al., 2009; Fischer et al., 2009).

Besides the hypothesis of an old, residual sulphate pool preserved at depth at Site U1417, another explanation for the active delivery of relatively young seawater sulphate to the base of the sediment succession could be possible at Site U1417. In the northern parts of the GOA, large-scale tectonic processes lead to plate bending as the Pacific Plate approaches the subduction zone (Masson, 1991; Reece et al., 2013). This bending could have generated new hydrological pathways near the study site through the opening of extensional normal faults. Extension due to plate bending generates an array of sub-parallel normal faults that are observed to offset both the sediment and top of the oceanic crust. Such normal faults have been proposed as seawater conduits into oceanic crust in the Pacific Ocean (Emry and Wiens, 2015; Naif et al., 2015). These faults could also act as a pathway for seawater, generating the observed deep sulphate pool at U1417. Based on existing seismic data within the GOA, plate bending faults are present within $\sim 250 \text{ km}$ of the Aleutian Trench (Figure 2.7). These faults occur near Site U1417 and for up to $\sim 176 \text{ km}$ to the SE measured parallel to Pacific Plate motion.

To distinguish between the possible processes that generated the deep sulphate pool at Site U1417, various geochemical tools can be applied. The analysis of S isotopes provides a highly diagnostic approach for tracing diagenetic S cycling, and is used here to unravel the source of deep pore-water sulphate at Site U1417. In marine sediments, bacterial sulphate reduction is accompanied by S isotope fractionation, whereby sulphate containing the lighter ^{32}S isotope is preferably reduced to sulphide. Consequently, the resulting sulphide, and the pyrite precipitated from it, is isotopically lighter (i.e. depleted in ^{34}S) than the parental seawater sulphate, whereas the remaining sulphate-S becomes isotopically heavier, i.e. enriched in ^{34}S (Strauss, 1997, 1999; Canfield, 2001; Strauss et al., 2012).

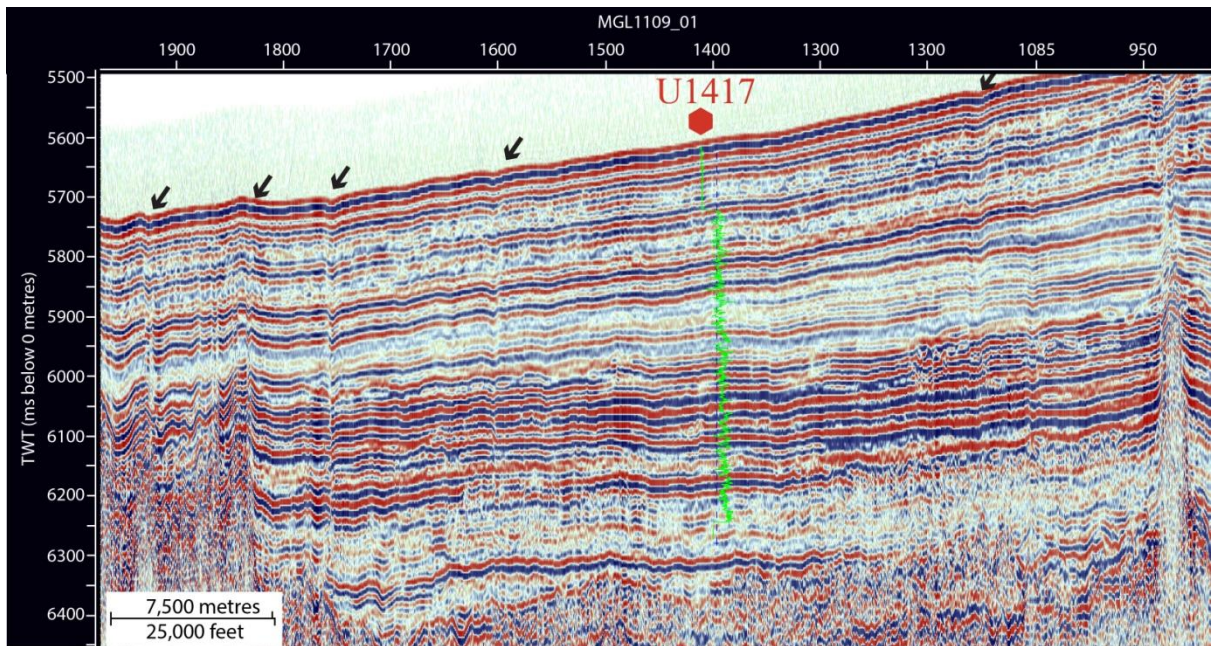


Figure 2.7: Seismic profile shown in two-way travel time across Site U1417; position as shown in Figure 2.1. Note presence of plate bending-related normal faults offsetting sediments from the seafloor to the top of ocean crust within the sediment adjacent to Site U1417 indicated by black arrows.

Modern seawater has $\delta^{34}\text{S}$ values around +21‰ (Böttcher et al., 2007). Sulphur isotopic fractionation associated with bacterial sulphate reduction can be as high as 70‰ (Ono, 2008; Sim et al., 2011), but maximum and constant isotopic fractionation is generally only expressed when an unlimited supply of sulphate with the same isotope signature is available for sulphate reduction (open system, i.e. sulphate consumption < sulphate supply) and other environmental parameters (e.g. type and availability of organic matter as electron donor) remain stable (e.g. Leavitt, 2014). In contrast, bacterial sulphate reduction occurring under sulphate-limited conditions (i.e. sulphate consumption > sulphate supply) leads to a progressive decrease of the sulphate pool, and its S isotopic composition becomes progressively more enriched in ^{34}S (i.e. isotopically heavier) due to the preferential bacterial turnover of $^{32}\text{SO}_4$ (closed system). The resulting sulphide, fixed in the sediment as pyrite, archives the increasingly ^{34}S -enriched signature. Sulphur isotopes of sedimentary sulphide and sulphate are hence diagnostic for identifying if sulphate was constantly supplied from an unlimited pool to a deep SMTZ under open system conditions, or not (Canfield, 2001).

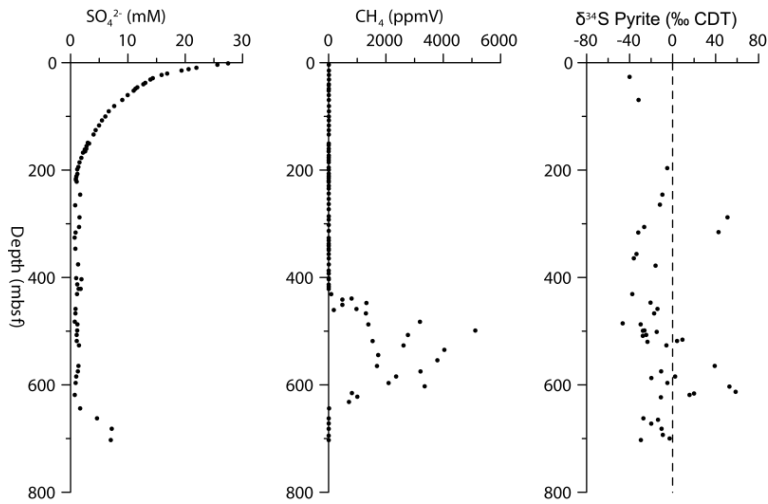


Figure 2.8: Pyrite-S-isotope data. Pore-water SO_4^{2-} (in mM), pore-gas CH_4 (in ppmV), $\delta^{34}\text{S}_{\text{py}}$ (‰), vertical dashed line indicates zero-reference V-CDT standard.

Pore-water sulphate-S-isotopes have not been measured for this study. Unpublished work (Strauss, pers. comm.) shows that sulphate-S-isotopes at Site U1417 are becoming heavier with increasing sediment depth, indicating ongoing sulphate reduction, but no sulphate limitation. Pyrite-S-isotopes below 640 mbsf are considerably negative (-10‰ to -30‰, Figure 2.8), indicating an open system without sulphate limitation. This does not necessarily mean that there is a constant supply of fresh sulphate, but rather that the sulphate pool is only unlimited with respect to the organic matter available for bacterial sulphate reduction. While there is little total Fe present in these intervals, about 40% of the total sedimentary Fe and up to 80% of the highly reactive Fe are pyritized. This near-complete pyritization suggests that at present no further authigenic pyrite precipitation takes place. It cannot be constrained at which point in time this stage of pyritization was reached and hence, the limitation conditions of which time period are recorded in the S isotopes. If pyritization was already complete before either the deep sulphate pool was cut-off or a deep aquifer was installed, the S isotopic composition of the pyrite would reflect the geochemical conditions before this event, because no further pyrite precipitation could have occurred due to the lack of FeHR. Within the SMTZ no pyrite is present and thus no sulphide-S-isotope analysis could be performed.

In the context of authigenic mineral formation associated with the SMTZ, in particular the presence of the SMTZ in its current position within the sediment succession, it is useful to

not only consider the presence of pyrite, but also barite. If a migration of the SMTZ would expose previously precipitated pyrite and barite to sulphate-free pore-water conditions, pyrite would remain enriched, but barite would gradually dissolve and re-precipitate at the new SMTZ position (Torres et al., 1996). Therefore, the relative positions of pyrite and barite peaks around an SMTZ can provide useful information about its past dynamics, and hence the supply of sulphate and methane from below and above, respectively. A pronounced Ba/Al peak is found in the centre of the current SMTZ (Figure 2.4). The absence of peaks further below or above in the record suggests that this discrete zone of barite precipitation must have been fixed within the current sediment interval. It also indicates that either no diagenetic barite ever formed above or below this layer, or that barite precipitated above has already been dissolved. In contrast, pyrite-rich layers occur above and below the current SMTZ. At ~570 m depth, a layer with up to 50% pyritization exists. Here, pyrite-S-isotopes are positive (up to +50‰), which match the isotope signature of the remaining pore-water sulphate at greater depth (Strauss, pers. comm). This could indicate that the SMTZ shifted from a previous position at shallower depth (i.e. at the position of the pyrite enrichments) to its present location further down. The lack of Ba layers coinciding with pyrite enrichments at ~570 m depth points to the dissolution of any diagenetic barite that would have formed at this past SMTZ position, whereas the simultaneously formed pyrite prevailed.

To assess the hypothesis of a deep residual sulphate pool that persisted within these deep Miocene deposits it is of critical importance to know the nature of the organic material in this zone. If the organic material was easily accessible for microorganisms, it should have been oxidized by sulphate over the last millions of years since its burial. If the organic material, by contrast, is highly refractory, it could persist for very long time periods in the Miocene sediments without reacting with the sulphate pool. Therefore, the reactivity of the organic matter within the sulphate-containing deep sediments at Site U1417 can indirectly provide useful information about the relative age of the deep sulphate pool. If the OM is low reactive, i.e. quasi-inert, it is feasible that the sulphate pool belongs to an old buried seawater reservoir, which was cut off from further seawater supply by elevated sedimentation rates. If, by contrast, the organic matter is still reactive (i.e. bioavailable), the sulphate pool must be comparably young as otherwise either the reactive OM or the sulphate would have been diagenetically consumed over geological time.

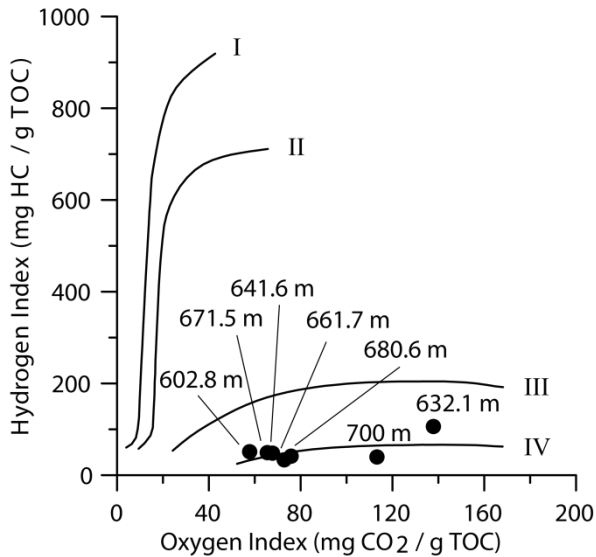


Figure 2.9: Pseudo-Van-Krevelen Plot for Site U1417 below 600 m CCSF-B. Low HI values indicate kerogen type 4 (Vandenbroucke and Largeau, 2007). Depth information in mbsf CCSF-B. Data from Childress (2016). Roman numbers indicate kerogen type (Vandebroucke and Largeau, 2007).

At Site U1417 below 600 mbsf, the sediments contain relatively high amounts of organic matter (up to 2 wt%), but according to a study by Childress (2016), the Hydrogen index (HI) is very low. Hydrogen index of 30 – 50 mg HC/g TOC and oxygen index (OI) of 60 – 140 mg CO₂/g TOC in the deepest sediment interval (Childress, 2016) indicates that all organic matter here is kerogen type IV, an unreactive material that is generally associated with coal-related carbon and can be considered an inert end-member of detrital organic matter that has experienced significant thermal oxidation, and/or sedimentary biological degradation (Vandenbroucke and Largeau, 2007; Figure 2.9). These values suggest that the remaining organic matter in the deepest deposits at U1417 is predominantly unreactive. Consequently, it is possible that microbes could not use this organic material for dissimilatory sulphate reduction, implying that a Miocene buried sulphate pool could have been preserved within these deep sediment layers at Site U1417. However, as there is a contact between the sulphate and the methane rich zone it is highly questionable if the sulphate would not have been reduced by AOM instead. To briefly assess this possibility the time it would take to deplete a sulphate pool at seawater sulphate concentration (29 mM) in these sediments by AOM was calculated. It is assumed that re-supply by diffusion is the limiting factor rather than AOM reaction rate, because no overlap is observed between sulphate and methane enriched layers.

Hence, this calculation can be done using Fick's first law of diffusion (Equation 2.1):

$$2.1. \quad J_{sed} = \Phi * D_{sed} * dC/dx$$

With: J_{sed} = diffusive SO_4^{2-} flux in the sediment, ϕ = sediment porosity, D_{sed} = SO_4^{2-} diffusion coefficient and dC/dx = SO_4^{2-} concentration gradient.

A diffusive flux of $672 \mu\text{mol m}^{-2} \text{a}^{-1}$ for sulphate is calculated. With this flux it would take ~ 2 Ma to bring all sulphate in the zone of AOM, where it will be reduced. This is a much shorter time required for the complete reduction of sulphate by AOM than the time since when this deep sulphate pool would have been originally buried. It can henceforth be concluded that the deep buried sulphate pool is an unrealistic scenario and that the sulphate-rich water is replenished by another process.

The geochemical and modelling data imply that the preservation of an old buried sulphate pool is a rather unlikely scenario and hence it can be assumed that a tectonic driver for the installation of a deep sulphate enriched aquifer exists.

Here, the plate bending process is proposed as a potential driver for the deep aquifer, but the possibility of the seamounts being the reason for seawater circulation cannot be excluded. This process has been shown to work on other sites (Juan de Fuca Ridge, Central Pacific) but in thinner sediment columns and on younger crust. Also the formally proposed 50 km maximum distance of water flow caused by seamounts is exceeded at Site U1417. The process of deep aquifer generation by plate bending is graphically illustrated in Figure 2.10.

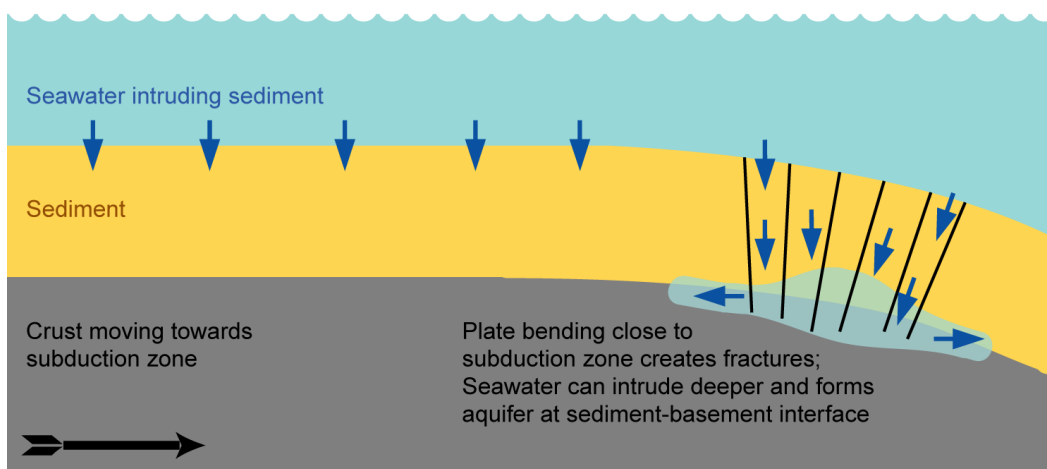


Figure 2.10: Schematic illustration of mechanism to create deep aquifer by plate bending faults (not to scale).

2.5 Conclusions

At IODP Site U1417 in the GOA, new inorganic and organic geochemical data unravel the complex evolution of early diagenetic processes with clear evidence for non-steady state conditions and a distinct deviation from the canonical catabolic sequence *sensu* Froelich. Two key observations are presented. First, auto-termination of anaerobic oxidation of methane and inhibition of an active SMTZ is suggested based on extensive authigenic carbonate precipitation, forming an efficient cap-rock that separates the methanogenic zone from the downward diffusing seawater sulphate. Second, an enrichment of sulphate in the deeper sediment layers well below a zone of sulphate depletion and a methane generating layer is observed. This sulphate-rich water in the deep subsurface causes a reversed diagenetic zonation close to the sediment-basement interface. It is assumed that a deep aquifer, which could be recharged through seamount conduits or through extensional faults generated by plate-bending, provides this sulphate containing sea water. Since SMTZs are important environments for microbial activity, observations of deep sulphate-bearing pore-water pools similar to the one from Site U1417 possibly have far-reaching implications for deep biosphere biomass estimations and the global carbon and sulphur cycles by extending the area of the seafloor in which deep SMTZs can be expected and thus extending the habitats for the deep biosphere.

Chapter 2 is currently submitted to *Geochimica et Cosmochimica acta* as:

“Deep Sulphate-Methane-Transition and sediment diagenesis in the Gulf of Alaska (IODP Site U1417)”

Authors

Mark Zindorf, Christian März, Thomas Wagner, Sean P.S. Gulick, Harald Strauss, Jeff Benowitz, John Jaeger, Bernhard Schnetger, Laurel Childress, Cees van der Land, Michelle La Rosa, Leah LeVay

Abstract

Sediment samples from the Gulf of Alaska (GOA, IODP Expedition 341, Site U1417) have been analysed to understand present and past diagenetic processes that overprint the primary sediment composition. We do not observe a shallow Sulphate-Methane Transition Zone (SMTZ) that characterises similar marine sediment successions worldwide, but a more than 200 m thick sulphate- and methane-free sediment interval between the depth of sulphate depletion (~200 m) and the onset of methanogenesis (~450 m). We suggest that this apparent gap in biogeochemical processing of organic matter is caused by the presence of highly indurated carbonate-cemented layers just above the methanogenic zone. These authigenic carbonates and associated barite enrichments likely document a paleo-SMTZ where progressive authigenic mineral formation mainly driven by anaerobic methane oxidation resulted in gradual cementation of the pore-space. Ultimately an impermeable barrier formed and prevents further methane supply from deeper sediment layers. Beneath the methanogenic zone, at ~650 m depth, pore-water sulphate concentrations increase again, indicating sulphate supply from greater depth feeding into a deep, inverse SMTZ. Diagenetic pyrite depleted in the heavier ^{34}S isotope provides evidence that pyrite formation is not sulphate-limited in the deep SMTZ. A likely explanation for this availability of sulphate in the deep seafloor at U1417 is the existence of a deep aquifer, which actively transports sulphate-rich water to, and potentially along, the interface between sediments and oceanic crust. Another, more unlikely possibility is the presence of a residual pool of old sulphate-rich water that was trapped in these deep sediment layers when they were closer to the sediment-water interface and not affected by significant sulphate reduction. Such reversed diagenetic zonations have been previously observed in marine sediments, but have

not yet been described from intra-plate locations, such as the GOA. The existence of the deep inverse SMTZ at Site U1417 is therefore at odds with existing models for deep seawater penetration, which typically invoke infiltration of seawater in hydrothermal settings or expulsion of deep brines in compressional regimes. With the discovery of a deep inverse SMTZ in an intraplate setting and the self-induced blocking of upward methane diffusion by former authigenic carbonate precipitation in a presently active SMTZ, Site U1417 provides new insights into sub-seafloor pore-fluid and gas dynamics, and their implications for global element cycling and the deep biosphere.

3. The plausibility of a deep buried pore-water sulphate reservoir in marine sediments assessed by reaction transport modelling

3.1 Introduction

Geochemical analyses can reveal the *status quo* of the diagenetic zonation in a sediment column. They can also, to some extent, show at which sediment depths diagenetic reactions have occurred over longer periods if these reactions have left imprints on the primary sediment composition, e.g. in the shape of authigenic mineral accumulations (Hein et al., 1979; Berner, 1984; Torres et al., 1996) or changes in the magnetic susceptibility (Riedinger et al., 2005). Even so, it is difficult to assess to which extent the primary sedimentary composition has been overprinted, e.g. how much OM has been decomposed, and the records of which inorganic paleo-proxies have been altered. Especially in the case of non-steady state diagenesis, i.e. a situation where variations in external forcing change the location and/or intensity of diagenetic reactions, it is crucial to understand how, when, and why diagenetic conditions changed over time. This information allows to better understand causal relationships between currently observable sediment composition and past climatic events, the impact of climate on diagenetic zonation (Contreras et al., 2013), and the habitability of sediments for microorganisms of the “deep biosphere” (Meister, 2015).

Reaction transport models can be used to address the connection between paleo-environmental conditions and early diagenetic processes (Regnier et al., 2002; Aguilera et al., 2005; Arndt et al., 2013; Wehrmann et al., 2013). Using available information on the primary input of electron acceptors, amounts and reactivity of OM, and sedimentation rate as input parameters, reaction transport models can calculate how the diagenetic zonation evolved over time in response to changing depositional conditions. Inverse modelling can reproduce the initial rates of OM deposition from estimated OM reactivities. Finally, comparing model runs with different input parameters to *in situ* observed sediment parameters can provide useful information on the conditions that must have prevailed at the time of sediment deposition, which can improve paleo-environmental reconstructions.

In the deep Gulf of Alaska, IODP Expedition 341 recovered a ~700 m long composite record of sediment and pore-water samples at Site U1417 (Figure 2.1), and shipboard and shore-based analyses revealed an uncommon diagenetic pattern (Jaeger et al., 2014; Chapter 2).

An exceptionally deep (~200 m below the seafloor) sulphate penetration is reported that is not terminated by an SMTZ, but by a ~200 m wide gap between sulphate-rich and methane-rich pore-waters. A heavily cemented carbonate layer caps the methanogenic layer and potentially prevents the methane from diffusing upwards and installing an SMTZ.

A second uncommon feature is the presence of sulphate-rich pore-waters in the deepest recovered pore-water samples. This sulphate pool installs a reversed diagenetic zonation (including an SMTZ with sulphate diffusing upwards and methane diffusing downwards) and influences diagenesis from ~700 m sediment depth to the oceanic basement in ~800 m. Such features in the global ocean are usually related to either hydrothermal circulation of seawater in sediments along oceanic ridges with thin sediment cover and high thermal energy (Engelen et al., 2008), or in accretionary wedges where subduction drives dewatering of the stacked slivers of oceanic plate and overlying sediments (Torres et al., 2015). In an open-ocean intraplate environment like at Site U1417, however, deep sulphate-bearing seawater aquifers have not been described conclusively before. In Chapter 2 it was suggested that the deep aquifer at Site U1417 was evoked by plate tectonic processes either linked to seamount eruptions or plate bending. Both can install pathways for seawater to enter the deeper sediment layers. While seamount flanks with their thin sediment covers could provide a potential entry point for water (Fisher et al., 2003a; Hutnak et al., 2006), plate bending leads to the opening of fractures where seawater circulation is easier than in more solid sediments (Naif et al., 2015; Korenaga, 2017). A third possibility is that a deep sulphate pool in old buried seawater has never been fully reduced by AOM (briefly suggested by Brumsack et al., 1992). Such a pool could be installed under conditions of low sedimentation rates where seawater could diffuse deeply into the sediments. In addition to the sedimentation rates, the second prerequisite is that there is either less organic matter in these sediments than required to reduce all the sulphate, or that the available organic matter is inert and inaccessible to sulphate-reducing bacteria. At some point in the past, increasing sedimentation rates would have led to the deep sulphate pool being cut-off from the overlying diagenetic regime, with the sulphate bearing pore-water pool remaining at depth until today.

In Chapter 3, the alternative hypothesis of Chapter 2 is tested. The Biogeochemical Reaction Network Simulator (Regnier et al., 2002) is used to (a) test if the observed diagenetic

zonation could result from a deep pool of old buried sulphate which has never been fully reduced by AOM, and (b) gain insights into the diagenetic history of the site over the last 16 Ma. It is shown that the diagenetic evolution of the sediment succession is closely linked to primary depositional processes and to global climate evolution. This study is, therefore, an example of how even unusual diagenetic features in marine sediments can be used to reconstruct past environmental changes.

3.2 Methods

One aim of this study is to test the plausibility that the observed diagenetic zonation results from a deep pool of old buried sulphate which has never been fully reduced by AOM. For this purpose, a reaction transport model is applied that allows simulating the evolution of diagenetic dynamics over the past 17 Ma, i.e. the accumulation of the 700 m of sediment at Site U1417. The model will be run inversely for a range of OM reactivity scenarios (and thus original OM deposition fluxes). Model outputs will be compared with present-day sediment and pore-water geochemical records at Site U1417 (Jaeger et al., 2014 and Chapter 2). If a model scenario reproduces the observed diagenetic features, it can be concluded that the persistence of a residual sulphate pool is plausible, while failure to reproduce observed profiles would indicate that such a scenario is unlikely.

Model strategy

The model used for this study is the Biogeochemical Reaction Network Simulator (BRNS, (Regnier et al., 2002; Aguilera et al., 2005)). This 1-dimensional reaction transport model allows simulating transient diagenetic dynamics in the sediment column as it accumulates over 16.86 Ma. Hence it can be used to (a) test the plausibility of a persistence of a residual sulphate pool in deep sediment layers, (b) potentially identify the depositional signal that best reproduces the observed profiles, and (c) reconstruct the diagenetic evolution during burial.

Model formulation

For the general description of dissolved or solid species, the following 1-dimensional conservation of dissolved and solid species was used (Boudreau, 1997 Equation 3.1):

$$3.1. \quad \frac{\partial \sigma C_i}{\partial t} = \frac{\partial}{\partial z} \left(D_{bio} \sigma \frac{\partial C_i}{\partial z} + D_i \sigma \frac{\partial C_i}{\partial z} \right) - \frac{\partial \sigma \omega C_i}{\partial z} + \alpha \sigma (C_i(0) - C_i) + \sum_j s_j^i R_j$$

C_i is the concentration of species i , σ equals porosity ϕ for dissolved species and $(1-\phi)$ for solids, z is the sediment depth, D_{bio} is the bioturbation coefficient, D_i is the molecular diffusion coefficient for dissolved species i and 0 for solid species. ω is the sedimentation rate, α is the bioirrigation coefficient, s_j^i is the stoichiometric coefficient of species i in the kinetically controlled reaction j with the reaction rate R_j .

Transport in the model consists of diffusion, bioturbation and bioirrigation. The effective diffusion coefficient D_i is calculated out of the diffusion coefficient in free solution D_{0i} (Boudreau, 1997) corrected for tortuosity f which is calculated according to a modified Weissberg relation from porosity (Boudreau, 1997; Equation 3.2):

$$3.2. \quad f = 1 - (\ln \phi^2)$$

Bioturbation is the process by which organisms (e.g. worms or clams) mix the sediment by burrowing. The bioturbation coefficient D_{bio} is a diffusive term which describes random displacement of solid and dissolved species up to a maximum depth χ_{biot} .

Bioirrigation (Equation 3.3) is the process by which animals flush their burrows with seawater. By this, water with seawater composition (e.g. oxygen-rich) is brought to deeper sediment layers. In the model, bioirrigation is analogous to a kinetic rate and calculated based on the bioirrigation coefficient α and the concentration of a dissolved species i relative to its concentration at the sediment surface. Bioirrigation intensity α was calculated for the bioirrigation coefficient at the sediment surface α_0 and the bioirrigation attenuation depth length χ_{irri} . α is 0 for all solids.

$$3.3. \quad \alpha = \alpha_0 * e^{(-z/\chi_{irri})}$$

Bioturbation and bioirrigation only affect the upper 10 cm of the sediment column.

Therefore, it could be assumed that they are insignificant when a long sediment column is

simulated (e.g. 700 m in the here-modelled scenario). However, both processes have far reaching effects which are observable deeper in the sediment column. The provision of oxidized pore-water species (e.g. oxygen) to deeper sediment layers and the reworking of reduced material has the potential to increase oxic degradation of OM and by this to affect the amount of OM which is ultimately buried in the deeper sediment layers (Burdige, 2007).

To simulate sediment compaction, porosity φ decreases exponentially with depth (Equation 3.4):

$$3.4. \quad \varphi(z) = ce^{(-bz)}$$

with $c=0.74$ and $b=0.0017$, values representative for a slope environment (LaRowe et al., 2017).

Parameters for the above-described formulas can be found in Table 3.1.

Table 3.1a: Transport parameters.

Parameter	Unit	Value	Reference
L	m	700	Jaeger et al. (2014)
ξ_c	m	100	-
c	m	0.74	LaRowe et al. (2017)
b	m	1.7e-3	LaRowe et al. (2017)
α_0	yr ⁻¹	45	Thullner et al. (2009)
χ_{irri}	m	0.035	Thullner et al. (2009)
D_{bio}	m ² yr ⁻¹	0.000483	Middelburg et al. (1997)
χ_{biot}	m	0.1	Boudreau (1997)
ω	m yr ⁻¹	variable (see Figs 3 and 6)	Jaeger et al. (2014)
D_{O_2}	m ² yr ⁻¹	0.0290	-
D_{NO_3}	m ² yr ⁻¹	0.0241	-
D_{SO_4}	m ² yr ⁻¹	0.0127	-
D_{CH_4}	m ² yr ⁻¹	0.0167	-
D_{NH_4}	m ² yr ⁻¹	0.0243	-
D_{H_2S}	m ² yr ⁻¹	0.0204	-
D_{CH_4g}	m ² yr ⁻¹	0.5	Dale et al. (2008)

Table 3.1b: Reaction parameters.

Parameter	Unit	Value	Reference
x/y/z	-	106/16/1	Redfield (1958)
v	-	variable (see text)	Boudreau and Ruddick (1991)
a	yr ⁻¹	variable (see text)	Boudreau and Ruddick (1991)
K _{O2}	M	8*10 ⁻⁶	Wang and Van Cappellen (1996)
K _{NO3}	M	1*10 ⁻⁵	Wang and Van Cappellen (1996)
K _{SO4}	M	1*10 ⁻³	Wang and Van Cappellen (1996)
k ₅	M ⁻¹ yr ⁻¹	1*10 ⁷	Wang and Van Cappellen (1996)
k ₆	M ⁻¹ yr ⁻¹	6*10 ⁸	Wang and Van Cappellen (1996)
k ₇	M ⁻¹ yr ⁻¹	1*10 ¹⁰	Jourabchi et al. (2005)
k ₈	M ⁻¹ yr ⁻¹	1*10 ⁴	Regnier et al. (2011)
k ₉	M yr ⁻¹	1*10 ⁷	Dale et al. (2008)
k ₁₀	yr ⁻¹	100	Dale et al. (2008)
k ₁₁	-	1.6	Berner (1980)

The model used here accounts for fluxes and transformations of organic matter, oxygen, nitrate, sulphate, methane, ammonium and hydrogen sulphide. The reaction network consists of a set of diagenetic redox reactions according to Froelich et al. (1979). Primary reactions comprise oxic degradation of organic matter (r1), nitrate reduction (r2), sulphate reduction (r3), and methanogenesis (r4). Iron oxide reduction and manganese oxide reduction were excluded due to the minor contribution to the organic matter degradation (Thullner et al., 2009). Secondary redox reactions were ammonium oxidation (r5), oxic hydrogen sulphide oxidation (r6), oxic methane oxidation (r7), and anaerobic oxidation of methane by sulphate (AOM, r8). Methane can fluctuate between aqueous and gaseous phases (r9 and r10). Ammonium can adsorb onto clay minerals in an equilibrium process (r11). Furthermore, the sediment age (r12) and the time of sulphate depletion (r13) are calculated by the model. Rate formulations can be found in Table 3.2.

Table 3.2: Reaction rates.

Stoichiometry		Reaction rate
Primary redox reactions		
r1	Oxic degradation $(CH_2O)_x(NH_3)_y(H_3PO_4)_z + (x + 2y)O_2 + (y + 2z)HCO_3^- \rightarrow (x + y + 2z)CO_2 + yNH_4^+ + zHPO_4^{2-} + (x + 2y + 2z)H_2O$	$r_1 = v * (a + age)^{-1} * CH_2O * f_{O_2}$
r2	Nitrate reduction $(CH_2O)_x(NH_3)_y(H_3PO_4)_z + \left(\frac{4x+3y}{5}\right)NO_3^- + \left(\frac{2x+4y}{5}\right)N_2 + \left(\frac{x-3y+10z}{5}\right)CO_2 + \left(\frac{4x+3y-10z}{5}\right)HCO_3^- + zHPO_4^{2-} + \left(\frac{3x+6y+10z}{5}\right)H_2O$	$r_2 = v * (a + age)^{-1} * CH_2O * f_{NO_3}$
r3	Sulphate reduction $(CH_2O)_x(NH_3)_y(H_3PO_4)_z + \frac{x}{2}SO_4^{2-} + (y - 2z)CO_2 + (y - 2z)H_2O \rightarrow (x + y - 2z)HCO_3^- + yNH_4^+ + zHPO_4^{2-} + \frac{x}{2}H_2S$	$r_3 = v * (a + age)^{-1} * CH_2O * f_{SO_4}$
r4	Methanogenesis $(CH_2O)_x(NH_3)_y(H_3PO_4)_z + (y - 2z)H_2O \rightarrow \left(\frac{x-2y+4z}{2}\right)CO_2 + (y - 2z)HCO_3^- + yNH_4^+ + zHPO_4^{2-} + \frac{x}{2}CH_4$	$r_3 = v * (a + age)^{-1} * CH_2O * (1 - (f_{O_2} + f_{NO_3} + f_{SO_4}))$
Secondary redox reactions		
r5	Ammonium oxidation $NH_4^+ + 2O_2 + 2HCO_4^- \rightarrow NO_3^- + 2CO_2 + 3H_2O$	$r_5 = k_5 * NH_4^+ * O_2$
r6	Sulphide oxidation $H_2S + 2O_2 + 2HCO_3^- \rightarrow SO_4^{2-} + 2CO_2 + 2H_2O$	$r_6 = k_6 * H_2S * O_2$
r7	Methane oxidation $CH_4 + 2O_2 \rightarrow CO_2 + 2H_2O$	$r_7 = k_7 * CH_4 * O_2$
r8	AOM $CH_4 + CO_2 + SO_4^{2-} \rightarrow 2HCO_3^- + H_2S$	$r_8 = k_8 * CH_4 * SO_4^{2-}$
Methane gas dynamics		
r9	$CH_4(g) \rightarrow CH_4(aq)$	$r_9 = k_9 * CH_{4g} * (CH_{4eq} - CH_4)$ if $CH_{4eq} > CH_4$ $r_9 = 0$ if $CH_{4eq} \leq CH_4$
r10	$CH_4(aq) \rightarrow CH_4(g)$	$r_{10} = k_{10} * (CH_4 - CH_{4eq})$ if $CH_{4eq} \leq CH_4$ $r_{10} = 0$ if $CH_{4eq} > CH_4$ with $CH_{4eq} = f(P, T, S)$
Adsorption		
r11	$NH_4^+ \xrightleftharpoons{K_{11}} NH_4^+$	equilibrium
Age		
r12	Age	$age = age_{biot}$ if $z < x_{biot}$ $r_{12} = 1$ if $z \geq x_{biot}$
r13	d_{SO_4}	$r_{13} = 0$ if $SO_4^{2-} > 0$; $r_{13} = 1$ if $SO_4^{2-} = 0$

The degradation of OM is described by the reactive continuum model (RCM; Boudreau and Ruddick, 1991). The RCM simulates the progressive decrease of OM reactivities with age/burial depth. The apparent reactivity of the bulk TOC decreases with burial time according to Equation 3.5:

$$3.5. \quad k(z) = (a + \text{age}(z))^v$$

where k is the apparent first order degradation rate constant (Boudreau and Ruddick, 1991). The model represents the reactivity of bulk organic matter as a continuous distribution over the reactivity spectrum. The shape of the distribution of organic matter reactivity is defined by two parameters, a and v , where a is the average lifetime of the more reactive species (in years) and v (dimensionless) describes the shape of the distribution of OM reactivities in the bulk OM near $k=0$. The scaling parameter v is lower if low reactive compounds dominate and higher when more reactive types prevail. High initial a values define a less reactive more homogenous pool, whereas low initial a values define a heterogeneous pool where reactivity decreases rapidly with burial time. Thus, the term $(a+\text{age}(z))$ in Equation 3.5 causes the reactivity of bulk OM to decrease with burial time. To account for sediment mixing by bioturbation, a constant age (age_{biot}) is assumed for the bioturbated layer χ_{biot} . In addition, organic matter degradation rates are kinetically limited by the availability of TEAs according to the Gibbs free energy of the respective reaction.

Numerical solution

The model was run for a simulation period of 16.86 Ma with an adaptive time step. Reaction transport equations were solved sequentially. First, advective transport was calculated, then reaction equations were solved subsequently. The continuity equation (Equation 3.1) was solved on an uneven grid (Boudreau, 1997; Equation 3.6):

$$3.6. \quad z(n) = \frac{L((\xi_n^2 + \xi_c^2)^{0.5} - \xi_c)}{(L^2 + \xi_c^2)^{0.5} - \xi_c}$$

with: $z(n)$ =depth of the n^{th} grid point, L = length of simulated sediment column, ξ_n =point on a hypothetical even grid, ξ_c =depth relative to which $z(n)$ is quadratically distributed for $\xi_n \ll \xi_c$

and linearly distributed for $\xi_n \gg \xi_n$. For the here used model all parameters describe a grid size which increases downwards.

Initial conditions and boundary conditions

The model is initialized and spun up with the TOC content at the deepest point of the TOC profile. The spin-up period allows pore-water profiles to reach steady state with respect to the initial background TOC profile. After this initial spin-up period, the model is forced with constant, fixed concentration boundary conditions (Table 3.3) for dissolved species. Constant concentrations for oxygen and for sulphate were chosen as no signs for reducing conditions in the bottom-water (e.g. redox sensitive trace metal enrichments) have been found at Site U1417. Initial organic matter deposition fluxes are calculated on the basis of the observed, present-day TOC profile according to:

$$3.7. \quad TOC_{at\ deposition} = TOC_{today} / \left(\frac{a}{a + age_{sediment}} \right)^v$$

(see Figure 3.1)

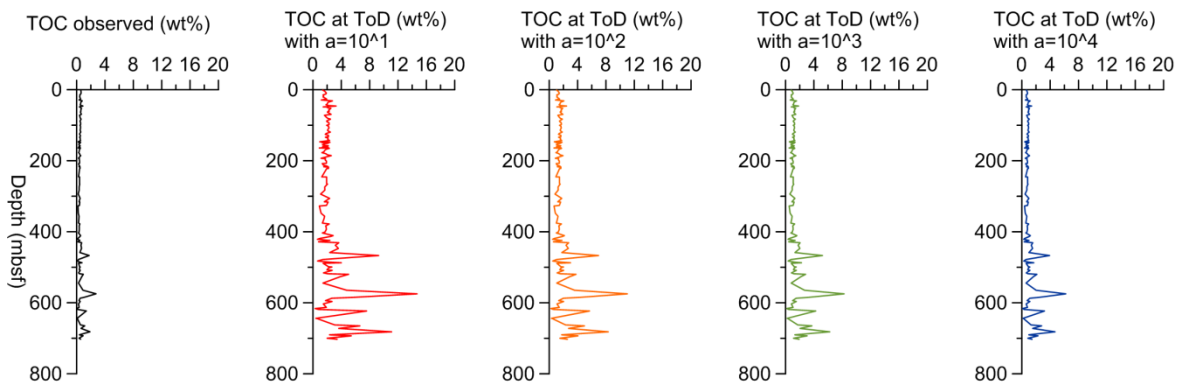


Figure 3.1: TOC profiles at time of deposition (ToD) calculated from observed TOC profile (left panel) by reactive continuum model (Boudreau and Ruddik, 1991). With $a=10^1$ to $a=10^4$ years (left to right).

At lower boundary (i.e. the basement) an open flux condition was specified for all species.

Table 3.3: Boundary conditions.

Parameter	Concentration
O ₂	174 μM
NO ₃	28 μM
SO ₄	28 mM
NH ₄	0
CH ₄	0
H ₂ S	0
TOC	Scenario dependent (Equation 7)

Iteration

It is assumed that organic matter of roughly similar quality has been deposited at Site U1417 over the past 17 Ma and therefore, the a and v parameters of the depositing TOC do not vary with time. Organic matter reactivity only decreases with burial depth and time according to Equation 3.5, accounting for preferred degradation of the most reactive organic matter. A large ensemble of TOC reactivity scenarios was initially run over the entire range of plausible OM degradation rate parameters ($a = 10^{-1}$ - 10^5 yrs, $v = 0.1$ - 0.4), reflecting varying organic matter reactivities and, thus, TOC deposition scenarios (see Equation 3.7). From this initial run, the scenarios that best fit present-day observed depth profiles were selected and a narrow, yet highly resolved ensemble of model runs was simulated for $v = 0.125$ and varying $a = 10^1$ to $a = 10^4$ years (Figure 3.1).

3.3 Results

The model was run for a set of organic matter reactivities in order to determine which one produces the best fit to the observed geochemical profiles (Figure 3.2). The best fit for all observed profiles has been determined to be between $a = 10^2$ years and $a = 10^3$ years. To improve the fit, various scenarios between these two values have been tested. The ultimate best fit has been found at $a = 10^{2.2}$ years. An a of $10^{2.2}$ years was able to reproduce the concave-down shape of the observed sulphate profile at the top of the sediment column, cause sulphate depletion and methane generation in the middle part of the sediment column, and maintain a deep sulphate pool in the deeper layers (Figure 3.3).

A slightly lower a of 10^2 years (higher reactivity) yields a better fit for the upper concave-down sulphate profile, but causes the deep sulphate pool to disappear completely. Also, methane generation extends into the zone which is not observed to generate methane in-situ. Figure 3.3 shows the best fit scenario (yellow) and a scenario with a slightly higher reactivity of $a=10^2$ years (orange).

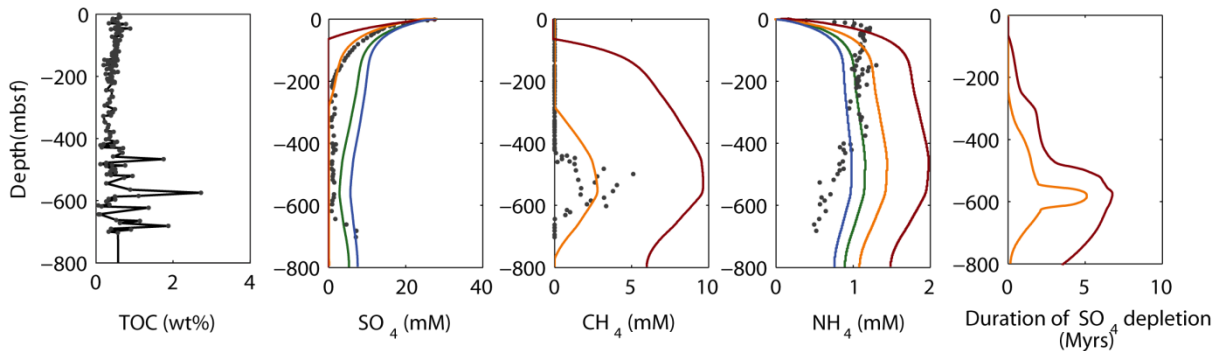


Figure 3.2: Modelled present-day scenarios for four different RCM parameters. Blue: $a=10^4$ years, green: $a=10^3$ years, yellow: $a=10^2$ years, red: $a=10^1$ years, TOC (wt%) = observed present day scenario, modelled scenarios: sulphate (mM), methane (mM), ammonium (mM), duration of sulphate depletion (Ma). Black dots represent measured values on pore-water and sediment samples (refer to Chapter 1.5.1 and Chapter 2). Please note: measured CH₄ in Vol%, not in mM, not directly comparable.

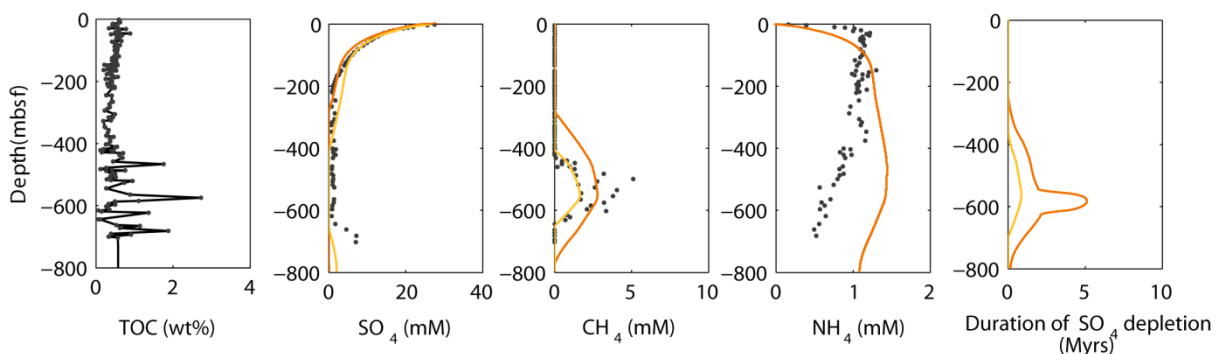


Figure 3.3: Modelled present-day best fit scenarios for RCM parameters $a=10^{2.2}$ years (yellow), $a=10^2$ years (orange). TOC (wt%) = observed present day scenario, modelled scenarios: sulphate (mM), methane (mM), ammonium (mM), duration of sulphate depletion (Ma). Black dots as in Figure 3.2.

Evolution of the modelled diagenetic profile over simulated time

Snapshots of the development of the diagenetic profile of sulphate and TOC have been taken at every sedimentation rate change (Figure 3.4) and for methane at a lower resolution depending on the onset of methane generation. Snapshots can be seen in Figure 3.5 for the

best fit scenario and in Figure 3.6 for the higher reactivity scenario. Plotted to the last time step is the observed profile of sulphate and methane for comparison. TOC does not have to be compared as the modelled profiles are calculated backwards from the observed profile.

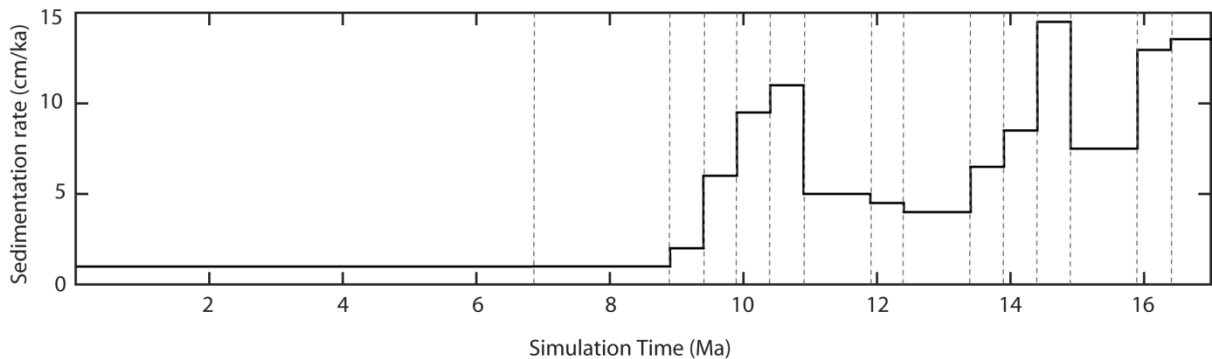


Figure 3.4: Sedimentation rate (cm ka^{-1}). Dashed lines indicate position of snapshots for transient profiles (Figures 3.5 and 3.6).

In the best fit scenario (orange in Figures 3.3 and 3.5), initially up to 4 wt% TOC are deposited. Sulphate penetrates relatively deeply into the sediment over the first 10 Ma of deposition and is only reduced incompletely. At the onset of higher sedimentation rates after 10 Ma, a zone of stronger sulphate reduction is installed in the shallow sediments reaching down to ~ 50 m depth. At the same time, contents of deposited TOC reach 20 wt%. The highest observed amounts of TOC today are below 4 wt%. However, as OM is decomposed after burial, the initially deposited TOC contents are expected to be much higher. Only about 500 ka later, around 75% of this TOC spike are already decomposed and only ~ 5 wt% TOC remain in the sediment. Below the sulphate reduction zone, a sulphate pool is maintained which, as time progresses, evolves into the observed pool of deep sulphate. Methane generation only sets in very late in this scenario, after around 16 Ma of sediment deposition.

In the alternative scenario (Figures 3.3 and 3.6) with $a=10^2$ years, initial TOC deposition exceeds 4 wt%. The TOC spike at 10 Ma also reaches nearly 20 wt% and is decomposed to ~ 5 wt% after 500 ka. The sulphate pool behaves similarly to the one observed in the first scenario, but the deep pool is depleted in the last time step at 17 Ma after the onset of sediment deposition. Short after the deposition of 20% TOC at 10.86 Ma, methane production at the upper sulphate reduction zone in 100 m depth sets in. However, methanogenesis here only yields insignificant amounts on nM scale which would not be

detected with shipboard geochemical methods. Methane production below 450 m depth starts much earlier compared to the best fit scenario, around 11 Ma after the onset of sediment deposition, and the methane pool increases steadily until the end of the simulation.

3.4 Discussion

With an organic matter reactivity parameter, a , of $10^{2.2}$ years, it was possible to simulate a sulphate profile for the upper 200 m of sediment which resembles the observed one. Furthermore, this a -value establishes methane generation and accumulation only in the zone where it is observed today and preserves a sulphate pool below the methanogenic layer.

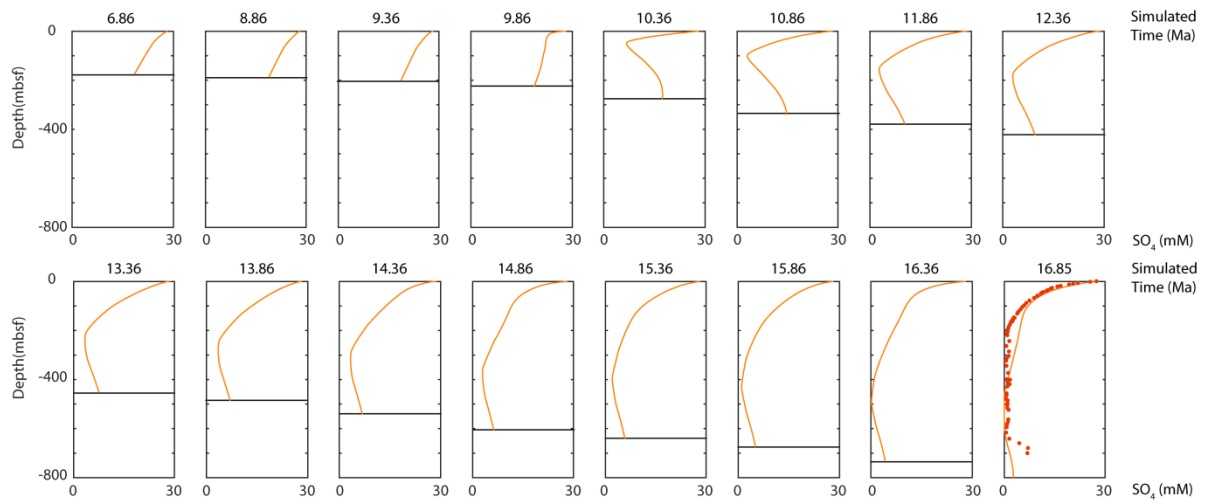
The diagenetic model does not account for the self-sealing of the methane reservoir by the carbonate layer generation. Furthermore, the same reactivity of organic matter is assumed for the entire depositional period. Even under these simplistic conditions, it is possible to model the concave-down sulphate profile and to constrain methane generation to the observed methanogenic layer. In other words, the carbonate layer is not necessary to prevent methane from reacting with the upper sulphate pool. It is also possible to maintain a deep sulphate pool in the deeper sediments under the assumption of low organic matter deposition and reactivity alone, without further assumptions such as a tectonically induced deep aquifer.

There is, however, a minor yet potentially significant difference between the modelled and the observed profiles. The deep sulphate pool exhibits a lower sulphate concentration and a less steep gradient in the model compared to *in situ* observations. The steeper concave-up gradient in the observed profile might indicate non-steady state diagenesis, potentially evoked by an active flux of sulphate from below into a zone of AOM. However, this profile only contains three data-points and is therefore potentially not very meaningful.

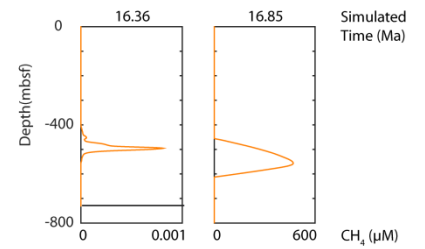
Evolution of the modelled diagenetic profile over simulated time

The transient evolution of the best fit scenario (Figure 3.5) reveals that the deep sulphate pool was separated from the overlying seawater around 10 Ma after deposition at Site

Sulphate



Methane



TOC

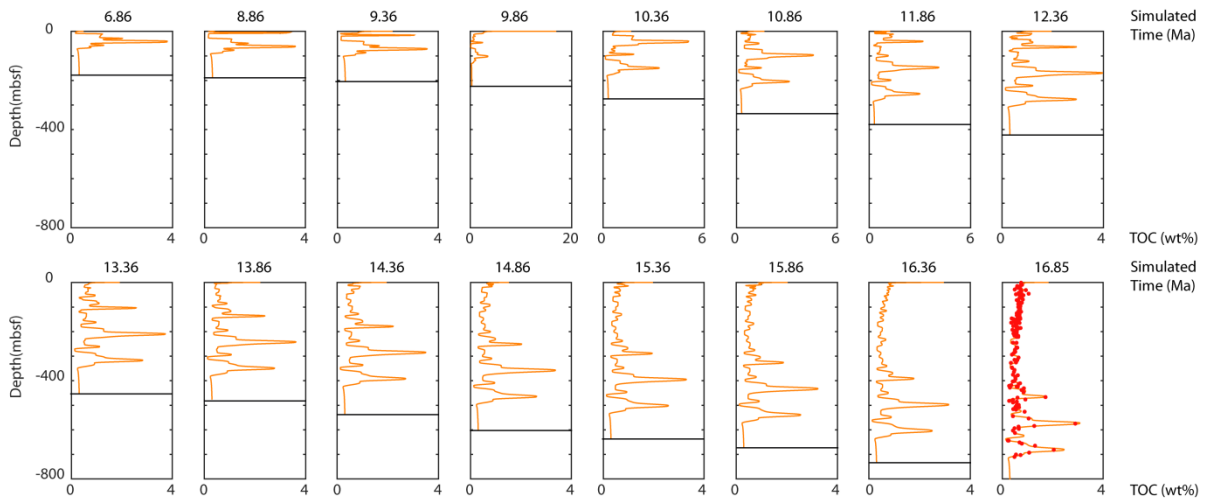


Figure 3.5: Transient evolution of sulphate (mM), methane (mM) and TOC (wt%) in best fit scenario ($a=10^{2.2}$ years), observed profiles in last panel for comparison (red dots).

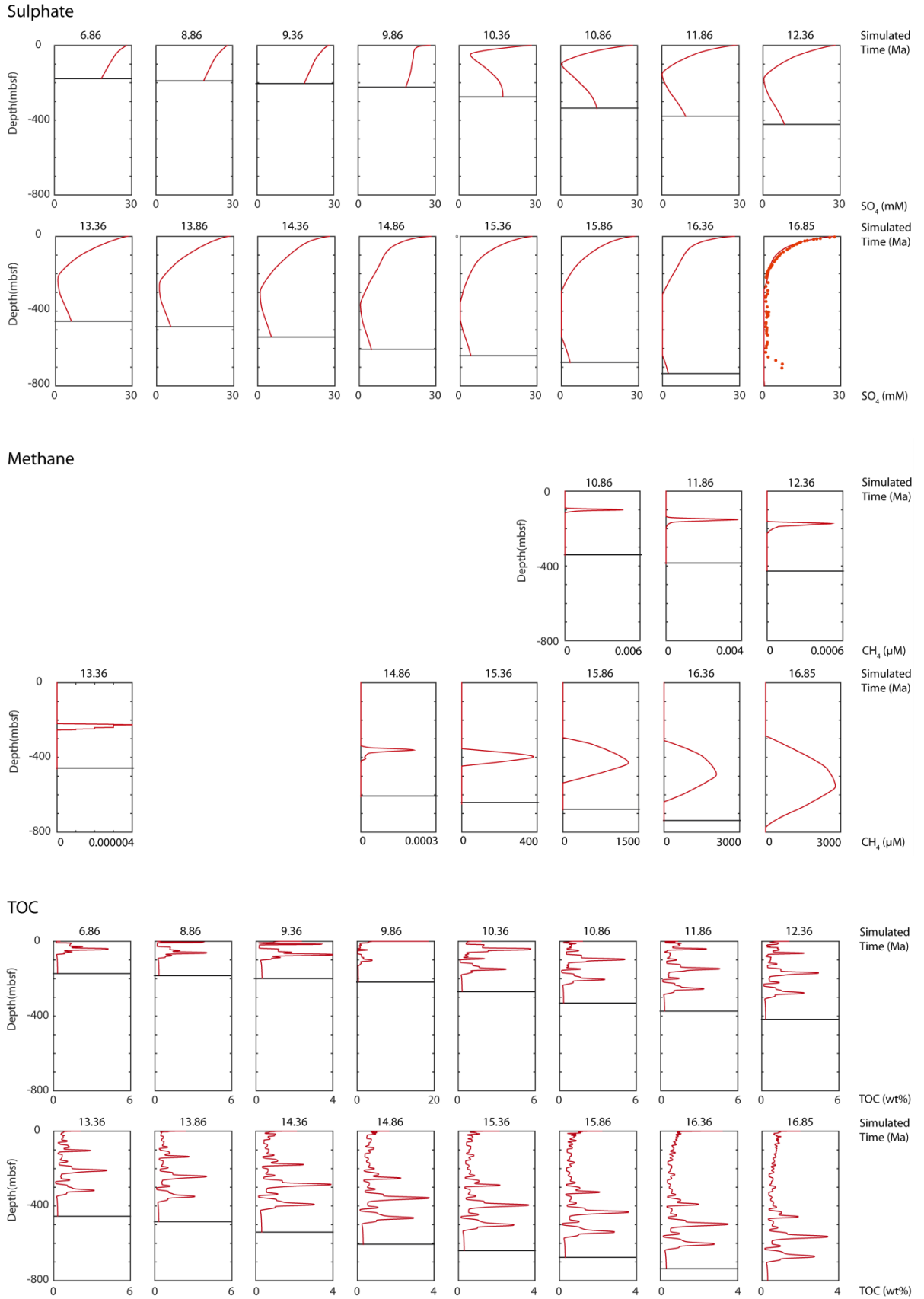


Figure 3.6: Transient evolution of sulphate (mM), methane (mM) and TOC (wt%) in alternative scenario ($a=10^2$ years), observed profiles in last panel for comparison (red dots).

U1417 started. At this point, increasing sedimentation rates coincide with a massive spike of OM deposition of 20 wt% TOC. This peak is decomposed to ~ 5 wt% TOC in the relatively short time span of 500 ka. During this decomposition process, high amounts of electron acceptors must be consumed as well within these rapidly deposited, organic-rich sediments. Diffusion from overlying seawater during early stages of slow sedimentation allowed a sulphate pool to accumulate deep in the sediments and sudden, high OM deposition led to its cut-off. The remaining OM in the lower sediment layers seems to be too unreactive to cause further sulphate reduction or methane production. In the upper sediment layers, sulphate diffusion is limited by sediment accumulation and sulphate reduction out-competes replenishment. In these layers, sufficient still-reactive OM is available for significant methanogenesis. It has to be noted that a sudden OM deposition of 20 wt% is a highly unlikely scenario at an open marine deep sea site. It is imaginable that a local phenomenon such as a whale fall can cause similar high OM deposition rates accompanied by high sulphate reduction rates (Treude et al., 2009), but this would be a localized event. It is questionable if a whale fall would be able to cause the modelled cut-off of the deep sulphate pool, because lateral sulphate diffusion would probably re-establish the connection between the deep sedimentary sulphate pool and the overlying seawater sulphate. More plausible is the assumption that the spike in observed OM is caused by the deposition of material with a lower reactivity, e.g. coal eroded from coal seams on land, which was not subsequently decomposed. The effect of this unreactive OM on sulphate reduction would, however, not adequately simulated by the here-described model.

In the scenario with a slightly higher OM reactivity (i.e. lower apparent initial age, Figure 3.6), the same processes take place. However, the higher OM reactivity eventually causes total depletion of the deep sulphate pool and a more extended methane production in the middle of the sediment column.

The fact that assumed higher OM reactivity would only cause sulphate depletion during the last time step of the simulation (i.e. relatively recently) could indicate that under the best fit scenario, as well as *in situ*, the deep sulphate pool might become fully consumed within the next <1 Ma. Alternatively, the remaining organic matter in the lower sediment layers could be so inert that no further organoclastic sulphate reduction will occur. Even in this case, however, AOM might still lead to partial or full sulphate depletion. AOM might especially

play a more significant role in the future as methanogenesis in the middle part of the sediment column only started to play a role in the best fit scenario during the last time step (i.e. the last 500 ka). Hence, AOM did not contribute to the depletion of the deep sulphate during the past, but is expected to do so in the future.

The finding that significant sulphate concentrations in deep pore-waters at Site U1417 can be maintained by assuming low OM reactivities and sedimentation rates, but without the influence of tectonic factors, contradicts the hypothesis that AOM would have led to the depletion of the deep sulphate pool over the last 10 Ma (Chapter 2). However, this latter hypothesis was based on the assumption that significant amounts of methane were produced over this entire time period of ~17 Ma since deposition at U1417 started. If methane production started only relatively recently, as indicated by the model, AOM would not have played a role and maintaining a deep sulphate pool over several Ma would be possible. The in situ observed sulphate pool would thus still be a transient feature and will be depleted in the future.

3.5 Further directions of modelling

The model parameters used in this study are relatively simplistic and could be improved in several ways in the future. All of these improvements come at the expense of longer calculation times. Therefore, it is critical to assess the scenarios for their plausibility before modelling them, which is also necessary to avoid simulating a perfectly working but environmentally unrealistic best fit scenario.

Arguably the first potential improvement to the model would be simulating the auto-termination of methane flux to the overlying sediment layers by the formation of the capping authigenic carbonate layer. In situ observations show that this feature exists and the biogeochemical processes generating such a cemented layer are relatively well understood (e.g. Pierre et al., 2016; Wehrmann et al., 2016). The chemical process of carbonate formation is not part of the reaction network of the BRNS, hence, to appropriately model the self-cementation, the exponential decrease in porosity (Equation 3.4) would have to be modified by manually decreasing the porosity at the time when the sulphate reduction zone reaches the respective sediment depth. This improvement would help understanding how

the blocking of the methane flux into upper sediment layers would affect its downward diffusion towards the deep sulphate pool, and if under these conditions it is still possible to maintain a deep sulphate pool. In the upper layers of the sediment succession, it could be tested how this cemented barrier would affect the shallow sulphate profile. Furthermore, it could be tested if a best fit scenario, comparable to the one described here, could still be reached by assuming a constant organic matter reactivity over the whole depositional period. A cemented layer above the methanogenic zone would potentially lead to an increased sulphate flux into deeper sediment layers and cause total sulphate depletion there. Under these conditions, a scenario maintaining the deep sulphate pool and accounting for the cemented layer would thus require lower organic matter reactivities to generate less methane in order to reduce less sulphate. This scenario would most likely change the sulphate profile in the upper sulphate reduction zone as well, which fits relatively well in the current best fit scenario.

Organic matter reactivity could be adjusted for different depositional periods, but would need to be backed by observations. The analysis of carbon isotopes, kerogen types and biomarkers on sample material could provide information on the reactivity of organic matter today and the relative contributions of terrestrial and marine material (Killops and Killops, 1997; Vandenbroucke and Largeau, 2007). This would potentially allow for assumptions on the initially deposited material from which assumptions on varying reactivity can be made. The amount and reactivity of the deposited OM could also be estimated from paleoclimate data. During glacial times, for example, lower amounts of terrestrial material can be expected as the coastal ranges along the GOA were glaciated (Montelli et al., 2017).

The model described in this paper, as well as the options for improvement described above, attempt to simulate a scenario without a deep influx of sulphate to test the plausibility of this scenario without the presence of a deep aquifer actively supplying sulphate from below. The opposite approach is possible as well, i.e. constructing a model that has an active sulphate source from below. This, however, would require testing several different scenarios of deep aquifer generation which could be cost-intensive with regards to calculation time. In general, there are three options for deep aquifer generation at Site U1417 with different timings (see Chapter 2). Either the aquifer has been in its current position since the beginning of deposition (26 Ma BP, see Chapter 2), or it was produced by seamount

eruptions, or it is related to plate bending faults. Each of these processes has its own temporal constraints.

Seamount eruptions in the vicinity to Site U1417 occurred around 20 Ma BP (Kodiak Seamount 22.6 Ma BP and Giacomini Guyot 19.9 Ma BP; Turner et al., 1973).

If plate bending was the responsible process, the deep aquifer would hence be no older than 3.9 Myr. This has been constrained using the global plate motion model MORVEL2010 (Mid-Ocean Ridge VELOCITY; DeMets et al., 2010) where the Pacific Plate at this location is moving at $\sim 53 \text{ mm a}^{-1}$ at a NW angle of -315.19° . It is calculated that Site U1417 passed through the location of expected onset of plate bending faults ($\sim 176 \text{ km to SE}$) $\sim 3.9 \text{ Ma ago}$ (Gulick, pers. comm.).

These dates would be potential time steps in the simulation to commence a deep influx of sulphate at the lower model boundary. Here, further adjustments on the concentrations of sulphate and potentially nitrate and oxygen can be made, depending on the biogeochemical modifications this aquifer water already experienced before reaching its current position. Another obstacle is that more exact assumptions would have to be made for the sedimentological and geochemical characteristics of the interval between the deepest cored sample at Site U1417 and the oceanic basement. At the moment, this interval is only simulated with open flux conditions and constant background concentrations for OM and other parameters. Organic matter concentrations and permeabilities are unknown for this sediment interval, as it has not been drilled by IODP Expedition 341 (Jaeger et al., 2014). In summary, the attempt to simulate the deep aquifer directly would potentially be the most precise approach, but also the most complicated one.

A way to improve each possible model would be to include sulphur isotopes into the model (Wehrmann et al., 2013). This can be used to constrain the biogeochemical reactions that the deep sulphate pool has undergone (Canfield, 2001). Especially for the deep sulphate pool, S isotopes can be used to assess if the slow reactions required to maintain a deep sulphate pool without additional sulphate influx would lead to the large isotope fractionation observed in situ (Chapter 2).

3.6 Conclusions

To simulate the evolution of the solid phase and pore-water geochemical profiles at IODP Site U1417 in the Gulf of Alaska a reaction transport model was formulated. Geochemical observations have shown that the sediment column at this site exhibits an uncommon diagenetic profile with an exceptionally deep sulphate penetration, no SMTZ at the depth of sulphate depletion, a heavily cemented carbonate layer which might prevent methane from diffusing upwards, and a reversed SMTZ at the bottom of the sediment column with sulphate supply from below.

Despite the simplifications made in the model, such as no implementation of the self-sealing carbonate layer and no change in organic matter reactivity over depositional time, it was possible to recreate the diagenetic profile with relative accuracy. No further geodynamic assumptions, such as a tectonically driven influx of sulphate-bearing seawater, had to be made to simulate the deep sulphate pool, the deep sulphate penetration, and the offset between sulphate depletion and methane generation.

The simulation reveals that it is possible to maintain a residual sulphate pool in sediment pore-waters over time periods of millions of years if dissimilatory sulphate reduction is limited by the availability of reactive organic matter. The original assumption that AOM would instead lead to a depletion of the sulphate in relatively short amounts of time (<1 Ma, Chapter 2) is potentially still true. However, the model implies that significant methane accumulation and thus AOM only set in relatively recently at the simulated Site U1417, and hence the deep sulphate pool is still observable today.

The scenario modelled here is not necessarily "true", but it is plausible. It reveals that the observed cemented layer is not required to install the profile in the upper sulphate reduction zone, and that no tectonically driven influx of sulphate-rich seawater is needed to maintain a deep sulphate pool. This information can only be provided by reaction transport modelling and not by geochemical *in situ* observations alone.

Part II

Anammox at Site U1419

4. Anammox and the oxygen deficient zone in the Gulf of Alaska during Late Glacial Maximum

4.1 Introduction

Along continental margins, Oxygen Deficient Zones (ODZs) usually form when the oxygen demand from the re-mineralization of organic matter (OM) exceeds its re-supply by ventilation. Thus, dissolved oxygen is eventually depleted in part of the water column. Reasons for that can be massive inputs of OM and/or insufficient mixing of the water column. These conditions are relatively common in restricted basins or estuaries, but also in the open ocean in western boundary current upwelling areas (e.g. off the western coasts of Africa, India, and the Americas; Paulmier and Ruiz-Pino, 2009). Oxygen limitation in ODZ sediments leads to the enhanced preservation of OM. As such, ODZs play a key role in the global carbon cycle by increasing the long-term removal of carbon from the ocean-atmosphere system into seafloor sediments. Global climate change will reduce the ability of the ocean to take up oxygen with increasing water temperature and ocean areas affected by ODZ conditions are believed to spread in the future (Oschlies et al., 2008; IPCC, 2014). This can have severe impacts on both humans (e.g. by affecting fisheries) and global biogeochemical cycles (e.g. by increasing organic carbon burial but also the loss of the essential nutrient nitrogen from the ocean). To assess how ODZs might behave under future climatic conditions, it is essential to understand their reactions to past climate changes.

The modern Gulf of Alaska (Figure 4.1; GOA) exhibits an ODZ between 670 and 1060 m water depth (Moffitt et al., 2015). Under current climatic conditions, this ODZ is most pronounced during spring and autumn, is present in winter, and disappears during summer (Paulmier and Ruiz-Pino, 2009). While the present behaviour of the ODZ in the GOA is well-constrained, its extent and intensity during the last glacial cycle is not fully understood. For the wider North Pacific area, ODZ paleo-records exist as far back as ~70 ka (e.g. Cannariato and Kennett, 1999; Zheng et al., 2000; Cartapanis et al., 2011). However, for regions north of Vancouver Island, the ODZ behaviour is only resolved for the last 17 ka (McKay et al., 2005; Barron et al., 2009; Addison et al., 2012). No data exist for the Last Glacial Maximum (LGM, 33 - 26.5 ka BP; Clark et al., 2009) or the preceding interglacial (Marine Isotope Stage 3, 57-29 ka BP; Lisiecki and Raymo, 2005).

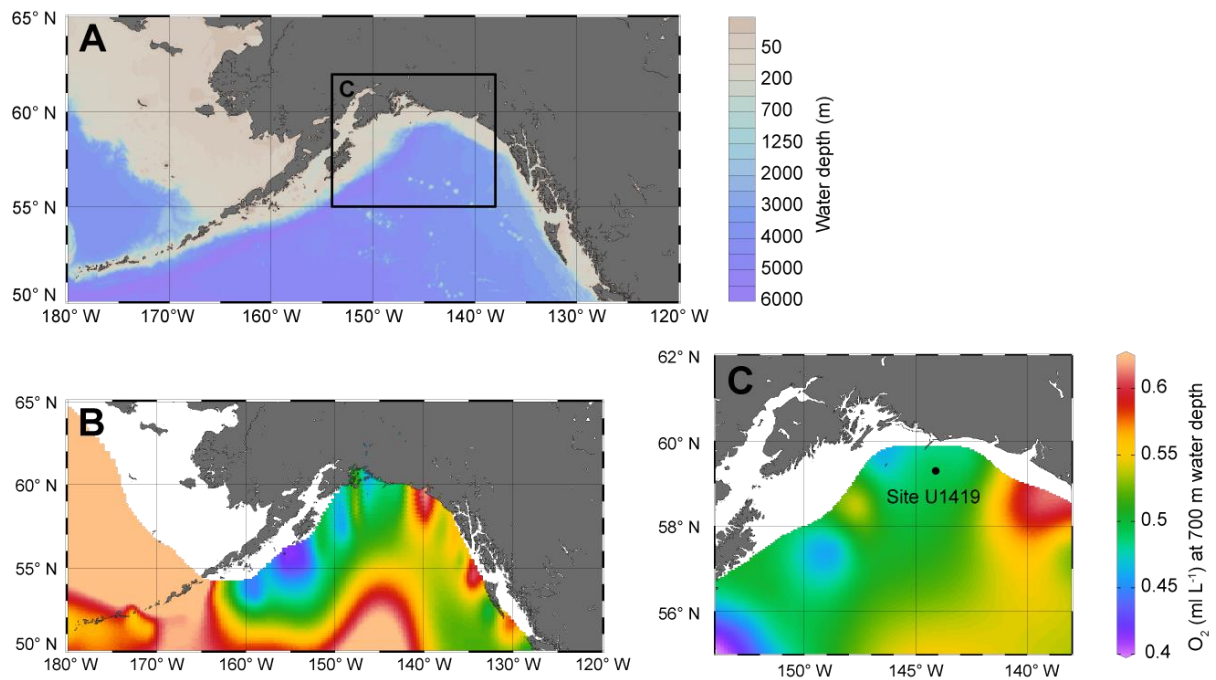


Figure 4.1: Area of investigation. **A)** Bathymetric map **B)** Annually averaged oxygen content (ml L^{-1}) in the Gulf of Alaska at 700 m water depth (Site U1419: 721 m); **C)** Position of Site U1419 within GOA ODZ (Map created with Ocean Data view; Schlitzer, 2015; O_2 data from World Ocean Atlas 2005; Garcia et al., 2006).

A number of studies (Cannariato and Kennett, 1999; Cartapanis et al., 2011) suggested that the North Pacific ODZ expanded during warmer periods (warm Dansgaard Oeschger (D/O) events, Bølling-Allerød, Holocene) and was less intense and extensive (or even not present) during cooler periods (cold D/O events, Last Glacial Maximum, Younger Dryas). It is not yet fully understood what caused these temporal ODZ fluctuations. Possible reasons include increased upwelling at the California margin that fuelled bioproductivity and thus oxygen consumption. Another possibility is increased water column stratification caused by changing ocean circulation in the northern parts of the North Pacific (McKay et al., 2005).

Reconstructions of past ODZ intensities have been approached in various ways. Many studies rely on the accumulation of redox sensitive trace metals (TM) which either precipitate as sulphides (or co-precipitate with pyrite) in the presence of hydrogen sulphide in sulfidic waters (e.g. Cu, Mo, Ni), or form less soluble species in sub- or anoxic waters (e.g. Cr, V and U; recent review by Calvert and Pedersen (2007)). Another approach to trace paleo-redox conditions at the seafloor is based on micropaleontology, specifically the diversity and speciation of benthic foraminifera (Bernhard and Reimers, 1991; Ohkushi et al., 2013).

Most studies on the North Pacific and GOA ODZs are based on the enrichment of TM in the sediments (e.g. Zheng et al., 2000; Cartapanis et al., 2014), the diversity and speciation of benthic foraminifera (e.g. Cannariato and Kennett, 1999; Ohkushi et al., 2013), and the occurrence of laminated sediments (e.g. Ortiz et al., 2004). Only one study (Nakakuni et al., 2017) in the North Pacific ODZ is based on biomarker lipids (stanol to sterol ratios).

ODZs play an important role in the global N cycle. Nitrogen fixation, denitrification and nitrous oxide (N₂O) production have been shown to be significantly enhanced under low oxygen conditions (Codispoti et al., 2001; Lam and Kuypers, 2011). Anaerobic ammonium oxidation (anammox) is a process by which specific bacteria (i.e. anammox bacteria) use nitrite to oxidize ammonium to N₂ gas, which is subsequently lost from the ocean to the atmosphere (Mulder et al., 1995; Van de Graaf et al., 1995). The anammox process occurs in marine sediments and ODZs (Kuypers et al., 2003; Hamersley et al., 2007; Lam and Kuypers, 2011; Pitcher et al., 2011), and it has been proposed to account for 29 % of total oceanic nitrogen loss (Ward, 2013). Important within the context of this study, anammox bacteria are inhibited by the presence of oxygen in the ambient seawater. Dalsgaard et al. (2014) report 50% inhibition at ~900 nM O₂, while the influence of hydrogen sulfide on the anammox process is still unclear (Dalsgaard et al., 2014; Lipssewers et al., 2016). Hence, molecular evidence of past anammox recorded in marine sediment cores can be applied as a proxy to reconstruct past ODZ dynamics.

Traditionally, ladderane lipids have been used as a biomarker for anammox (e.g. Kuypers et al., 2003; Jaeschke et al., 2009 a,b), but these molecules are relatively labile in the sedimentary record (Jaeschke et al., 2008). Bacteriohopanepolyols (BHP) are terpenoids which are synthesized by bacteria. In the sediment record they can be used as biomarker lipids for specific processes and environmental conditions (e.g. Rohmer et al., 1984; Summons et al., 1999; Talbot et al., 2001; van Winden et al., 2012; Berndmeyer et al., 2013). The bacteriohopanetetrol (BHT) lipid and its stereoisomer (BHT isomer) are synthesised by anammox bacteria (Rush et al., 2014). BHT is ubiquitous in marine sediments and is produced by a diverse range of bacterial species. However, anammox bacteria are the only known marine source for the BHT isomer, and this lipid has already been used as a biomarker for anammox in an ODZ setting (i.e. Chilean Margin; Matys et al., 2017). A ratio between total BHT and BHT isomer can be used to determine the contribution of anammox

bacteria relative to all BHT-producing bacteria in marine environments (Matys et al., 2017). BHPs are generally well-preserved in marine sediments (Rush et al., 2014). Hence, BHP biomarkers are applicable in much older sediments than ladderanes. Furthermore, BHP analysis is much more common in organic geochemical laboratories (e.g. Pearson et al., 2001; Sturt et al., 2004; Talbot et al., 2001, 2008), compared to ladderane lipids. Therefore BHT isomer biomarker can be used as an alternative biomarker to ladderanes to infer the presence of past ODZs.

This study is the first to combine BHT biomarker data with inorganic redox and bioproductivity proxies to establish a ~50 ka record of past ODZ behaviour. Different organic and inorganic paleo-redox proxies are directly compared and a new dataset is presented to highlight the potential of the BHT-isomer biomarker, to provide a note of caution against the uncritical use of certain TM records in very high sedimentation rate settings, and to discuss how oxygen depletion in the GOA was linked to global climatic patterns in the late Pleistocene.

4.2 Methods

For this study, sediment samples from IODP Expedition 341, Site U1419 in the Gulf of Alaska (Figure 4.1) have been used. The investigated sediment record spans the time between 15 and 55 ka (6 – 90 m CCSF-B) as for this segment the age model is confirmed (Walczak, pers. comm.). All depth information in this chapter will be given in mbsf (meters below seafloor) on the CCSF-B depth scale (Jaeger et al., 2014).

A total of 114 samples were taken (on board and during the post-cruise sampling party) at an average depth resolution of ~1.3 m. All samples were freeze-dried and homogenized using an agate mortar and pestle or an agate ball mill.

All 114 samples were analysed for Al and trace metals (Cr, Cu, Ni and V). A subset of 55 samples was analysed for BHPs, TOC and TS and a subset of 23 samples was analysed for K, Mg, Mo, Si and U.

Anammox Biomarker - Lipid Extraction

Lipids were extracted using a modified Bligh and Dyer extraction (Bligh and Dyer, 1959; Cooke et al., 2009). Briefly, ~3 g of freeze-dried sediment was extracted using 19 ml of a H₂O/MeOH/Chloroform solution (4:10:5; v:v:v). This mixture was sonicated for 15 min at 40°C and centrifuged at 12,000 rpm for 15 min. The supernatant was collected and the extraction procedure was repeated twice. Then, the chloroform and the aqueous phase in the supernatant were separated by adding water until a H₂O:MeOH ratio of 1:1 (v:v) was reached. The chloroform phase containing the total lipid extract was removed and this step was repeated twice more. The Bligh-Dyer extract was subsequently dried by rotary evaporation. A known amount of 5 α -pregnane-3 β ,20 β -diol internal standard was added to the extracts. They were then acetylated in 0.5 mL of 1:1(v:v) acetic anhydride and pyridine mixture for 1h at 50°C, then overnight at room temperature. For liquid chromatography analysis, the lipid extracts were dissolved in 1ml MeOH/propan-2-ol (60:40 v:v).

Anammox Biomarker - Lipid analyses

BHT and BHT isomer were analysed by high performance liquid chromatography coupled to positive ion atmospheric pressure chemical ionization mass spectrometry HPLC/APCI-MSⁿ. The standard error of this method was \pm 20% checked on triplicate analyses of every 10th sample and triplicate extractions of one sample. However, one triplicate analysis with very low BHT content caused a standard error of 42 %. The results are presented as a ratio between BHT isomer and total BHT. Both compounds are assumed to degrade in the same way during diagenesis. By this practise, misinterpretations which can arise from absolute concentration changes of BHT isomer during organic matter degradation, are excluded. The ratio approach makes the BHT isomer a robust proxy against diagenetic alteration and dilution by detrital background.

To exclude the possibility of a terrigenous source of BHPs, lipid extracts were also screened for soil marker BHPs (Zhu et al., 2011). These compounds were only found in low abundance below quantification limit in 4 samples, indicating the BHTs derived from a marine source. Here, only the BHT isomer vs BHT_{tot} ratio is discussed as interpretation of anammox and the absence of oxygen in the GOA ODZ from 50 to 15 ka BP.

Inorganic geochemistry

For 23 samples, wavelength-dispersive XRF (Panalytical Axios max, 4 kW) was used. 700 mg of sample were mixed with 4200 mg di-lithiumtetraborate, pre-oxidized with 1 g ammonium nitrate at 500° C, and fused to homogenous glass beads. Root mean squared error of this method was <1% for all major elements and <10ppm for all minor elements except Ni (13ppm). Precision for the inhouse standard was <0.5 rel% for all major and <10 rel% for all minor elements except for U (16 rel%).

For 91 samples, an Element 2 ICP-MS has been used. Analytical uncertainty was better than $\pm 5\%$ for all elements (Kamenov et al., 2009; Penkrot et al., 2018).

The reason for using two different methods for bulk element geochemistry was that in order to increase resolution, datasets from two different research groups were combined. Where one element was analysed by both XRF and ICP-MS, the results are combined into one dataset. Comparability of the analysis has been established by comparing averages and co-plotting results of individual elements.

Total organic carbon (TOC) was analysed using a Leco combustion analyser. Reproducibility was better than 5 % as checked on duplicates of every 10th sample.

XRF and ICP-MS data as well as TOC are presented as weight percent of dry sediment (wt%) or element/Al ratios (wt%/wt% or ppm/wt%).

4.3 Results

General sediment composition

The general geochemical sediment composition is fairly uniform over the length of the core. Silicon makes up for about 27 wt% of the sediment, and Al about 8 wt%. The Si/Al ratio, an indicator for either coarse-grained sediment components or biogenic silica, is stable around 3.3 which is slightly above the average shale (AS; Wedepohl, 1971; 1991) value of 3.1. This indicates that no consistent enrichments in biosilica or sand exist in the sediments. Average shale does not necessarily provide the most suitable reference composition here. Recent research (Penkrot et al., in prep) has shown that the Chugach-Prince-William-Terrane is the

major sediment source to Site U1419. Table 4.1 shows average element values for the metamorphic rocks of the Chugach Terrane (CT, Barker et al., 1992) in comparison with average shale.

Table 4.1: Average element values for comparison material Average Shale (AS, Wedepohl, 1971; 1991) and Chugach Terrane (CT, Barker et al., 1992).

Element	Average Shale	As/Al	Chugach Terrane	CT/Al
Si	27.53 %	3.11	31.59 %	3.74
Al	8.84 %	-	8.45 %	-
Fe	4.83 %	0.55	2.94 %	0.35
Ca	1.57 %	0.18	1.45 %	0.17
K	2.99 %	0.34	1.94 %	0.23
Mg	1.57 %	0.18	1.45 %	0.17
Mn	0.09 %	0.01	0.08 %	0.01
Cr	90 ppm	10.18 ppm/%	63 ppm	7.46 ppm/%
Cu	45 ppm	5.09 ppm/%	38 ppm	4.50 ppm/%
Mo	1.3 ppm	0.15 ppm/%	-	-
Ni	68 ppm	7.69 ppm/%	33 ppm	3.91 ppm/%
U	3.7 ppm	0.42 ppm/%	2.1 ppm	0.25 ppm/%
V	130 ppm	14.71 ppm/%	-	-

The K/Al ratio varies between 0.17 and 0.21 and Mg/Al ranges between 0.2 and 0.3. Arithmetic averages and AS values for these elements are: K: 1.54 and 2.99 and Mg: 2.08 and 1.57 (these data are not shown). Hence, Mg exceeds AS values, whereas K falls below AS concentration. Both are closer to the values of the CT material (Barker et al., 1992). TOC content (Figure 4.4) is on average 0.53 and ranges between 0.32 and 0.82 over the whole record.

Bacteriohopanetetrol Lipids

As described above, the ratio between BHT isomer and total BHT is a robust proxy and insensitive to changes in detrital background. The ratio spans from 0 (absence of BHT isomer) to 0.69 and averages at 0.22. The highest peak occurs at 83.31 m CCSF-B/46.8 ka BP.

Secondary peaks can be found at 71.28 m/41.1 ka BP, 62.38 m/37.7 ka BP, 36.51 m/28.6 ka BP and 18.23 m/16.8 ka BP (Figure 4.2).

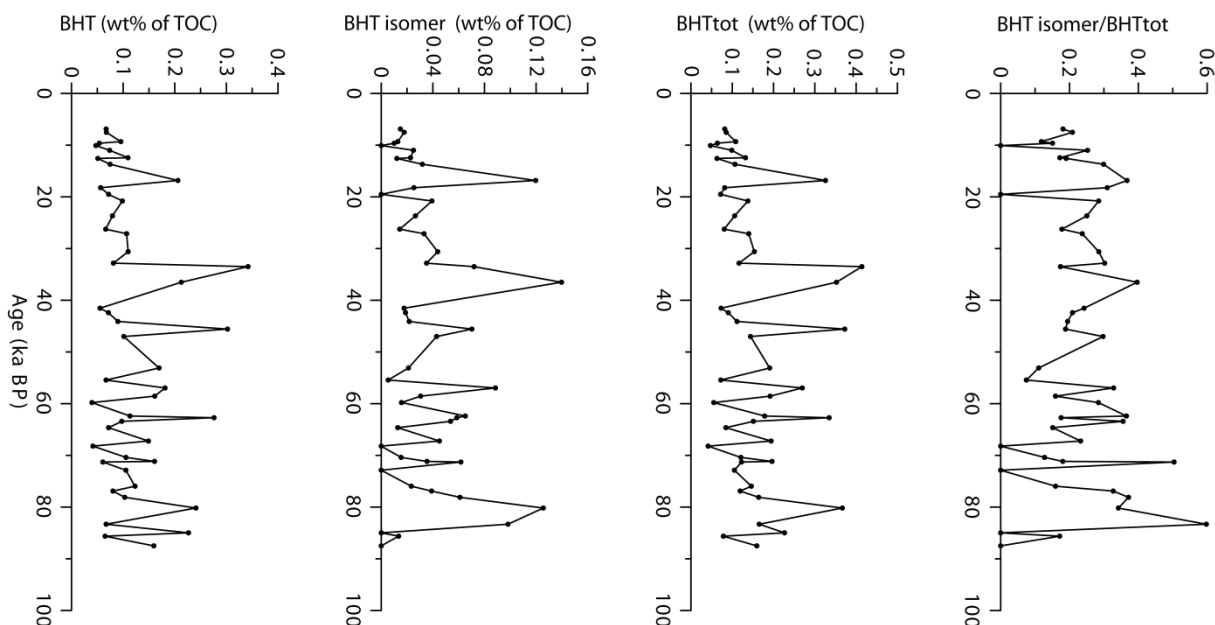


Figure 4.2: Components of BHT isomer biomarker. BHT, BHT isomer, BHTtot (BHT+BHT isomer (all as wt% of TOC), BHT isomer/BHTtot (as wt%/wt%).

Inorganic redox proxies

No long-term trends are observable in the TM records (Figure 4.3). Average contents are 6 wt% Fe, 102 ppm Cr, 45 ppm Cu, 44 ppm Ni and 171 ppm V. Iron, Cr and V are slightly above the AS values (4.8 wt % Fe, 90 ppm Cr, 130 ppm V) but Fe and Cr are below CT. Copper is equal to AS (45 ppm) and Ni is lower than AS (68 ppm). Both, Cu and Ni are higher than the CT background. Element/Al ratios for the above mentioned TM are (Average, Min, Max) Fe %/% (0.69, 0.58, 0.82), Cr ppm/% (11.8, 8.7, 14.9), Cu ppm/% (5.2, 3.6, 7.7), Ni ppm/% (5.1, 3.8, 6.7) and V ppm/% (19.8, 15.4, 24.3).

Molybdenum and U contents have only been analyzed on 23 samples by XRF and are both close to quantification limit (detection limit U and Mo: 1 ppm; quantification limit U: 3 ppm, Mo: 2 ppm). This indicates no significant enrichment in the sediments. Molybdenum ranges from 0 - 3 ppm (Mo/Al = 0 - 0.4, Average = 0.1) and U varies between 1-6 ppm (U/Al = 0.1 - 0.7, Average = 0.4). Parts per million results for these elements are in discrete 1 ppm steps due to proximity to quantification limit. In most samples Mo and U contents lie below AS (Mo: 1.3 ppm; U: 3.7 ppm) and around the CT background.

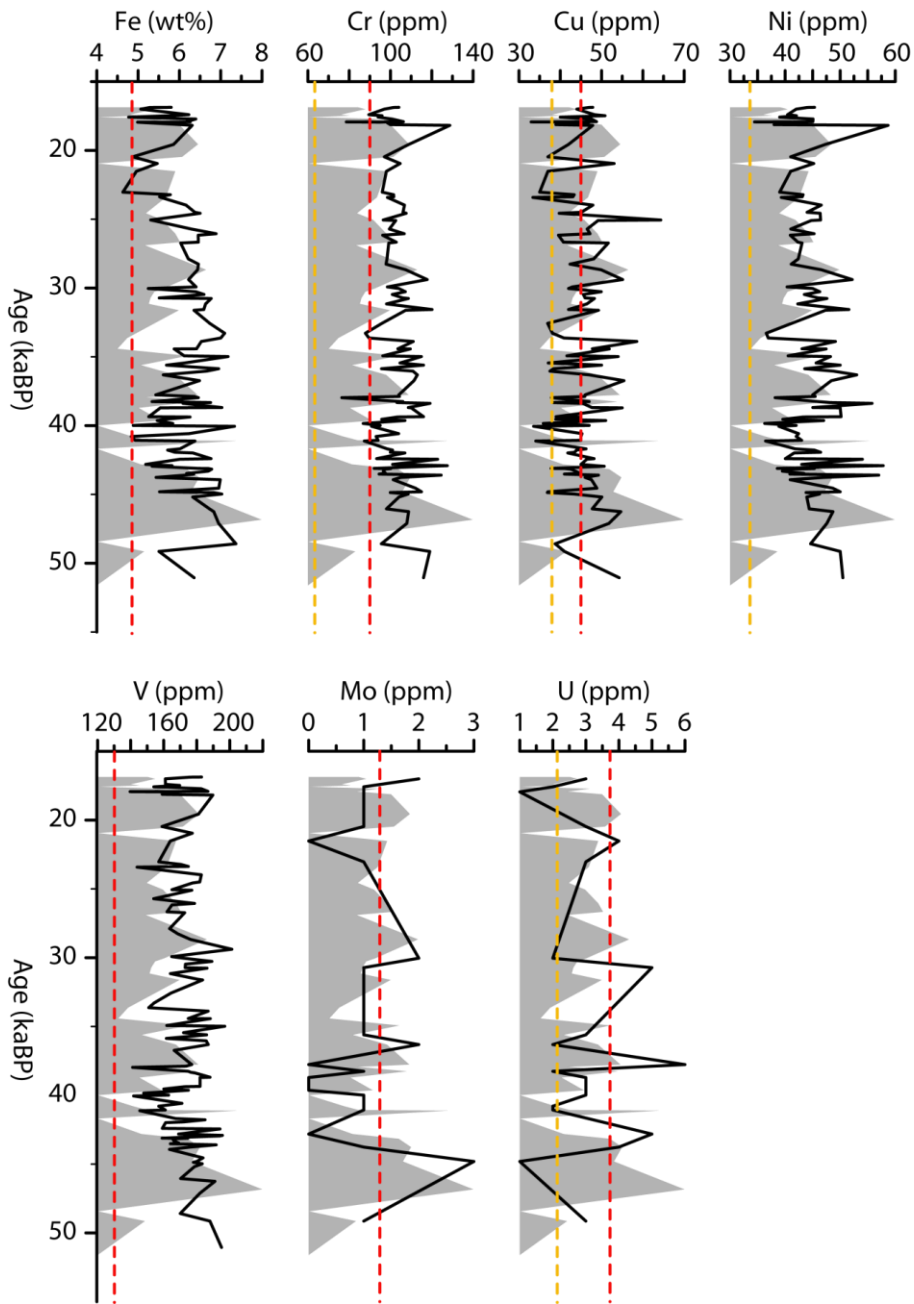


Figure 4.3: Inorganic geochemical data at Site U1419. Contents of Fe (wt%) and trace metals (wt ppm). Dashed red lines indicate average shale content (Wedepohl, 1971) except for Ni (out of range). Dashed yellow lines indicate Chugach Terrane content (Barker et al., 1992) except for Fe, (out of range), V and Mo (data not available). Shaded area in each plot is BHT ratio for comparison. Refer to Figure 4.2 for values.

4.4 Discussion

Anammox in the GOA in relation to northern hemispheric paleoclimate as recorded by NGRIP

Between 50 and 30 ka BP, northern hemispheric climate as recorded by the $\delta^{18}\text{O}$ signal of the NGRIP ice core followed a gradual cooling trend (Figure 4.4). This trend was interrupted by repeated several hundred to thousand year-long warming and subsequent cooling events, called Dansgaard/Oeschger Events (D/O Events; Dansgaard et al., 1983). After 30 ka BP, the climate warmed again until 17 ka BP. This warming episode was also interrupted by D/O Events which were, however, shorter and less extreme.

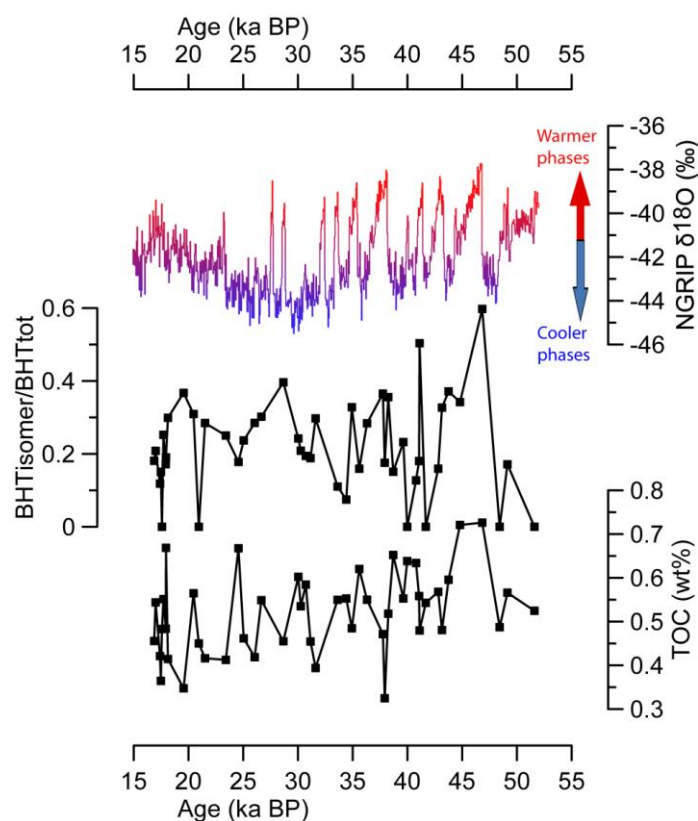


Figure 4.4: Organic geochemical data at Site U1419. From this study: $\text{BHT}_{\text{tot}}/\text{BHT}_{\text{isomer}}$, TOC (wt %), From (Rasmussen et al., 2014; Seierstad et al., 2014): $\delta^{18}\text{O}$ from NGRIP ice core as reference for Northern Hemispheric climate. Reddish colours in NGRIP $\delta^{18}\text{O}$ record indicate warmer periods, bluish colours indicate cooler phases, colours do not correspond to specific temperatures.

The BHT ratio, as a biomarker for anoxia, generally follows this global atmospheric temperature trend. Over the investigated period, the highest anammox peak in this GOA record occurs during a D/O event between 46.7 and 43.7 ka BP. Also anammox peaks at 41,

38, 35, 32, 28 and 19.5 ka BP coincide with warm phases of the NGRIP record (Figure 4.4). This confirms that the extent of oxygen deficiency in the GOA water column at Site U1419 was related to northern hemispheric climate conditions over the last glacial, as previously shown for the last deglacial in the GOA (McKay et al., 2005; Barron et al., 2009; Addison et al., 2012) and for the wider North Pacific area (Cannariato and Kennett, 1999; Zheng et al., 2000; Cartapanis et al., 2011). It has to be noted that the here-described peaks in NGRIP $\delta^{18}\text{O}$ and BHT isomer occur at slightly different ages deviating by a few decades. This makes it difficult to prove their relationship statistically, e.g. by crossplotting. The most plausible reason for this are the different age models of both cores. The age model for Site U1419 used in this study is still a preliminary one and deviations by a few years BP have to be expected.

The observed temperature-ODZ relationship could have been implemented by changes in OM deposition and/or a rearrangement of ocean currents. As TOC content and TOC/Al ratio do not systematically increase in intervals with higher BHT ratios at Site U1419 (Figure 4.5), there is no direct evidence for enhanced OM deposition during intervals with a more intense ODZ (as indicated by the BHT ratio). However, the TOC record could have been overprinted by early diagenetic degradation; in fact, this is highly likely as the very process creating oxygen deficiency in the water column is its consumption by OM degradation. Increased OM input from land was suggested by Addison et al. (2012). The authors propose that rising sea levels could have introduced nutrients from the shelves. This assumption was made for the last deglaciation (Addison et al., 2012). Whether the same process of nutrient mobilisation also occurred during minor sea level changes related to D/O Events is questionable. Also, even during warmer D/O Events, the continental margins along the GOA were likely fully glaciated (Montelli et al., 2017). Melting glaciers could have introduced Fe into the ocean and thus fertilized marine phytoplankton blooms (Raiswell et al., 2006; Statham et al., 2008). The Fe/Al record at Site U1419 possibly supports this theory, but the signal is not very clearly expressed (Figure 4.6). Praetorius et al. (2015) noted that increasing hypoxic conditions could have led to a release of Fe^{2+} from the sediments. This process would have overprinted the original Fe record and potentially masked a clear primary signal. No distinct indicator for increased bioproductivity, such as elevated TOC or Si/Al contents can be found during times of intensified oxygen deficiency at Site U1419. Therefore, it is also possible that oxygen

limitation was caused by limited oxygen supply to the mid-water masses through stronger thermohaline stratification in the GOA rather than by enhanced consumption from OM decomposition. This theory has also been put forward by Cartapanis et al. (2011, 2012) who proposed a re-organization of global ocean circulation and teleconnections as a reason for this, as well as changes in stratification due to freshwater input during glacier melting events.

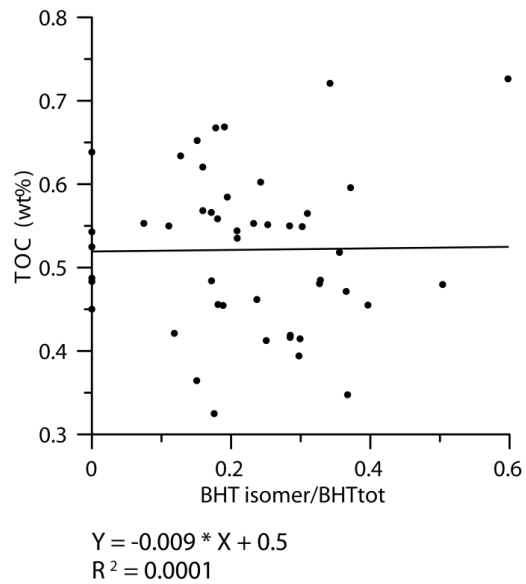


Figure 4.5: Crossplot of BHT/BHTisomer versus TOC (in wt%). Black line indicates fit. Formula of fit and coefficient of determination (R^2) given below plot.

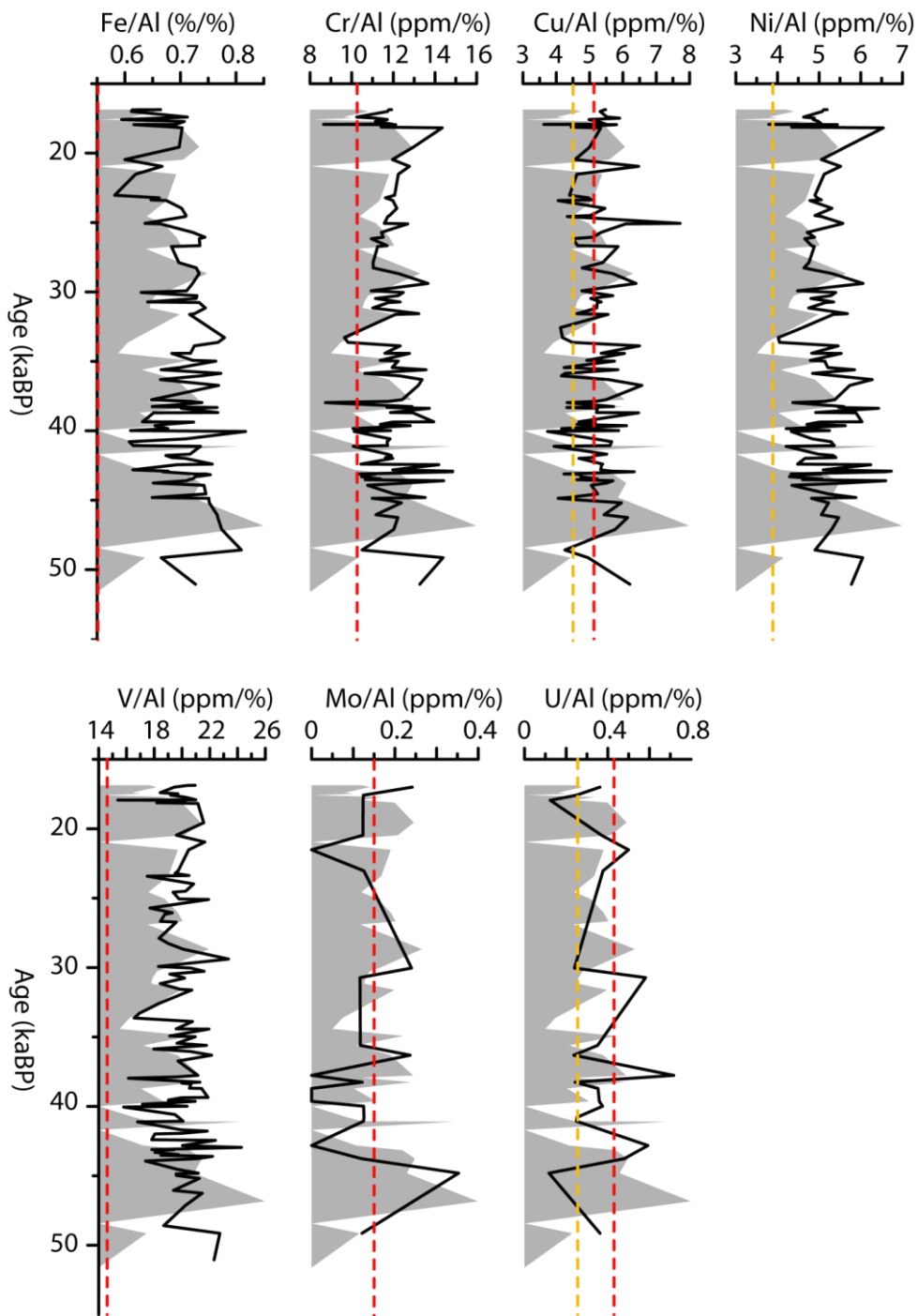


Figure 4.6: Element/Al ratios for inorganic geochemical data at Site U1419. Ratios of Fe/Al (wt%/wt%) and trace metal/Al (ppm/%) and. Dashed red lines indicate average shale content (Wedepohl, 1971) expect for Ni/Al (out of range). Dashed yellow lines indicate Chugach Terrane content (Barker et al., 1992) expect for Fe/Al and Cr/Al (out of range), V/Al and Mo/Al (data not available). Shaded area in each plot is BHT ratio for comparison. Refer to Figure 4.2 for values.

ODZ behaviour recorded by redox sensitive trace metals

A range of TM as well-established inorganic proxies for ODZ intensity and bottom-water redox conditions was analysed. However, no good match between BHT/BHT isomer ratio and any of the TM records, and consequently between NGRIP $\delta^{18}\text{O}$ and TM, can be observed (Figures 4.6 and 4.7).

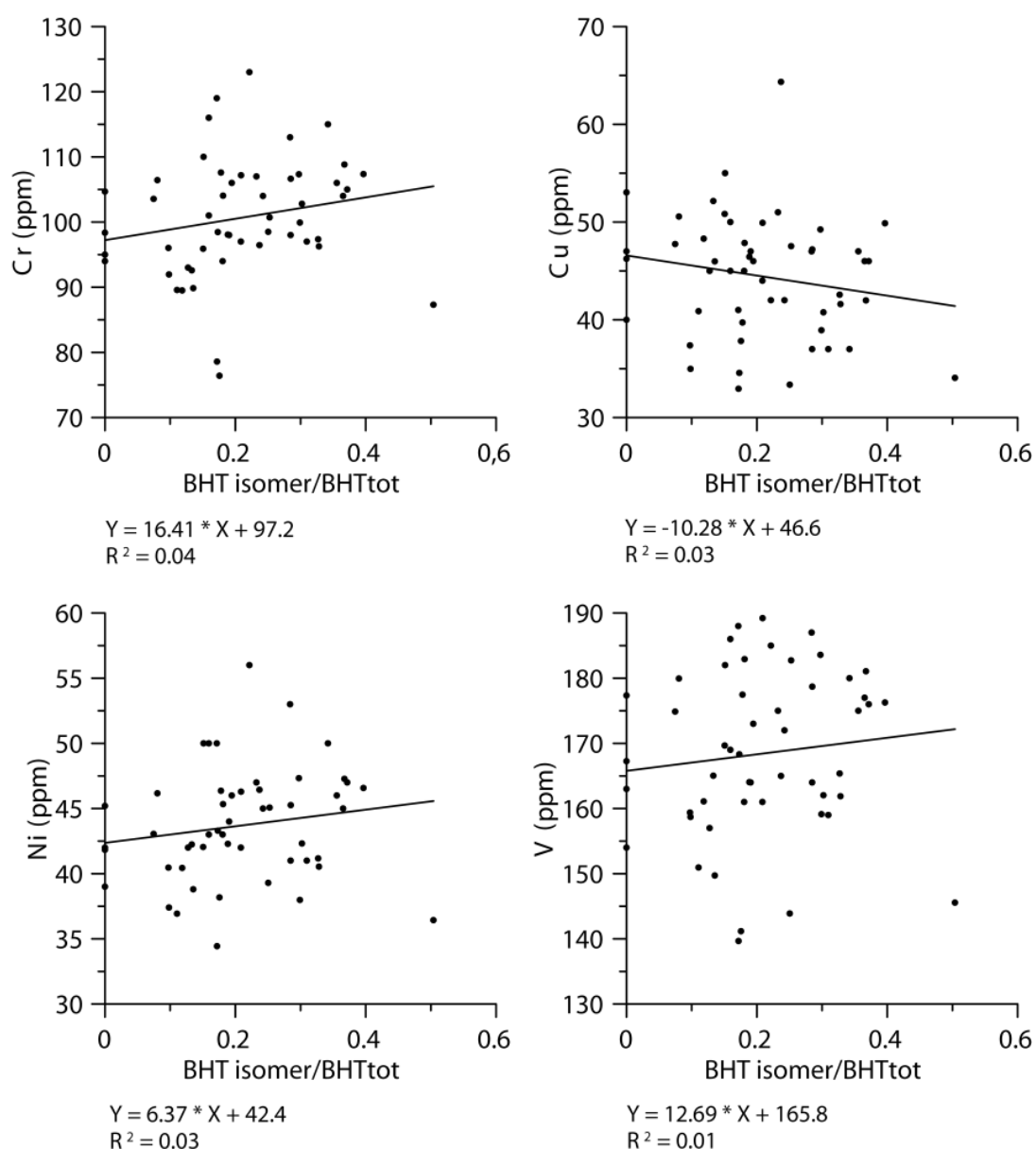


Figure 4.7: Crossplots of BHT/BHTisomer versus trace metals (all in ppm). Formula of fit and coefficient of determination (R^2) given below each plot.

Two of the most commonly used TM for paleo-redox reconstructions are Mo and U. Both elements have not been analysed in sufficient resolution to match their pattern directly to

the anammox record or the NGRIP $\delta^{18}\text{O}$ record. However, their contents are close to XRF quantification limit over the whole record and below AS values (Wedepohl, 1971; 1991) in most samples, implying no significant enrichment of these TM due to water column anoxia (Figure 4.6). With 0 - 3 ppm and 1 - 6 ppm, the enrichments of Mo and U, respectively, are similar to values recorded at other sites along the NP margin. For comparison, McKay et al. (2005) reported enrichments of up to 3.7 ppm for Mo and up to 5.8 ppm for U in sediments deposited under anoxic conditions off Vancouver Island. In modern sediments of the ODZ in the Arabian Sea, U enrichments exceed 12 ppm (Sirocko et al., 2000). Van der Weijden et al. (2006) reported U/Al ratios exceeding 2 ppm/% and Mo/Al ratios exceeding 4 ppm/% from the ODZ in the Arabian Sea, and Acharya et al. (2015) conclude that average U contents of 4.1 ppm indicate an oxic depositional environment.

Uranium exists as U(VI) in oxic seawater and is reduced to U(IV) in nitrogenous (= suboxic) waters. Uranium(IV) is less soluble than U(VI) and precipitates from the water into solid phases. In oxic bottom-waters, this reduction process happens within the nitrogenous (suboxic) parts of the sediment, and U is provided through diffusion across the sediment-water interface (Klinkhammer and Palmer, 1991). If U is mostly provided by diffusion from seawater, the authigenic U accumulation in the sediment is diluted by the input of detrital material. Higher detrital sedimentation rates can mask the authigenic U accumulation so that no significant enrichment is observable even below an anoxic water column (Klinkhammer and Palmer, 1991).

Sedimentation rates at Site U1419 are exceptionally high, nearly constantly exceeding 200 cm ka^{-1} , and episodically exceeding 600 cm ka^{-1} , translating into mass accumulation rates (MAR) between 120 and 900 $\text{g cm}^{-2} \text{ka}^{-1}$ in the studied time period (Figure 4.8). For comparison, the sites in the ODZ in the Arabian Sea with higher U and Mo contents have an order of magnitude lower sedimentation rates of 17 cm ka^{-1} (Acharya et al., 2015) and mass accumulation rates of $<20 \text{ g cm}^{-2} \text{ka}^{-1}$ (van der Weijden et al., 2006). Taken together, these data support the notion that sedimentation rates can control the degree of sedimentary U accumulations even under sub- to anoxic bottom-water conditions.

This can further be tested by a simple "back-of-the-envelope" calculation with numbers from McManus et al. (2005), who calculated a removal of $2.0 \times 10^{-10} \text{ mols U cm}^{-2} \text{a}^{-1}$ for an exemplary environment within the ODZ at the California Margin. Transferred to the average

mass accumulation rate at Site U1419 of $\sim 400 \text{ g cm}^{-2} \text{ ka}^{-1}$, this would only cause a 0.119 ppm change in U concentration in the here-deposited sediments. The suboxic U accumulation process is hence not significant under high sedimentation rates.

Molybdenum is mainly enriched in the sediments under sulfidic conditions where it reacts with H_2S to form Mo-S species (Helz et al., 1996; Erickson and Helz, 2000) or is incorporated into authigenic pyrite (Morse and Luther, 1999). These processes are controlled by the availability of H_2S which is produced by bacterial sulphate reduction. As anammox occurs in sub- to anoxic but non-sulphidic waters (although the influence of H_2S is not yet conclusively constrained; Dalsgaard et al., 2014; Lipssewers et al., 2016), it is possible that the water column at Site U1419 was never fully sulphidic. While Mo is not a tracer for a suboxic (i.e. nitrogenous) water column (Calvert and Pedersen, 2007), its accumulation in sediments can be more efficient under such mildly reducing bottom-water conditions as H_2S is generated closer to the sediment-water interface and, hence, to the dissolved Mo source. In this case, higher sedimentation rates would also lead to a lower enrichment of Mo because less H_2S will be produced in a specific sediment layer and less Mo will get fixed in authigenic phases (Sundby et al., 2004).

The element/Al ratios of Cr, Cu, Ni and V show some similarities to the BHT ratio (Figure 4.6), but these relationships are not systematic nor constant throughout the record. The BHT ratio only matches Cr and V between 35 and 25 ka BP, and Cu and Ni between 40 and 30 ka BP. From the abundances of these TM and their missing match to the NGRIP record, no presence of an ODZ would have been concluded at Site U1419 during the studied time period.

Similar to Mo, the enrichment of Cu and Ni is associated with sulphidic conditions. These elements are incorporated into pyrites or form sulphide minerals on their own (Huerta-Diaz and Morse, 1992; Morse and Luther, 1999) and hence would also only be significantly enriched if the bottom-waters were sufficiently sulfidic.

The inhibition of TM accumulation by high detrital sedimentation rates described above for Mo and U should also prevent the accumulation of Cr, Cu, Ni and V that tend to be enriched in sediments under suboxic to sulfidic conditions (Huerta-Diaz and Morse, 1992; Tribouillard et al., 2006). However, Cr, Cu and V contents at U1419 are on average slightly above AS

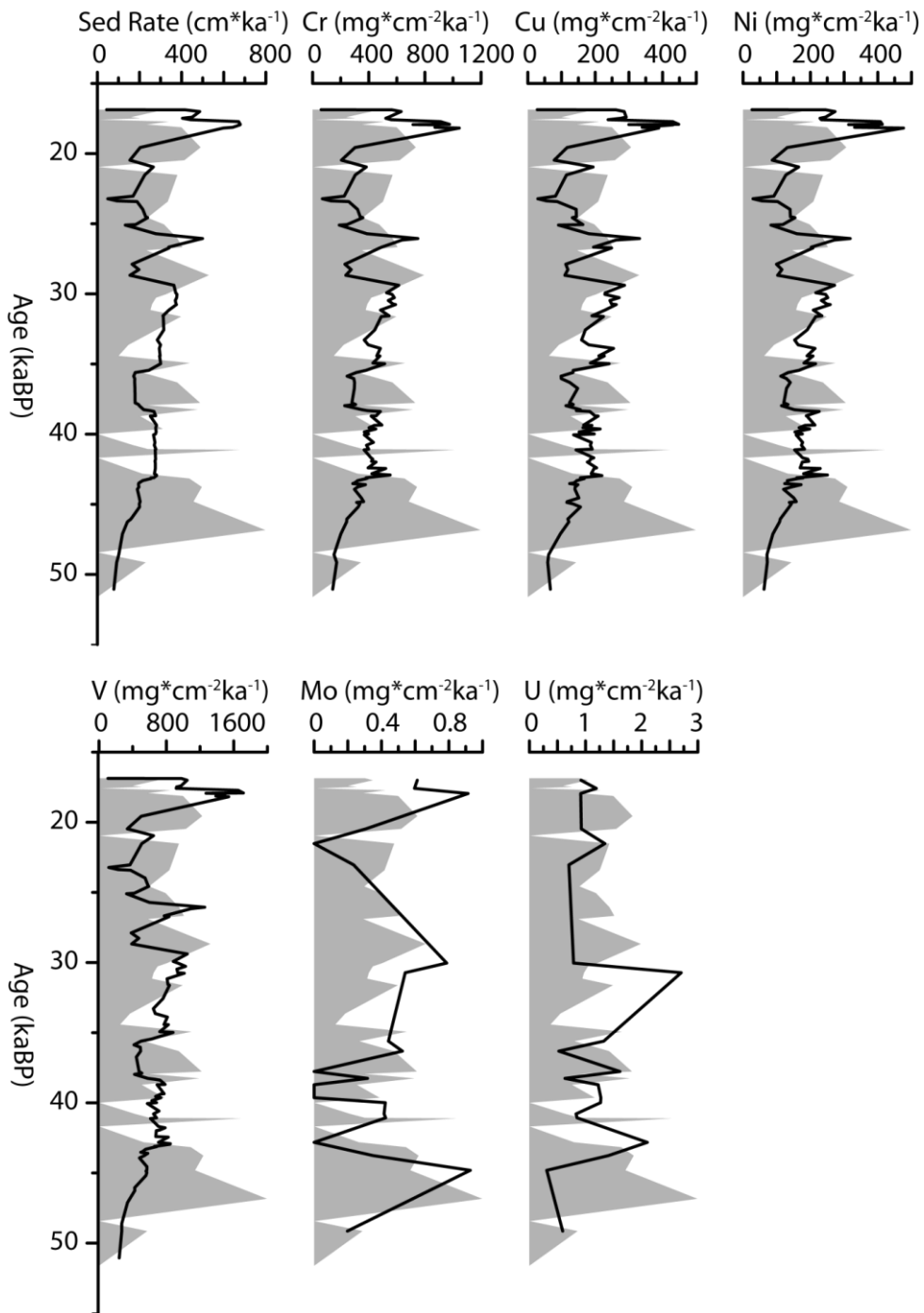


Figure 4.8: Accumulation rates of inorganic geochemical sediment components at Site U1419. Sedimentation rate in $\text{cm}\cdot\text{ka}^{-1}$, element accumulation rates in $\text{mg}\cdot\text{cm}^{-2}\cdot\text{ka}^{-1}$. Shaded area in each plot is BHT ratio for comparison. Refer to Figure 4.2 for values.

(Wedepohl, 1971; 1991) and only Ni is depleted. In comparison to the CT background material, Cr at Site U1419 is lower while Cu and Ni are slightly higher. Furthermore, the individual accumulation rates for these TM follow the trends in sediment accumulation rate and Al content (Figure 4.8), whereas the amounts (in wt ppm of dry sediment) of these elements in the sediments are unrelated to sedimentation rate (i.e. higher sedimentation rates do not lead to dilution of the elements; Figure 4.9). This indicates that slightly elevated TM contents are unrelated to redox conditions, but instead have significant detrital contributions from lithologies on land with higher contents of these TMs than AS. Differences from the CT values (Table 4.1) may arise from admixture of secondary source materials (Penkrot et al., in press) or sorting processes during transport and deposition. Elevated Mg and lower K contents relative to AS indicate some mafic contribution to the detrital background (Le Maitre, 1976). Both Mg and K contents are much closer to CT than to AS, supporting this hypothesis. It can be concluded that any redox-related accumulation of Cr, Cu, Ni and V was prevented at U1419 by high background sedimentation rates (as for Mo and U), but that this background material had slightly elevated Cr and potentially V contents (V not reported in Barker et al., 1992) that were imprinted onto the newly deposited sediments.

Copper and Ni, which are both enriched in our sediment samples relative to the CT material, also play a role as micronutrients during primary production (Boyle et al., 1977; Böning et al., 2015; Steiner et al., 2017) and are removed from the water column by OM deposition. Hence, they can also be affected by changes in bioproductivity (Nameroff et al., 2002). Yet, it has to be noted that Cu and Ni do not show an observable relationship to TOC (Figure 4.10). Due to the general low amount of OM this process is probably negligible at Site U1419. The Ni depletion relative to AS is another indicator that deoxygenation was probably not driven by enhanced TOC export to the seafloor.

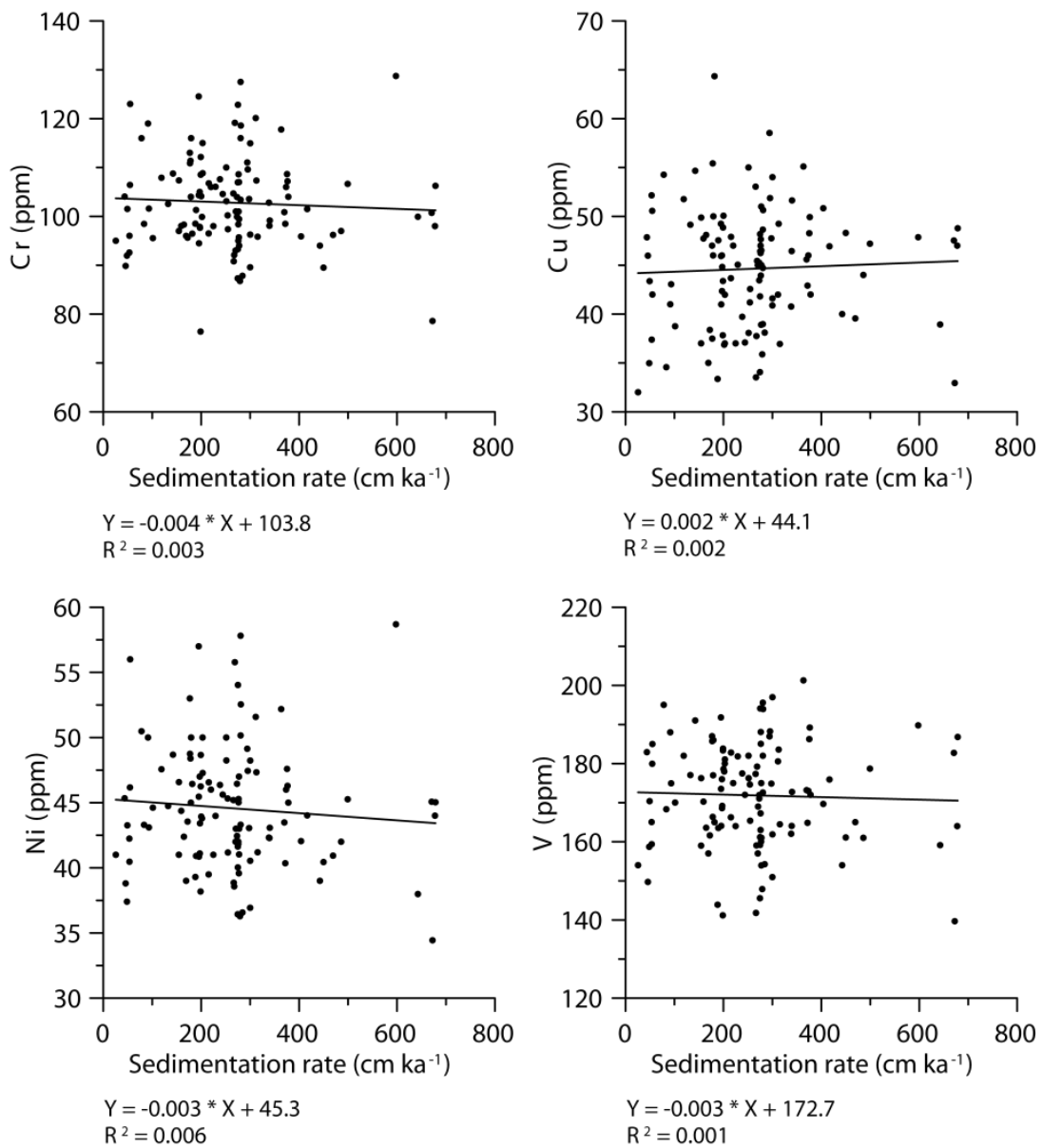


Figure 4.9: Crossplot of sedimentation rate at Site U1419 (in cm*ka⁻¹) versus TM content (in ppm). Black line indicates fit. Formula of fit and coefficient of determination (R²) given below each plot.

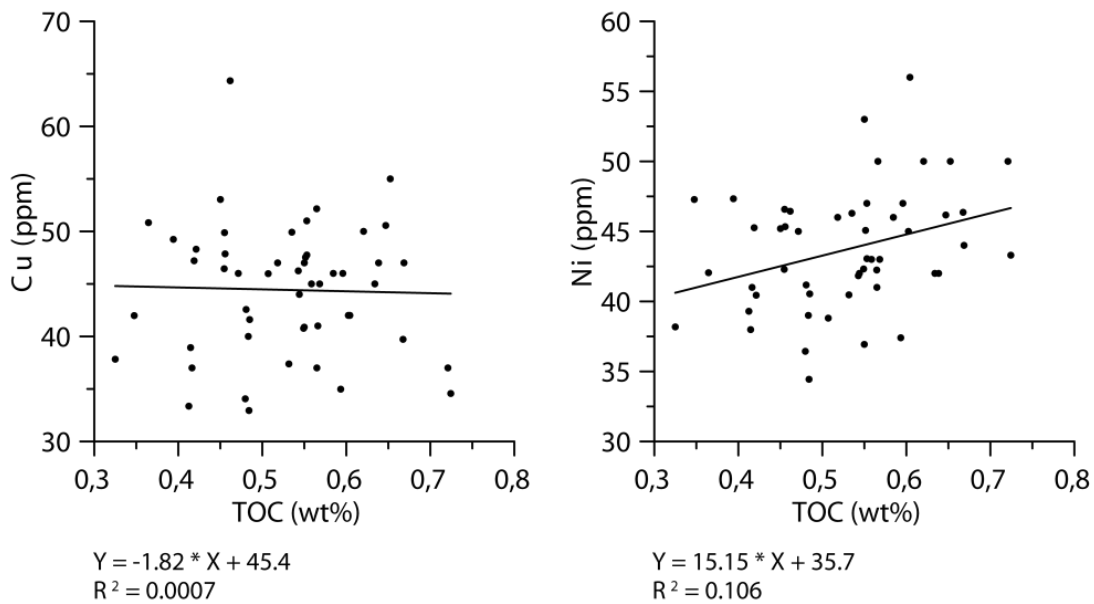


Figure 4.10: Crossplot of TOC (in wt%) versus Cu and Ni (in ppm). Black line indicates fit. Formula of fit and coefficient of determination (R^2) given below each plot.

Influence of diagenesis on TM records

The SMTZ at Site U1419 lies in 18 mbsf (Figure 1.7). It is well-expressed and no sign of non-steady state diagenesis can be found. This depth corresponds to 20 ka BP. Therefore all redox sensitive elements below this depth can be reworked by diagenetic dissolution or authigenic mineral formation. This process might have overprinted the original TM records and potentially flattened previously existing peaks corresponding to ODZ maxima.

Furthermore, to some extent OM degradation has to be assumed. However, under the high sedimentation rates at Site U1419, a certain degree of OM preservation can be expected.

Degradation of OM will not affect the BHT isomer biomarker, as it is a ratio calculated out of two similarly degrading compounds.

BHT isomer and TM records show an apparent discrepancy. Given that BHT ratio and the NGRIP $\delta^{18}\text{O}$ record agree with each other and also follow the pattern reported by other studies for the North Pacific and the GOA during deglaciation - general warming enhancing the ODZ and cooling leading to a less intense ODZ (Cannariato and Kennett, 1999; Cartapanis et al., 2011) - the BHT biomarker most likely records the intensity of the ODZ whereas redox sensitive TM records at Site U1419 are unreliable as paleo-redox proxies under a system influenced by high sedimentation rates. Caution has to be taken if TM are used as paleo-

redox proxies without further comparison to other indicators. Settings with high sedimentation rates such as at Site U1419, or variations in the geochemical composition of the detrital input, can lead to unreliable TM records (Tribovillard et al., 2006; Steiner et al., 2017). Also in environments which are not sufficiently reducing for H₂S production in the bottom-waters TM cannot effectively be enriched in the sediments. Processes occurring in and around ODZs and leading to the enrichment of TM and BHT biomarkers are depicted in Figure 4.11.

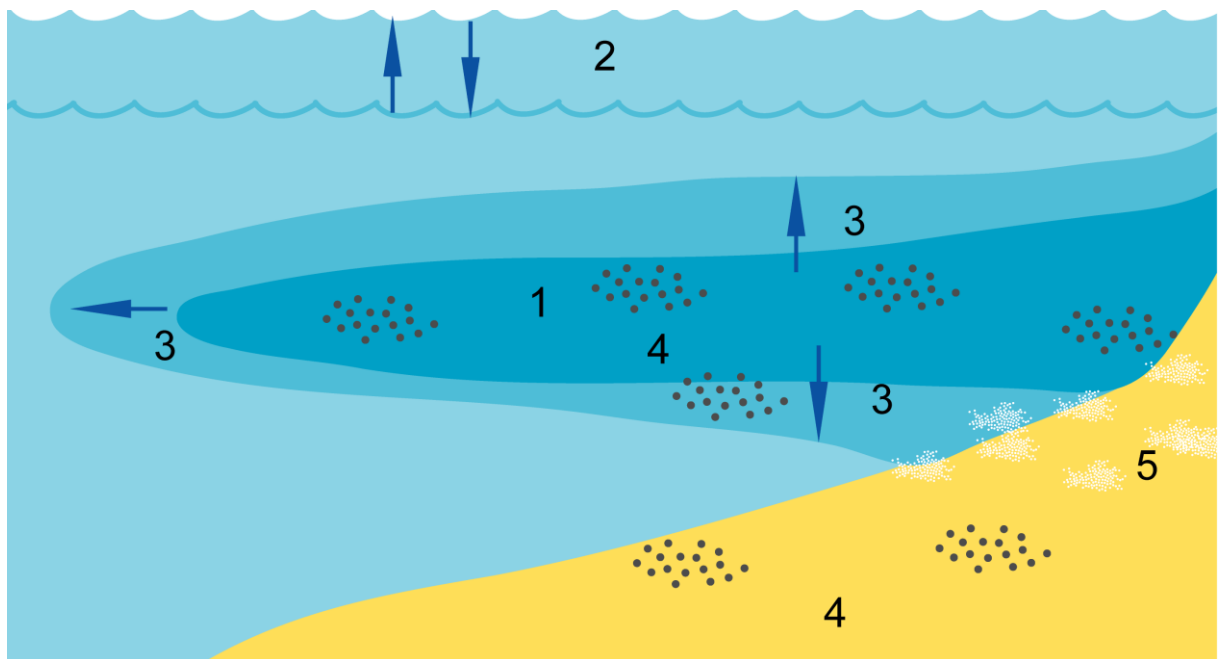


Figure 4.11: Schematic illustration of processes related to ODZ dynamics. 1. Oxygen deficient conditions in mid-water along continental shelves (dark blue). 2. Sea level fluctuations over glacial-interglacial transitions affecting sediment and nutrient supply to the shelf sea. 3. Horizontal and lateral expansion of ODZ (medium blue) in response to oxygen consumption and re-supply. 4. BHT isomer biomarker production (black dots) in ODZ and deposition below oxygen deficient waters. 5. Trace element accumulation (white dots) in zones with oxygen deficient conditions at the seafloor.

4.5 Conclusions

Sediment samples from Site U1419 in the Gulf of Alaska spanning the time between 50 and 15 ka BP were examined. The material was used to reconstruct anammox activity using the new BHT isomer biomarker and compare the results to redox-sensitive trace metal accumulations. The anammox biomarker record varies with northern hemispheric climate as recorded by Greenland ice cores. The fit between BHT ratio and NGRIP $\delta^{18}\text{O}$ was interpreted as a sign of northern hemispheric climate driving the extent and/or intensity of the ODZ in the GOA over the past 50 ka, much in the same way as it has been reported by previous studies across the North Pacific over the past 17 ka. The ODZ became more intense (less oxygenated) during warmer periods and less intense (better oxygenated) during colder ones. This is also another evidence for the applicability of the BHT-biomarker for the presence of anammox and its first application in a high latitude setting. Redox sensitive trace metals do not record the ODZ dynamics in the same way. Accumulations are minor compared to other sites in the North Pacific and in the Arabian Sea ODZ, and do not follow a clear trend. It is postulated that the high sedimentation rates at Site U1419 do not allow for the instalment of anoxic-sulfidic redox conditions close to the sediment-water interface, preventing the diffusion of U into the sediments and diluting any enrichments of Cu, Mo and Ni in authigenic phases. Changes in sedimentary provenance may have additionally compromised the enrichment patterns of Cr, Cu, Ni and V by delivering material with a composition different from average shale.

Chapter 4 will be submitted to Chemical Geology as:

“Anammox and the oxygen deficient zone in the Gulf of Alaska during Late Glacial Maximum”

Authors

Mark Zindorf, Darci Rush, John Jaeger, Helen Talbot, Alexandra Crawford, Frances Sidgwick, Thomas Wagner, Cees van der Land, Bernhard Schmetzer, Michelle Penkrot, Christian März

Abstract

Marine anaerobic oxidation of ammonium (anammox) plays a central role in the nitrogen cycle of modern Oxygen Deficient Zones (ODZs). The newly developed bacteriohopanetetrol stereoisomer (BHT isomer) biomarker for anammox, which is relatively unaffected by short-term diagenesis in sediments, allows for the reconstruction of the presence and dynamics of past ODZs along continental margins. In this study, we investigate the development and dynamics of the ODZ in the Gulf of Alaska (GOA) between 50 and 15 ka BP using sediment samples from IODP Site U1419. We combine records of redox sensitive trace metals (TM) and the BHT isomer anammox biomarker. The biomarker record indicates that the ODZ in the GOA was affected by global climate conditions in the late Pleistocene. Anammox was more pronounced during warmer periods and diminished during cooler periods, as indicated by correlation with the $\delta^{18}\text{O}$ signal of the NGRIP ice core. Trace metal enrichments, however, do not match the trend in BHT isomer and are not systematically enriched in sediment intervals where the biomarker record documents more intense water column deoxygenation. This proxy discrepancy might be caused by environmental factors other than water column redox conditions having a stronger influence on TM distribution in this specific depositional setting. The records of Cr, Cu, Ni and V can be affected by the provenance of the terrigenous sediment fraction, while Cu and Ni may also be impacted by primary productivity and marine organic matter deposition. Two of the most commonly used and reliable redox indicators, Mo and U, are not significantly enriched in any sample from Site U1419. Both of these TM normally accumulate in sediments under oxygen-deficient conditions by diffusion of their dissolved species across the sediment-water interface and fixation in authigenic phases. Site U1419 has experienced some of the highest sedimentation rates ever reported for late

Pleistocene continental margin sediments at ~700 m water depth, leading to the continuous and fast upward migration of the sediment-water interface. We therefore suggest that even despite bottom-water oxygen depletion, significant sedimentary enrichments of redox sensitive trace elements, like Mo and U, were prevented by a limited time for diffusion across the sediment-water interface and subsequent authigenic mineral formation. Similar discrepancies of organic and inorganic redox proxies could exist in other high sedimentation rate environments, potentially putting constraints on paleo-redox interpretations in such settings.

5. Synthesis

This work addresses various aspects of chemical processes affecting sediment composition at and below the seafloor both during and after deposition. Mineral dissolution, (re-)precipitation as well as element enrichments and depletions are driven by an interplay between climatologic, tectonic, oceanographic and biological influences. These processes can lead to contradictory signals in sedimentary records and overprint the original depositional signature. The PhD thesis "Paleoenvironment and post-depositional changes recorded in the chemical composition of marine sediments from the Gulf of Alaska" thus adds a contribution to a better understanding of the formation, and potential alteration, of geochemical proxies in marine sediments.

On a deep sea drill site with non-steady state sedimentation, a complex interplay between depositional, climatologic and tectonic factors can have a severe impact on the diagenetic overprint of a sediment succession. Site U1417 exhibits a complex diagenetic zonation with an exceptionally deep ~200 m sulphate penetration that does not develop into an SMTZ. Instead, sulphate and methane are separated by a ~200 m wide gap of sulphate- and methane-free sediments. Below this zone, methane is trapped under a carbonate layer which potentially acts as a caprock. Below the methanogenic zone, another sulphate-enriched zone exists, where pore-water sulphate diffuses from deeper sediment layers. Here, a well-expressed SMTZ develops and minerals, such as authigenic barite and pyrite, precipitate.

In Chapter 2, a set of geochemical proxies and calculations was applied to investigate the diagenetic zonation at Site U1417 and to test the plausibility of the different potential causes for the sulphate enrichment, which are (a) plate bending fault generation, (b) seawater conduits through outcrops at seamount flanks, and (c) an old buried pool of pore-water which still contains sulphate. New records of diagenetic mineral formation in response to early diagenetic reactions are presented. At Site U1417 pyrite, barite and carbonate form authigenic accumulations in delimited horizons in response to early diagenetic reactions. Biogenic barite dissolves in the zone of sulphate depletion and the Ba-profile is completely altered by re-precipitation in SMTZs. This makes Ba essentially useless as a paleoproductivity proxy as which it is often used (Von Breyman et al., 1992). Authigenic carbonates form a

caprock, potentially trapping methane underneath. The diagenetic pyrite profile is partly influenced by the supply of reactive Fe during deposition, but also by past fluctuations of SMTZs. Another important finding of Chapter 2 was that plate bending could be a working mechanism for the installation of a deep reversed SMTZ at an open ocean site. Furthermore, it was shown that Site U1417 represents a new environment for deep SMTZ formation as previously this diagenetic feature was only known from continental margins or oceanic spreading centres.

With plate bending, a new mechanism enabling seawater to transport electron acceptors to the deeper layers of the sediment is proposed. This process has never been described in the context of early diagenesis, but has been put forward as a mechanism to hydrate subducted plates (Emry and Wiens, 2015; Naif et al., 2015).

Chapter 3 delves further into the sequence of diagenetic events that occurred at Site U1417. The diagenetic evolution was modelled using the Biogeochemical Reaction Network Simulator (Regnier et al., 2002). The modelling strategy was to find a set of parameters for organic matter (OM) reactivity that can reproduce the observed diagenetic patterns in sediment and pore-water geochemistry. The initial approach was simplistic, with the least possible inclusion of geochemical boundary conditions, such as tectonically induced inflow of electron acceptor-rich water or self-cementation events, and using observed sedimentation rates. The motivation for this simplistic approach was to test if it is possible to create the observed diagenetic patterns by varying the fundamental depositional parameters (e.g. OM reactivity) alone. It was possible to model a depositional scenario with a constant OM reactivity that reproduces the sulphate profile, leads to methane generation only in the layers which produce methane in-situ, and maintains a deep sulphate enrichment without sulphate replenishment from below.

Interestingly, the conclusions of Chapter 2 and 3 somewhat contradict each other. While the geochemical observations and diffusion calculations in Chapter 2 suggest that an old buried pool of sulphate-rich seawater is unlikely to persist in the deep sediment layers (because sulphate would be depleted by AOM) and a tectonic process is favoured to supply deep pore-waters with sulphate, the model in Chapter 3 is able to reproduce the observed geochemical patterns with sufficient fidelity in the absence of any external source of sulphate. The model further implies that methane generation only started relatively recently

(0.5 Ma BP) giving AOM not enough time to deplete the deep sulphate pool. In a scenario with higher OM reactivity, methane generation would start earlier after sediment deposition and AOM would lead to complete sulphate consumption within 2 Ma. This also implies that the deep sulphate pool, currently preserved in the best-fit model scenario, will be depleted in the future, and the in-situ observed deep sulphate pool might only be a transient feature that will not exist for much longer.

The timing of the onset of methane generation at Site U1417 cannot be tested exclusively with the geochemical tools used in Chapter 2. Thus, Chapter 3 provides a good example of how biogeochemical modelling can complement geochemical observations. However, it has to be noted that just because a modelled scenario is plausible, it does not necessarily mean that it is true. The modelling approach is based on very limited assumptions and by no means depicts the complexity of a real biogeochemical sediment system. Prominent limitations of the model are the assumption of a constant OM reactivity, the exclusion of the capping carbonate layer, and the insufficient exploration of alternative scenarios such as the supply of sulphate-bearing water by a deep aquifer either generated by plate bending or circulating through seamount flanks.

A more general drawback of the whole approach of Part 1 of the thesis is that only one sediment record was used to describe a complex system. Sediment cores are by nature one-dimensional. A sedimentary system influenced by lateral groundwater flow, potentially driven by tectonic features which extend over hundreds of square kilometres, is a three-dimensional system. Time taken into account, it can well be viewed as four-dimensional. This is a general limitation of sediment drilling which cannot easily be overcome.

The combined approaches used in Chapters 2 and 3 were not able to ultimately solve the question of the mechanism generating the deep sulphate pool at Site U1417. Instead, the plausibility of several processes was discussed and assessed. To further discriminate between these processes, the model could be improved in the ways discussed in Chapter 3. The most obvious improvement would be to include the carbonate layer in the model as a layer of lower porosity. It then has to be assessed if the "old buried sulphate" scenario is still possible. The carbonate layer would prevent upward methane diffusion and thus could potentially cause increased downward methane diffusion and thus, faster sulphate consumption by AOM. To compensate for this effect, lower OM reactivity would have to be

assumed. This would likely change the sulphate profile in the upper sulphate reduction zone which in the current best fit scenario (with an RCM parameter $a = 10^{2.2}$ years) fits the observed profile relatively well. A best fit for both profiles could then only be achieved by applying different OM reactivities to different depositional intervals. These intervals could be defined operationally (i.e. by arbitrary partition of the sediment succession into segments and by then iterating the parameters in each segment until a best fit is achieved). A more evidence-based approach would be to geochemically assess the OM reactivity of the drilled material in the sediment core. Possible proxies would be the kerogen type and molecular O/C and H/C ratios of the OM (Vandenbroucke and Largeau, 2007). This could further be complemented by C-isotopes and biomarker molecules (Killops and Killops, 1997) which are indicative for OM source material. Significant changes of any of these parameters over the sediment succession could be used to define intervals with higher or lower OM reactivity.

As a comparison, the alternative scenarios "deep aquifer by plate bending" and "deep aquifer by seamounts" could be modelled, too. However, this would require to construct multiple models for each scenario and to test a variety of unknown boundary conditions. Each scenario has its unique timing for the beginning of the inflow of the deep aquifer. Seamounts, the flanks of which could provide entry points for aquifers, erupted ~20-25 Ma ago (Chapter 2), plate bending is assumed to have started 3.9 Ma ago at Site U1417 (Chapter 3). Also, the assumption that the aquifer formed at the beginning of deposition has to be considered. It is further complicating that the initial oxidation state and composition of the inflowing water is not clear. Depending on travel time and microbial reactions, the water underwent on its way, it could still be fully oxic when reaching the basement of Site U1417, or several electron acceptors in the redox cascade could already have been used up. Site U1417 has been drilled to a depth 50 - 100 m above basement. In the here-used model, only the depositional history of this segment was simulated. The sediment composition between the deepest drilled interval and the basement, especially its reactive Fe content and the amount and reactivity of the here-deposited OM, influence the reactions, the water provided by the deep aquifer undergoes and its composition, once it reached the deepest drilled interval of Site U1417. To fully assess all possible scenarios, many different model runs would have to be completed with different assumptions for water and sediment composition below Site U1417 and it can be expected that this will produce several plausible

scenarios. This makes modelling the hypothesis of a deep aquifer a very laborious task with uncertain outcome.

If an unlimited financial budget was available, further drilling operations could drill a transect across the forefront of the subduction zone and geochemical observations could assess the composition of the pore-water in various distances from the potential sources. Further geochemical modelling would allow to calculate the amount of time required for the aquifer to transport sulphate-rich water to Site U1417. Further drilling would also reveal the lateral extent of the carbonate layer(s). It is currently unclear if the layer formed at Site U1417 represents only a relatively small lens of cemented rocks, or a solid ceiling traversing vast areas of the sub-seafloor in the GOA. Expedition reports from DSDP Site 178, drilled ~1.5 km away from Site U1417 in 1971 (Kulm and von Huene, 1973) note the existence of some cemented carbonate intervals between 400 and 500 mbsf, however, due to the different depth scales used by the drilling programmes DSDP and IODP it is not clear if they represent the same feature found at Site U1417.

Confirming the nature of the carbonate layer can have some implications for element budgets in the GOA, and potentially on a global scale. The fixing of methane under a cap rock prevents sulphate from being reduced by AOM in the sediment layers lying above. Thus, sulphate reduction above the capping layer can lead to a more efficient OM oxidation because it is not outcompeted by AOM (Niewöhner et al., 1998). The carbon, fixed in the methane underneath the cap rock, could be effectively prevented from escaping into the atmosphere where it could act as a greenhouse gas (Etiope, 2012; potentially oxidized to CO₂; Boetius and Wenzhöfer, 2013). To assess the impact of diagenetic carbonate cap rocks on global element budgets, several further pieces of information are required. To date, authigenic carbonate layers have been described in other regions of the ocean as well (e.g. in the Bering Sea; Pierre et al., 2016; Wehrmann et al., 2016; or at methane seeps; Sauer et al., 2017) but their overall spatial extent is not known. Apart from drilling, this information can also be drawn from a more sound assessment of the required formation conditions for carbonate layers, e.g. the nature of the OM, more precise sedimentation rate constraints and Ca²⁺ flux into and out of the seafloor. Sun and Turchyn (2014) calculated $1 \cdot 10^{12}$ mol a⁻¹ authigenic carbonate precipitation in the global ocean and identified regions in the ocean with a net Ca²⁺ flux into the ocean floor (including sections of the GOA). However, it remains

unclear if these precipitated authigenic carbonates always form impermeable ceilings in the sediments. Furthermore, it would be important to know the efficiency of methane trapping by carbonate layers and the time scale on which the carbonate layers are actively sealing a reservoir. At Site U1417, for example, plate bending could potentially lead to a fracturing of these layers. Kessler (2014) discussed tectonic fractures as a potential pathway for methane into the atmosphere or the ocean with an unknown contribution to the global greenhouse gas budget. If all this information was available, it would be possible to estimate how much carbon could efficiently be revoked from the carbon cycle at the earth's surface and buried in subduction zones.

The work of Sun and Turchyn (2014) gives indications for possible geographic regions, where it could be tested if carbonate cementation is a widespread phenomenon. The paper identifies large areas of the North Atlantic Ocean as well as regions along the eastern and western Pacific margins (off North and South America and off China and Japan) as areas of net authigenic carbonate precipitation. Drilling operations in these areas could provide insight in the formation of impermeable carbonate layers and their potential to trap methane on a global scale. The regions along the Pacific margin represent subduction zones and would thus be of special interest to test the influence of subduction related processes, such as plate bending, on the formation or fracturing of carbonate layers. Drilling in the forefield of one of these subduction zones would yield a valuable comparison to the conditions found in the GOA.

A second setting of interest would be carbonate formations at recent methane seeps at the seafloor (e.g. Sauer et al., 2017). The impact of methane venting from sediments on global climate change is currently discussed (e.g. Shakhova et al., 2010; Pohlman et al., 2017; Ruppel and Kessler, 2017). If carbonate formation has the potential for self cementation of seafloor methane seeps as well, this mechanism would limit the impact of seafloor-derived methane on climate change. Currently, seafloor methane seeps can be found in Arctic seas, e.g. around Svalbard (Pohlman et al., 2017) and along the Siberian Shelf (Shakhova et al., 2017), but are not limited to these locations. Geologically important events of methane seepage occurred during the last deglaciation (e.g. Tesi et al., 2016) and are potentially responsible for the paleocene-eocene-thermal-maximum (e.g. Thomas et al., 2002). Potentially these events have left behind traces of excessive carbonate formation.

Further implications from the work on the deep SMTZ at Site U1417 arise for the global S cycle. The global ocean contains 40×10^{18} mol S, which has a residence time of ~ 10 -15 Ma (Paytan et al., 2004). Sulphur undergoing bacterial sulphate reduction can be sequestered as pyrite and exported to the earth's interior. However, significant amounts of the reduced sulphate are re-oxidized (Turchyn and Schrag, 2006 report 83% re-oxidized sulphate globally, drawn from an isotope fractionation model; Tostevin et al., 2014 estimate an S loss of 10-45% from the ocean by pyrite burial). As sulphate reduced in the deeper layers of the sediment is potentially less exposed to oxidants, most of this re-oxidation can be assumed to happen in the upper sediment layers. The reduced sulphate in deep SMTZs like the one at Site U1417 would be much more efficiently sequestered into subduction zones than the "shallow" reduced sulphate in conventional SMTZs close to the sediment-water interface. The microbial activity in deep SMTZs also affects the carbon cycle, as it oxidizes OM which could escape to overlying sediment layers as CO_2 instead of being sequestered in subduction zones (unless trapped underneath a capping carbonate layer).

In this context, it would be important to verify the origin of deep sulphate rich pore-waters at other continental margin sites. An obvious example to test this would be ODP Sites 796 and 797 in the Japan Sea where Brumsack et al. (1992) proposed an old buried pool of sulphate rich pore-water. A diagenetic model, as the one used at Site U1417, could be applied to verify this hypothesis. Furthermore, sites where plate bending plays a role could be specifically probed for deep aquifers and the same modelling approach as used at Site U1417 can be applied to verify if plate bending can result in the observed diagenetic zonation.

Lastly, the extent of deep aquifers and the efficiency of electron acceptor supply determines the habitability of the seafloor for the deep biosphere (Huber et al., 2006). SMTZs are hotspots for microbial life (e.g. D'Hondt et al., 2004) and information on the spatial extent specifically of deep SMTZs, other than along ridge flanks and subduction zones, has the potential to correct the estimations of global living biomass to higher values (DeLong, 2004; Engelen et al., 2008).

The second part of the thesis (Chapter 4) addressed factors which change the sedimentary composition during deposition at Site U1419 on the continental slope of the GOA. Here, the same redox reactions which are at work during early diagenesis already commence in the water column due to low oxygen availability. At Site U1419, it was shown that different

paleo-environmental proxies can produce contradicting information - at least at first view - and thus should not be used uncritically. In particular, the biomarker for marine anammox, BHT isomer (Rush et al., 2014), seems to be a much better suited proxy for the extent of the Oxygen Deficient Zone (ODZ) in the GOA than redox sensitive trace metals (TM). The reasons for this can be found in the very special depositional environment of Site U1419. This site exhibits extraordinarily high sedimentation rates, regularly exceeding 200 cm ka^{-1} and episodically even exceeding 600 cm ka^{-1} . These values are amongst the highest sedimentation rates observed at a continental margin site. High sedimentation rates can influence the sedimentary enrichment of TM by dilution with TM-poor background material (Klinkhammer and Palmer, 1991; McKay and Pedersen, 2014). An enrichment due to redox processes is not observable if the detrital material dilutes them at the same time. On the other hand, if the TM is a significant component of the detrital material, like Cr, Cu, Ni and V, it would not be depleted, but a redox-sensitive enrichment would be masked by much more pronounced fluctuations in detrital input. It would also be possible that TM records are overprinted by diagenetic reactions or that TM which act as micronutrients could be transported to the sediment by OM (Böning et al., 2015; Steiner et al., 2017). At Site U1419, no signs have been found that diagenetic overprint or biological TM supply play a major role, yet they have to be taken into account when interpreting TM profiles. It has to be noted that these conclusions have been drawn for the special environment of Site U1419 and with limitations for the North Pacific eastern margin, and cannot be generalized. Trace metals might be a much better redox proxy in other settings with low sedimentation rates and more reducing conditions at the seafloor or in the water column. In these environments, biomarkers might be less reliable. In environments with lower sedimentation rates, OM decomposition plays a greater role and biomarker molecules could be more easily decomposed. Furthermore, it is not clear how the BHT isomer-producing bacteria react to sulphidic environments (Dalsgaard et al., 2014; Lipsewers et al., 2016). A depletion in this molecule and a simultaneous enrichment in sulphide-bound TM could actually be a sign for even more reducing, i.e. sulphidic, conditions.

The scientific outcome of Chapter 4 is the reconstruction of the GOA ODZ back to 55 ka BP. It has been shown that the ODZ reacts synchronously with northern hemispheric climate on this time scale. The same assumption was previously limited to the last 17 ka (McKay et al.,

2005; Barron et al., 2009; Addison et al., 2012). Here, the observations were mainly based on the reaction of the ODZ to the rather pronounced changes in climate at the Deglaciation-Bølling/Allerød-transition and the Younger Dryas-Holocene-transition. Chapter 4 confirmed that the ODZ in the GOA also reacts in the same fashion to the less severe changes during Dansgaard/Oeschger Events. A second advancement presented by this study is the application of the relatively new BHT-isomer biomarker. Chapter 4 is the first study to apply this biomarker in the North Pacific and the first to combine BHT-isomer with TM proxies. So far, only few studies used the BHT isomer to reconstruct past ODZ behaviour (Rush et al., 2014; Matys et al., 2017). Chapter 4 thus provides a valuable proof of the meaningfulness and global applicability of this new proxy. The comparison between BHT isomer and TM also revealed environment-dependent performance differences between both proxies. BHT isomer seems to be much better suited to high sedimentation environments, where the applicability of TM proxies can be limited by superimposing signals. BHT isomer is unaffected by changes in sedimentation rate because it is used as a ratio to BHT. It might, however, be susceptible to OM degradation and potentially is influenced by changes in OM deposition, especially if other sources of BHT (not of BHT isomer) exist. The study in Chapter 4 thus helps to define the optimal application fields and limits of this newly developed proxy and generally contributes to a better proxy understanding for BHT isomer.

The setting used as a comparison in Chapter 4 was the Arabian Sea, where lower sedimentation rates prevail (Sirocko et al., 2000; Acharya et al., 2015). The new BHT isomer biomarker has not been applied here, yet. A further step would therefore be to compare the records of TM to the ODZ behaviour recorded by BHT isomer in this region to confirm that a better match is archived under lower sedimentation rates. Other ODZs that could be used to establish a broader data base can be found along the North and South American coast. Alternatively TM records could be gathered at sites, where BHT isomer has been used as a proxy for past ODZ behaviour. These are the Golfo Dulce (Rush et al., 2014) and the Peru margin (Matys et al., 2017).

The findings of Chapter 4 generally highlight the need for multi-proxy studies in paleoceanography and the consideration of the general depositional environment. This is emphasized by the discrepancy between BHT-isomer and TM proxies in relation to the exceptionally high sedimentation rates.

The detailed reconstruction of the behaviour of ODZs in the global ocean is important for the prediction of their behaviour in response to a changing climate in the future. At Site U1419, we confirmed that the GOA ODZ expanded under warmer climates. Predicting the behaviour of ODZs may be important for fisheries, but also for the prediction of the chemistry of the ocean. By a significant expansion of oxygen-limited conditions, "death-zones" without macro-biological activity can spread (Oschlies et al., 2008; IPCC, 2014). These zones will be futile for fisheries (Gilly et al., 2013), potentially putting the basic food resource of entire populations at stake. A recent example of such a dead-zone is the Gulf of Mexico (e.g. Rabalais et al., 2002; Diaz and Rosenberg, 2008), earth-historic examples of large-scale ocean anoxia are ocean anoxic events (OAEs) in the Cretaceous period (e.g. Wagner et al., 2004; Brumsack, 2006; März et al., 2008b).

Throughout the thesis, it has become clear that the composition of marine sediments can be influenced by a variety of factors, from the composition of primarily deposited material, to chemical changes in the water column, overprint during early diagenesis and, potentially, even overprint by tectonic processes. Challenges arise from distinguishing between these different processes. This is further complicated by the different results yielded by different tools and proxies which thus have to be used in functional interaction. Each proxy has to be validated by other markers, and discrepancies have to be explained by boundary conditions. This might appear tedious, but will lead to a much better understanding of complex natural systems.

Literature

- Acharya, S.S., Panigrahi, M.K., Gupta, A.K., Tripathy, S., 2015. Response of trace metal redox proxies in continental shelf environment: The Eastern Arabian Sea scenario. *Cont. Shelf Res.* 106, 70–84. <https://doi.org/10.1016/j.csr.2015.07.008>
- Addison, J.A., Finney, B.P., Dean, W.E., Davies, M.H., Mix, A.C., Stoner, J.S., Jaeger, J.M., 2012. Productivity and sedimentary $\delta^{15}\text{N}$ variability for the last 17,000 years along the northern Gulf of Alaska continental slope. *Paleoceanography* 27. <https://doi.org/10.1029/2011PA002161>
- Aguilera, D.R., Jourabchi, P., Spiteri, C., Regnier, P., 2005. A knowledge-based reactive transport approach for the simulation of biogeochemical dynamics in Earth systems. *Geochemistry, Geophys. Geosystems* 6. <https://doi.org/10.1029/2004GC000899>
- Arndt, S., Jørgensen, B.B., LaRowe, D.E., Middelburg, J.J., Pancost, R.D., Regnier, P., 2013. Quantifying the degradation of organic matter in marine sediments: A review and synthesis. *Earth-Science Rev.* <https://doi.org/10.1016/j.earscirev.2013.02.008>
- Barker, F., Farmer, G.L., Ayuso, R.A., Plafker, G., Lull, J.S., 1992. The 50 Ma Granodiorite of the Eastern Gulf of Alaska: Melting in an Accretionary Prism in the Forearc. *J. Geophys. Res.* 97, 6757–6778.
- Barron, J.A., Bukry, D., Dean, W.E., Addison, J.A., Finney, B., 2009. Paleoceanography of the Gulf of Alaska during the past 15,000 years: Results from diatoms, silicoflagellates, and geochemistry. *Mar. Micropaleontol.* 72, 176–195. <https://doi.org/10.1016/j.marmicro.2009.04.006>
- Beck, R.H., Lehner, P., 1974. Oceans, new frontier in exploration. *Am. Assoc. Pet. Geol. Bull.*
- Benowitz, J.A., Layer, P.W., Vanlaningham, S., 2014. Persistent long-term (c. 24 Ma) exhumation in the Eastern Alaska Range constrained by stacked thermochronology. *Geol. Soc. London, Spec. Publ.* 378, 225–243. <https://doi.org/10.1144/SP378.12>
- Berndmeyer, C., Thiel, V., Schmale, O., Blumenberg, M., 2013. Biomarkers for aerobic methanotrophy in the water column of the stratified Gotland Deep (Baltic Sea). *Org. Geochem.* 55, 103–111. <https://doi.org/10.1016/j.orggeochem.2012.11.010>

- Berner, R.A., 1984. Sedimentary pyrite formation: An update. *Geochim. Cosmochim. Acta* 48, 605–615. [https://doi.org/10.1016/0016-7037\(84\)90089-9](https://doi.org/10.1016/0016-7037(84)90089-9)
- Berner, R.A., 1980. *Early Diagenesis: A Theoretical Approach*, Princeton Series in Geochemistry.
- Bernhard, J.M., Reimers, C.E., 1991. Benthic foraminiferal population fluctuations related to anoxia: Santa Barbara Basin. *Biogeochemistry* 15, 127–149.
<https://doi.org/10.1007/BF00003221>
- Bligh, E.G., Dyer, W.J., 1959. A rapid method of total lipid extraction and purification. *Can. J. Biochem. Physiol.* 37, 911–917. <https://doi.org/10.1139/o59-099>
- Boetius, A., Ravensschlag, K., Schubert, C.J., Rickert, D., Widdel, F., Gieseke, A., Amann, R., Jørgensen, B.B., Witte, U., Pfannkuche, O., 2000. A marine microbial consortium apparently mediating anaerobic oxidation of methane. *Nature* 407, 623–626.
<https://doi.org/10.1038/35036572>
- Boetius, A., Wenzhöfer, F., 2013. Seafloor oxygen consumption fuelled by methane from cold seeps. *Nat. Geosci.* <https://doi.org/10.1038/ngeo1926>
- Böning, P., Fröllje, H., Beck, M., Schnetger, B., Brumsack, H.J., 2012. Underestimation of the authigenic fraction of Cu and Ni in organic-rich sediments. *Mar. Geol.* 323–325, 24–28.
<https://doi.org/10.1016/j.margeo.2012.07.004>
- Böning, P., Shaw, T., Pahnke, K., Brumsack, H.J., 2015. Nickel as indicator of fresh organic matter in upwelling sediments. *Geochim. Cosmochim. Acta* 162, 99–108.
<https://doi.org/10.1016/j.gca.2015.04.027>
- Borowski, W.S., Paull, C.K., Ussler, W., 1996. Marine pore-water sulfate profiles indicate in situ methane flux from underlying gas hydrate. *Geology* 24, 655–658.
[https://doi.org/10.1130/0091-7613\(1996\)024<0655:MPWSP>2.3.CO](https://doi.org/10.1130/0091-7613(1996)024<0655:MPWSP>2.3.CO)
- Böttcher, M., Brumsack, H.-J., de Lange, G., 1998. Sulfate Reduction and Related Stable Isotope (³⁴S, ¹⁸O) Variations in Interstitial Waters From the Eastern Mediterranean. *Proc. Ocean Drill. Program, Sci. Results* 160, 365–373.

- Böttcher, M.E., Brumsack, H.J., Dürselen, C.D., 2007. The isotopic composition of modern seawater sulfate: I. Coastal waters with special regard to the North Sea. *J. Mar. Syst.* 67, 73–82. <https://doi.org/10.1016/j.jmarsys.2006.09.006>
- Boudreau, B.P., 1997. Diagenetic models and their implementation. Modelling transport and reactions in aquatic sediments, Springer, New York.
<https://doi.org/10.1007/978-3-642-60421-5>
- Boudreau, B.P., Ruddick, B.R., 1991. On a reactive continuum representation of organic matter diagenesis. *Am. J. Sci.* 291, 507–538. <https://doi.org/10.2475/ajs.291.5.507>
- Bowles, M.W., Mogollón, J.M., Kasten, S., Zabel, M., Hinrichs, K.U., 2014. Global rates of marine sulfate reduction and implications for sub-sea-floor metabolic activities. *Science* (80-.). 344, 889–891. <https://doi.org/10.1126/science.1249213>
- Boyle, E.A., Sclater, F.R., Edmond, J.M., 1977. The distribution of dissolved copper in the Pacific. *Earth Planet. Sci. Lett.* 37, 38–54.
[https://doi.org/10.1016/0012-821X\(77\)90144-3](https://doi.org/10.1016/0012-821X(77)90144-3)
- Brumsack, H.J., 2006. The trace metal content of recent organic carbon-rich sediments: Implications for Cretaceous black shale formation. *Palaeogeogr. Palaeoclimatol. Palaeoecol.* <https://doi.org/10.1016/j.palaeo.2005.05.011>
- Brumsack, H. J., Zuleger, E., Gohn, E., & Murray, R. W., 1992. 36. Stable and Radiogenic Isotopes in Pore Waters from Leg 127, Japan Sea. *Proceedings of the Ocean Drilling Program, Scientific Results, Vol. 127/128, Pt. 1.*
- Burdige, D.J., 2007. Preservation of organic matter in marine sediments: Controls, mechanisms, and an imbalance in sediment organic carbon budgets? *Chem. Rev.* 107, 467–485. <https://doi.org/10.1021/cr050347q>
- Calvert, S.E., Pedersen, T.F., 2007. Chapter Fourteen Elemental Proxies for Palaeoclimatic and Palaeoceanographic Variability in Marine Sediments: Interpretation and Application. *Dev. Mar. Geol.* [https://doi.org/10.1016/S1572-5480\(07\)01019-6](https://doi.org/10.1016/S1572-5480(07)01019-6)
- Canfield, D.E., 2001. Biogeochemistry of sulfur isotopes. *Rev. Mineral. Geochem.* 43, 607-636. <https://doi.org/10.2138/gsrmg.43.1.607>

- Canfield, D.E., Raiswell, R., Bottrell, S., 1992. The reactivity of sedimentary iron minerals toward sulfide. *Am. J. Sci.* 292, 659–683. <https://doi.org/10.2475/ajs.292.9.659>
- Canfield, D.E., Raiswell, R., Westrich, J.T., Reaves, C.M., Berner, R.A., 1986. The use of chromium reduction in the analysis of reduced inorganic sulfur in sediments and shales. *Chem. Geol.* 54, 149–155. [https://doi.org/10.1016/0009-2541\(86\)90078-1](https://doi.org/10.1016/0009-2541(86)90078-1)
- Cannariato, K.G., Kennett, J.P., 1999. Climatically related millennial-scale fluctuations in strength of California margin oxygen-minimum zone during the past 60 k.y. *Geology* 27, 975–978. [https://doi.org/10.1130/0091-7613\(1999\)027<0975:CRMSFI>2.3.CO;2](https://doi.org/10.1130/0091-7613(1999)027<0975:CRMSFI>2.3.CO;2)
- Cartapanis, O., Tachikawa, K., Bard, E., 2012. Latitudinal variations in intermediate depth ventilation and biological production over northeastern Pacific Oxygen Minimum Zones during the last 60 ka. *Quat. Sci. Rev.* 53, 24–38. <https://doi.org/10.1016/j.quascirev.2012.08.009>
- Cartapanis, O., Tachikawa, K., Bard, E., 2011. Northeastern Pacific oxygen minimum zone variability over the past 70 kyr: Impact of biological production and oceanic ventilation. *Paleoceanography* 26. <https://doi.org/10.1029/2011PA002126>
- Cartapanis, O., Tachikawa, K., Romero, O.E., Bard, E., 2014. Persistent millennial-scale link between Greenland climate and northern Pacific oxygen minimum zone under interglacial conditions. *Clim. Past* 10, 405–418. <https://doi.org/10.5194/cp-10-405-2014>
- Childress, L. B., 2016. *The Active Margin Carbon Cycle: Influences of Climate and Tectonics in Variable Spatial and Temporal Records.* Earth and Planetary Sciences. Evanston, IL: Northwestern University. ProQuest Number: 10117251
- Clark, P.U., Archer, D., Pollard, D., Blum, J.D., Rial, J.A., Brovkin, V., Mix, A.C., Pisias, N.G., Roy, M., 2006. The middle Pleistocene transition: characteristics, mechanisms, and implications for long-term changes in atmospheric pCO₂. *Quat. Sci. Rev.* 25, 3150–3184. <https://doi.org/10.1016/j.quascirev.2006.07.008>
- Clark, P.U., Dyke, A.S., Shakun, J.D., Carlson, A.E., Clark, J., Wohlfarth, B., Mitrovica, J.X., Hostetler, S.W., McCabe, A.M., 2009. The Last Glacial Maximum. *Science* (80-.). 325, 710–714. <https://doi.org/10.1126/science.1172873>

- Codispoti, L.A., Brandes, J.A., Christensen, J.P., Devol, A.H., Naqvi, S.W.A., Paerl, H.W., Yoshinari, T., 2001. The oceanic fixed nitrogen and nitrous oxide budgets: Moving targets as we enter the anthropocene? *Sci. Mar.* 65, 85–105.
<https://doi.org/10.3989/scimar.2001.65s285>
- Condie, K.C., 1993. Chemical composition and evolution of the upper continental crust: Contrasting results from surface samples and shales. *Chem. Geol.* 104, 1–37.
[https://doi.org/10.1016/0009-2541\(93\)90140-E](https://doi.org/10.1016/0009-2541(93)90140-E)
- Contreras, S., Meister, P., Liu, B., Prieto-Mollar, X., Hinrichs, K.-U., Khalili, A., Ferdelman, T.G., Kuypers, M.M.M., Jørgensen, B.B., 2013. Cyclic 100-ka (glacial-interglacial) migration of subseafloor redox zonation on the Peruvian shelf. *Proc. Natl. Acad. Sci.* 110, 18098–18103. <https://doi.org/10.1073/pnas.1305981110>
- Cooke, M.P., van Dongen, B.E., Talbot, H.M., Semiletov, I., Shakhova, N., Guo, L., Gustafsson, Ö., 2009. Bacteriohopanepolyol biomarker composition of organic matter exported to the Arctic Ocean by seven of the major Arctic rivers. *Org. Geochem.* 40, 1151–1159.
<https://doi.org/10.1016/j.orggeochem.2009.07.014>
- D'Hondt, S., Jørgensen, B.B., Miller, D.J., Batzke, A., Blake, R., Cragg, B.A., Cypionka, H., Dickens, G.R., Ferdelman, T., Hinrichs, K.U., Holm, N.G., Mitterer, R., Spivack, A., Wang, G., Bekins, B., Engelen, B., Ford, K., Gettemy, G., Rutherford, S.D., Sass, H., Skilbeck, C.G., Aiello, I.W., Guèrin, G., House, C.H., Inagaki, F., Meister, P., Naehr, T., Niitsuma, S., Parkes, R.J., Schippers, A., Smith, D.C., Teske, A., Wiegand, J., Padilla, C.N., Acosta, J.L.S., 2004. Distributions of microbial activities in deep subseafloor sediments. *Science* (80-.). 306, 2216–2221. <https://doi.org/10.1126/science.1101155>
- D'Hondt, S., Rutherford, S., Spivack, A.J., 2002. Metabolic activity of subsurface life in deep-sea sediments. *Science* (80-.). 295, 2067–2070.
<https://doi.org/10.1126/science.1064878>
- D'Hondt, S., Spivack, A.J., Pockalny, R., Ferdelman, T.G., Fischer, J.P., Kallmeyer, J., Abrams, L.J., Smith, D.C., Graham, D., Hasiuk, F., Schrum, H., Stancin, A.M., 2009. Subseafloor sedimentary life in the South Pacific Gyre. *Proc. Natl. Acad. Sci.* 106, 11651–11656.
<https://doi.org/10.1073/pnas.0811793106>

- Dale, A.W., Aguilera, D.R., Regnier, P., Fossing, H., Knab, N.J., Jørgensen, B.B., 2008. Seasonal dynamics of the depth and rate of anaerobic oxidation of methane in Aarhus Bay (Denmark) sediments. *J. Mar. Res.* 66, 127–155.
<https://doi.org/10.1357/002224008784815775>
- Dalsgaard, T., Stewart, F.J., Thamdrup, B., De Brabandere, L., Revsbech, N.P., Ulloa, O., Canfield, D.E., Delong, E.F., 2014. Oxygen at nanomolar levels reversibly suppresses process rates and gene expression in anammox and denitrification in the oxygen minimum zone off Northern Chile. *MBio* 5. <https://doi.org/10.1128/mBio.01966-14>
- Dansgaard, W., Oeschger, H., Langway, C.C., 1983. Ice Core Indications of Abrupt Climatic Changes, *Palaeoclimatic Research and Models*. Springer, pp. 72-73.
- Davies, M.H., Mix, A.C., Stoner, J.S., Addison, J.A., Jaeger, J., Finney, B., Wiest, J., 2011. The deglacial transition on the southeastern Alaska Margin: Meltwater input, sea level rise, marine productivity, and sedimentary anoxia. *Paleoceanography* 26.
<https://doi.org/10.1029/2010PA002051>
- Dean, W.E., 2007. Sediment geochemical records of productivity and oxygen depletion along the margin of western North America during the past 60,000 years: teleconnections with Greenland Ice and the Cariaco Basin. *Quat. Sci. Rev.* 26, 98–114.
<https://doi.org/10.1016/j.quascirev.2006.08.006>
- DeLong, E.F., 2004. Microbial life breathes deep. *Science* (80-).
<https://doi.org/10.1126/science.1107241>
- DeMets, C., Gordon, R.G., Argus, D.F., 2010. Geologically current plate motions. *Geophys. J. Int.* 181, 1–80. <https://doi.org/10.1111/j.1365-246X.2009.04491.x>
- Diaz, R.J., Rosenberg, R., 2008. Spreading dead zones and consequences for marine ecosystems. *Science* (80-). <https://doi.org/10.1126/science.1156401>
- Egger, M., Hagens, M., Sapart, C.J., Dijkstra, N., van Helmond, N.A.G.M., Mogollón, J.M., Risgaard-Petersen, N., van der Veen, C., Kasten, S., Riedinger, N., Böttcher, M.E., Röckmann, T., Jørgensen, B.B., Slomp, C.P., 2017. Iron oxide reduction in methane-rich deep Baltic Sea sediments. *Geochim. Cosmochim. Acta* 207, 256–276.
<https://doi.org/10.1016/j.gca.2017.03.019>

- Elderfield, H., Wheat, C.G., Mottl, M.J., Monnin, C., Spiro, B., 1999. Fluid and geochemical transport through oceanic crust: A transect across the eastern flank of the Juan de Fuca Ridge. *Earth Planet. Sci. Lett.* 172, 151–165.
[https://doi.org/10.1016/S0012-821X\(99\)00191-0](https://doi.org/10.1016/S0012-821X(99)00191-0)
- Emry, E.L., Wiens, D.A., 2015. Incoming plate faulting in the Northern and Western Pacific and implications for subduction zone water budgets. *Earth Planet. Sci. Lett.* 414, 176–186. <https://doi.org/10.1016/j.epsl.2014.12.042>
- Engelen, B., Ziegelmüller, K., Wolf, L., Köpke, B., Gittel, A., Cypionka, H., Treude, T., Nakagawa, S., Inagaki, F., Lever, M.A., Steinsbu, B.O., 2008. Fluids from the oceanic crust support microbial activities within the deep biosphere. *Geomicrobiol. J.* 25, 56–66.
<https://doi.org/10.1080/01490450701829006>
- Erickson, B.E., Helz, G.R., 2000. Molybdenum(VI) speciation in sulfidic waters: Stability and lability of thiomolybdates. *Geochim. Cosmochim. Acta* 64, 1149–1158.
[https://doi.org/10.1016/S0016-7037\(99\)00423-8](https://doi.org/10.1016/S0016-7037(99)00423-8)
- Etioppe, G., 2012. Climate science: Methane uncovered. *Nat. Geosci.*
<https://doi.org/10.1038/ngeo1483>
- Expedition 201 Shipboard Scientific Party, 2002. Leg 201 Preliminary Results. ODP Preliminary Reports 201.
- Fischer, J.P., Ferdelman, T.G., D'Hondt, S., Røy, H., Wenzhöfer, F., 2009. Oxygen penetration deep into the sediment of the south pacific gyre. *Biogeosciences* 6, 1467–1478.
<https://doi.org/10.5194/bg-6-1467-2009>
- Fisher, A.T., Davis, E.E., Hutnak, M., Spiess, V., Zühlsdorff, L., Cherkaoui, A., Christiansen, L., Edwards, K., Macdonald, R., Villinger, H., Mottl, M.J., Wheat, C.G., Becker, K., 2003a. Hydrothermal recharge and discharge across 50 km guided by seamounts on a young ridge flank. *Nature* 421, 618–621. <https://doi.org/10.1038/nature01352>
- Fisher, A.T., Stein, C.A., Harris, R.N., Wang, K., Silver, E.A., Pfender, M., Hutnak, M., Cherkaoui, A., Bodzin, R., Villinger, H., 2003b. Abrupt thermal transition reveals hydrothermal boundary and role of seamounts within the Cocos Plate. *Geophys. Res. Lett.* 30. <https://doi.org/10.1029/2002GL016766>

- Froelich, P.N., Klinkhammer, G.P., Bender, M.L., Luedtke, N.A., Heath, G.R., Cullen, D., Dauphin, P., Hammond, D., Hartman, B., Maynard, V., 1979. Early oxidation of organic matter in pelagic sediments of the eastern equatorial Atlantic: suboxic diagenesis. *Geochim. Cosmochim. Acta* 43, 1075–1090.
[https://doi.org/10.1016/0016-7037\(79\)90095-4](https://doi.org/10.1016/0016-7037(79)90095-4)
- Garcia, H.E., Locarnini, R. a., Boyer, T.P., Antonov, J.I., 2006. World Ocean Atlas 2005, Volume 3: Dissolved Oxygen, Apparent Oxygen Utilization, and Oxygen Saturation. NOAA Atlas NESDIS 63 3, 342.
- Gee, J.S., Kent, D. V., 2007. Source of Oceanic Magnetic Anomalies and the Geomagnetic Polarity Timescale, in: *Treatise on Geophysics*. pp. 455–507.
<https://doi.org/10.1016/B978-044452748-6.00097-3>
- Gieskes, J.M., Elderfield, H., Lawrence, J.R., Johnson, J., Meyers, B., Campbell, A., 1982. Geochemistry of Interstitial Waters and Sediments, Leg 64, Gulf of California, in: *Initial Reports of the Deep Sea Drilling Project*, 64.
<https://doi.org/10.2973/dsdp.proc.64.116.1982>
- Gilly, W.F., Beman, J.M., Litvin, S.Y., Robison, B.H., 2013. Oceanographic and Biological Effects of Shoaling of the Oxygen Minimum Zone. *Ann. Rev. Mar. Sci.* 5, 393–420.
<https://doi.org/10.1146/annurev-marine-120710-100849>
- Gulick, S.P.S., Jaeger, J.M., Mix, A.C., Asahi, H., Bahlburg, H., Belanger, C.L., Berbel, G.B.B., Childress, L., Cowan, E., Drab, L., Forwick, M., Fukumura, A., Ge, S., Gupta, S., Kioka, A., Konno, S., LeVay, L.J., März, C., Matsuzaki, K.M., McClymont, E.L., Moy, C., Müller, J., Nakamura, A., Ojima, T., Ribeiro, F.R., Ridgway, K.D., Romero, O.E., Slagle, A.L., Stoner, J.S., St-Onge, G., Suto, I., Walczak, M.D., Worthington, L.L., Bailey, I., Enkelmann, E., Reece, R., Swartz, J.M., 2015. Mid-Pleistocene climate transition drives net mass loss from rapidly uplifting St. Elias Mountains, Alaska. *Proc. Natl. Acad. Sci.* 112, 15042–15047. <https://doi.org/10.1073/pnas.1512549112>
- Hamersley, M.R., Lavik, G., Woebken, D., Rattray, J.E., Lam, P., Hopmans, E.C., Damsté, J.S.S., Krüger, S., Graco, M., Gutiérrez, D., Kuypers, M.M.M., 2007. Anaerobic ammonium oxidation in the Peruvian oxygen minimum zone. *Limnol. Ocean.* 52, 923–933.
<https://doi.org/10.4319/lo.2007.52.3.0923>

- Harrison, A.G., Thode, H.G., 1958. Mechanism of the bacterial reduction of sulphate from isotope fractionation studies. *Trans. Faraday Soc.* 54, 84–92.
- Harrison, B.K., Zhang, H., Berelson, W., Orphan, V.J., 2009. Variations in archaeal and bacterial diversity associated with the sulfate-methane transition zone in continental margin sediments (Santa Barbara Basin, California). *Appl. Environ. Microbiol.* 75, 1487–1499. <https://doi.org/10.1128/AEM.01812-08>
- Hartnett, H., Keil, R., Hedges, J., Devol, A., 1998. Influence of oxygen exposure time on organic carbon preservation in continental margin sediments. *Nature* 391, 572–575. <https://doi.org/10.1038/35351>
- Hathaway, J.C., Degens, E.T., 1969. Methane-Derived Marine Carbonates of Pleistocene Age. *Science* (80-.). 165, 690–692. <https://doi.org/10.1126/science.165.3894.690>
- Haug, G.H., Sigman, D.M., Tiedemann, R., Pedersen, T.F., Sarnthein, M., 1999. Onset of permanent stratification in the subarctic Pacific Ocean. *Nature* 401, 779–782. <https://doi.org/10.1038/44550>
- Haughton, P.D.W., Todd, S.P., Morton, A.C., 1991. Sedimentary provenance studies. *Geol. Soc. London, Spec. Publ.* 57, 1–11. <https://doi.org/10.1144/GSL.SP.1991.057.01.01>
- Hedges, J.I., Keil, R.G., 1995. Sedimentary organic matter preservation: an assessment and speculative synthesis. *Mar. Chem.* 49, 81–115. [https://doi.org/10.1016/0304-4203\(95\)00008-F](https://doi.org/10.1016/0304-4203(95)00008-F)
- Hein, J.R., O’Neil, J.R., Jones, M.G., 1979. Origin of authigenic carbonates in sediment from the deep Bering Sea. *Sedimentology* 26, 681–705. <https://doi.org/10.1111/j.1365-3091.1979.tb00937.x>
- Helz, G.R., Miller, C. V., Charnock, J.M., Mosselmans, J.F.W., Pattrick, R.A.D., Garner, C.D., Vaughan, D.J., 1996. Mechanism of molybdenum removal from the sea and its concentration in black shales: EXAFS evidence. *Geochim. Cosmochim. Acta* 60, 3631–3642. [https://doi.org/10.1016/0016-7037\(96\)00195-0](https://doi.org/10.1016/0016-7037(96)00195-0)

- Hensen, C., Zabel, M., Pfeifer, K., Schwenk, T., Kasten, S., Riedinger, N., Schulz, H.D., Boetius, A., 2003. Control of sulfate pore-water profiles by sedimentary events and the significance of anaerobic oxidation of methane for the burial of sulfur in marine sediments. *Geochim. Cosmochim. Acta* 67, 2631–2647.
[https://doi.org/10.1016/S0016-7037\(03\)00199-6](https://doi.org/10.1016/S0016-7037(03)00199-6)
- Hofmann, A.F., Peltzer, E.T., Walz, P.M., Brewer, P.G., 2011. Hypoxia by degrees: Establishing definitions for a changing ocean. *Deep. Res. Part I Oceanogr. Res. Pap.* 58, 1212–1226.
<https://doi.org/10.1016/j.dsr.2011.09.004>
- Holmkvist, L., Ferdelman, T.G., Jørgensen, B.B., 2011. A cryptic sulfur cycle driven by iron in the methane zone of marine sediment (Aarhus Bay, Denmark). *Geochim. Cosmochim. Acta* 75, 3581–3599. <https://doi.org/10.1016/j.gca.2011.03.033>
- Hsü, K.J., Montadert, L., Bernoulli, D., Cita, M.B., Erickson, A., Garrison, R.E., Kidd, R.B., Mèlières, F., Müller, C., Wright, R., 1977. History of the mediterranean salinity crisis. *Nature* 267, 399–403. <https://doi.org/10.1038/267399a0>
- Hsü, K.J., Ryan, W.B.F., Cita, M.B., 1973. Late miocene desiccation of the mediterranean. *Nature* 242, 240–244. <https://doi.org/10.1038/242240a0>
- Huber, J.A., Johnson, H.P., Butterfield, D.A., Baross, J.A., 2006. Microbial life in ridge flank crustal fluids. *Environ. Microbiol.* 8, 88–99.
<https://doi.org/10.1111/j.1462-2920.2005.00872.x>
- Huerta-Diaz, M.A., Morse, J., 1992. Pyritization of trace metals in anoxic marine sediments. *Geochim. Cosmochim. Acta* 56, 2681–2702.
- Hutnak, M., Fisher, A.T., Zühlsdorf, L., Spiess, V., Stauffer, P.H., Gable, C.W., 2006. Hydrothermal recharge and discharge guided by basement outcrops on 0.7–3.6 Ma seafloor east of the Juan de Fuca Ridge: Observations and numerical models. *Geochemistry, Geophys. Geosystems* 7. <https://doi.org/10.1029/2006GC001242>
- IPCC, 2013. Working Group I Contribution to the IPCC Fifth Assessment Report, Climate Change 2013: The Physical Science Basis. *Ipcc AR5*, 2014.
<https://doi.org/10.1017/CBO9781107415324.Summary>

- IPCC, 2014. Climate Change 2014: Synthesis Report. Contribution of Working Groups I, II and III to the Fifth Assessment Report of the Intergovernmental Panel on Climate Change, Core Writing Team, R.K. Pachauri and L.A. Meyer.
<https://doi.org/10.1017/CBO9781107415324.004>
- Jaeger, J.M., Gulick, S.P.S., LeVay, L.J., Asahi, H., Bahlburg, H., Belanger, C.L., Berbel, G.B.B., Childress, L.B., Cowan, E.A., Drab, L., Forwick, M., Fukumura, A., Ge, S., Gupta, S., Kioka, A., Konno, S., März, C., Matsuzaki, K.M., McClymont, E.L., Mix, A.C., Moy, C., Müller, J., Nakamura, A., Ojima, T., Ridgway, K.D., Ribeiro, F.R., Romero, O.E., Slagle, A.L., Stoner, J.S., St-Onge, G., Suto, I., Walczak, M.D. and Worthington, L.L., 2014. Proceedings of the Integrated Ocean Drilling Program Vol. 341: Expedition reports Southern Alaska margin. Integrated Ocean Drilling Program.
- Jaeschke, A., Lewan, M.D., Hopmans, E.C., Schouten, S., Sinninghe Damsté, J.S., 2008. Thermal stability of ladderane lipids as determined by hydrous pyrolysis. *Org. Geochem.* 39, 1735–1741. <https://doi.org/10.1016/j.orggeochem.2008.08.006>
- Jaeschke, A., Rooks, C., Trimmer, M., Nicholls, J.C., Hopmans, E.C., Schouten, S., Sinninghe Damsté, J.S., 2009a. Comparison of ladderane phospholipid and core lipids as indicators for anaerobic ammonium oxidation (anammox) in marine sediments. *Geochim. Cosmochim. Acta* 73, 2077–2088. <https://doi.org/10.1016/j.gca.2009.01.013>
- Jaeschke, A., Ziegler, M., Hopmans, E.C., Reichart, G.J., Lourens, L.J., Schouten, S., Damsté, J.S.S., 2009b. Molecular fossil evidence for anaerobic ammonium oxidation in the Arabian Sea over the last glacial cycle. *Paleoceanography* 24, 11.
<https://doi.org/10.1029/2008pa001712>
- Johnson, W.K., Miller, L.A., Sutherland, N.E., Wong, C.S., 2005. Iron transport by mesoscale Haida eddies in the Gulf of Alaska. *Deep. Res. Part II Top. Stud. Oceanogr.* 52, 933–953.
<https://doi.org/10.1016/j.dsr2.2004.08.017>
- Jørgensen, B.B., 2006. Bacteria and marine biogeochemistry, in: *Marine Geochemistry*. pp. 169–206. https://doi.org/10.1007/3-540-32144-6_5

- Jourabchi, P., Van Cappellen, P., Regnier, P., 2005. Quantitative interpretation of pH distributions in aquatic sediments: A reaction-transport modeling approach. *Am. J. Sci.* 305, 919–956. <https://doi.org/10.2475/ajs.305.9.919>
- Kamenov, G.D., Brenner, M., Tucker, J.L., 2009. Anthropogenic versus natural control on trace element and Sr-Nd-Pb isotope stratigraphy in peat sediments of southeast Florida (USA), ~1500 AD to present. *Geochim. Cosmochim. Acta* 73, 3549–3567. <https://doi.org/10.1016/j.gca.2009.03.017>
- Kaplan, I.R., Rittenberg, S.C., 1964. Microbiological Fractionation of Sulphur Isotopes. *J. Gen. Microbiol.* 34, 195–212. <https://doi.org/10.1099/00221287-34-2-195>
- Kasten, S., Freudenthal, T., Gingele, F.X., Schulz, H.D., 1998. Simultaneous formation of iron-rich layers at different redox boundaries in sediments of the Amazon deep-sea fan. *Geochim. Cosmochim. Acta* 62, 2253–2264. [https://doi.org/10.1016/S0016-7037\(98\)00093-3](https://doi.org/10.1016/S0016-7037(98)00093-3)
- Kasten, S., Haese, R.R., Zabel, M., Rühlemann, C., Schulz, H.D., 2001. Barium peaks at glacial terminations in sediments of the equatorial Atlantic Ocean - Relicts of deglacial productivity pulses? *Chem. Geol.* 175, 635–651. [https://doi.org/10.1016/S0009-2541\(00\)00377-6](https://doi.org/10.1016/S0009-2541(00)00377-6)
- Kasten, S., Zabel, M., Heuer, V., Hensen, C., 2003. Processes and Signals of Nonsteady-State Diagenesis in Deep-Sea Sediments and their Pore Waters, in: *The South Atlantic in the Late Quaternary*. pp. 431–459. https://doi.org/10.1007/978-3-642-18917-3_20
- Kessler, J., 2014. Seafloor methane: Atlantic bubble bath. *Nat. Geosci.* <https://doi.org/10.1038/ngeo2238>
- Kharbush, J.J., Kejriwal, K., Aluwihare, L.I., 2016. Distribution and Abundance of Hopanoid Producers in Low-Oxygen Environments of the Eastern Pacific Ocean. *Microb. Ecol.* 71, 401–408. <https://doi.org/10.1007/s00248-015-0671-y>
- Kharbush, J.J., Ugalde, J.A., Hogle, S.L., Allen, E.E., Aluwihare, L.I., 2013. Composite bacterial hopanoids and their microbial producers across oxygen gradients in the water column of the California current. *Appl. Environ. Microbiol.* 79, 7491–7501. <https://doi.org/10.1128/AEM.02367-13>

- Killops, S. D., Killops, V. J., 1997. Introduction to organic geochemistry. John Wiley & Sons.
- Klinkhammer, G.P., Palmer, M.R., 1991. Uranium in the oceans: Where it goes and why. *Geochim. Cosmochim. Acta* 55, 1799–1806.
[https://doi.org/10.1016/0016-7037\(91\)90024-Y](https://doi.org/10.1016/0016-7037(91)90024-Y)
- Knittel, K., Boetius, A., 2009. Anaerobic Oxidation of Methane: Progress with an Unknown Process. *Annu. Rev. Microbiol.* 63, 311–334.
<https://doi.org/10.1146/annurev.micro.61.080706.093130>
- Korenaga, J., 2017. On the extent of mantle hydration caused by plate bending. *Earth Planet. Sci. Lett.* 457, 1–9. <https://doi.org/10.1016/j.epsl.2016.10.011>
- Kuhn, T., Versteegh, G.J.M., Villinger, H., Dohrmann, I., Heller, C., Koschinsky, A., Kaul, N., Ritter, S., Wegorzewski, A. V., Kasten, S., 2017. Widespread seawater circulation in 18–22 Ma oceanic crust: Impact on heat flow and sediment geochemistry. *Geology* 45, 799–802. <https://doi.org/10.1130/G39091.1>
- Kulm, L.D. and Von Huene, R., 1973. Initial reports of the deep sea drilling project. XVIII: Washington, DC, US Govt. Printing Office.
- Kuypers, M.M.M., Sliemers, A.O., Lavrentyev, P.J., Schmid, M., Jørgensen, B.B., Kuenen, J.G., S., S.D.J., Strous, M., Jetten, M.S.M., 2003. Anaerobic Ammonium Oxidation by Anammox Bacteria in the Black Sea. *Nature* 422, 608–611.
<https://doi.org/10.1038/nature01526.1>
- Lam, P., Kuypers, M.M.M., 2011. Microbial Nitrogen Cycling Processes in Oxygen Minimum Zones. *Ann. Rev. Mar. Sci.* 3, 317–345.
<https://doi.org/10.1146/annurev-marine-120709-142814>
- LaRowe, D.E., Burwicz, E., Arndt, S., Dale, A.W., Amend, J.P., 2017. Temperature and volume of global marine sediments. *Geology* 45, 275–278. <https://doi.org/10.1130/G38601.1>
- Le Maitre, R.W., 1976. The chemical variability of some common igneous rocks. *J. Petrol.* 17, 589–598. <https://doi.org/10.1093/petrology/17.4.589>

- Leavitt, W.D., 2014. On the mechanisms of sulfur isotope fractionation during microbial sulfate reduction. *Earth and Planetary Sciences*. Cambridge, MA: Harvard University, ProQuest.
- Leithold, E.L., Blair, N.E., 2001. Watershed control on the carbon loading of marine sedimentary particles. *Geochim. Cosmochim. Acta* 65, 2231–2240.
[https://doi.org/10.1016/S0016-7037\(01\)00593-2](https://doi.org/10.1016/S0016-7037(01)00593-2)
- Li Y.-H., 2000. A compendium of geochemistry: from solar nebula to the human brain. Princeton University Press. <https://doi.org/10.1029/01EO00037>
- Lin, Q., Wang, J., Taladay, K., Lu, H., Hu, G., Sun, F., Lin, R., 2016. Coupled pyrite concentration and sulfur isotopic insight into the paleo sulfate-methane transition zone (SMTZ) in the northern South China Sea. *J. Asian Earth Sci.* 115, 547–556.
<https://doi.org/10.1016/j.jseaes.2015.11.001>
- Lipsewers, Y.A., Hopmans, E.C., Meysman, F.J.R., Sinninghe Damsté, J.S., Villanueva, L., 2016. Abundance and diversity of denitrifying and anammox bacteria in seasonally hypoxic and sulfidic sediments of the saline lake grevelingen. *Front. Microbiol.* 7.
<https://doi.org/10.3389/fmicb.2016.01661>
- Lisiecki, L.E., Raymo, M.E., 2005. A Pliocene-Pleistocene stack of 57 globally distributed benthic δ 18O records. *Paleoceanography* 20, 1–17.
<https://doi.org/10.1029/2004PA001071>
- Martin, J.H., 1990. Glacial-interglacial CO₂ change: The Iron Hypothesis. *Paleoceanography* 5, 1–13. <https://doi.org/10.1029/PA005i001p00001>
- Martin, J.H., Gordon, R.M., Fitzwater, S., Broenkow, W.W., 1989. Vertex: phytoplankton/iron studies in the Gulf of Alaska. *Deep Sea Res. Part A, Oceanogr. Res. Pap.* 36, 649–680.
[https://doi.org/10.1016/0198-0149\(89\)90144-1](https://doi.org/10.1016/0198-0149(89)90144-1)
- März, C., Hoffmann, J., Bleil, U., de Lange, G.J., Kasten, S., 2008a. Diagenetic changes of magnetic and geochemical signals by anaerobic methane oxidation in sediments of the Zambezi deep-sea fan (SW Indian Ocean). *Mar. Geol.* 255, 118–130.
<https://doi.org/10.1016/j.margeo.2008.05.013>

- März, C., Poulton, S.W., Beckmann, B., Küster, K., Wagner, T., Kasten, S., 2008b. Redox sensitivity of P cycling during marine black shale formation: Dynamics of sulfidic and anoxic, non-sulfidic bottom waters. *Geochim. Cosmochim. Acta* 72, 3703–3717. <https://doi.org/10.1016/j.gca.2008.04.025>
- März, C., Poulton, S.W., Brumsack, H.J., Wagner, T., 2012. Climate-controlled variability of iron deposition in the Central Arctic Ocean (southern Mendeleev Ridge) over the last 130,000 years. *Chem. Geol.* 330–331, 116–126. <https://doi.org/10.1016/j.chemgeo.2012.08.015>
- Maslin, M.A., Haug, G.H., Sarnthein, M., Tiedemann, R., 1996. The progressive intensification of northern hemisphere glaciation as seen from the North Pacific. *Geol. Rundschau* 85, 452–465. <https://doi.org/10.1007/BF02369002>
- Masson, D.G., 1991. Fault patterns at outer trench walls. *Mar. Geophys. Res.* 13, 209–225. <https://doi.org/10.1007/BF00369150>
- Matys, E.D., Sepúlveda, J., Pantoja, S., Lange, C.B., Caniupán, M., Lamy, F., Summons, R.E., 2017. Bacteriohopanepolyols along redox gradients in the Humboldt Current System off northern Chile. *Geobiology* 15, 844–857. <https://doi.org/10.1111/gbi.12250>
- McKay, J.L., Pedersen, T.F., 2014. Geochemical response to pulsed sedimentation: Implications for the use of Mo as a paleo-proxy. *Chem. Geol.* 382, 83–94. <https://doi.org/10.1016/j.chemgeo.2014.05.009>
- McKay, J.L., Pedersen, T.F., Mucci, A., 2007. Sedimentary redox conditions in continental margin sediments (N.E. Pacific) - Influence on the accumulation of redox-sensitive trace metals. *Chem. Geol.* 238, 180–196. <https://doi.org/10.1016/j.chemgeo.2006.11.008>
- McKay, J.L., Pedersen, T.F., Southon, J., 2005. Intensification of the oxygen minimum zone in the northeast Pacific off Vancouver Island during the last deglaciation: Ventilation and/or export production? *Paleoceanography* 20. <https://doi.org/10.1029/2003PA000979>
- McManus, J., Berelson, W.M., Klinkhammer, G.P., Hammond, D.E., Holm, C., 2005. Authigenic uranium: Relationship to oxygen penetration depth and organic carbon rain. *Geochim. Cosmochim. Acta* 69, 95–108. <https://doi.org/10.1016/j.gca.2004.06.023>

- Meister, P., 2015. For the deep biosphere, the present is not always the key to the past: What we can learn from the geological record. *Terra Nov.* 27, 400–408.
<https://doi.org/10.1111/ter.12174>
- Meister, P., Liu, B., Ferdelman, T.G., Jørgensen, B.B., Khalili, A., 2013. Control of sulphate and methane distributions in marine sediments by organic matter reactivity. *Geochim. Cosmochim. Acta* 104, 183–193. <https://doi.org/10.1016/j.gca.2012.11.011>
- Middelburg, J.J., Soetaert, K., Herman, P.M.J., 1997. Empirical relationships for use in global diagenetic models. *Deep. Res. Part I Oceanogr. Res. Pap.* 44, 327–344.
[https://doi.org/10.1016/S0967-0637\(96\)00101-X](https://doi.org/10.1016/S0967-0637(96)00101-X)
- Moffitt, S.E., Moffitt, R.A., Sauthoff, W., Davis, C. V., Hewett, K., Hill, T.M., 2015. Paleooceanographic insights on recent oxygen minimum zone expansion: Lessons for modern oceanography. *PLoS One*. <https://doi.org/10.1371/journal.pone.0115246>
- Montelli, A., Gulick, S.P.S., Worthington, L.L., Mix, A., Davies-Walczak, M., Zellers, S.D., Jaeger, J.M., 2017. Late Quaternary glacial dynamics and sedimentation variability in the bering trough, gulf of Alaska. *Geology* 45, 251–254.
<https://doi.org/10.1130/G38836.1>
- Morford, J.L., Emerson, S., 1999. The geochemistry of redox sensitive trace metals in sediments. *Geochim. Cosmochim. Acta* 63, 1735–1750.
[https://doi.org/10.1016/S0016-7037\(99\)00126-X](https://doi.org/10.1016/S0016-7037(99)00126-X)
- Morford, J.L., Martin, W.R., Carney, C.M., 2009. Uranium diagenesis in sediments underlying bottom waters with high oxygen content. *Geochim. Cosmochim. Acta* 73, 2920–2937.
<https://doi.org/10.1016/j.gca.2009.02.014>
- Morse, J.W., Luther, G.W., 1999. Chemical influences on trace metal-sulfide interactions in anoxic sediments. *Geochim. Cosmochim. Acta* 63, 3373–3378.
[https://doi.org/10.1016/S0016-7037\(99\)00258-6](https://doi.org/10.1016/S0016-7037(99)00258-6)
- Mulder, A., van de Graaf, A.A., Robertson, L.A., Kuenen, J.G., 1995. Anaerobic ammonium oxidation discovered in a denitrifying fluidized bed reactor. *FEMS Microbiol. Ecol.* 16, 177–183. [https://doi.org/10.1016/0168-6496\(94\)00081-7](https://doi.org/10.1016/0168-6496(94)00081-7)

- Naif, S., Key, K., Constable, S., Evans, R.L., 2015. Water-rich bending faults at the Middle America Trench. *Geochemistry, Geophys. Geosystems* 16, 2582–2597.
<https://doi.org/10.1002/2015GC005927>
- Nakakuni, M., Dairiki, C., Kaur, G., Yamamoto, S., 2017. Stanol to sterol ratios in late Quaternary sediments from southern California: An indicator for continuous variability of the oxygen minimum zone. *Org. Geochem.* 111, 126–135.
<https://doi.org/10.1016/j.orggeochem.2017.06.009>
- Nameroff, T.J., Balistrieri, L.S., Murray, J.W., 2002. Suboxic trace metal geochemistry in the Eastern Tropical North Pacific. *Geochim. Cosmochim. Acta* 66, 1139–1158.
[https://doi.org/10.1016/S0016-7037\(01\)00843-2](https://doi.org/10.1016/S0016-7037(01)00843-2)
- Niewöhner, C., Hensen, C., Kasten, S., Zabel, M., Schulz, H.D., 1998. Deep sulfate reduction completely mediated by anaerobic methane oxidation in sediments of the upwelling area off Namibia. *Geochim. Cosmochim. Acta* 62, 455–464.
[https://doi.org/10.1016/S0016-7037\(98\)00055-6](https://doi.org/10.1016/S0016-7037(98)00055-6)
- Ohkushi, K., Kennett, J.P., Zeleski, C.M., Moffitt, S.E., Hill, T.M., Robert, C., Beaufort, L., Behl, R.J., 2013. Quantified intermediate water oxygenation history of the NE Pacific: A new benthic foraminiferal record from Santa Barbara basin. *Paleoceanography* 28, 453–467.
<https://doi.org/10.1002/palo.20043>
- Ono, S., 2008. Multiple-sulphur isotope biosignatures. *Space Sci. Rev.* 135, 203–220.
<https://doi.org/10.1007/s11214-007-9267-2>
- Ortiz, J.D., O’Connell, S.B., DelViscio, J., Dean, W., Carriquiry, J.D., Marchitto, T., Zheng, Y., van Geen, A., 2004. Enhanced marine productivity off western North America during warm climate intervals of the past 52 k.y. *Geology* 32, 521–524.
<https://doi.org/10.1130/G20234.1>
- Oschlies, A., Schulz, K.G., Riebesell, U., Schmittner, A., 2008. Simulated 21st century’s increase in oceanic suboxia by CO₂-enhanced biotic carbon export. *Global Biogeochem. Cycles* 22. <https://doi.org/10.1029/2007GB003147>

- Parkes, R.J., Webster, G., Cragg, B.A., Weightman, A.J., Newberry, C.J., Ferdelman, T.G., Kallmeyer, J., Jørgensen, B.B., Aiello, I.W., Fry, J.C., 2005. Deep sub-seafloor prokaryotes stimulated at interfaces over geological time. *Nature* 436, 390–394.
<https://doi.org/10.1038/nature03796>
- Paulmier, A., Ruiz-Pino, D., 2009. Oxygen minimum zones (OMZs) in the modern ocean. *Prog. Oceanogr.* 80, 113–128. <https://doi.org/10.1016/j.pocean.2008.08.001>
- Paytan, A., Kastner, M., Campbell, D., Thiemens, M.N., 2004. Seawater sulfur isotope fluctuations in the Cretaceous. *Science* (80-.). 304, 1663–1665.
<https://doi.org/10.1126/science.1095258>
- Pearson, A., McNichol, A.P., Benitez-Nelson, B.C., Hayes, J.M., Eglinton, T.I., 2001. Origins of lipid biomarkers in Santa Monica Basin surface sediment: A case study using compound-specific $\Delta^{14}\text{C}$ analysis. *Geochim. Cosmochim. Acta* 65, 3123–3137.
[https://doi.org/10.1016/S0016-7037\(01\)00657-3](https://doi.org/10.1016/S0016-7037(01)00657-3)
- Peketi, A., Mazumdar, A., Joshi, R.K., Patil, D.J., Srinivas, P.L., Dayal, A.M., 2012. Tracing the Paleo sulfate-methane transition zones and H_2S seepage events in marine sediments: An application of C-S-Mo systematics. *Geochemistry, Geophys. Geosystems* 13.
<https://doi.org/10.1029/2012GC004288>
- Penkrot, M.L., Jaeger, J.M., Cowan, E.A., St-Onge, G., LeVay, L., 2018. Multivariate modeling of glacial marine lithostratigraphy combining scanning XRF, multisensory core properties, and CT imagery: IODP Site U1419. *Geosphere* 14, 1935–1960.
<https://doi.org/10.1130/GES01635.1>
- Pierre, C., Blanc-Valleron, M.M., Caquineau, S., März, C., Ravelo, A.C., Takahashi, K., Alvarez Zarikian, C., 2016. Mineralogical, geochemical and isotopic characterization of authigenic carbonates from the methane-bearing sediments of the Bering Sea continental margin (IODP Expedition 323, Sites U1343-U1345). *Deep. Res. Part II Top. Stud. Oceanogr.* 125–126, 133–144. <https://doi.org/10.1016/j.dsr2.2014.03.011>

- Pitcher, A., Villanueva, L., Hopmans, E.C., Schouten, S., Reichart, G.J., Sinninghe Damsté, J.S., 2011. Niche segregation of ammonia-oxidizing archaea and anammox bacteria in the Arabian Sea oxygen minimum zone. *ISME J.* 5, 1896–1904.
<https://doi.org/10.1038/ismej.2011.60>
- Plafker, G., 1987. Regional geology and petroleum potential of the northern Gulf of Alaska continental margin. In Scholl, D.W., Grantz, A., and Vedder, J.G. (Eds.), *Geology and Resource Potential of the Continental Margin of Western North America and Adjacent Ocean Basins—Beaufort Sea to Baja California*. *Earth Sci. Ser. (N. Y.)*, 6: 229–268.
- Pohlman, J.W., Greinert, J., Ruppel, C., Silyakova, A., Vielstädte, L., Casso, M., Mienert, J., Bünz, S., 2017. Enhanced CO₂ uptake at a shallow Arctic Ocean seep field overwhelms the positive warming potential of emitted methane. *Proc. Natl. Acad. Sci.* 114, 5355–5360. <https://doi.org/10.1073/pnas.1618926114>
- Poulton, S.W., Canfield, D.E., 2005. Development of a sequential extraction procedure for iron: Implications for iron partitioning in continentally derived particulates. *Chem. Geol.* 214, 209–221. <https://doi.org/10.1016/j.chemgeo.2004.09.003>
- Poulton, S.W., Raiswell, R., 2005. Chemical and physical characteristics of iron oxides in riverine and glacial meltwater sediments. *Chem. Geol.* 218, 203–221.
<https://doi.org/10.1016/j.chemgeo.2005.01.007>
- Poulton, S.W., Raiswell, R., 2002. The low-temperature geochemical cycle of iron: From continental fluxes to marine sediment deposition. *Am. J. Sci.* 302, 774–805.
<https://doi.org/10.2475/ajs.302.9.774>
- Poulton, S.W., Krom, M.D., Raiswell, R., 2004. A revised scheme for the reactivity of iron (oxyhydr)oxide minerals towards dissolved sulfide. *Geochim. Cosmochim. Acta* 68, 3703–3715. <https://doi.org/10.1016/j.gca.2004.03.012>
- Praetorius, S.K., Mix, A.C., Walczak, M.H., Wolhowe, M.D., Addison, J.A., Prahl, F.G., 2015. North Pacific deglacial hypoxic events linked to abrupt ocean warming. *Nature* 527, 362–366. <https://doi.org/10.1038/nature15753>

- Rabalais, N.N., Turner, R.E., Wiseman, W.J., 2002. Gulf of Mexico Hypoxia, A.K.A. "The Dead Zone." *Annu. Rev. Ecol. Syst.* 33, 235–263.
<https://doi.org/10.1146/annurev.ecolsys.33.010802.150513>
- Raiswell, R., Berner, R.A., 1986. Pyrite and organic matter in Phanerozoic normal marine shales. *Geochim. Cosmochim. Acta* 50, 1967–1976.
[https://doi.org/10.1016/0016-7037\(86\)90252-8](https://doi.org/10.1016/0016-7037(86)90252-8)
- Raiswell, R., Canfield, D.E., 1998. Sources of iron for pyrite formation in marine sediments. *Am. J. Sci.* 298, 219–245. <https://doi.org/10.2475/ajs.298.3.219>
- Raiswell, R., Tranter, M., Benning, L.G., Siegert, M., De'ath, R., Huybrechts, P., Payne, T., 2006. Contributions from glacially derived sediment to the global iron (oxyhydr)oxide cycle: Implications for iron delivery to the oceans. *Geochim. Cosmochim. Acta* 70, 2765–2780. <https://doi.org/10.1016/j.gca.2005.12.027>
- Rasmussen, S.O., Bigler, M., Blockley, S.P., Blunier, T., Buchardt, S.L., Clausen, H.B., Cvijanovic, I., Dahl-Jensen, D., Johnsen, S.J., Fischer, H., Gkinis, V., Guillevic, M., Hoek, W.Z., Lowe, J.J., Pedro, J.B., Popp, T., Seierstad, I.K., Steffensen, J.P., Svensson, A.M., Vallelonga, P., Vinther, B.M., Walker, M.J.C., Wheatley, J.J., Winstrup, M., 2014. A stratigraphic framework for abrupt climatic changes during the Last Glacial period based on three synchronized Greenland ice-core records: Refining and extending the INTIMATE event stratigraphy. *Quat. Sci. Rev.* 106, 14–28.
<https://doi.org/10.1016/j.quascirev.2014.09.007>
- Rea, D.K., Snoeckx, H., 1995. Sediment fluxes in the Gulf of Alaska: Paleoceanographic Record from Site 887 on the Patton-Murray Seamount Platform, in: *Proceeding of the Ocean Drilling Program, Scientific Results*. p. 247-256.
- Redfield, A.C., 1958. The Biological Control of Chemical Factors in the Environment. *Am. Sci.* 46, 205–221. <https://doi.org/10.5194/bg-11-1599-2014>
- Reeburgh, W.S., 1980. Anaerobic methane oxidation: Rate depth distributions in Skan Bay sediments. *Earth Planet. Sci. Lett.* 47, 345–352.
[https://doi.org/10.1016/0012-821X\(80\)90021-7](https://doi.org/10.1016/0012-821X(80)90021-7)

- Reece, R.S., Gulick, S.P.S., Christeson, G.L., Horton, B.K., Van Avendonk, H., Barth, G., 2013. The role of farfield tectonic stress in oceanic intraplate deformation, Gulf of Alaska. *J. Geophys. Res. Solid Earth* 118, 1862–1872. <https://doi.org/10.1002/jgrb.50177>
- Reece, R.S., Gulick, S.P.S., Horton, B.K., Christeson, G.L., Worthington, L.L., 2011. Tectonic and climatic influence on the evolution of the Surveyor Fan and Channel system, Gulf of Alaska. *Geosphere* 7, 830–844. <https://doi.org/10.1130/GES00654.1>
- Regnier, P., Dale, A.W., Arndt, S., LaRowe, D.E., Mogollón, J., Van Cappellen, P., 2011. Quantitative analysis of anaerobic oxidation of methane (AOM) in marine sediments: A modeling perspective. *Earth-Science Rev.* <https://doi.org/10.1016/j.earscirev.2011.01.002>
- Regnier, P., O’Kane, J.P., Steefel, C.I., Vanderborght, J.P., 2002. Modeling complex multi-component reactive-transport systems: towards a simulation environment based on the concept of a Knowledge Base. *Appl. Math. Model.* 26, 913–927. [https://doi.org/10.1016/S0307-904X\(02\)00047-1](https://doi.org/10.1016/S0307-904X(02)00047-1)
- Riedinger, N., Kasten, S., Gröger, J., Franke, C., Pfeifer, K., 2006. Active and buried authigenic barite fronts in sediments from the Eastern Cape Basin. *Earth Planet. Sci. Lett.* 241, 876–887. <https://doi.org/10.1016/j.epsl.2005.10.032>
- Riedinger, N., Pfeifer, K., Kasten, S., Garming, J.F.L., Vogt, C., Hensen, C., 2005. Diagenetic alteration of magnetic signals by anaerobic oxidation of methane related to a change in sedimentation rate. *Geochim. Cosmochim. Acta* 69, 4117–4126. <https://doi.org/10.1016/j.gca.2005.02.004>
- Rohmer, M., Bouvier-Nave, P., Ourisson, G., 1984. Distribution of Hopanoid Triterpenes in Prokaryotes. *Microbiology* 130, 1137–1150. <https://doi.org/10.1099/00221287-130-5-1137>
- Rona, P.A., 2008. The changing vision of marine minerals. *Ore Geol. Rev.* 33, 618–666. <https://doi.org/10.1016/j.oregeorev.2007.03.006>
- Ruppel, C.D., Kessler, J.D., 2017. The interaction of climate change and methane hydrates. *Rev. Geophys.* <https://doi.org/10.1002/2016RG000534>

- Rush, D., Sinninghe Damsté, J.S., Poulton, S.W., Thamdrup, B., Garside, A.L., Acuña González, J., Schouten, S., Jetten, M.S.M., Talbot, H.M., 2014. Anaerobic ammonium-oxidising bacteria: A biological source of the bacteriohopanetetrol stereoisomer in marine sediments. *Geochim. Cosmochim. Acta* 140, 50–64.
<https://doi.org/10.1016/j.gca.2014.05.014>
- Sáenz, J. P., Wakeham, S. G., Eglinton, T. I., & Summons, R. E., 2011. New constraints on the provenance of hopanoids in the marine geologic record: bacteriohopanepolyols in marine suboxic and anoxic environments. *Org. Geochem.*, 42, 1351–1362.
<https://doi.org/10.1016/j.orggeochem.2011.08.016>
- Sauer, S., Crémière, A., Knies, J., Lepland, A., Sahy, D., Martma, T., Noble, S.R., Schönenberger, J., Klug, M., Schubert, C.J., 2017. U-Th chronology and formation controls of methane-derived authigenic carbonates from the Hola trough seep area, northern Norway. *Chem. Geol.* 470, 164–179.
<https://doi.org/10.1016/j.chemgeo.2017.09.004>
- Schlitzer, R., 2015. Ocean Data View. <http://odv.awi.de>
- Schulz, H.D., Zabel, M., Fütterer, D.K., Breitzke, M., Rullkötter, J., Jørgensen, B.B., Hensen, C., Schulz, H.N., Haese, R.R., Kasten, S., Schneider, R.R., Bickert, T., Glasby, G.P., Herzig, P.M., Hannington, M.D., Bohrmann, G., Torres, M.E., 2006. *Marine Geochemistry, Vol. 2*, Springer. <https://doi.org/10.1017/CBO9781107415324.004>
- Seierstad, I.K., Abbott, P.M., Bigler, M., Blunier, T., Bourne, A.J., Brook, E., Buchardt, S.L., Buizert, C., Clausen, H.B., Cook, E., Dahl-Jensen, D., Davies, S.M., Guillevic, M., Johnsen, S.J., Pedersen, D.S., Popp, T.J., Rasmussen, S.O., Severinghaus, J.P., Svensson, A., Vinther, B.M., 2014. Consistently dated records from the Greenland GRIP, GISP2 and NGRIP ice cores for the past 104ka reveal regional millennial-scale $\delta^{18}\text{O}$ gradients with possible Heinrich event imprint. *Quat. Sci. Rev.* 106, 29–46.
<https://doi.org/10.1016/j.quascirev.2014.10.032>

- Shakhova, N., Semiletov, I., Gustafsson, O., Sergienko, V., Lobkovsky, L., Dudarev, O., Tumskey, V., Grigoriev, M., Mazurov, A.K., Salyuk, A., Ananiev, R., Koshurnikov, A., Kosmach, D., Charkin, A., Dmitrevsky, N., Karnaukh, V., Gunar, A., Meluzov, A., Chernykh, D., 2017. Current rates and mechanisms of subsea permafrost degradation in the East Siberian Arctic Shelf. *Nat. Commun.* 8. <https://doi.org/10.1038/ncomms15872>
- Shakhova, N., Semiletov, I., Salyuk, A., Yusupov, V., Kosmach, D., Gustafsson, Ö., 2010. Extensive methane venting to the atmosphere from sediments of the East Siberian Arctic Shelf. *Science* (80-). 327, 1246–1250. <https://doi.org/10.1126/science.1182221>
- Shaw, T.J., Gieskes, J.M., Jahnke, R.A., 1990. Early diagenesis in differing depositional environments: The response of transition metals in pore water. *Geochim. Cosmochim. Acta* 54, 1233–1246. [https://doi.org/10.1016/0016-7037\(90\)90149-F](https://doi.org/10.1016/0016-7037(90)90149-F)
- Silver, E.A., von Huene, R., Crouch, J.K., 1974. Tectonic significance of the kodiak-bowie seamount chain, Northeastern Pacific. *Geology* 2, 147–150. [https://doi.org/10.1130/0091-7613\(1974\)2<147:TSOTKS>2.0.CO;2](https://doi.org/10.1130/0091-7613(1974)2<147:TSOTKS>2.0.CO;2)
- Sim, M.S., Bosak, T., Ono, S., 2011. Large sulfur isotope fractionation does not require disproportionation. *Science* (80-). 333, 74–77. <https://doi.org/10.1126/science.1205103>
- Sirocko, F., Garbe-Schönberg, D., Devey, C., 2000. Processes controlling trace element geochemistry of Arabian Sea sediments during the last 25,000 years. *Glob. Planet. Change* 26, 217–303. [https://doi.org/Doi: 10.1016/s0921-8181\(00\)00046-1](https://doi.org/Doi:10.1016/s0921-8181(00)00046-1)
- Soetaert, K., Hofmann, A.F., Middelburg, J.J., Meysman, F.J.R., Greenwood, J., 2007. The effect of biogeochemical processes on pH (Reprinted from *Marine Chemistry*, vol 105, pg 30-51, 2007). *Mar. Chem.* 106, 380–401. <https://doi.org/10.1016/j.marchem.2007.06.008>
- Stabeno, P.J., Bond, N.A., Hermann, A.J., Kachel, N.B., Mordy, C.W., Overland, J.E., 2004. Meteorology and oceanography of the Northern Gulf of Alaska. *Cont. Shelf Res.* <https://doi.org/10.1016/j.csr.2004.02.007>

- Statham, P.J., Skidmore, M., Tranter, M., 2008. Inputs of glacially derived dissolved and colloidal iron to the coastal ocean and implications for primary productivity. *Global Biogeochem. Cycles* 22. <https://doi.org/10.1029/2007GB003106>
- Stein, R., Blackman, D., Inagaki, F., Larsen, H.C., 2014. Earth and Life Processes Discovered from Subseafloor Environments, in: *Climate Change 2013 - The Physical Science Basis*. pp. 1–30. <https://doi.org/10.1017/CBO9781107415324.004>
- Steiner, Z., Lazar, B., Torfstein, A., Erez, J., 2017. Testing the utility of geochemical proxies for paleoproductivity in oxic sedimentary marine settings of the Gulf of Aqaba, Red Sea. *Chem. Geol.* 473, 40–49. <https://doi.org/10.1016/j.chemgeo.2017.10.012>
- Stramma, L., Johnson, G.C., Sprintall, J., Mohrholz, V., 2008. Expanding oxygen-minimum zones in the tropical oceans. *Science* (80-.). 320, 655–658. <https://doi.org/10.1126/science.1153847>
- Strauss, H., 1999. Geological evolution from isotope proxy signals - Sulfur. *Chem. Geol.* 161, 89–101. [https://doi.org/10.1016/S0009-2541\(99\)00082-0](https://doi.org/10.1016/S0009-2541(99)00082-0)
- Strauss, H., 1997. The isotopic composition of sedimentary sulfur through time. *Palaeogeogr. Palaeoclimatol. Palaeoecol.* [https://doi.org/10.1016/S0031-0182\(97\)00067-9](https://doi.org/10.1016/S0031-0182(97)00067-9)
- Strauss, H., Bast, R., Cording, A., Diekrup, D., Fugmann, A., Garbe-Schönberg, D., Lutter, A., Oeser, M., Rabe, K., Reinke, D., Teichert, B.M.A., Westernströer, U., 2012. Sulphur diagenesis in the sediments of the Kiel Bight, SW Baltic Sea, as reflected by multiple stable sulphur isotopes. *Isotopes Environ. Health Stud.* 48, 166–179. <https://doi.org/10.1080/10256016.2012.648930>
- Strauss, H., Schieber, J., 1990. A sulfur isotope study of pyrite genesis: The mid-proterozoic Newland formation, belt supergroup, Montana. *Geochim. Cosmochim. Acta* 54, 197–204. [https://doi.org/10.1016/0016-7037\(90\)90207-2](https://doi.org/10.1016/0016-7037(90)90207-2)
- Sturt, H.F., Summons, R.E., Smith, K., Elvert, M., Hinrichs, K.U., 2004. Intact polar membrane lipids in prokaryotes and sediments deciphered by high-performance liquid chromatography/electrospray ionization multistage mass spectrometry - New biomarkers for biogeochemistry and microbial ecology. *Rapid Commun. Mass Spectrom.* 18, 617–628. <https://doi.org/10.1002/rcm.1378>

- Summons, R.E., Jahnke, L.L., Hope, J.M., Logan, G.A., 1999. 2-Methylhopanoids as biomarkers for cyanobacterial oxygenic photosynthesis. *Nature* 400, 554–557. <https://doi.org/10.1038/23005>
- Sun, X., Turchyn, A. V., 2014. Significant contribution of authigenic carbonate to marine carbon burial. *Nat. Geosci.* 7, 201–204. <https://doi.org/10.1038/ngeo2070>
- Sundby, B., Martinez, P., Gobeil, C., 2004. Comparative geochemistry of cadmium, rhenium, uranium, and molybdenum in continental margin sediments. *Geochim. Cosmochim. Acta* 68, 2485–2493. <https://doi.org/10.1016/j.gca.2003.08.011>
- Takahashi, K., Ravelo, A.C., Zarkian, C.A., 2011. IODP Expedition 323-pliocene and pleistocene paleoceanographic changes in the Bering Sea. *Sci. Drill.* 4–13. <https://doi.org/10.2204/iodp.sd.11.01.2011>
- Talbot, H.M., Summons, R.E., Jahnke, L.L., Cockell, C.S., Rohmer, M., Farrimond, P., 2008. Cyanobacterial bacteriohopanepolyol signatures from cultures and natural environmental settings. *Org. Geochem.* 39, 232–263. <https://doi.org/10.1016/j.orggeochem.2007.08.006>
- Talbot, H.M., Watson, D.F., Murrell, J.C., Carter, J.F., Farrimond, P., 2001. Analysis of intact bacteriohopanepolyols from methanotrophic bacteria by reversed-phase high-performance liquid chromatography-atmospheric pressure chemical ionisation mass spectrometry. *J. Chromatogr. A* 921, 175–185. [https://doi.org/10.1016/S0021-9673\(01\)00871-8](https://doi.org/10.1016/S0021-9673(01)00871-8)
- Tesi, T., Muschitiello, F., Smittenberg, R.H., Jakobsson, M., Vonk, J.E., Hill, P., Andersson, A., Kirchner, N., Noormets, R., Dudarev, O., Semiletov, I., Gustafsson, 2016. Massive remobilization of permafrost carbon during post-glacial warming. *Nat. Commun.* 7. <https://doi.org/10.1038/ncomms13653>
- Thamdrup, B., Finster, K., Hansen, J.W., Bak, F., 1993. Bacterial disproportionation of elemental sulfur coupled to chemical reduction of iron or manganese. *Appl. Environ. Microbiol.* 59, 101–108.

- Thomas, D.J., Zachos, J.C., Bralower, T.J., Thomas, E., Bohaty, S.M., 2002. Warming the Fuel for the Fire : Evidence for the Thermal Dissociation of Methane Hydrate During the Paleocene-Eocene Thermal Maximum. *Geology* 30, 1067–1070.
[https://doi.org/10.1130/0091-7613\(2002\)030<1067:WTFFTF>2.0.CO;2](https://doi.org/10.1130/0091-7613(2002)030<1067:WTFFTF>2.0.CO;2)
- Thullner, M., Dale, A.W., Regnier, P., 2009. Global-scale quantification of mineralization pathways in marine sediments: A reaction-transport modeling approach. *Geochemistry, Geophys. Geosystems* 10. <https://doi.org/10.1029/2009GC002484>
- Torres, M.E., Bohrmann, G., Suess, E., 1996. Authigenic barites and fluxes of barium associated with fluid seeps in the Peru subduction zone. *Earth Planet. Sci. Lett.* 144, 469–481. [https://doi.org/10.1016/S0012-821X\(96\)00163-X](https://doi.org/10.1016/S0012-821X(96)00163-X)
- Torres, M.E., Cox, T., Hong, W.L., Mcmanus, J., Sample, J.C., Destrigneville, C., Gan, H.M., Gan, H.Y., Moreau, J.W., 2015. Crustal fluid and ash alteration impacts on the biosphere of Shikoku Basin sediments, Nankai Trough, Japan. *Geobiology* 13, 562–580.
<https://doi.org/10.1111/gbi.12146>
- Tostevin, R., Turchyn, A. V., Farquhar, J., Johnston, D.T., Eldridge, D.L., Bishop, J.K.B., McIlvin, M., 2014. Multiple sulfur isotope constraints on the modern sulfur cycle. *Earth Planet. Sci. Lett.* 396, 14–21. <https://doi.org/10.1016/j.epsl.2014.03.057>
- Treude, T., Smith, C.R., Wenzhöfer, F., Carney, E., Bernardino, A.F., Hannides, A.K., Krgüer, M., Boetius, A., 2009. Biogeochemistry of a deep-sea whale fall: Sulfate reduction, sulfide efflux and methanogenesis. *Mar. Ecol. Prog. Ser.* 382, 1–21.
<https://doi.org/10.3354/meps07972>
- Tribovillard, N., Algeo, T.J., Lyons, T., Riboulleau, A., 2006. Trace metals as paleoredox and paleoproductivity proxies: An update. *Chem. Geol.* 232, 12–32.
<https://doi.org/10.1016/j.chemgeo.2006.02.012>
- Turchyn, A. V., Schrag, D.P., 2006. Cenozoic evolution of the sulfur cycle: Insight from oxygen isotopes in marine sulfate. *Earth Planet. Sci. Lett.* 241, 763–779.
<https://doi.org/10.1016/j.epsl.2005.11.007>

- Turner, D.L., Forbes, R.B., Naeser, C.W., 1973. Radiometric ages of Kodiak seamount and Giacomini Guyot, Gulf of Alaska: implications for circum-Pacific tectonics. *Science* 182, 579–81. <https://doi.org/10.1126/science.182.4112.579>
- Van de Graaf, A.A., Mulder, A., De Bruijn, P., Jetten, M.S.M., Robertson, L.A., Kuenen, J.G., 1995. Anaerobic oxidation of ammonium is a biologically mediated process. *Appl. Environ. Microbiol.* 61, 1246–1251. <https://doi.org/PMC167380>
- van der Weijden, C.H., Reichert, G.J., van Os, B.J.H., 2006. Sedimentary trace element records over the last 200 kyr from within and below the northern Arabian Sea oxygen minimum zone. *Mar. Geol.* 231, 69–88. <https://doi.org/10.1016/j.margeo.2006.05.013>
- Van Geen, A., Smethie, J.M., Homeman, A., Lee, H., 2006. Sensitivity of the North Pacific oxygen minimum zone to changes in ocean circulation: A simple model calibrated by chlorofluorocarbons. *J. Geophys. Res. Ocean.* 111. <https://doi.org/10.1029/2005JC003192>
- van Winden, J.F., Talbot, H.M., Kip, N., Reichert, G.J., Pol, A., McNamara, N.P., Jetten, M.S.M., Op den Camp, H.J.M., Sinninghe Damsté, J.S., 2012. Bacteriohopanepolyol signatures as markers for methanotrophic bacteria in peat moss. *Geochim. Cosmochim. Acta* 77, 52–61. <https://doi.org/10.1016/j.gca.2011.10.026>
- Vandenbroucke, M., Largeau, C., 2007. Kerogen origin, evolution and structure. *Org. Geochem.* <https://doi.org/10.1016/j.orggeochem.2007.01.001>
- Von Breyman, M.T., Emeis, K.-C., Suess, E., 1992. Water depth and diagenetic constraints on the use of barium as a palaeoproductivity indicator. *Geol. Soc. London, Spec. Publ.* 64, 273–284. <https://doi.org/10.1144/GSL.SP.1992.064.01.18>
- Wagner, T., Sinninghe Damsté, J.S., Hofmann, P., Beckmann, B., 2004. Euxinia and primary production in Late Cretaceous eastern equatorial Atlantic surface waters fostered orbitally driven formation of marine black shales. *Paleoceanography.* <https://doi.org/10.1029/2003PA000898>

- Wakeham, S.G., Turich, C., Schubotz, F., Podlaska, A., Li, X.N., Varela, R., Astor, Y., Sáenz, J.P., Rush, D., Sinninghe Damsté, J.S., Summons, R.E., Scranton, M.I., Taylor, G.T., Hinrichs, K.U., 2012. Biomarkers, chemistry and microbiology show chemoautotrophy in a multilayer chemocline in the Cariaco Basin. *Deep. Res. Part I Oceanogr. Res. Pap.* 63, 133–156. <https://doi.org/10.1016/j.dsr.2012.01.005>
- Wang, Y., Van Cappellen, P., 1996. A multicomponent reactive transport model of early diagenesis: Application to redox cycling in coastal marine sediments. *Geochim. Cosmochim. Acta* 60, 2993–3014. [https://doi.org/10.1016/0016-7037\(96\)00140-8](https://doi.org/10.1016/0016-7037(96)00140-8)
- Ward, B.B., 2013. How nitrogen is lost. *Science* (80-.). <https://doi.org/10.1126/science.1240314>
- Wedepohl, K.H., 1971. Environmental influences on the chemical composition of shales and clays. *Phys. Chem. Earth.* [https://doi.org/10.1016/0079-1946\(71\)90020-6](https://doi.org/10.1016/0079-1946(71)90020-6)
- Wedepohl, K.H., 1991. The composition of the upper earth's crust and the natural cycles of selected metals. *Metals in natural raw materials. Natural Resources.* In: Merian, E.(Ed.), *Metals and Their Compounds in the Environment.* VCH, Weinheim, 3-17.
- Wefer, G., Berger, W.H., Bijma, J., Fischer, G., 1999. Clues to Ocean History: a Brief Overview of Proxies, in: *Use of Proxies in Paleoceanography.* pp. 1–68. https://doi.org/10.1007/978-3-642-58646-0_1
- Wehrmann, L.M., Arndt, S., März, C., Ferdelman, T.G., Brunner, B., 2013. The evolution of early diagenetic signals in Bering Sea subseafloor sediments in response to varying organic carbon deposition over the last 4.3Ma. *Geochim. Cosmochim. Acta* 109, 175–196. <https://doi.org/10.1016/j.gca.2013.01.025>
- Wehrmann, L.M., Ferdelman, T.G., 2014. Biogeochemical Consequences of the Sedimentary Subseafloor Biosphere. *Dev. Mar. Geol.* 7, 217–252. <https://doi.org/10.1016/B978-0-444-62617-2.00009-8>

- Wehrmann, L.M., Ockert, C., Mix, A.C., Gussone, N., Teichert, B.M.A., Meister, P., 2016. Repeated occurrences of methanogenic zones, diagenetic dolomite formation and linked silicate alteration in southern Bering Sea sediments (Bowers Ridge, IODP Exp. 323 Site U1341). *Deep. Res. Part II Top. Stud. Oceanogr.* 125–126, 117–132.
<https://doi.org/10.1016/j.dsr2.2013.09.008>
- Wehrmann, L.M., Risgaard-Petersen, N., Schrum, H.N., Walsh, E.A., Huh, Y., Ikehara, M., Pierre, C., D'Hondt, S., Ferdelman, T.G., Ravelo, A.C., Takahashi, K., Zarikian, C.A., 2011. Coupled organic and inorganic carbon cycling in the deep seafloor sediment of the northeastern Bering Sea Slope (IODP Exp. 323). *Chem. Geol.* 284, 251–261.
<https://doi.org/10.1016/j.chemgeo.2011.03.002>
- Weingartner, T.J., Danielson, S.L., Royer, T.C., 2005. Freshwater variability and predictability in the Alaska Coastal Current. *Deep. Res. Part II Top. Stud. Oceanogr.* 52, 169–191.
<https://doi.org/10.1016/j.dsr2.2004.09.030>
- Whitney, F., Robert, M., 2002. Structure of Haida Eddies and their transport of nutrient from coastal margins into the NE pacific ocean. *J. Oceanogr.* 58, 715–723.
<https://doi.org/10.1023/A:1022850508403>
- Zheng, Y., Van Geen, A., Anderson, R.F., Gardner, J. V., Dean, W.E., 2000. Intensification of the Northeast Pacific oxygen minimum zone during the Bölling-Alleröd warm period. *Paleoceanography* 15, 528–536. <https://doi.org/10.1029/1999PA000473>
- Zhu, C., Talbot, H. M., Wagner, T., Pan, J. M., Pancost, R. D., 2011. Distribution of hopanoids along a land to sea transect: implications for microbial ecology and the use of hopanoids in environmental studies. *Limnol. Oceanogr.*, 56(5), 1850-1865.
<https://doi.org/10.4319/lo.2011.56.5.1850>

Appendix A: Summary of the Analysis for 3 basalt basal core samples from DSDP LEG 18 Site 178

(contribution to Chapter 2 by Jeff Benowitz)

For $^{40}\text{Ar}/^{39}\text{Ar}$ analysis, 3 samples were submitted to the Geochronology laboratory at UAF where the samples were washed and hand-picked for phenocryst free whole rock chips depending on what mineral phases were present. The monitor mineral TCR-2 with an age of 28.619 Ma (Renne et al., 2010) was used to monitor neutron flux and calculate the irradiation parameter (J) for all samples. The samples and standards were wrapped in aluminum foil and loaded into aluminum cans of 2.5 cm diameter and 6 cm height. The samples were irradiated in position 8c of the uranium enriched research reactor of McMaster University in Hamilton, Ontario, Canada for 20 megawatt-hours.

Upon their return from the reactor, the samples and monitors were loaded into 2 mm diameter holes in a copper tray that was then loaded in a ultra-high vacuum extraction line. The monitors were fused, and samples heated, using a 6-watt argon-ion laser following the technique described in York et al. (1981), Layer et al. (1987) and Benowitz (2014). Argon purification was achieved using a liquid nitrogen cold trap and a SAES Zr-Al getter at 400C. The samples were analyzed in a VG-3600 mass spectrometer at the Geophysical Institute, University of Alaska Fairbanks. The argon isotopes measured were corrected for system blank and mass discrimination, as well as calcium, potassium and chlorine interference reactions following procedures outlined in McDougall and Harrison (1999). Typical full-system 8 min laser blank values (in moles) were generally 2×10^{-16} mol ^{40}Ar , 3×10^{-18} mol ^{39}Ar , 9×10^{-18} mol ^{38}Ar and 2×10^{-18} mol ^{36}Ar , which are 10–50 times smaller than the sample/standard volume fractions. Correction factors for nucleogenic interferences during irradiation were determined from irradiated CaF_2 and K_2SO_4 as follows: $(^{39}\text{Ar}/^{37}\text{Ar})\text{Ca} = 7.06 \times 10^{-4}$, $(^{36}\text{Ar}/^{37}\text{Ar})\text{Ca} = 2.79 \times 10^{-4}$ and $(^{40}\text{Ar}/^{39}\text{Ar})\text{K} = 0.0297$. Mass discrimination was monitored by running calibrated air shots. The mass discrimination during these experiments was 0.8% per mass unit. While doing our experiments, calibration measurements were made on a weekly– monthly basis to check for changes in mass discrimination with no significant variation seen during these intervals.

A summary of all the $^{40}\text{Ar}/^{39}\text{Ar}$ results is given in Table 1, with all ages quoted to the ± 1 sigma level and calculated using the constants of Renne et al. (2010). The integrated age is

the age given by the total gas measured and is equivalent to a potassium-argon (K-Ar) age. The spectrum provides a plateau age if three or more consecutive gas fractions represent at least 50% of the total gas release and are within two standard deviations of each other (Mean Square Weighted Deviation less than 2.5).

Sample	Min.	Integrated Age (Ma)	Plateau Age (Ma)	Plateau Information	Isochron Age (Ma)	Isochron or other Information
18-178-58R-CCW-10-12 cm	WR	23.79 ± 0.39	25.80 ± 0.36	3 of 8 fractions 63.9% ³⁹ Ar release MSWD = 0.14	--	--
18-178-59R-01W-70-72 cm	WR	27.73 ± 0.49	27.73 ± 0.74	8 of 8 fractions 100.0% ³⁹ Ar release MSWD = 2.23	26.60 ± 0.49	8 of 8 fractions ⁴⁰ Ar/ ³⁶ Ar _i = 422.0 ± 79.3 MSWD = 0.94
18-178-59R-CCW-30-32 cm	WR	24.80 ± 0.26	26.44 ± 0.43*	6 of 8 fractions 47.8% ³⁹ Ar release MSWD = 0.78	26.39 ± 0.40	6 of 8 fractions ⁴⁰ Ar/ ³⁶ Ar _i = 293.8 ± 7.5 MSWD = 0.95

Table 1: ⁴⁰Ar/³⁹Ar step heating results.

Samples analyzed with standard TCR-2 an age of 28.619 Ma.

Most robust age in **bold**.

*Does not meet all the criteria for a plateau age.

Discussion

18-178-58R-CCW-10-12 cm

Whole Rock (WR)

A whole rock separate from sample **18-178-58R-CCW-10-12 cm** was analyzed. The analysis produced an irregular age spectrum that stepped up in age that is associated with loss/alteration (modeled loss 8%).

No isochron regression was possible because of the documented loss/alteration. The integrated age 23.79 ± 0.39 Ma) is not within error of the plateau age (25.80 ± 0.36 Ma). We prefer the plateau age of **25.80 ± 0.36 Ma** because of the documented loss/alteration.

18-178-59R-01W-70-72 cm

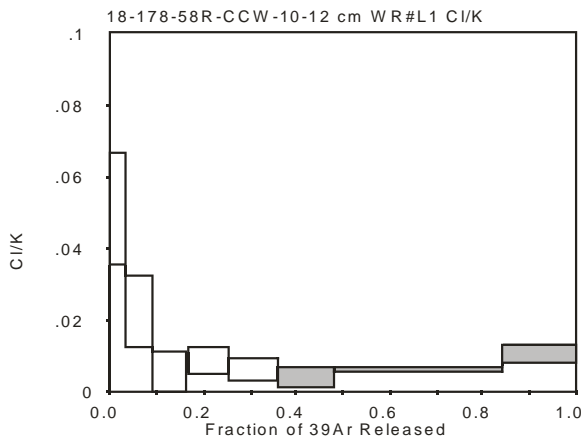
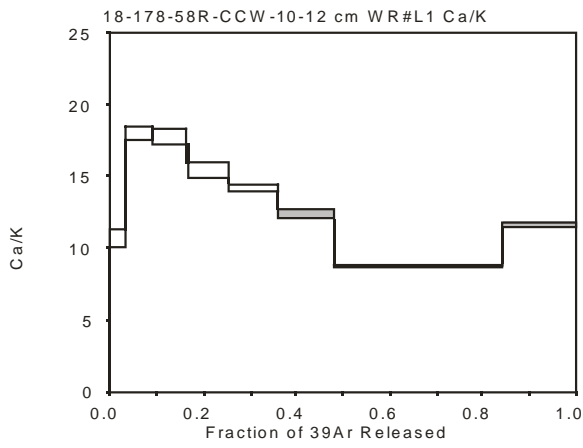
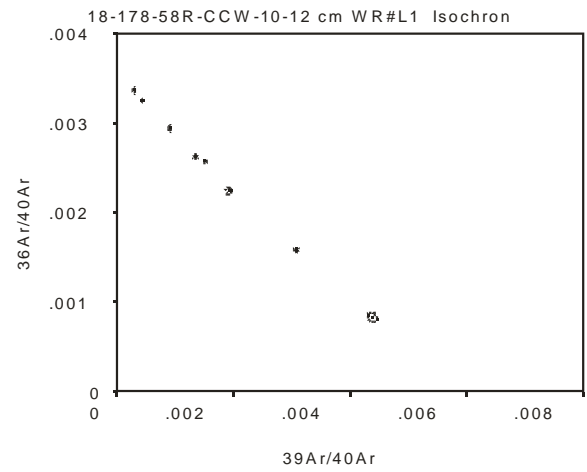
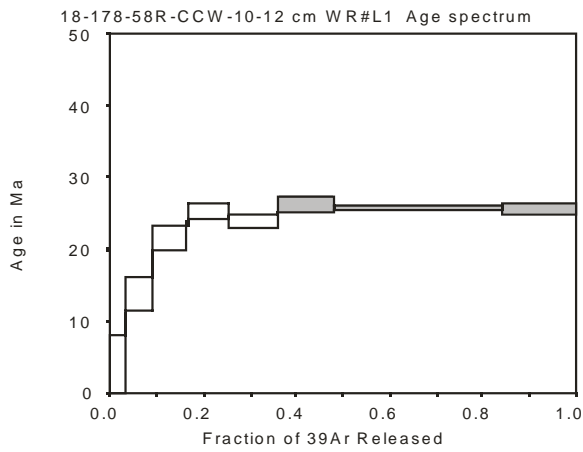
Whole Rock (WR)

A whole rock separate from sample **18-178-59R-01W-70-72 cm** was analyzed. The integrated age 27.73 ± 0.49 Ma) is within broad error of the plateau age (27.73 ± 0.74 Ma) and the isochron age (26.39 ± 0.40 Ma). Based on the isochron regression to initial $^{40}\text{Ar}/^{36}\text{Ar}$ (422.0 ± 79.3) this sample has minor excess ^{40}Ar . We prefer the weighted average age of **26.39 ± 0.49 Ma** because of the documented excess ^{40}Ar .

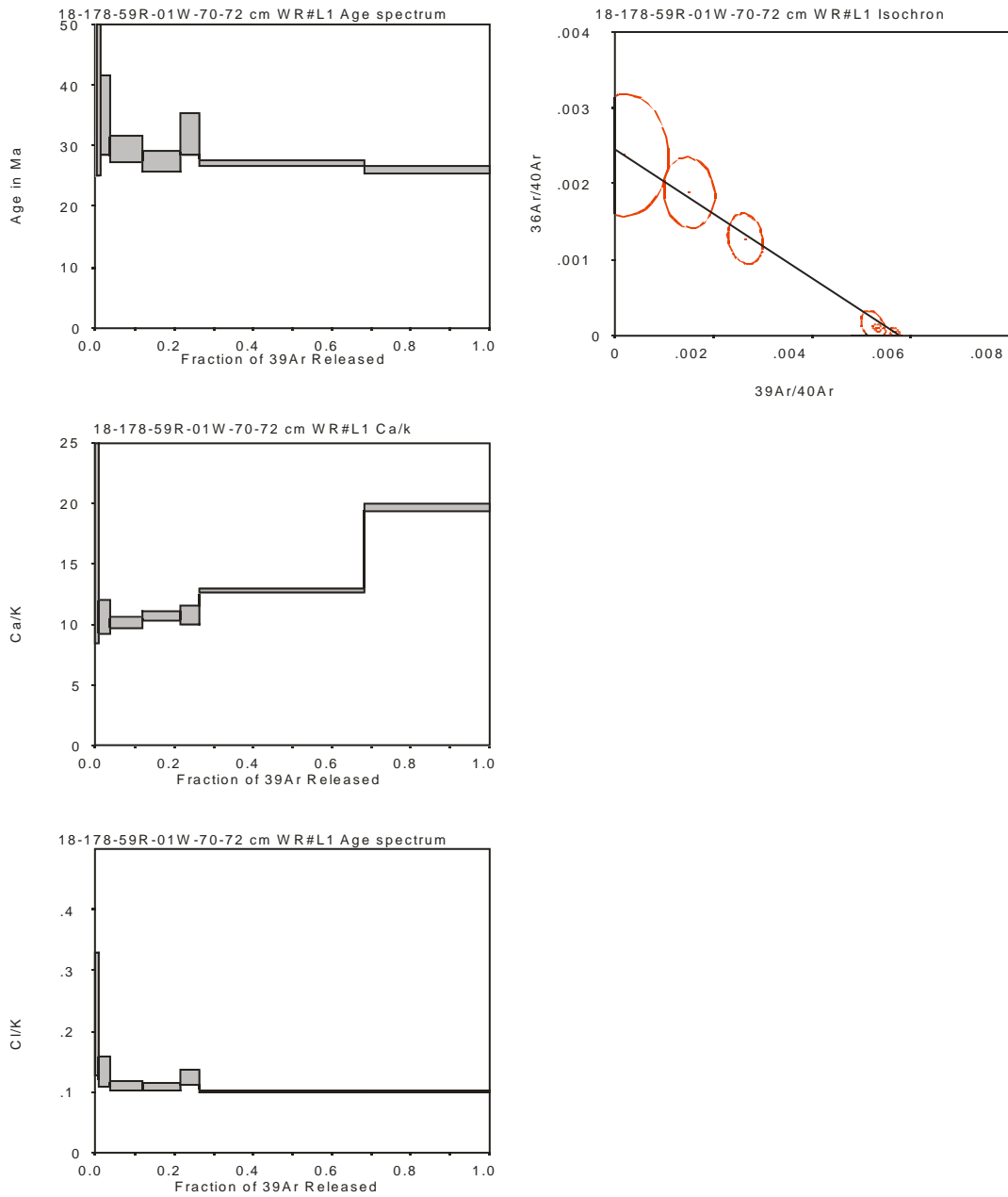
18-178-59R-CCW-30-32 cm

Whole Rock (WR)

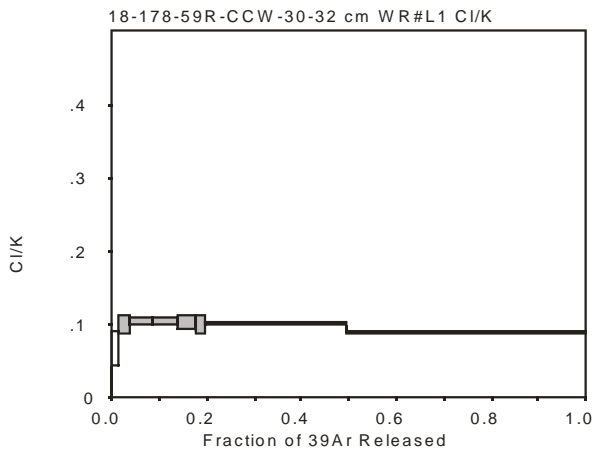
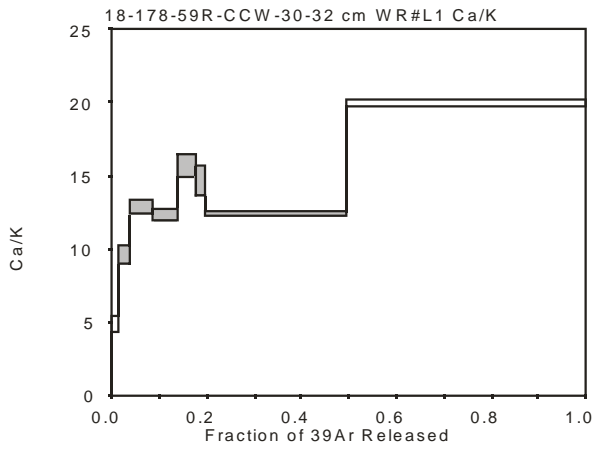
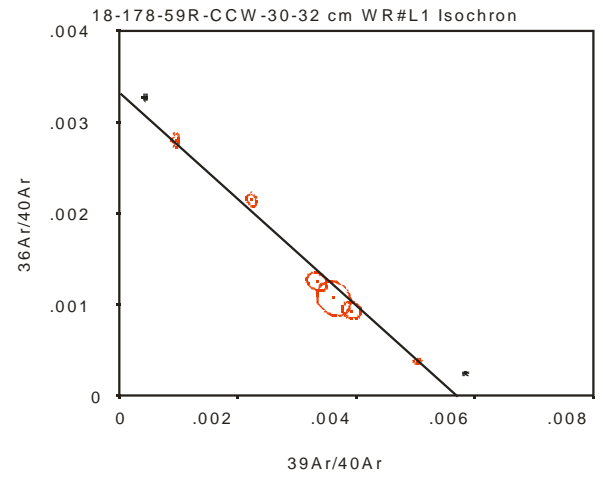
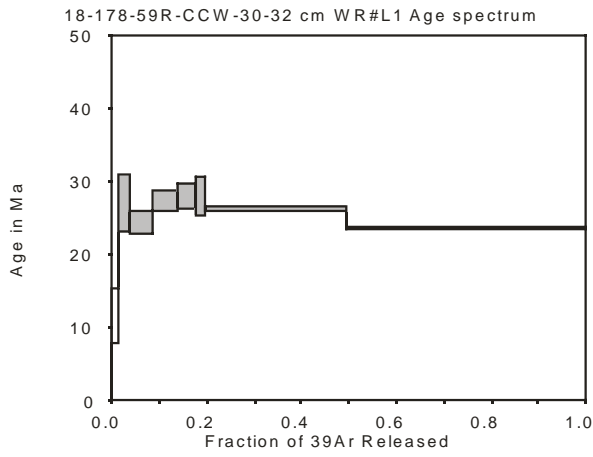
A whole rock separate from sample **18-178-59R-CCW-30-32 cm** was analyzed. A plateau age determination was not possible because the age determinations did not meet all the criteria for a plateau age (>50% of ^{39}Ar gas release), hence a weighted average age is presented. Based on the isochron regression to initial $^{40}\text{Ar}/^{36}\text{Ar}$ (293.8 ± 7.5) this sample was not affect by excess ^{40}Ar . The integrated age 24.80 ± 0.26 Ma) is not within error of the weighted average age (26.44 ± 0.43 Ma) or the isochron age (26.39 ± 0.40 Ma). We prefer the isochron age of **26.39 ± 0.40 Ma** because of the higher precision over the weighted average age.



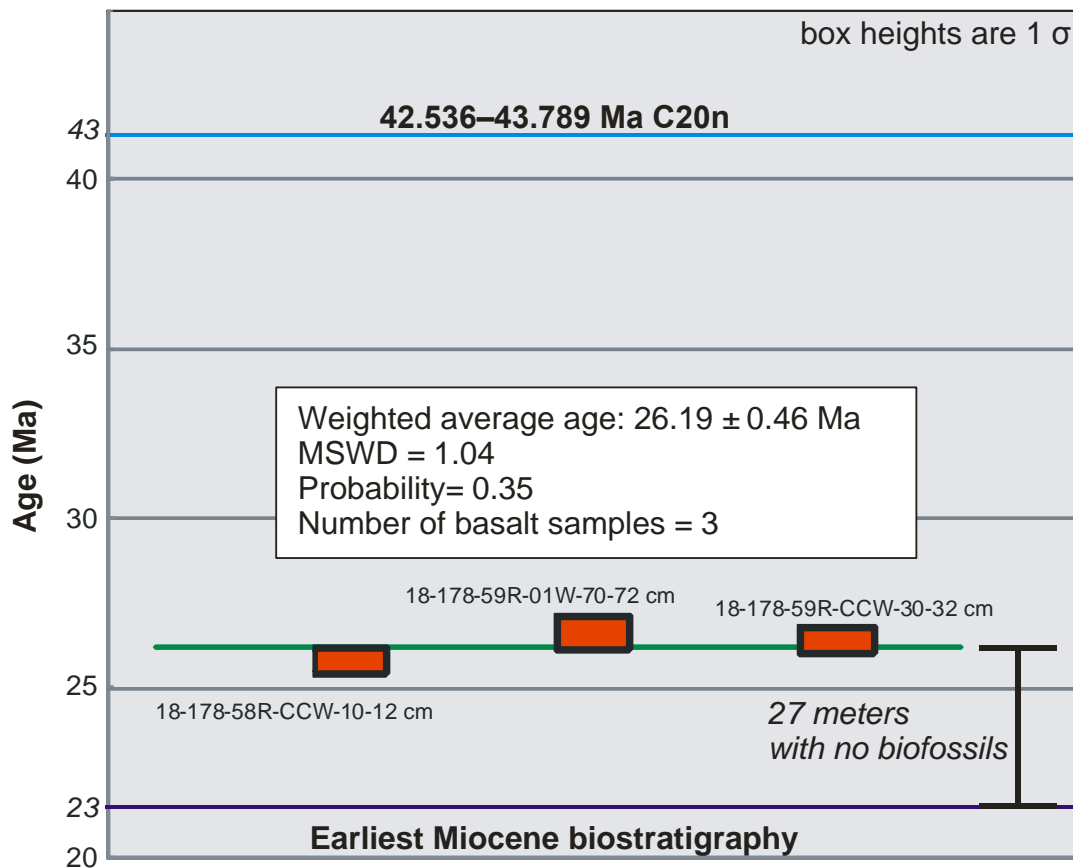
Supplemental Figure 1: $^{40}\text{Ar}/^{39}\text{Ar}$ age spectra, Ca/K and Cl/K ratios for the sample 18-178-58-CCW-10-12cm. Steps filled in grey were used for plateau age determinations.



Supplemental Figure 2: $^{40}\text{Ar}/^{39}\text{Ar}$ age spectra, Ca/K and Cl/K ratios for the sample 18-178-59R-1W-70-72cm. Steps filled in grey were used for plateau age determinations.



Supplemental Figure 3: $^{40}\text{Ar}/^{39}\text{Ar}$ age spectra, Ca/K and Cl/K ratios for the sample 18-178-59R-CCW-30-32cm. Steps filled in grey were used for plateau age determinations.



Supplemental Figure 4: Stratigraphy at Site U1417

The anomaly 20 (42.536-43.789 Ma C20n; Gee and Kent, 2007) age for the basalt bedrock drilled during expedition DSDP leg 18 site 178 was questioned by the ship board scientific party because of an earliest Miocene biostratigraphy age determination for the lower sediments (Kulm and von Huene, 1973). Though the team recovered no micro fossils in the 27 meters above the basalt they inferred the ~20 Ma age discrepancy between the biostratigraphy call and the anomaly 20 age was likely due to the anomaly 20 oceanic basement being covered by a series of pillows (Kulm and von Huene, 1973). We performed $^{40}\text{Ar}/^{39}\text{Ar}$ dating on whole rock phenocryst chips from three different bedrock samples recovered from site 178 and got overlapping preferred ages (plateau and isochron age determinations) indicating a near geologically simultaneous magmatic event with a weighted average age of 26.19 ± 0.46 Ma. These results confirm the initial concerns of the DSDP leg 18 scientific party and provides a more robust bedrock age for calculating sedimentation rates for the lowest recovered cores from IODP Expedition 341 site U1417. In addition Turner et al. (1973) hypothesised a rough estimate age for the basal basalt at site 178 as ~23 Ma and

inferred the Site 178 basalt as being related to the Pratt-Welker seamount chain. Turner et al. (1973) also linked this magmatic event to a small hump near site 178 that maybe a volcanic edifice. The preponderance evidence indicates the basalt at the bottom of site 178 is not ~40 Ma oceanic basement, but instead is at its documented youngest **25.80 ± 0.36 Ma** pillow basalt.

Literature

- Benowitz J. A., Layer P. W., and Vanlaningham S., (2014). Persistent long-term (c. 24 Ma) exhumation in the Eastern Alaska Range constrained by stacked thermochronology. *Geol. Soc. Sp.* 378(1), 225-243. <https://doi.org/10.1144/SP378.12>
- Gee, J.S., Kent, D. V., 2007. Source of Oceanic Magnetic Anomalies and the Geomagnetic Polarity Timescale, in: *Treatise on Geophysics*. pp. 455–507. <https://doi.org/10.1016/B978-044452748-6.00097-3>
- Kulm, L.D. and Von Huene, R., 1973. Initial reports of the deep sea drilling project. XVIII: Washington, DC, US Govt. Printing Office.
- Layer P.W., Hall C.M., and York D., (1987). The derivation of $^{40}\text{Ar}/^{39}\text{Ar}$ age spectra of single grains of hornblende and biotite by laser step heating, *Geophys. Res. Lett.* 14, 757-760. <https://doi.org/10.1029/GL014i007p00757>
- McDougall I., and Harrison T.M., (1999). *Geochronology and Thermochronology by the $^{40}\text{Ar}/^{39}\text{Ar}$ method*-2nd ed, Oxford University Press, New York, 269pp.
- Renne P. R., Mundil R., Balco G., Min K. and Ludwig K. R. (2010). Joint determination of 40K decay constants and $^{40}\text{Ar}^*/^{40}\text{K}$ for the Fish Canyon sanidine standard, and improved accuracy for $^{40}\text{Ar}/^{39}\text{Ar}$ geochronology. *Geochim. Cosmochim. Ac.* 74(18), 5349. <https://doi.org/10.1016/j.gca.2010.06.017>
- Renne P. R., Deino A. L., Walter R. C., Turrin B. D., Swisher C. C., Becker T. A., Curtis G.H., Sharp W.D. and Jaouni A. R., (1994). Intercalibration of astronomical and radioisotopic time. *Geology* 22(9), 783-786. <https://doi.org/10.1130/0091-7613>

Samson S. D. and Alexander E. C., (1987). Calibration of the interlaboratory $^{40}\text{Ar}/^{39}\text{Ar}$ dating standard, MMhb1. *Chem. Geol.* 66, 27-34. [https://doi.org/10.1016/0168-9622\(87\)90025-X](https://doi.org/10.1016/0168-9622(87)90025-X)

Steiger R.H. and Jaeger E., (1977). Subcommittee on geochronology: Convention on the use of decay constants in geo and cosmochronology, *Earth Planet. Sc. Lett.* 36, 359-362.

Turner, D.L., Forbes, R.B., Naeser, C.W., 1973. Radiometric ages of kodiak seamount and giacomini guyot, gulf of alaska: implications for circum-pacific tectonics. *Science* 182, 579–81. <https://doi.org/10.1126/science.182.4112.579>

York D., Hall C.M., Yanase Y., Hanes J.A. and Kenyon W.J. (1981). $^{40}\text{Ar}/^{39}\text{Ar}$ dating of terrestrial minerals with a continuous laser, *Geophys. Res. Lett.* 8, 1136-1138. <https://doi.org/10.1029/GL008i011p01136>

Appendix B: Data Site U1417

Sample	Text identif.	Depth (m) CCSF-B	Age (ma)	Sedrate (cm/ka)	Ba (ppm)	Ba/Al (ppm/%)	Si (wt%)	Al (wt%)	Fe (wt%)	S (wt%)
341 U1417 A 1 H 1	CAKE4632181	1.27	0.0094	13.55	768	86.99	25.49	8.83	5.81	0.08
341 U1417 A 1 H 3	CAKE4632301	3.87	0.0286	13.55	754	83.26	25.46	9.06	5.91	0.19
341 U1417 A 2 H 2	CAKE4632821	9.45	0.0698	13.55	818	95.28	26.03	8.59	5.45	0.20
341 U1417 A 2 H 4	CAKE4632941	12.05	0.0890	13.55	808	91.96	24.94	8.79	5.85	0.04
341 U1417 A 2 H 6	CAKE4633061	14.64	0.1081	13.55	968	113.80	26.02	8.51	5.68	0.18
341 U1417 A 3 H 2	CUBE4642281	17.79	0.1313	13.55	967	112.77	25.87	8.57	5.71	0.24
341 U1417 A 3 H 3	CAKE4633511	20.27	0.1497	13.55	723	86.67	25.21	8.34	5.39	0.18
341 U1417 A 3 H 5	CAKE4633631	22.87	0.1688	13.55	782	87.47	25.75	8.94	6.16	0.14
341 U1417 A 4 H 2	CUBE4639111	26.44	0.1952	13.55	1063	128.24	25.88	8.29	5.92	0.26
341 U1417 A 4 H 3	CAKE4634041	28.86	0.2130	13.55	776	92.44	24.95	8.39	6.11	0.13
341 U1417 A 4 H 5	CAKE4634161	31.38	0.2317	13.55	802	87.99	25.98	9.11	5.78	0.17
341 U1417 A 5 H 2	CUBE4640091	35.20	0.2598	13.55	832	91.12	25.94	9.13	5.94	0.09
341 U1417 A 5 H 3	CAKE4634591	37.59	0.2775	13.55	828	93.73	25.45	8.83	5.85	0.16
341 U1417 A 5 H 5	CAKE4634711	40.19	0.2967	13.55	790	86.42	25.86	9.14	6.15	0.15
341 U1417 A 6 H 1	CUBE4640471	42.32	0.3124	13.55	913	105.63	25.92	8.64	6.15	0.18
341 U1417 A 7 H 2	CUBE4641371	44.55	0.3289	13.55	816	92.04	25.31	8.87	6.01	0.22
341 U1417 A 7 H 3	CAKE4635361	45.90	0.3389	13.55	824	91.31	26.27	9.02	5.64	0.17
341 U1417 A 7 H 5	CUBE4641381	48.39	0.3572	13.55	1459	170.47	25.45	8.56	6.05	0.18
341 U1417 A 7 H 5	CAKE4635481	48.50	0.3580	13.55	1366	159.01	25.54	8.59	5.75	0.16
341 U1417 A 8 H 1	CAKE4636051	52.14	0.3849	13.55	700	78.63	25.29	8.90	6.01	0.15
341 U1417 A 8 H 2	CUBE4642861	52.27	0.3859	13.55	780	85.88	25.92	9.08	5.85	0.12
341 U1417 A 9 H 2	CUBE4643371	57.94	0.4277	13.55	839	92.75	25.80	9.05	5.91	0.09
341 U1417 A 9 H 3	CAKE4636751	60.39	0.4458	13.55	834	96.02	26.20	8.69	5.41	0.16
341 U1417 A 9 H 5	CUBE4643301	62.90	0.4644	13.55	1054	117.34	25.57	8.98	5.90	0.12
341 U1417 A 10 H 2	CUBE4643701	66.93	0.4941	13.55	793	90.31	26.78	8.78	5.43	
341 U1417 A 10 H 3	CAKE4637341	69.41	0.5130	12.95	951	120.10	26.85	7.92	5.79	0.79
341 U1417 A 10 H 5	CUBE4643511	71.96	0.5327	12.95	1280	155.52	26.07	8.23	5.47	0.24
341 U1417 A 11 H 2	CUBE4644341	78.34	0.5819	12.95	955	116.18	28.03	8.22	4.89	0.03
341 U1417 A 11 H 3	CAKE4637721	80.79	0.6008	12.95	661	74.73	25.22	8.84	6.22	0.03
341 U1417 A 11 H 5	CUBE4644351	82.82	0.6165	12.95	761	85.07	25.95	8.95	5.90	0.02
341 U1417 A 12 H 2	CUBE4644681	88.11	0.6573	12.95	639	73.61	24.91	8.68	6.09	0.03
341 U1417 A 12 H 3	CAKE4638491	90.54	0.6761	12.95	912	103.11	25.68	8.84	6.26	0.07
341 U1417 A 12 H 5	CUBE4644691	93.02	0.6952	12.95	776	87.06	26.33	8.91	5.91	0.03
341 U1417 A 13 H 2	CUBE4644931	97.77	0.7319	12.95	1272	156.97	25.68	8.10	5.24	0.35
341 U1417 A 13 H 3	CAKE4638931	100.20	0.7507	12.95	951	113.14	27.44	8.41	5.25	0.13
341 U1417 A 13 H 5	CUBE4644941	102.68	0.7698	12.95	747	84.11	25.95	8.88	5.85	0.11
341 U1417 A 14 H 2	CUBE4645381	105.05	0.7881	12.95	763	85.40	25.80	8.93	5.84	0.12
341 U1417 A 14 H 3	CAKE4639521	107.48	0.8069	12.95	822	94.52	25.90	8.70	5.78	0.02
341 U1417 A 14 H 5	CUBE4645391	109.95	0.8259	12.95	760	85.47	25.99	8.89	5.94	0.12
341 U1417 A 15 H 2	CUBE4645801	114.40	0.8603	12.95	824	92.67	26.24	8.89	5.87	0.12
341 U1417 A 15 H 3	CAKE4640001	116.83	0.8791	12.95	741	83.43	25.67	8.88	5.99	0.15
341 U1417 A 15 H 5	CUBE4645811	119.30	0.8981	12.95	1041	114.55	26.00	9.09	5.71	0.11

Sample						Text identif.	Depth (m) CCSF-B	Age (ma)	Sedrate (cm/ka)	Ba (ppm)	Ba/Al (ppm/%)	Si (wt%)	Al (wt%)	Fe (wt%)	S (wt%)
341	U1417	A	16	H	2	CUBE4646011	123.12	0.9276	12.95	619	70.79	25.45	8.74	6.45	0.10
341	U1417	A	16	H	3	CAKE4641041	125.60	0.9467	12.95	753	85.65	26.40	8.79	6.13	0.07
341	U1417	A	16	H	5	CUBE4646021	128.10	0.9660	12.95	753	85.80	26.52	8.78	5.64	0.07
341	U1417	A	17	H	2	CUBE4646411	131.34	0.9911	12.95	749	84.68	25.65	8.84	6.12	0.08
341	U1417	A	17	H	3	CAKE4640921	133.75	1.0167	7.50	1117	130.59	25.35	8.55	5.60	0.16
341	U1417	A	17	H	5	CUBE4646421	136.27	1.0503	7.50	763	86.47	26.12	8.82	5.87	0.20
341	U1417	A	18	H	2	CUBE4646891	139.81	1.0975	7.50	790	88.53	26.38	8.92	5.76	0.12
341	U1417	A	18	H	5	CUBE4646931	143.24	1.1432	7.50	747	84.66	25.88	8.82	5.91	0.20
341	U1417	C	17	H	2	CUBE4668591	144.03	1.1538	7.50	773	88.73	26.69	8.71	5.88	0.09
341	U1417	C	17	H	4	CUBE4668601	146.63	1.1884	7.50	1678	214.20	27.56	7.83	5.04	0.03
341	U1417	A	19	H	2	CUBE4647381	148.08	1.2077	7.50	738	84.15	25.62	8.77	6.01	0.02
341	U1417	C	17	H	5	CAKE4662111	149.09	1.2213	7.50	2375	291.37	26.52	8.15	5.53	0.14
341	U1417	A	19	H	3	CAKE4642121	150.52	1.2402	7.50	744	84.27	25.83	8.83	6.00	0.12
341	U1417	A	19	H	5	CUBE4647421	152.03	1.2604	7.50	1140	130.61	26.56	8.73	5.38	0.08
341	U1417	C	18	H	2	CUBE4669331	152.79	1.2706	7.50	1119	126.97	26.77	8.81	5.67	0.06
341	U1417	C	18	H	3	CAKE4662631	155.27	1.3036	7.50	699	80.77	26.07	8.65	6.21	0.11
341	U1417	C	18	H	5	CUBE4669341	157.88	1.3384	7.50	784	88.22	26.56	8.89	5.88	0.02
341	U1417	A	21	H	2	CUBE4648041	159.17	1.3555	7.50	1022	113.85	25.77	8.98	5.94	0.26
341	U1417	A	21	H	2	CAKE4642741	160.29	1.3705	7.50	1023	121.94	26.43	8.39	5.65	0.15
341	U1417	C	19	H	1	CAKE4663221	161.69	1.3893	7.50	748	88.99	24.98	8.41	5.75	0.10
341	U1417	C	19	H	2	CUBE4669901	162.94	1.4059	7.50	842	94.46	26.04	8.91	5.87	0.13
341	U1417	A	22	H	2	CUBE4648751	164.00	1.4200	7.50	2343	285.59	25.79	8.20	5.82	0.10
341	U1417	C	20	H	2	CUBE4670201	165.04	1.4339	7.50	743	82.48	25.37	9.01	6.25	0.14
341	U1417	A	22	H	2	CAKE4643241	165.14	1.4352	7.50	757	85.74	26.09	8.83	5.78	0.13
341	U1417	C	20	H	3	CAKE4663391	167.51	1.4669	7.50	1179	136.32	26.29	8.65	5.78	0.02
341	U1417	C	20	H	5	CUBE4670211	170.14	1.5017	7.50	1023	124.69	27.30	8.20	5.53	0.13
341	U1417	C	21	H	2	CUBE4670531	174.77	1.5568	7.50	1335	157.15	26.37	8.50	6.05	0.10
341	U1417	C	21	H	3	CAKE4663871	177.24	1.5861	7.50	1268	150.29	26.30	8.44	6.12	0.18
341	U1417	C	21	H	5	CUBE4670541	179.88	1.6175	7.50	845	97.23	26.45	8.69	5.81	0.09
341	U1417	C	22	H	2	CUBE4670901	183.54	1.6665	7.50	910	100.90	26.22	9.02	5.83	0.12
341	U1417	C	22	H	3	CAKE4664501	185.63	1.6955	7.50	912	107.22	26.96	8.51	5.56	0.08
341	U1417	C	22	H	5	CUBE4670911	187.87	1.7267	7.50	840	95.09	26.15	8.83	5.62	0.02
341	U1417	C	23	H	1	CUBE4671201	193.10	1.7996	7.50	1612	185.03	26.15	8.71	6.01	0.12
341	U1417	C	23	H	2	CAKE4664661	194.18	1.8145	7.50	804	91.18	26.64	8.82	5.78	0.12
341	U1417	C	24	H	2	CUBE4671551	196.38	1.8452	7.50	884	103.09	26.42	8.57	5.97	0.26
341	U1417	C	24	H	4	CAKE4665051	198.58	1.8758	7.50	914	103.15	27.12	8.86	5.74	0.10
341	U1417	C	24	H	6	CUBE4671561	200.82	1.9071	7.50	898	101.41	25.87	8.86	6.01	0.02
341	U1417	D	32	H	2	CAKE4675051	207.15	1.9952	7.50	856	97.07	26.47	8.82	5.87	0.10
341	U1417	D	32	H	3	CUBE4680241	207.95	2.0039	14.50	1169	138.04	26.10	8.47	6.16	0.08
341	U1417	C	25	H	2	CUBE4671871	209.59	2.0181	14.50	1231	140.02	25.31	8.79	6.41	0.11
341	U1417	C	25	H	3	CAKE4665431	211.67	2.0361	14.50	1358	162.69	26.61	8.35	5.54	0.14
341	U1417	D	35	H	2	CAKE4675861	215.99	2.0735	14.50	827	97.77	25.34	8.46	5.69	0.05

Sample					Text identif.	Depth (m) CCSF-B	Age (ma)	Sedrate (cm/ka)	Ba (ppm)	Ba/Al (ppm/%)	Si (wt%)	Al (wt%)	Fe (wt%)	S (wt%)	
341	U1417	D	35	H	3	CUBE4680421	216.86	2.0810	14.50	851	98.64	24.82	8.63	6.25	0.09
341	U1417	C	25	H	2	CUBE4671871	209.59	2.0181	14.50	1231	140.02	25.31	8.79	6.41	0.11
341	U1417	C	25	H	3	CAKE4665431	211.67	2.0361	14.50	1358	162.69	26.61	8.35	5.54	0.14
341	U1417	D	35	H	2	CAKE4675861	215.99	2.0735	14.50	827	97.77	25.34	8.46	5.69	0.05
341	U1417	D	35	H	3	CUBE4680421	216.86	2.0810	14.50	851	98.64	24.82	8.63	6.25	0.09
341	U1417	C	26	H	2	CAKE4665781	218.02	2.0911	14.50	790	90.84	25.11	8.70	5.93	0.12
341	U1417	C	26	H	3	CUBE4672181	219.03	2.0998	14.50	812	90.78	26.28	8.95	5.97	0.08
341	U1417	C	28	H	1	CAKE4666261	221.65	2.1225	14.50	1044	117.69	26.06	8.87	5.99	0.12
341	U1417	C	28	H	2	CUBE4672361	222.14	2.1267	14.50	782	88.36	25.40	8.85	6.39	0.05
341	U1417	D	40	X	2	CUBE4681381	245.38	2.2785	14.50	841	98.51	24.59	8.54	6.27	0.02
341	U1417	D	40	X	2	CAKE4677631	245.74	2.2808	14.50	850	100.37	24.06	8.47	6.14	0.06
341	U1417	D	42	X	2	CUBE4682201	264.44	2.4004	14.50	887	102.00	25.13	8.70	6.11	0.04
341	U1417	D	42	X	2	CAKE4678351	265.60	2.4079	14.50	1011	113.83	25.62	8.88	6.25	0.02
341	U1417	D	43	X	2	CUBE4682881	273.83	2.4605	14.50	1034	117.61	25.17	8.79	6.44	0.02
341	U1417	D	44	X	1	CUBE4683091	282.62	2.5308	8.50	772	95.58	27.00	8.08	5.57	0.02
341	U1417	D	45	X	1	CAKE4679211	288.00	2.5941	8.50	920	111.21	24.42	8.27	6.62	0.05
341	U1417	D	46	X	1	CUBE4683531	293.85	2.6629	8.50	958	110.84	24.86	8.64	6.32	0.07
341	U1417	D	47	X	1	CAKE4680141	305.99	2.8058	8.50	1015	115.38	25.71	8.80	5.90	0.16
341	U1417	D	48	X	1	CUBE4683941	315.52	2.9179	8.50	1010	124.88	25.11	8.09	6.21	0.11
341	U1417	D	48	X	1	CAKE4680771	316.30	2.9271	8.50	1097	125.53	25.65	8.74	5.92	0.07
341	U1417	D	49	X	1	CAKE4681241	325.80	3.0508	6.50	1070	125.87	26.48	8.50	6.20	0.18
341	U1417	D	49	X	3	CUBE4684081	327.45	3.0762	6.50	2689	352.31	26.93	7.63	5.27	0.11
341	U1417	D	51	X	2	CAKE4682361	346.51	3.3694	6.50	2574	327.04	27.04	7.87	5.34	0.13
341	U1417	D	51	X	4	CUBE4684501	348.40	3.3985	6.50	1098	124.52	24.73	8.82	6.23	0.11
341	U1417	D	52	X	2	CUBE4685231	356.31	3.5328	4.00	1162	138.95	25.53	8.36	5.60	0.31
341	U1417	D	53	X	1	CUBE4685311	364.31	3.7328	4.00	840	118.79	26.29	7.07	6.58	0.42
341	U1417	D	54	X	2	CAKE4683911	375.63	4.0158	4.00	1885	370.97	31.40	5.08	3.57	0.04
341	U1417	D	54	X	4	CUBE4685601	378.00	4.0750	4.00	1039	119.99	25.07	8.66	6.27	0.26
341	U1417	D	55	X	1	WDGE4686151	383.58	4.2145	4.00	1017	115.47	25.01	8.81	6.50	0.14
341	U1417	D	55	X	3	WDGE4686181	387.13	4.3033	4.00	1186	132.59	25.03	8.95	6.93	0.38
341	U1417	D	56	X	1	WDGE4686461	393.38	4.4595	4.00	985	119.06	26.08	8.27	5.54	0.20
341	U1417	E	7	R	2	CAKE4689521	401.26	4.6391	4.50	950	111.27	25.41	8.54	5.85	0.04
341	U1417	D	57	X	1	CAKE4685051	403.32	4.6849	4.50	1578	262.90	29.97	6.00	4.49	0.03
341	U1417	D	58	X	1	WDGE4686751	410.83	4.8518	4.50	1015	114.62	24.93	8.86	6.34	0.07
341	U1417	E	8	R	3	CAKE4689991	412.90	4.8978	4.50	1163	129.55	25.39	8.98	6.22	0.11
341	U1417	E	9	R	1	WDGE4691651	418.50	5.0182	5.50	1353	173.66	26.87	7.79	6.29	0.14
341	U1417	D	59	X	1	WDGE4686871	418.82	5.0239	5.50	3079	597.24	31.33	5.16	3.64	0.07
341	U1417	D	59	X	2	CAKE4686051	421.23	5.0677	5.50	1988	376.34	27.56	5.28	5.22	0.05
341	U1417	E	9	R	2	CAKE4690351	421.25	5.0682	5.50	1859	336.09	29.72	5.53	5.19	0.03
341	U1417	E	9	R	4	WDGE4691681	424.26	5.1229	5.50	1015	117.21	26.37	8.66	5.69	0.14
341	U1417	D	59	X	4	WDGE4686911	424.36	5.1246	5.50	1103	125.31	25.31	8.80	6.16	0.19

Sample					Text identif.	Depth (m) CCSF-B	Age (ma)	Sedrate (cm/ka)	Ba (ppm)	Ba/Al (ppm/%)	Si (wt%)	Al (wt%)	Fe (wt%)	S (wt%)	
341	U1417	E	10	R	1	WDGE4692011	428.29	5.1962	5.50	1008	122.23	26.97	8.25	6.27	0.19
341	U1417	E	10	R	2	CAKE4690721	430.95	5.2445	5.50	858	106.23	28.31	8.08	4.88	0.27
341	U1417	E	11	R	1	WDGE4693161	438.02	5.3731	5.50	904	108.99	28.83	8.29	4.89	0.14
341	U1417	D	63	X	1	CUBE4687661	446.89	5.5344	5.50	1008	106.27	25.67	9.49	6.30	0.06
341	U1417	E	13	R	1	CAKE4691451	458.57	5.7467	5.50	884	114.00	28.59	7.75	4.58	0.06
341	U1417	E	14	R	1	CAKE4692571	466.94	5.8989	5.50	978	119.05	27.12	8.21	5.11	0.22
341	U1417	E	15	R	2	CUBE4694441	478.10	6.0509	11.00	421	124.28	35.09	3.39	2.29	0.01
341	U1417	E	15	R	4	CAKE4692451	482.39	6.0899	11.00	783	124.73	29.57	6.28	4.70	0.03
341	U1417	E	15	R	6	CUBE4694451	485.46	6.1178	11.00	1299	141.21	24.89	9.20	6.60	0.18
341	U1417	E	16	R	1	CAKE4692941	487.33	6.1348	11.00	963	121.62	28.06	7.92	4.77	0.13
341	U1417	E	16	R	2	CUBE4694561	488.81	6.1483	11.00	1007	116.72	26.95	8.63	6.04	0.07
341	U1417	E	17	R	2	CAKE4693571	498.71	6.2383	11.00	974	115.23	25.53	8.45	5.32	0.20
341	U1417	E	17	R	3	CUBE4694821	499.24	6.2431	11.00	919	113.85	29.42	8.07	4.33	0.24
341	U1417	E	17	R	4	CUBE4694851	501.35	6.2623	11.00	915	106.84	28.38	8.56	4.69	0.12
341	U1417	E	18	R	1	CAKE4694091	507.00	6.3136	11.00	894	106.77	27.11	8.37	5.40	0.28
341	U1417	E	18	R	3	CUBE4695311	508.70	6.3291	11.00	965	108.59	27.43	8.89	5.33	0.46
341	U1417	E	19	R	1	CUBE4695631	515.84	6.3940	11.00	860	110.53	30.43	7.78	3.63	0.16
341	U1417	E	19	R	2	CAKE4694391	518.27	6.4161	11.00	901	105.34	26.70	8.55	5.20	0.22
341	U1417	E	19	R	3	CUBE4695671	519.87	6.4306	11.00	856	90.80	25.27	9.43	5.93	0.34
341	U1417	E	20	R	1	CAKE4695051	526.45	6.4905	11.00	844	101.69	27.21	8.30	5.01	0.53
341	U1417	E	22	R	1	CUBE4696321	544.50	6.6789	9.50	766	90.79	28.60	8.44	4.91	0.02
341	U1417	E	24	R	1	CAKE4695941	564.74	6.8920	9.50	830	100.13	26.81	8.29	5.76	1.37
341	U1417	E	25	R	1	CAKE4696221	574.85	6.9984	9.50	812	102.07	25.89	7.96	6.34	2.24
341	U1417	E	26	R	1	CAKE4696991	584.46	7.1577	6.00	843	104.16	27.31	8.09	5.09	0.65
341	U1417	E	26	R	3	WDGE4697921	587.28	7.2047	6.00	903	109.08	28.91	8.28	4.53	0.21
341	U1417	E	27	R	1	WDGE4698311	593.90	7.3150	6.00	938	98.51	25.37	9.52	6.94	0.14
341	U1417	E	27	R	3	CAKE4697521	596.41	7.3568	6.00	934	100.38	25.43	9.31	6.30	0.08
341	U1417	E	28	R	1	WDGE4698511	603.22	7.4703	6.00	865	98.51	25.82	8.78	7.56	0.14
341	U1417	E	29	R	1	WDGE4698941	612.97	7.8985	2.00	914	104.28	26.89	8.77	6.27	0.21
341	U1417	E	29	R	3	WDGE4698971	616.09	8.1090	1.00	614	90.49	30.64	6.79	3.06	0.14
341	U1417	E	29	R	5	CAKE4698091	618.76	8.3760	1.00	547	96.22	30.61	5.68	4.25	0.06
341	U1417	E	30	R	1	WDGE4699141	623.15	8.8150	1.00	997	114.65	26.52	8.70	5.53	0.42
341	U1417	E	32	R	2	CAKE4698891	643.84	10.8945	0.99	7547	1096.80	23.75	6.88	5.91	0.20
341	U1417	E	32	R	3	WDGE4699251	644.25	10.9360	0.99	8774	1180.67	26.99	7.43	6.36	0.21
341	U1417	E	35	R	1	CAKE4699671	662.31	12.7634	0.99	981	100.56	24.72	9.75	6.12	0.16
341	U1417	E	35	R	3	WDGE4700581	665.02	13.0376	0.99	854	109.02	28.35	7.83	5.46	1.46
341	U1417	E	36	R	2	WDGE4700591	672.25	13.7692	0.99	902	98.68	27.10	9.14	5.44	0.15
341	U1417	E	37	R	1	CAKE4700081	681.75	14.7305	0.99	1031	135.64	27.48	7.60	6.33	2.87
341	U1417	E	38	R	1	WDGE4701321	690.25	15.5906	0.99	1025	113.38	26.21	9.04	6.29	0.05
341	U1417	E	38	R	3	WDGE4701351	693.16	15.8851	0.99	968	113.95	27.74	8.50	5.27	0.53
341	U1417	E	39	R	1	WDGE4701591	699.87	16.5640	0.99	884	97.67	26.67	9.05	6.72	0.16
341	U1417	E	39	R	3	CAKE4701111	702.77	16.8575	0.99	977	100.81	24.35	9.69	6.06	0.40

Sample					Text identif.	Depth (m) CCSF-B	Age (ma)	TOC (wt%)	Fe-S (wt%)	Fe HR	FeHr/ FeT	Fe-S/ FeT	Fe-S/ FeHR	$\delta^{34}\text{S Py.}$ (‰)	$\delta^{34}\text{S STD}$ (%)	
341	U1417	A	1	H	1	CAKE4632181	1.27	0.0094	0.59	0.04	1.44	0.25	0.01	0.03		
341	U1417	A	1	H	3	CAKE4632301	3.87	0.0286	0.61	0.04	1.39	0.23	0.01	0.03		
341	U1417	A	2	H	2	CAKE4632821	9.45	0.0698	0.63	0.05	1.27	0.23	0.01	0.04		
341	U1417	A	2	H	4	CAKE4632941	12.05	0.0890	0.58	0.01	1.34	0.23	0.00	0.01		
341	U1417	A	2	H	6	CAKE4633061	14.64	0.1081	0.44	0.03	1.04	0.18	0.00	0.03		
341	U1417	A	3	H	2	CUBE4642281	17.79	0.1313	0.46		1.10	0.19				
341	U1417	A	3	H	3	CAKE4633511	20.27	0.1497	0.43	0.02	1.17	0.22	0.00	0.02		
341	U1417	A	3	H	5	CAKE4633631	22.87	0.1688	0.49	0.02	1.33	0.22	0.00	0.01		
341	U1417	A	4	H	2	CUBE4639111	26.44	0.1952	0.57	0.17	0.96	0.16	0.03	0.18	-40.0	0.43
341	U1417	A	4	H	3	CAKE4634041	28.86	0.2130	0.34	0.01	1.06	0.17	0.00	0.01		
341	U1417	A	4	H	5	CAKE4634161	31.38	0.2317	0.78	0.02	1.30	0.22	0.00	0.02		
341	U1417	A	5	H	2	CUBE4640091	35.20	0.2598	0.60	0.00	1.05	0.18	0.00	0.00		
341	U1417	A	5	H	3	CAKE4634591	37.59	0.2775	0.57	0.03	1.25	0.21	0.01	0.03		
341	U1417	A	5	H	5	CAKE4634711	40.19	0.2967	0.56	0.02	1.28	0.21	0.00	0.02		
341	U1417	A	6	H	1	CUBE4640471	42.32	0.3124	0.50	0.10	1.19	0.19	0.02	0.08		
341	U1417	A	7	H	2	CUBE4641371	44.55	0.3289	0.60		1.09	0.18				
341	U1417	A	7	H	3	CAKE4635361	45.90	0.3389	0.89	0.04	1.38	0.24	0.01	0.03		
341	U1417	A	7	H	5	CUBE4641381	48.39	0.3572	0.39		0.99	0.16				
341	U1417	A	7	H	5	CAKE4635481	48.50	0.3580	0.51	0.00	0.94	0.16	0.00	0.00		
341	U1417	A	8	H	1	CAKE4636051	52.14	0.3849	0.60	0.02	1.27	0.21	0.00	0.02		
341	U1417	A	8	H	2	CUBE4642861	52.27	0.3859	0.68		1.13	0.19				
341	U1417	A	9	H	2	CUBE4643371	57.94	0.4277	0.58		1.08	0.18				
341	U1417	A	9	H	3	CAKE4636751	60.39	0.4458	0.61	0.00	1.19	0.22	0.00	0.00		
341	U1417	A	9	H	5	CUBE4643301	62.90	0.4644	0.53		0.95	0.16				
341	U1417	A	10	H	2	CUBE4643701	66.93	0.4941			0.00	0.00				
341	U1417	A	10	H	3	CAKE4637341	69.41	0.5130	0.66	0.67	1.44	0.25	0.12	0.46	-31.7	0.36
341	U1417	A	10	H	5	CUBE46443511	71.96	0.5327	0.42		0.83	0.15				
341	U1417	A	11	H	2	CUBE4644341	78.34	0.5819	0.49	0.01	0.85	0.17	0.00	0.02		
341	U1417	A	11	H	3	CAKE4637721	80.79	0.6008	0.53	0.01	1.13	0.18	0.00	0.01		
341	U1417	A	11	H	5	CUBE4644351	82.82	0.6165	0.62	0.02	1.05	0.18	0.00	0.02		
341	U1417	A	12	H	2	CUBE4644681	88.11	0.6573	0.48	0.02	1.13	0.19	0.00	0.02		
341	U1417	A	12	H	3	CAKE4638491	90.54	0.6761	0.50	0.02	1.11	0.18	0.00	0.02		
341	U1417	A	12	H	5	CUBE4644691	93.02	0.6952	0.56	0.01	1.10	0.19	0.00	0.01		
341	U1417	A	13	H	2	CUBE4644931	97.77	0.7319	0.56		0.76	0.14				
341	U1417	A	13	H	3	CAKE4638931	100.20	0.7507	0.48	0.08	0.98	0.19	0.01	0.08		
341	U1417	A	13	H	5	CUBE4644941	102.68	0.7698	0.54	0.02	1.04	0.18	0.00	0.02		
341	U1417	A	14	H	2	CUBE4645381	105.05	0.7881	0.54	0.02	1.01	0.17	0.00	0.02		
341	U1417	A	14	H	3	CAKE4639521	107.48	0.8069	0.55	0.00	1.13	0.20	0.00	0.00		
341	U1417	A	14	H	5	CUBE4645391	109.95	0.8259	0.53	0.00	0.96	0.16	0.00	0.00		
341	U1417	A	15	H	2	CUBE4645801	114.40	0.8603	0.50	0.00	1.03	0.18	0.00	0.00		
341	U1417	A	15	H	3	CAKE4640001	116.83	0.8791	0.53	0.02	1.11	0.18	0.00	0.01		
341	U1417	A	15	H	5	CUBE4645811	119.30	0.8981	0.59	0.00	1.05	0.18	0.00	0.00		

Sample	Text identif.					Depth (m)	Age	TOC	Fe-S	Fe	FeHr/	Fe-S/	Fe-S/	$\delta^{34}\text{S Py.}$	$\delta^{34}\text{S STD}$
						CCSF-B	(ma)	(wt%)	(wt%)	HR	FeT	FeT	FeHR	(‰)	(%)
341	U1417	A	16	H	2	CUBE4646011	123.12	0.9276	0.45	0.00	0.99	0.15	0.00	0.00	
341	U1417	A	16	H	3	CAKE4641041	125.60	0.9467	0.42	0.01	0.95	0.15	0.00	0.01	
341	U1417	A	16	H	5	CUBE4646021	128.10	0.9660	0.52	0.04	1.05	0.19	0.01	0.04	
341	U1417	A	17	H	2	CUBE4646411	131.34	0.9911	0.53		1.00	0.16			
341	U1417	A	17	H	3	CAKE4640921	133.75	1.0167	0.42	0.07	0.99	0.18	0.01	0.08	
341	U1417	A	17	H	5	CUBE4646421	136.27	1.0503	0.51		0.94	0.16			
341	U1417	A	18	H	2	CUBE4646891	139.81	1.0975	0.49	0.03			0.01		
341	U1417	A	18	H	5	CUBE4646931	143.24	1.1432	0.55		0.98	0.17			
341	U1417	C	17	H	2	CUBE4668591	144.03	1.1538	0.46	0.01	0.99	0.17	0.00	0.01	
341	U1417	C	17	H	4	CUBE4668601	146.63	1.1884	0.22	0.00	0.55	0.11	0.00	0.01	
341	U1417	A	19	H	2	CUBE4647381	148.08	1.2077	0.56	0.00	0.93	0.16	0.00	0.00	
341	U1417	C	17	H	5	CAKE4662111	149.09	1.2213	0.29	0.03	0.93	0.17	0.01	0.03	
341	U1417	A	19	H	3	CAKE4642121	150.52	1.2402	0.50	0.00	1.06	0.18	0.00	0.00	
341	U1417	A	19	H	5	CUBE4647421	152.03	1.2604	0.37	0.00	0.81	0.15	0.00	0.00	
341	U1417	C	18	H	2	CUBE4669331	152.79	1.2706	0.37	0.00	0.83	0.15	0.00	0.00	
341	U1417	C	18	H	3	CAKE4662631	155.27	1.3036	0.31	0.00	1.00	0.16	0.00	0.00	
341	U1417	C	18	H	5	CUBE4669341	157.88	1.3384	0.49	0.00	1.00	0.17	0.00	0.00	
341	U1417	A	21	H	2	CUBE4648041	159.17	1.3555	0.45		0.93	0.16			
341	U1417	A	21	H	2	CAKE4642741	160.29	1.3705	0.31	0.05	0.90	0.16	0.01	0.06	
341	U1417	C	19	H	1	CAKE4663221	161.69	1.3893	0.44	0.00	0.95	0.17	0.00	0.00	
341	U1417	C	19	H	2	CUBE4669901	162.94	1.4059	0.50	0.00	0.96	0.16	0.00	0.00	
341	U1417	A	22	H	2	CUBE4648751	164.00	1.4200	0.20	0.00	0.77	0.13	0.00	0.00	
341	U1417	C	20	H	2	CUBE4670201	165.04	1.4339	0.51	0.02	1.12	0.18	0.00	0.02	
341	U1417	A	22	H	2	CAKE4643241	165.14	1.4352	0.53		1.10	0.19			
341	U1417	C	20	H	3	CAKE4663391	167.51	1.4669	0.43	0.01	1.04	0.18	0.00	0.01	
341	U1417	C	20	H	5	CUBE4670211	170.14	1.5017	0.38	0.03	0.97	0.18	0.00	0.03	
341	U1417	C	21	H	2	CUBE4670531	174.77	1.5568	0.35	0.02	0.85	0.14	0.00	0.02	
341	U1417	C	21	H	3	CAKE4663871	177.24	1.5861	0.28	0.06	0.92	0.15	0.01	0.07	
341	U1417	C	21	H	5	CUBE4670541	179.88	1.6175	0.40	0.00	0.78	0.13	0.00	0.00	
341	U1417	C	22	H	2	CUBE4670901	183.54	1.6665	0.46	0.00	1.10	0.19	0.00	0.00	
341	U1417	C	22	H	3	CAKE4664501	185.63	1.6955	0.57	0.01	0.89	0.16	0.00	0.02	
341	U1417	C	22	H	5	CUBE4670911	187.87	1.7267	0.48	0.00	0.91	0.16	0.00	0.00	
341	U1417	C	23	H	1	CUBE4671201	193.10	1.7996	0.25	0.00	0.92	0.15	0.00	0.00	
341	U1417	C	23	H	2	CAKE4664661	194.18	1.8145	0.39	0.02	1.06	0.18	0.00	0.02	
341	U1417	C	24	H	2	CUBE4671551	196.38	1.8452	0.38	0.17	1.02	0.17	0.03	0.17	-5.0
341	U1417	C	24	H	4	CAKE4665051	198.58	1.8758	0.38	0.00	0.93	0.16	0.00	0.00	0.17
341	U1417	C	24	H	6	CUBE4671561	200.82	1.9071	0.42	0.01	0.90	0.15	0.00	0.01	
341	U1417	D	32	H	2	CAKE4675051	207.15	1.9952	0.41	0.00	0.92	0.16	0.00	0.00	
341	U1417	D	32	H	3	CUBE4680241	207.95	2.0039	0.29	0.00	0.83	0.13	0.00	0.00	
341	U1417	C	25	H	2	CUBE4671871	209.59	2.0181	0.30	0.00	0.91	0.14	0.00	0.00	
341	U1417	C	25	H	3	CAKE4665431	211.67	2.0361	0.31	0.03	0.82	0.15	0.00	0.03	
341	U1417	D	35	H	2	CAKE4675861	215.99	2.0735	0.45	0.04	1.21	0.21	0.01	0.03	

Sample	Text identif.			Depth (m)	Age	TOC	Fe-S	Fe	FeHr/	Fe-S/	Fe-S/	$\delta^{34}\text{S Py.}$	$\delta^{34}\text{S STD}$			
				CCSF-B	(ma)	(wt%)	(wt%)	HR	FeT	FeT	FeHR	(‰)	(%)			
341	U1417	D	35	H	3	CUBE4680421	216.86	2.0810	0.33	0.00	1.14	0.18	0.00	0.00		
341	U1417	C	25	H	2	CUBE4671871	209.59	2.0181	0.30	0.00	0.91	0.14	0.00	0.00		
341	U1417	C	25	H	3	CAKE4665431	211.67	2.0361	0.31	0.03	0.82	0.15	0.00	0.03		
341	U1417	D	35	H	2	CAKE4675861	215.99	2.0735	0.45	0.04	1.21	0.21	0.01	0.03		
341	U1417	D	35	H	3	CUBE4680421	216.86	2.0810	0.33	0.00	1.14	0.18	0.00	0.00		
341	U1417	C	26	H	2	CAKE4665781	218.02	2.0911	0.48	0.02	1.17	0.20	0.00	0.02		
341	U1417	C	26	H	3	CUBE4672181	219.03	2.0998	0.46	0.01	0.98	0.17	0.00	0.01		
341	U1417	C	28	H	1	CAKE4666261	221.65	2.1225	0.48	0.00	1.08	0.18	0.00	0.00		
341	U1417	C	28	H	2	CUBE4672361	222.14	2.1267	0.42	0.03	1.15	0.18	0.01	0.03		
341	U1417	D	40	X	2	CUBE4681381	245.38	2.2785	0.27	0.00	1.11	0.18	0.00	0.00		
341	U1417	D	40	X	2	CAKE4677631	245.74	2.2808	0.41	0.05	1.52	0.25	0.01	0.03	-9.5	0.01
341	U1417	D	42	X	2	CUBE4682201	264.44	2.4004	0.41	0.01	1.20	0.20	0.00	0.01	-11.8	
341	U1417	D	42	X	2	CAKE4678351	265.60	2.4079	0.44	0.00	1.07	0.17	0.00	0.00		
341	U1417	D	43	X	2	CUBE4682881	273.83	2.4605	0.35	0.00	1.13	0.18	0.00	0.00		
341	U1417	D	44	X	1	CUBE4683091	282.62	2.5308	0.36	0.00	0.92	0.16	0.00	0.00		
341	U1417	D	45	X	1	CAKE4679211	288.00	2.5941	0.30	0.06	1.06	0.16	0.01	0.06	51.0	0.09
341	U1417	D	46	X	1	CUBE4683531	293.85	2.6629	0.23	0.00	0.90	0.14	0.00	0.00		
341	U1417	D	47	X	1	CAKE4680141	305.99	2.8058	0.49	0.04	1.21	0.20	0.01	0.03	-26.4	0.39
341	U1417	D	48	X	1	CUBE4683941	315.52	2.9179	0.33	0.04	0.87	0.14	0.01	0.05	42.7	0.08
341	U1417	D	48	X	1	CAKE4680771	316.30	2.9271	0.44	0.06	0.98	0.17	0.01	0.06	-32.0	0.28
341	U1417	D	49	X	1	CAKE4681241	325.80	3.0508	0.39	0.05	0.90	0.14	0.01	0.05		
341	U1417	D	49	X	3	CUBE4684081	327.45	3.0762	0.19	0.00	0.53	0.10	0.00	0.00		
341	U1417	D	51	X	2	CAKE4682361	346.51	3.3694	0.23	0.00	0.56	0.10	0.00	0.00		
341	U1417	D	51	X	4	CUBE4684501	348.40	3.3985	0.24	0.00	1.16	0.19	0.00	0.00		
341	U1417	D	52	X	2	CUBE4685231	356.31	3.5328	0.33	0.20	1.01	0.18	0.04	0.20	-33.6	0.58
341	U1417	D	53	X	1	CUBE4685311	364.31	3.7328	0.31	0.25	1.28	0.19	0.04	0.20	-36.1	0.01
341	U1417	D	54	X	2	CAKE4683911	375.63	4.0158	0.27		0.54	0.15				
341	U1417	D	54	X	4	CUBE4685601	378.00	4.0750	0.46	0.11	1.51	0.24	0.02	0.07	-15.9	0.34
341	U1417	D	55	X	1	WDGE4686151	383.58	4.2145	0.36	0.00	1.34	0.21	0.00	0.00		
341	U1417	D	55	X	3	WDGE4686181	387.13	4.3033	0.37	0.14	1.57	0.23	0.02	0.09		
341	U1417	D	56	X	1	WDGE4686461	393.38	4.4595	0.37	0.05	1.07	0.19	0.01	0.05		
341	U1417	E	7	R	2	CAKE4689521	401.26	4.6391	0.33	0.03	1.15	0.20	0.00	0.02		
341	U1417	D	57	X	1	CAKE4685051	403.32	4.6849	0.26	0.00	0.67	0.15	0.00	0.00		
341	U1417	D	58	X	1	WDGE4686751	410.83	4.8518	0.55	0.06	1.47	0.23	0.01	0.04		
341	U1417	E	8	R	3	CAKE4689991	412.90	4.8978	0.50	0.00	0.79	0.13	0.00	0.00		
341	U1417	E	9	R	1	WDGE4691651	418.50	5.0182	0.20	0.00	0.67	0.11	0.00	0.00		
341	U1417	D	59	X	1	WDGE4686871	418.82	5.0239	0.19	0.00	0.30	0.08	0.00	0.00		
341	U1417	D	59	X	2	CAKE4686051	421.23	5.0677	0.12	0.00	0.48	0.09	0.00	0.00		
341	U1417	E	9	R	2	CAKE4690351	421.25	5.0682	0.15	0.01	0.49	0.09	0.00	0.02		
341	U1417	E	9	R	4	WDGE4691681	424.26	5.1229	0.42	0.11	1.26	0.22	0.02	0.09		
341	U1417	D	59	X	4	WDGE4686911	424.36	5.1246	0.46	0.08	1.29	0.21	0.01	0.06		

Sample					Text identif.	Depth (m) CCSF-B	Age (ma)	TOC (wt%)	Fe-S (wt%)	Fe HR	FeHr/ FeT	Fe-S/ FeT	Fe-S/ FeHR	$\delta^{34}\text{S}$ Py. (‰)	$\delta^{34}\text{S}$ STD (%)	
341	U1417	E	10	R	1	WDGE4692011	428.29	5.1962	0.15	0.07	0.86	0.14	0.01	0.08		
341	U1417	E	10	R	2	CAKE4690721	430.95	5.2445	0.70	0.12	0.81	0.16	0.02	0.14	-37.5	0.37
341	U1417	E	11	R	1	WDGE4693161	438.02	5.3731	0.61	0.05	0.96	0.20	0.01	0.05		
341	U1417	D	63	X	1	CUBE4687661	446.89	5.5344	0.69	0.08	1.40	0.22	0.01	0.05	-20.6	0.40
341	U1417	E	13	R	1	CAKE4691451	458.57	5.7467	0.45	0.05	0.86	0.19	0.01	0.06	-14.1	0.32
341	U1417	E	14	R	1	CAKE4692571	466.94	5.8989	1.76	0.06	1.07	0.21	0.01	0.05	-17.2	0.22
341	U1417	E	15	R	2	CUBE4694441	478.10	6.0509	0.27	0.03	0.31	0.13	0.01	0.09		
341	U1417	E	15	R	4	CAKE4692451	482.39	6.0899	0.12		0.66	0.14				
341	U1417	E	15	R	6	CUBE4694451	485.46	6.1178	0.42	0.14	1.20	0.18	0.02	0.11	-46.5	0.40
341	U1417	E	16	R	1	CAKE4692941	487.33	6.1348	0.76	0.10	0.98	0.20	0.02	0.10	-29.7	0.24
341	U1417	E	16	R	2	CUBE4694561	488.81	6.1483	0.27	0.00	0.87	0.14	0.00	0.00		
341	U1417	E	17	R	2	CAKE4693571	498.71	6.2383	0.42	0.14	1.18	0.22	0.03	0.12	-26.2	0.08
341	U1417	E	17	R	3	CUBE4694821	499.24	6.2431	0.50	0.17	0.89	0.21	0.04	0.19	-27.6	0.02
341	U1417	E	17	R	4	CUBE4694851	501.35	6.2623	0.43	0.10	0.84	0.18	0.02	0.11	-14.8	0.42
341	U1417	E	18	R	1	CAKE4694091	507.00	6.3136	0.37	0.20	1.20	0.22	0.04	0.17	-24.6	0.19
341	U1417	E	18	R	3	CUBE4695311	508.70	6.3291	0.51	0.27	1.27	0.24	0.05	0.22	-27.7	0.24
341	U1417	E	19	R	1	CUBE4695631	515.84	6.3940	0.28	0.13	0.80	0.22	0.04	0.16	9.1	0.94
341	U1417	E	19	R	2	CAKE4694391	518.27	6.4161	0.39	0.09	1.21	0.23	0.02	0.07	4.1	0.15
341	U1417	E	19	R	3	CUBE4695671	519.87	6.4306	0.95	0.25	1.44	0.24	0.04	0.18	-23.4	0.34
341	U1417	E	20	R	1	CAKE4695051	526.45	6.4905	0.73	0.34	1.52	0.30	0.07	0.22	-5.8	0.27
341	U1417	E	22	R	1	CUBE4696321	544.50	6.6789	0.27	0.02	0.94	0.19	0.00	0.02		
341	U1417	E	24	R	1	CAKE4695941	564.74	6.8920	0.89	1.09	2.37	0.41	0.19	0.46	39.2	1.15
341	U1417	E	25	R	1	CAKE4696221	574.85	6.9984	2.73	1.73	2.93	0.46	0.27	0.59	-10.7	0.10
341	U1417	E	26	R	1	CAKE4696991	584.46	7.1577	1.11	0.39	1.42	0.28	0.08	0.28	2.3	0.47
341	U1417	E	26	R	3	WDGE4697921	587.28	7.2047	0.49	0.15	1.03	0.23	0.03	0.15	-19.8	0.30
341	U1417	E	27	R	1	WDGE4698311	593.90	7.3150	0.33	0.00	1.59	0.23	0.00	0.00		
341	U1417	E	27	R	3	CAKE4697521	596.41	7.3568	0.50	0.07	1.23	0.19	0.01	0.05	-4.9	0.14
341	U1417	E	28	R	1	WDGE4698511	603.22	7.4703	0.27	0.10	1.03	0.14	0.01	0.10	52.8	0.11
341	U1417	E	29	R	1	WDGE4698941	612.97	7.8985	0.35	0.19	1.03	0.16	0.03	0.18	58.6	0.32
341	U1417	E	29	R	3	WDGE4698971	616.09	8.1090	0.06	0.14	0.34	0.11	0.04	0.40	19.9	0.47
341	U1417	E	29	R	5	CAKE4698091	618.76	8.3760	0.14	0.07	0.55	0.13	0.02	0.12	15.7	0.29
341	U1417	E	30	R	1	WDGE4699141	623.15	8.8150	1.37	0.31	1.26	0.23	0.06	0.24	-10.9	0.01
341	U1417	E	32	R	2	CAKE4698891	643.84	10.8945	0.07	0.00	0.46	0.08	0.00	0.00		
341	U1417	E	32	R	3	WDGE4699251	644.25	10.9360	0.10	0.00	0.48	0.08	0.00	0.00		
341	U1417	E	35	R	1	CAKE4699671	662.31	12.7634	0.53	0.14	1.25	0.20	0.02	0.11	-27.2	0.45
341	U1417	E	35	R	3	WDGE4700581	665.02	13.0376	1.14	1.46	2.13	0.39	0.27	0.69	-13.6	0.51
341	U1417	E	36	R	2	WDGE4700591	672.25	13.7692	0.62	0.15	1.04	0.19	0.03	0.14	-19.9	0.42
341	U1417	E	37	R	1	CAKE4700081	681.75	14.7305	1.88	2.16	2.83	0.45	0.34	0.76	-10.3	
341	U1417	E	38	R	1	WDGE4701321	690.25	15.5906	0.39	0.02	0.88	0.14	0.00	0.02		
341	U1417	E	38	R	3	WDGE4701351	693.16	15.8851	0.91	0.41	1.20	0.23	0.08	0.34	-9.1	0.06
341	U1417	E	39	R	1	WDGE4701591	699.87	16.5640	0.33	0.14	1.19	0.18	0.02	0.11	-2.8	0.06
341	U1417	E	39	R	3	CAKE4701111	702.77	16.8575	0.57	0.32	1.52	0.25	0.05	0.21	-29.5	0.86

Appendix C: Data U1419

Text Identif.	Depth (m) CCSFB	Age (a)	Fe (wt%)	Cr (ppm)	Cu (ppm)	Ni (ppm)	V (ppm)	Fe/Al	Cr/Al	Cu/Al	Ni/Al	V/Al
U1419D2H2w80	6.88	16870	5.80	104.04	47.86	45.34	182.92	0.66	11.91	5.48	5.19	20.95
U1419D2H2w85	6.92	16880	5.29	101.49	46.93	44.02	175.92	0.61	11.78	5.45	5.11	20.41
CAKE4782041	7.51	17002	5.06	97.00	44.00	42.00	161.00	0.61	11.72	5.32	5.07	19.45
U1419D2H4w65	9.32	17403	6.23	89.50	48.30	40.44	161.09	0.71	10.24	5.53	4.63	18.43
U1419D2H4w102	9.63	17480	5.73	95.90	50.83	42.05	169.67	0.67	11.14	5.90	4.88	19.70
CAKE4782141	10.08	17581	4.77	94.00	40.00	39.00	154.00	0.59	11.71	4.98	4.86	19.18
U1419D2H5w112	11.00	17719	6.40	100.71	47.53	45.07	182.73	0.71	11.13	5.25	4.98	20.19
U1419E2H4w29	12.31	17912	6.17	106.24	48.78	45.03	186.80	0.69	11.94	5.48	5.06	21.00
U1419E2H4w44	12.44	17931	6.26	78.58	32.94	34.44	139.67	0.69	8.65	3.63	3.79	15.37
CAKE4782561	12.57	17950	4.99	98.00	47.00	44.00	164.00	0.62	12.11	5.81	5.44	20.26
U1419E2H5w42	13.71	18128	6.04	99.92	38.93	37.98	159.13	0.69	11.42	4.45	4.34	18.18
U1419E2H5w79	14.02	18180	6.31	128.72	47.86	58.69	189.78	0.70	14.34	5.33	6.54	21.15
U1419D3H3w29	16.84	19568	5.86	108.83	41.98	47.28	181.06	0.70	12.96	5.00	5.63	21.56
CAKE4782671	18.23	20467	4.87	97.00	37.00	41.00	159.00	0.60	11.95	4.56	5.05	19.60
U1419D3H5w43	19.52	20953	5.46	104.68	53.03	45.20	177.34	0.67	12.77	6.47	5.52	21.64
CAKE4782771	20.79	21519	4.96	98.00	37.00	41.00	164.00	0.62	12.24	4.62	5.12	20.48
CAKE4782871	23.36	23034	4.63	96.00	35.00	39.00	157.00	0.58	12.06	4.40	4.90	19.72
U1419E3H6w16	23.45	23220	5.78	101.51	43.37	43.26	170.38	0.66	11.62	4.96	4.95	19.50
U1419E3H6w33	23.59	23370	5.52	101.59	43.05	43.10	174.94	0.65	11.91	5.05	5.05	20.50
U1419E3H6w43	23.68	23417	5.55	98.50	33.36	39.29	143.88	0.67	11.98	4.06	4.78	17.49
U1419E3H7w37	24.88	23974	6.16	106.76	47.90	46.56	182.81	0.70	12.17	5.46	5.31	20.84
U1419D4H2w92	26.08	24497	6.37	106.05	45.05	43.98	181.84	0.71	11.82	5.02	4.90	20.26
U1419D4H2w111	26.25	24568	6.50	107.59	39.72	46.36	177.47	0.71	11.73	4.33	5.06	19.35
U1419D4H3w67	27.14	25058	5.30	96.46	64.34	46.44	164.99	0.64	11.57	7.71	5.57	19.78
U1419D4H3w75	27.19	25096	5.37	102.54	49.14	44.74	177.05	0.66	12.69	6.08	5.54	21.91
U1419D4H4w129	28.90	25712	6.29	99.44	46.51	41.03	153.95	0.72	11.43	5.34	4.71	17.69
U1419B4H3w89	30.61	26054	6.89	106.64	47.20	45.26	178.70	0.74	11.52	5.10	4.89	19.30
U1419B4H4w3	31.12	26163	6.45	96.20	39.55	40.93	165.01	0.73	10.94	4.50	4.65	18.76
U1419B4H5w57	32.83	26668	6.46	102.80	40.77	42.32	162.04	0.73	11.70	4.64	4.82	18.44
U1419B4H5w83	33.04	26730	6.03	99.15	51.63	43.07	172.74	0.68	11.24	5.85	4.88	19.59
U1419B4H5w136	33.50	26891	6.19	612.34	49.48	221.16	177.12	0.70	69.00	5.58	24.92	19.96
U1419B4H7w32	35.14	27886	6.22	98.30	48.09	42.38	163.58	0.70	11.02	5.39	4.75	18.34
U1419D5H2w99	35.89	28266	6.46	97.84	42.35	41.10	168.59	0.73	11.03	4.78	4.64	19.01
U1419D5h3w29	36.52	28674	6.44	107.36	49.88	46.57	176.27	0.73	12.23	5.68	5.31	20.08
U1419D5H5w37	39.11	29386	6.22	117.77	55.10	52.18	201.28	0.72	13.66	6.39	6.05	23.35
U1419C6H2w98	41.10	29921	6.40	98.47	42.91	40.35	164.84	0.71	10.94	4.77	4.48	18.31
CAKE4783781	41.53	30036	5.25	104.00	42.00	45.00	172.00	0.63	12.48	5.04	5.40	20.63
U1419C6H3w107	42.41	30269	6.39	107.18	49.92	46.29	189.21	0.73	12.23	5.70	5.28	21.59
U1419C6H4w51	43.15	30469	6.59	100.85	45.59	43.48	173.19	0.73	11.14	5.04	4.80	19.13
CAKE4783891	44.10	30722	5.51	106.00	46.00	46.00	173.00	0.64	12.32	5.35	5.35	20.11
U1419C6H5w35	44.24	30761	6.77	108.65	48.27	47.59	186.26	0.73	11.77	5.23	5.16	20.18
U1419C6H6w45	45.58	31155	6.63	98.07	46.44	42.29	164.05	0.74	11.01	5.22	4.75	18.42
U1419C6H7w48	46.85	31563	6.59	120.11	41.99	51.58	180.56	0.73	13.22	4.62	5.68	19.87
U1419C6H7w67	47.02	31617	6.35	107.33	49.24	47.33	183.57	0.72	12.10	5.55	5.34	20.70
U1419D9H5w71	50.02	32569	6.73	95.83	36.94	41.19	164.46	0.75	10.71	4.13	4.60	18.37
U1419B7H2w85	52.06	33286	7.10	87.83	38.10	36.57	154.25	0.78	9.65	4.18	4.02	16.94
U1419B7H3w63	53.10	33633	7.00	89.57	40.88	36.93	150.95	0.77	9.82	4.48	4.05	16.55
U1419B7H5w44	53.84	33884	6.53	111.03	58.53	49.14	186.95	0.72	12.33	6.50	5.45	20.75
U1419B7H5w47	55.43	34418	6.41	103.55	47.75	43.05	174.87	0.72	11.59	5.35	4.82	19.58

Text Identif.	Depth (m) CCSFB	Age (a)	Fe (wt%)	Cr (ppm)	Cu (ppm)	Ni (ppm)	V (ppm)	Fe/Al	Cr/Al	Cu/Al	Ni/Al	V/Al
U1419B7H6w77	55.46	34428	5.87	109.60	51.87	47.44	188.24	0.68	12.77	6.05	5.53	21.94
U1419B7H6w95	56.96	34928	6.12	96.26	41.60	40.54	161.88	0.72	11.37	4.91	4.79	19.12
U1419B7H7w4	57.12	34981	7.18	114.95	54.01	48.23	196.98	0.76	12.23	5.75	5.13	20.96
U1419D10H3w13	58.26	35448	6.12	104.57	37.09	45.62	172.00	0.70	11.94	4.23	5.21	19.64
CUBE4785261	58.54	35605	5.69	116.00	50.00	50.00	186.00	0.67	13.57	5.85	5.85	21.76
U1419D10H3w99	58.99	35865	6.95	95.63	38.38	43.55	161.62	0.77	10.63	4.27	4.84	17.96
U1419D10H3w135	59.30	36040	6.66	110.86	37.49	48.75	185.74	0.74	12.28	4.15	5.40	20.58
CAKE4784331	59.78	36312	5.61	113.00	47.00	53.00	187.00	0.66	13.38	5.56	6.27	22.14
U1419D10H4w133	60.53	36732	6.49	111.37	55.42	48.39	166.35	0.77	13.20	6.57	5.73	19.71
CAKE4784431	62.38	37765	5.43	104.00	46.00	45.00	177.00	0.65	12.42	5.49	5.37	21.14
U1419E12H1w123	62.61	37883	6.36	104.32	45.94	45.46	173.52	0.72	11.76	5.18	5.13	19.57
U1419E12H1w146	62.78	37969	6.46	76.41	37.83	38.18	141.17	0.74	8.74	4.33	4.37	16.14
CUBE4785271	63.41	38255	5.34	106.00	47.00	46.00	175.00	0.65	12.90	5.72	5.60	21.29
U1419E12H2w104	63.58	38323	6.75	103.10	38.07	48.24	176.27	0.77	11.69	4.32	5.47	19.99
U1419E12H2w130	63.74	38382	6.09	119.14	45.44	55.78	179.22	0.70	13.73	5.24	6.43	20.65
U1419E12H3w97	64.58	38686	7.03	108.61	47.65	45.02	188.07	0.77	11.86	5.20	4.92	20.53
CAKE4784531	64.64	38708	5.54	110.00	55.00	50.00	182.00	0.65	12.94	6.47	5.88	21.41
U1419E12H5w54	66.44	39351	5.26	116.00	38.97	50.16	181.99	0.63	13.94	4.68	6.03	21.87
U1419E12H5w63	66.50	39373	6.26	103.40	44.72	43.31	172.60	0.72	11.96	5.17	5.01	19.96
U1419A9H2w93	66.97	39542	5.65	95.70	38.90	39.58	160.05	0.67	11.38	4.63	4.70	19.03
CUBE4786971	67.22	39632	5.46	107.00	51.00	47.00	175.00	0.65	12.81	6.11	5.63	20.95
U1419A9H3W17	67.81	39844	5.84	86.76	35.88	36.28	147.88	0.68	10.06	4.16	4.21	17.15
CAKE4784881	68.20	39987	4.88	95.00	47.00	42.00	163.00	0.61	11.87	5.87	5.25	20.37
U1419B12H2w33	68.37	40049	7.33	90.79	33.53	38.86	141.79	0.82	10.12	3.74	4.33	15.80
U1419B9H2w113	69.83	40583	6.23	103.95	45.25	42.44	171.06	0.71	11.84	5.15	4.84	19.49
CAKE4784991	70.39	40790	4.83	93.00	45.00	42.00	157.00	0.61	11.70	5.66	5.28	19.75
CUBE4786981	71.16	41067	4.93	94.00	45.00	43.00	161.00	0.61	11.72	5.61	5.36	20.08
U1419B9H3w33	71.30	41119	6.38	87.31	34.06	36.43	145.55	0.74	10.08	3.93	4.21	16.80
U1419B9H5w107	72.87	41688	6.01	98.36	46.24	41.83	167.26	0.72	11.73	5.51	4.99	19.95
U1419B9H5w141	73.12	41778	5.71	100.99	43.94	45.28	185.05	0.67	11.90	5.18	5.34	21.81
U1419B9H6w54	73.55	41935	5.89	99.90	43.45	46.45	171.95	0.68	11.62	5.05	5.40	20.00
U1419B9H6w74	73.69	41986	6.33	106.96	41.81	41.63	161.17	0.71	11.97	4.68	4.66	18.04
U1419E14H2w78	74.83	42401	6.77	93.28	48.18	40.03	159.17	0.76	10.44	5.39	4.48	17.82
U1419E14H2w26	74.95	42445	6.01	122.83	46.42	54.03	194.10	0.69	14.18	5.36	6.24	22.41
CUBE4789071	75.96	42816	5.18	101.00	45.00	43.00	169.00	0.61	11.97	5.33	5.10	20.03
U1419E14H3w56	76.22	42910	5.82	127.51	48.64	57.81	195.58	0.68	14.85	5.66	6.73	22.78
U1419E14H3w73	76.34	42953	5.34	118.58	50.64	52.54	193.95	0.67	14.85	6.34	6.58	24.28
U1419A10H3w102	76.76	43110	6.46	92.09	37.75	38.57	159.05	0.72	10.32	4.23	4.32	17.83
U1419A10H3w105	76.78	43118	6.70	100.20	41.19	45.32	174.64	0.75	11.15	4.58	5.04	19.43
U1419A10H3w121	76.90	43165	6.78	97.36	42.56	41.17	165.37	0.75	10.82	4.73	4.58	18.38
U1419A10H4w15	77.21	43309	6.70	96.50	43.67	39.49	166.25	0.73	10.48	4.74	4.29	18.05
U1419A10H4w61	77.54	43476	6.17	97.65	44.82	43.41	169.17	0.72	11.40	5.23	5.07	19.75
U1419E15H1w109	77.63	43522	6.35	94.48	40.99	40.86	164.06	0.72	10.65	4.62	4.60	18.49
U1419E15H1w127	77.78	43599	6.14	124.54	49.24	57.00	191.80	0.71	14.42	5.70	6.60	22.20
CUBE4789081	78.10	43763	5.43	105.00	46.00	47.00	176.00	0.65	12.58	5.51	5.63	21.09
U1419E15H2w73	78.42	43930	6.99	101.30	47.55	40.91	163.52	0.74	10.76	5.05	4.35	17.37
U1419C12H1w131	79.65	44547	6.95	112.14	48.85	48.66	183.83	0.75	12.03	5.24	5.22	19.72
CUBE4789091	80.18	44808	5.52	115.00	37.00	50.00	180.00	0.65	13.53	4.35	5.88	21.18
U1419C12H2w81	80.29	44863	6.83	99.88	36.86	43.80	177.97	0.75	10.98	4.05	4.82	19.57
U1419C12H2w111	80.51	44973	7.03	108.52	43.38	46.25	183.35	0.75	11.60	4.64	4.94	19.60
U1419C12H3w28	80.94	45188	6.32	104.12	50.06	43.93	178.59	0.75	12.39	5.95	5.23	21.24
U1419D14H1w53	82.31	46048	6.73	98.03	47.73	44.37	170.26	0.77	11.16	5.43	5.05	19.39
U1419D16H1w91	82.60	46252	6.83	108.76	54.66	48.68	191.02	0.77	12.22	6.14	5.47	21.45
U1419D16H2w87	83.62	47109	6.95	107.90	51.76	47.56	181.99	0.77	12.02	5.77	5.30	20.27
U1419B1H1w139	85.12	48588	7.37	95.54	38.75	44.61	170.02	0.81	10.50	4.26	4.90	18.68
CAKE4785941	85.63	49141	5.50	119.00	41.00	50.00	188.00	0.67	14.38	4.96	6.04	22.72
U1419E17H3w49	87.12	51053	6.36	115.99	54.26	50.48	195.02	0.73	13.27	6.21	5.78	22.31

Text Identif.	Depth (m) CCSFB	Age (a)	Acc. rate (g/cm ² /ka)	Fe (g cm ⁻² ka ⁻¹)	Cr (mg cm ⁻² ka ⁻¹)	Cu (mg cm ⁻² ka ⁻¹)	Ni (mg cm ⁻² ka ⁻¹)	V (mg cm ⁻² ka ⁻¹)
U1419D2H2w80	6.88	16870	58.45	3.39	60.81	27.97	26.50	106.91
U1419D2H2w85	6.92	16880	556.90	29.44	565.19	261.37	245.15	979.72
CAKE4782041	7.51	17002	650.31	32.93	630.80	286.14	273.13	1047.00
U1419D2H4w65	9.32	17403	604.67	37.66	541.18	292.05	244.53	974.06
U1419D2H4w102	9.63	17480	543.34	31.14	521.06	276.18	228.46	921.88
CAKE4782141	10.08	17581	595.72	28.42	559.98	238.29	232.33	917.41
U1419D2H5w112	11.00	17719	904.79	57.88	911.21	430.05	407.79	1653.32
U1419E2H4w29	12.31	17912	917.98	56.62	975.27	447.79	413.37	1714.79
U1419E2H4w44	12.44	17931	910.01	56.99	715.12	299.78	313.38	1270.98
CAKE4782561	12.57	17950	917.16	45.74	898.81	431.06	403.55	1504.14
U1419E2H5w42	13.71	18128	872.10	52.65	871.36	339.53	331.26	1387.76
U1419E2H5w79	14.02	18180	811.84	51.22	1045.03	388.57	476.47	1540.68
U1419D3H3w29	16.84	19568	277.46	16.25	301.95	116.48	131.17	502.38
CAKE4782671	18.23	20467	211.67	10.30	205.32	78.32	86.79	336.56
U1419D3H5w43	19.52	20953	365.33	19.96	382.43	193.75	165.11	647.89
CAKE4782771	20.79	21519	310.01	15.37	303.81	114.70	127.11	508.42
CAKE4782871	23.36	23034	234.66	10.86	225.27	82.13	91.52	368.41
U1419E3H6w16	23.45	23220	68.38	3.95	69.41	29.65	29.58	116.50
U1419E3H6w33	23.59	23370	129.35	7.14	131.41	55.69	55.75	226.30
U1419E3H6w43	23.68	23417	260.96	14.48	257.03	87.05	102.54	375.48
U1419E3H7w37	24.88	23974	299.81	18.47	320.08	143.61	139.59	548.08
U1419D4H2w92	26.08	24497	319.73	20.38	339.07	144.04	140.62	581.39
U1419D4H2w111	26.25	24568	332.55	21.62	357.79	132.09	154.17	590.17
U1419D4H3w67	27.14	25058	254.07	13.48	245.06	163.46	117.98	419.19
U1419D4H3w75	27.19	25096	185.23	9.94	189.93	91.02	82.87	327.95
U1419D4H4w129	28.90	25712	389.19	24.46	386.99	181.01	159.67	599.15
U1419B4H3w89	30.61	26054	702.85	48.42	749.52	331.74	318.11	1255.99
U1419B4H4w3	31.12	26163	661.46	42.70	636.32	261.63	270.74	1091.48
U1419B4H5w57	32.83	26668	478.65	30.91	492.06	195.13	202.55	775.59
U1419B4H5w83	33.04	26730	481.34	29.02	477.25	248.52	207.31	831.47
U1419B4H5w136	33.50	26891	405.19	25.07	2481.12	200.48	896.11	717.67
U1419B4H7w32	35.14	27886	234.20	14.56	230.23	112.64	99.26	383.11
U1419D5H2w99	35.89	28266	280.74	18.14	274.68	118.89	115.38	473.30
U1419D5H3w29	36.52	28674	220.36	14.19	236.58	109.91	102.63	388.42
U1419D5H5w37	39.11	29386	520.93	32.41	613.49	287.03	271.82	1048.52
U1419C6H2w98	41.10	29921	535.17	34.27	526.98	229.64	215.94	882.18
CAKE4783781	41.53	30036	544.56	28.57	566.35	228.72	245.05	936.65
U1419C6H3w107	42.41	30269	543.25	34.74	582.25	271.19	251.47	1027.88
U1419C6H4w51	43.15	30469	534.66	35.26	539.23	243.76	232.47	926.01
CAKE4783891	44.10	30722	540.91	29.81	573.37	248.82	248.82	935.78
U1419C6H5w35	44.24	30761	543.86	36.82	590.90	262.52	258.82	1012.99
U1419C6H6w45	45.58	31155	493.15	32.71	483.62	229.03	208.53	808.99
U1419C6H7w48	46.85	31563	453.61	29.89	544.86	190.46	233.97	819.06
U1419C6H7w67	47.02	31617	455.86	28.96	489.26	224.46	215.76	836.84
U1419D9H5w71	50.02	32569	462.24	31.13	442.96	170.75	190.40	760.19
U1419B7H2w85	52.06	33286	418.60	29.70	367.66	159.49	153.08	645.69
U1419B7H3w63	53.10	33633	442.62	30.99	396.45	180.94	163.46	668.13
U1419B7H5w44	53.84	33884	434.63	28.38	482.56	254.39	213.56	812.55
U1419B7H5w47	55.43	34418	441.61	28.33	457.29	210.87	190.11	772.24

Text Identif.	Depth (m) CCSFB	Age (a)	Acc. rate (g/cm ² /ka)	Fe (g cm ⁻² ka ⁻¹)	Cr (mg cm ⁻² ka ⁻¹)	Cu (mg cm ⁻² ka ⁻¹)	Ni (mg cm ⁻² ka ⁻¹)	V (mg cm ⁻² ka ⁻¹)
U1419B7H6w77	55.46	34428	437.65	25.70	479.65	227.00	207.62	823.84
U1419B7H6w95	56.96	34928	446.27	27.29	429.59	185.66	180.91	722.43
U1419B7H7w4	57.12	34981	446.51	32.05	513.26	241.16	215.35	879.54
U1419D10H3w13	58.26	35448	363.81	22.28	380.42	134.92	165.96	625.75
CUBE4785261	58.54	35605	267.77	15.23	310.61	133.89	133.89	498.05
U1419D10H3w99	58.99	35865	257.23	17.88	245.99	98.72	112.01	415.72
U1419D10H3w135	59.30	36040	264.73	17.63	293.49	99.24	129.05	491.71
CAKE4784331	59.78	36312	264.50	14.84	298.89	124.32	140.19	494.62
U1419D10H4w133	60.53	36732	266.89	17.31	297.23	147.91	129.15	443.96
CAKE4784431	62.38	37765	269.04	14.60	279.80	123.76	121.07	476.19
U1419E12H1w123	62.61	37883	293.52	18.67	306.20	134.83	133.43	509.32
U1419E12H1w146	62.78	37969	299.00	19.31	228.47	113.11	114.15	422.11
CUBE4785271	63.41	38255	331.34	17.68	351.22	155.73	152.41	579.84
U1419E12H2w104	63.58	38323	378.97	25.60	390.72	144.27	182.81	668.01
U1419E12H2w130	63.74	38382	405.11	24.66	482.65	184.08	225.97	726.04
U1419E12H3w97	64.58	38686	417.22	29.32	453.14	198.81	187.83	784.66
CAKE4784531	64.64	38708	379.38	21.01	417.32	208.66	189.69	690.47
U1419E12H5w54	66.44	39351	425.14	22.35	493.19	165.69	213.24	773.73
U1419E12H5w63	66.50	39373	425.25	26.61	439.69	190.15	184.15	733.96
U1419A9H2w93	66.97	39542	420.19	23.73	402.13	163.47	166.29	672.51
CUBE4786971	67.22	39632	420.77	22.98	450.23	214.59	197.76	736.35
U1419A9H3W17	67.81	39844	424.33	24.78	368.14	152.25	153.96	627.52
CAKE4784881	68.20	39987	419.48	20.48	398.51	197.16	176.18	683.75
U1419B12H2w33	68.37	40049	405.44	29.73	368.11	135.93	157.54	574.86
U1419B9H2w113	69.83	40583	416.82	25.98	433.26	188.61	176.91	713.00
CAKE4784991	70.39	40790	412.68	19.94	383.79	185.70	173.32	647.90
CUBE4786981	71.16	41067	424.66	20.94	399.18	191.10	182.60	683.70
U1419B9H3w33	71.30	41119	420.14	26.79	366.81	143.10	153.08	611.52
U1419B9H5w107	72.87	41688	423.33	25.45	416.39	195.75	177.08	708.07
U1419B9H5w141	73.12	41778	424.41	24.25	428.61	186.48	192.17	785.36
U1419B9H6w54	73.55	41935	419.82	24.73	419.42	182.43	194.99	721.86
U1419B9H6w74	73.69	41986	422.47	26.73	451.85	176.64	175.86	680.87
U1419E14H2w78	74.83	42401	423.55	28.66	395.09	204.07	169.55	674.17
U1419E14H2w26	74.95	42445	423.93	25.48	520.72	196.79	229.05	822.86
CUBE4789071	75.96	42816	418.09	21.67	422.27	188.14	179.78	706.57
U1419E14H3w56	76.22	42910	433.30	25.23	552.51	210.76	250.49	847.45
U1419E14H3w73	76.34	42953	434.24	23.18	514.94	219.89	228.16	842.20
U1419A10H3w102	76.76	43110	413.57	26.72	380.86	156.12	159.52	657.79
U1419A10H3w105	76.78	43118	392.92	26.34	393.71	161.84	178.07	686.20
U1419A10H3w121	76.90	43165	393.85	26.71	383.46	167.63	162.16	651.32
U1419A10H4w15	77.21	43309	333.22	22.32	321.56	145.52	131.59	553.98
U1419A10H4w61	77.54	43476	306.01	18.89	298.82	137.15	132.84	517.68
U1419E15H1w109	77.63	43522	302.94	19.23	286.22	124.17	123.77	497.00
U1419E15H1w127	77.78	43599	302.06	18.56	376.18	148.73	172.17	579.34
CUBE4789081	78.10	43763	305.40	16.60	320.67	140.49	143.54	537.51
U1419E15H2w73	78.42	43930	294.13	20.55	297.96	139.86	120.33	480.97
U1419C12H1w131	79.65	44547	309.81	21.54	347.43	151.35	150.75	569.53
CUBE4789091	80.18	44808	315.81	17.43	363.19	116.85	157.91	568.46
U1419C12H2w81	80.29	44863	314.00	21.44	313.62	115.74	137.52	558.82
U1419C12H2w111	80.51	44973	310.08	21.79	336.51	134.52	143.40	568.54
U1419C12H3w28	80.94	45188	312.00	19.72	324.85	156.19	137.06	557.20
U1419D14H1w53	82.31	46048	248.95	16.75	244.04	118.82	110.46	423.86
U1419D16H1w91	82.60	46252	222.76	15.22	242.27	121.76	108.44	425.51
U1419D16H2w87	83.62	47109	186.37	12.95	201.10	96.47	88.65	339.18
U1419B1H1w139	85.12	48588	159.31	11.74	152.20	61.73	71.07	270.85
CAKE4785941	85.63	49141	143.88	7.92	171.22	58.99	71.94	270.50
U1419E17H3w49	87.12	51053	123.27	7.83	142.99	66.89	62.23	240.41

Sample identif.	Depth (m) CCSF-B	Age (a)	Sedimentation rate (cm/ka)	TOC (wt%)	BHT I (wt %)	BHT II (wt %)	BHTIso/ BHTtot	BHTtot
CYL4508042	6.87	16868	32.08548546	0.4557	0.0670	0.0148	0.1812	0.0819
CAKE4782041	7.51	17002	477.6383279	0.5441	0.0675	0.0178	0.2085	0.0853
CUBE4442622	9.31	17401	450.1849514	0.4212	0.0956	0.0128	0.1185	0.1084
CYL4508062	9.63	17480	399.3449886	0.3645	0.0539	0.0101	0.1506	0.0640
CAKE4782141	10.08	17581	446.5944609	0.4833	0.0471	0.0000	0.0000	0.0471
CYL4508072	10.99	17717	673.8315894	0.5514	0.0739	0.0250	0.2526	0.0989
CYL4508112	12.43	17930	676.7293328	0.4841	0.1094	0.0227	0.1719	0.1321
CAKE4782561	12.57	17950	670.7782522	0.6686	0.0509	0.0121	0.1905	0.0631
CYL4508122	13.70	18126	641.2603733	0.4146	0.0748	0.0319	0.2991	0.1067
CUBE4452892	16.83	19556	219.2154627	0.3475	0.2062	0.1197	0.3673	0.3259
CAKE4782671	18.23	20467	153.32569	0.5649	0.0564	0.0253	0.3096	0.0817
CUBE4453542	19.51	20949	265.7590493	0.4501	0.0718	0.0000	0.0000	0.0718
CAKE4782771	20.79	21519	225.3232969	0.4163	0.0986	0.0393	0.2848	0.1379
CUBE4474172	23.67	23412	152.0442804	0.4125	0.0793	0.0265	0.2505	0.1058
CUBE4454372	26.25	24568	222.643651	0.6675	0.0662	0.0143	0.1780	0.0806
CYL4508082	27.13	25050	182.7290439	0.4617	0.1068	0.0332	0.2370	0.1399
CUBE4412512	30.60	26052	346.3570358	0.4188	0.1098	0.0438	0.2850	0.1535
CUBE4413062	32.82	26665	362.7146353	0.5491	0.0812	0.0351	0.3022	0.1163
CUBE4413242	33.50	26891	299.6511845	0.6681	0.3420	0.0720	0.1738	0.4139
CUBE4455792	36.51	28670	169.4418475	0.4550	0.2126	0.1397	0.3965	0.3524
CAKE4783781	41.53	30036	367.6208987	0.6024	0.0553	0.0177	0.2424	0.0730
CUBE4430472	42.40	30266	375.3446828	0.5352	0.0715	0.0188	0.2088	0.0904
CAKE4783891	44.10	30722	372.5428932	0.5845	0.0899	0.0217	0.1945	0.1116
CUBE4431242	45.57	31152	342.8557076	0.4546	0.3023	0.0702	0.1885	0.3725
CUBE4431602	47.01	31614	310.8459891	0.3941	0.1014	0.0429	0.2975	0.1443
CUBE4416032	53.09	33629	301.9794608	0.5499	0.1696	0.0211	0.1105	0.1907
CYL4507952	55.43	34418	296.0194664	0.5530	0.0669	0.0054	0.0747	0.0723
CYL4507972	56.96	34928	300.1811674	0.4849	0.1811	0.0885	0.3282	0.2697
CUBE4785261	58.54	35605	234.1302406	0.6205	0.1612	0.0305	0.1593	0.1917
CAKE4784331	59.78	36312	175.2977731	0.5500	0.0396	0.0157	0.2840	0.0553
CAKE4784431	62.38	37765	178.7835988	0.4714	0.1132	0.0652	0.3653	0.1784
CYL4508152	62.71	37933	198.5041756	0.3249	0.2761	0.0586	0.1757	0.3347
CUBE4785271	63.41	38255	216.4928483	0.5182	0.0974	0.0537	0.3557	0.1511
CAKE4784531	64.64	38708	270.4717752	0.6523	0.0718	0.0128	0.1513	0.0846
CUBE4786971	67.22	39632	279.6279607	0.5529	0.1490	0.0451	0.2324	0.1941
CAKE4784881	68.20	39987	277.9336786	0.6384	0.0415	0.0000	0.0000	0.0415
CAKE4784991	70.39	40790	271.9784277	0.6339	0.1055	0.0154	0.1275	0.1209
CUBE4786981	71.16	41067	277.6836874	0.5585	0.1610	0.0355	0.1805	0.1964
CYL4507982	71.28	41112	270.8060799	0.4797	0.0608	0.0617	0.5039	0.1225
CUBE4421722	72.86	41684	276.6687972	0.5428	0.1053	0.0000	0.0000	0.1053
CUBE4789071	75.96	42816	273.2544643	0.5683	0.1230	0.0233	0.1593	0.1464
CYL4507852	76.89	43161	271.7338593	0.4807	0.0802	0.0390	0.3270	0.1192
CUBE4789081	78.10	43763	201.0598824	0.5958	0.1031	0.0610	0.3716	0.1641
CUBE4789091	80.18	44808	198.6427402	0.7209	0.2410	0.1256	0.3420	0.3666
CUBE4439972	83.31	46836	154.1745809	0.7263	0.0670	0.0982	0.5977	0.1653
CUBE4466582	84.97	48430	104.6147658	0.4874	0.2267	0.0000	0.0000	0.2267
CAKE4785941	85.63	49141	91.66170297	0.5661	0.0650	0.0135	0.1716	0.0785
CUBE4423032	87.49	51605	75.82256246	0.5248	0.1595	0.0000	0.0000	0.1595